Detecting and Understanding Extragalactic Lyman α Emission Using 3D Spectroscopy

Edmund Christian Herenz

Potsdam 2016

Detecting and Understanding Extragalactic Lyman α Emission Using 3D Spectroscopy

Edmund Christian Herenz

Dissertation
an der Mathematisch-Naturwissenschaftlichen Fakultät
der Universität Potsdam

vorgelegt von
Edmund Christian Herenz

Potsdam, den 1.6.2016

Erstgutachter: Prof. Dr. Lutz Wiskotzki
Zweitgutachter: Prof. Dr. Martin Roth

Published online at the
Institutional Repository of the University of Potsdam:
URN urn:nbn:de:kobv:517-opus4-102341
http://nbn-resolving.de/urn:nbn:de:kobv:517-opus4-102341

Abstract

In this thesis we use integral-field spectroscopy to detect and understand of *Lyman α* (Lyα) emission from high-redshift galaxies.

Intrinsically the Lyα emission at $\lambda_{\mathrm{Ly}\alpha} = 1215.67$Å is the strongest recombination line from galaxies. It arises from the 2p→1s transition in hydrogen. In star-forming galaxies the line is powered by ionisation of the interstellar gas by hot O- and B- stars. Galaxies with star-formation rates of $1-10\ \mathrm{M_{\odot}yr^{-1}}$ are expected to have intrinsic Lyα luminosities of $\sim 10^{42}-10^{43}\,\mathrm{erg\,s^{-1}}$ corresponding to fluxes $\sim 10^{-17}-10^{-16}\,\mathrm{erg\,s^{-1}cm^{-2}}$ at redshifts $z \gtrsim 3$, where Lyα is easily accessible with ground-based telescopes. However, star-forming galaxies do not show these expected Lyα fluxes. Primarily this is a consequence of the high-absorption cross-section of neutral hydrogen for Lyα photons $\sigma_{\mathrm{Ly}\alpha} \sim 10^{-14}\mathrm{cm^2}$. Therefore, in typical interstellar environments Lyα photons have to undergo a complex radiative transfer. The exact conditions under which Lyα photons can escape a galaxy are poorly understood.

Here we present results from three observational projects. In Chapter 2, we show integral field spectroscopic observations of 14 nearby star-forming galaxies in Balmer α radiation (Hα, $\lambda_{\mathrm{H}\alpha} = 6562.8$Å). These observations were obtained with the *Potsdam Multi Aperture Spectrophotometer* at the *Calar-Alto 3.5m Telescope*. Hα directly traces the intrinsic Lyα radiation field. We present Hα velocity fields and velocity dispersion maps spatially registered onto *Hubble Space Telescope* Lyα and Hα images. From our observations, we conjecture a causal connection between spatially resolved Hα kinematics and Lyα photometry for individual galaxies. Statistically, we find that dispersion-dominated galaxies are more likely to emit Lyα photons than galaxies where ordered gas-motions dominate. This result indicates that turbulence in actively star-forming systems favours an escape of Lyα radiation.

Not only massive stars can power Lyα radiation, but also non-thermal emission from an accreting super-massive black hole in the galaxy centre. If a galaxy harbours such an active galactic nucleus, the rate of hydrogen-ionising photons can be more than 10^3 times higher than that of a typical star-forming galaxy. This radiation can potentially ionise large regions well outside the main stellar body of galaxies. Therefore, it is expected that the neutral hydrogen from these circum-galactic regions shines fluorescently in Lyα. Circum-galactic gas plays a crucial role in galaxy formation. It may act as a reservoir for fuelling star formation, and it is also subject to feedback processes that expel galactic material. If Lyα emission from this circum-galactic medium (CGM) was detected, these important processes could be studied in-situ around high-z galaxies. In Chapter 3, we show observations of five radio-quiet quasars with PMAS to search for possible extended CGM emission in the Lyα line. However, in four of the five objects, we find no significant traces of this emission. In the fifth object, there is evidence for a weak and spatially quite compact Lyα excess at several kpc outside the nucleus. Using fake source-recovery experiments we calculate detection limits of 10^{-16}–$10^{-17}\mathrm{erg\,s^{-1}cm^{-2}arcsec{-}2}$ for extended, smoothly distributed Lyα emission. The faintness of these structures is consistent with the idea that radio-quiet quasars typically reside in dark matter haloes of modest masses. While we were not able to detect Lyα CGM emission, our upper limits provide constraints for the new generation of IFS instruments at 8–10m class telescopes.

The *Multi Unit Spectroscopic Explorer* (MUSE) at *ESOs Very Large Telescope* is such an unique instrument. One of the main motivating drivers in its construction was the use as a survey instrument for Lyα emitting galaxies at high-z. Currently, we are conducting such a survey that will cover a total area of $\sim 100\,\mathrm{arcmin^2}$ with 1 hour exposures for each $1\,\mathrm{arcmin^2}$ MUSE pointing. As a first result from this survey we present in Chapter 5 a catalogue of 831 emission-line selected galaxies from a $22.2\,\mathrm{arcmin^2}$ region in the *Chandra* Deep Field South. In order to construct the catalogue, we developed and implemented a novel source detection algorithm – LSDCat – based on matched filtering for line emission in 3D spectroscopic datasets (Chapter 4). Our catalogue contains 237 Lyman α emitting galaxies in the redshift range $3 \lesssim z \lesssim 6$. Only four of those previously had spectroscopic redshifts in the literature. We conclude this thesis with an outlook on the construction of a Lyα luminosity function based on this unique sample (Chapter 6).

Zusammenfassung

In der vorliegenden Doktorarbeit präsentieren wir Resultate aus drei integralfeldspektroskopischen Beobachtungskampagnen die mit der Intention Lyman α (Lyα) Strahlung von hoch-rotverschobenen Galaxien zu detektieren und zu verstehen durchgeführt wurden.

Die Lyα Emissionslinie im ultravioletten Teil des elektromagnetischen Spektrums ($\lambda_{\mathrm{Ly}\alpha}$ = 1215.67Å) ist intrinsisch die stärkste Rekombinationslinie im Linienspektrum sternbildender Galaxien. Die Linie ist eine Folge der Ionisation des interstellaren Gases durch heiße O- und B- Sterne. Man erwartet von Galaxien mit Sternentstehungsraten $1-10$ $\mathrm{M}_{\odot}\mathrm{yr}^{-1}$ intrinsische Lyα Leuchtkräfte von $\sim 10^{42}-10^{43}\,\mathrm{erg\,s}^{-1}$, was bei Rotverschiebungen von $z \sim 3$, bei denen Lyα mit bodengebundenen Teleskopen zu beobachten ist, einem Strahlungsstrom von $\sim 10^{-17}-10^{-16}\,\mathrm{erg\,s}^{-1}\mathrm{cm}^{-2}$ entspricht. Allerdings werden nicht von allen sternbildenen Galaxien derartige Lyα Strahlungsströme gemessen. Dies ist in erster Linie eine direkte Konsequenz des hohen Absorptionsquerschnitts von neutralem Wasserstoff für Lyα Photonen. Deshalb erfahren Lyα Photonen einen komplexen Strahlungstransportprozess in typischen interstellaren Umgebungen. Die exakten Bedingungen bei denen Lyα Strahlung eine Galaxie verlassen sind noch nicht hinreichend gut verstanden.

Diesbezüglich werden in Kapitel 2 dieser Arbeit integralfeldspektroskopische Beobachtungsergebnisse der Balmer α Strahlung (Hα, $\lambda_{\mathrm{H}\alpha}$ = 6562.8Å) von 14 nahen sternbildenden Galaxien gezeigt. Die Beobachtungsdaten wurden mit dem Potsdam Multi Aperture Spectrophotometer (PMAS) am Calar Alto 3.5m Teleskop gewonnen. Hα Strahlung ist eine direkte Kopie des intrinischen Lyα Strahlungsfeldes der Galaxien. Wir zeigen unsere Hα Geschwindigkeitsfelder und Geschwindigkeitsdispersionsfelder räumlich überlagert zu Hubble-Weltraumteleskop-Bildaufnahmen der Lyα und Hα Strahlungsströme. Aus diesen Beobachtungen können wir schlussfolgern, dass in einigen Galaxien kausale Zusammenhänge zwischen der Hα-Kinematik und der Lyα-Photometrie bestehen. Statistisch signifikant finden wir, dass Galaxien, bei denen chaotische Dispersionsbewegungen dominieren, wahrscheinlicher Lyα Strahlung abgeben als Galaxien bei denen die Gasbewegungen durch geordnete Bewegungen dominiert sind. Dieses Resultat ist ein Indiz dafür, dass Turbulenz im interstellaren Medium aktiv sternbildender Galaxien schafft, welche ein Austreten der Lyα-Strahlung begünstigen.

Neben massereichen Sternen kann nicht-thermische Strahlung eines akretierenden supermassereichen schwarzen Loches eine weitere Energiequelle zur Erzeugung von Lyα Strahlung sein. Wenn eine Galaxie einen solchen aktiven Galaxienkern enthält, kann die Rate der ionisierenden Photonen 10^3-mal höher sein als bei einer normalen sternbildenden Galaxie. Diese Strahlung hat das Potential große Bereiche weit ausserhalb der Sternansammlungen der Galaxien zu ionisieren. Deshalb ist zu erwarten, dass der neutrale Wasserstoff in diesen zirkum-galaktischen Gebieten in Lyα-Strahlung fluoresziert. Dieses zirkum-galaktische Gas spielt eine wesentliche Rolle bei der Entwicklung von Galaxien. Zum Einen ist es das Reservoir aus denen Sternentstehungsprozesse ihr Gas beziehen, zum Anderen ist es Wechselwirkungsprozessen ausgesetzt, bei denen Gas aus der Galaxie hinausgeschleudert wird. Wenn Lyα-Strahlung dieses zirkum-galaktischen Mediums detektiert werden könnte, ließen sich diese fundamentalen Prozesse der Galaxienentwicklung detaillierter studieren. In Kapitel 3 dieser Arbeit zeigen wir PMAS Beobachtungsdaten von 5 radio-leisen Quasaren in denen wir nach dieser ausgedehnten Lyα-Strahlung gesucht haben. Jedoch haben wir für 4 unserer Quasare keine signifikanten Spuren dieser ausgedehnten Strahlung entdecken können. Im fünften Objekt finden wir in Entfernung von einigen Kiloparsec zum Kern Anzeichen für eine schwache und räumlich eher kompakte Quelle. Wir bestimmen unser Detektionslimit von 10^{-16}–$10^{-17}\mathrm{erg\,s}^{-1}\mathrm{cm}^{-2}\mathrm{arcsec}^{-2}$ für ausgedehnte Lyα-Strahlung in dem wir künstlich derartige Quellen in unsere Daten implantieren und sie wiederzufinden versuchen. Derartig schwache Flüsse von solchen Strukturen erscheinen konsistent mit der Annahme, dass radio-leise Quasare sich in Halos aus dunkler Materie mit eher moderaten Massen befinden. Obwohl wir nicht direkt Lyα-Strahlung vom zirkum-galaktischen Medium detektieren konnten, sind unsere Detektionsgrenzen von Nutzem bei der Planung von diesbezüglichen Beobachtungen mit der neuen Generation von Integralfeldspektrographen an 8–10 m Teleskopen.

Ein derartiges Instrument ist der Multi Unit Spectroscopic Explorer (MUSE) am ESO Very Large Telescope. Einer der Hauptbeweggründe für dessen Konstruktion war die Verwendung als Durchmusterungsinstrument für Lyα emittierende Galaxien bei hohen Rotverschiebungen. Aktuell führen wir eine derartige Durchmusterungskampagne durch. Nach deren Abschluss, werden wir eine Fläche von $100\,\mathrm{arcmin}^2$ durchmustert haben. In Kapitel 5 dieser Arbeit präsentieren wir als erstes Resultat einen Katalog von 831 Emissionslinienselektierten Galaxien in einer $22.2\,\mathrm{arcmin}^2$ großen Region im Chandra Deep Field South. Um diesen Katalog zu erzeugen, haben wir eine neuartige Quellendetektionsmethode für integralfeldspektroskopische Datensätze entwickelt und implementiert (Kapitel 4). Unser Katalog enthält 237 Lyα emittierende Galaxien bei Rotverschiebungen $3 \lesssim z \lesssim 6$. Aufgrund ihrer geringen Kontinuumsflussdichten existierten zuvor nur von 4 dieser Galaxien spektroskopische Rotverschiebungen. Als Abschluss dieser Arbeit präsentieren wir einen Ausbick bezüglich der Konstruktion einer Leuchtkraftfunktion dieser einzigartigen Lyα Galaxienstichprobe (Kapitel 6.)

Contents

Chapter 1

Introduction

1.1 Motivation and general framework

One major goal of astrophysics is to understand the evolutionary processes that shape galaxies. Light or, more generally, electromagnetic radiation is the main carrier of information by which these processes can be studied observationally[1]. The timescales involved in galaxy evolution are, however, extremely large. For example, the sun orbits the centre of the Milky Way at a period of $200-250\times10^6$ yr, and of similar magnitude are the timescales over which major galaxy mergers happen (e.g. Toomre & Toomre 1972). Thus, time resolved studies of stellar and gaseous motions relevant to galaxy evolution are, with a few exceptions, impossible. Nevertheless, due to the finite speed of photons we can observe light from the universe of the past. Therefore, telescopes can act as time-machines allowing us to reconstruct galaxy formation and evolution as it happened.

Not only are the more distant galaxies further away in time. we also observe that the further away they are, the more redshifted their light appears (Slipher 1917; Hubble 1929)[2]. Redshift refers to a stretching of the electromagnetic spectrum of a distant extragalactic source according to

$$\lambda_{\rm obs.} = (1+z)\times\lambda_{\rm em.}\ , \tag{1.1}$$

where $\lambda_{\rm em.}$ is the emitted wavelength, $\lambda_{\rm obs.}$ is the observed wavelength, and z parametrises the redshift.

It is now widely accepted that redshift from distant extragalactic sources arises from an expansion of the universe (e.g., Davis & Lineweaver 2004; Jackson 2015). In particular in a general-relativistic description of a homogeneous and isotropic universe, this cosmic expansion is driven by the energy-matter content of the universe. According to the observationally well-established cosmological concordance model, it appears that we exist in a universe that originated in a space-time singularity 13.8×10^9 years ago (big bang), and that is dominated by an unknown form of energy (dark energy, e.g. Carroll 2001) and an unknown manifestation of mass (dark matter, e.g. Sumner 2002; Lahav & Suto 2004). Quantitatively, the free parameters of this so-called ΛCDM model that are relevant for this thesis are observationally inferred to be $\Omega_M = 0.3$, $\Omega_\Lambda = 0.7$, and $h = 0.7$ (Jarosik et al. 2011, to one significant figure). Here Ω_M and Ω_Λ

[1] Gravitational waves also carry information about astrophysical processes. Indeed, during the work on this thesis gravitational waves from an extragalactic black hole merger where observed for the first time (Abbott et al. 2016).

[2] The discovery of the distance–redshift relation is commonly attributed to Hubble (1929). However, as noted by Peacock (2013) the redshifts used by Hubble in his 1929 paper were already published by Slipher (1917) and most of Hubble's distances where flawed.

refer to the present-day contribution of all matter and dark energy (related to the cosmological constant Λ in *Einstein*'s field equation), respectively. All matter refers to the combined contribution of baryonic and dark matter, with the former contributing only $\sim 15\%$ to Ω_M. The Ω's are dimensionless, since they express the ratio of the total density to a critical density that would halt the expansion of the universe. Moreover, h is the dimensionless present-day value of the *Hubble* constant $H_0 = 100\,h\,\mathrm{km\,s^{-1}Mpc^{-1}}$ that parametrises the slope of the local distance-redshift relation, i.e., the rate at which the universe expands now (see Croton 2013, for possible pitfalls when using dimensionless h). In the context of this thesis these values are important when converting observed quantities (e.g., fluxes, flux-densities, or angular sizes) to physical quantities (e.g., luminosities, luminosity-densities, or sizes) of distant high-redshift galaxies (see, e.g., Hogg 1999 or Wright 2006 for the relevant formalism), and whenever such a conversion occurs above values are assumed. More generally, in the context of galaxy formation and evolution, the cosmological model defines the canvas on which structure formation processes occur.

In the ΛCDM model the dark matter is cold (which is the origin of the abbreviation CDM $\hat{=}$ "*C*old *D*ark *M*atter"). That means it consists of non-relativistic collisionless particles that evolve exclusively under gravitational forces. After the big bang, quantum fluctuations result in small density perturbations in the primordial matter field. With the universe's expansion they evolve into more over-dense regions. Over time these over-dense regions grow into bound structures – so called "dark matter haloes" – that are much denser than the mean cosmic density. Numerical simulations establish that structure formation proceeds hierarchically (e.g. Loeb 2013): At early times most of the dark matter is in low-mass halos and that merge over time to form high-mass halos. Dark-matter haloes are essentially the potential wells into which the baryonic matter flows to form stars and galaxies. A complete picture of galaxy formation and evolution must thus include the interplay between the hierarchical growth of dark-matter haloes, the fuelling and ignition of star-formation processes, and the regulation (or quenching) by feedback processes. In order to build this picture we have to observationally infer physical parameters such as star-formation rates, stellar masses, dark-matter halo masses, ages of stellar populations, dust contents, chemical compositions, and kinematical properties of high-z galaxies.

The current generation of powerful 8 – 10m telescopes (e.g., the European Southern Observatory's *Very Large Telescope*, in operation since 1999; see Renzini 2009) and the *Hubble* Space Telescope (launched 1990; see Dalcanton 2009) allow to collect light from galaxies at distances where the age of the universe was less than $\sim$5% of its present age and its size was $\lesssim$10% of its present size (see Zitrin et al. 2015 and Oesch et al. 2016 for the most recent redshift records of spectroscopically confirmed galaxies at $z = 8.68$ and $z = 11.1$). This "*expansion of exploration*" (Ellis 2008) has revolutionised our knowledge of galaxies in the first billion years of cosmic time (see e.g. reviews by Shapley 2009, 2011; Dunlop 2013).

Two methods are mainly used to detect young star-forming galaxies in high-z surveys: UV selection targeting the Lyman break and Lyman α (Lyα) emitter selection.

The UV selection method is based on the rest-frame UV colours of galaxies. Specifically, it exploits the expected significant decrease of rest-frame Lyman-continuum ($\lambda < 912$Å) emission in the spectral energy distribution of distant galaxies. This wavelength of the so-called Lyman break corresponds to a photon energy of $h\nu > 13.6\,\mathrm{eV}$. These photons are able to ionise hydrogen – the most abundant element in the universe. Now, UV bright galaxies display the Lyman break in their spectral energy distribution due to a combination of the 912Å break in stellar photospheres and photo-electric absorption in the interstellar medium (see Sect. 1.2 below). Moreover, at redshifts $z \gtrsim 4.5$ also the intervening neutral hydrogen in the intergalactic medium starts to attenuate the Lyman continuum. At very high redshifts ($z \gtrsim 6$) the path length to the observer is so long that even absorption of $\lambda = 1216$Å Lyα photons in denser clouds along

the line-of-sight becomes relevant. Hence, for those high-z galaxies a significant spectral break is expected already at a rest-frame wavelength of $\lambda = 1216$Å. These breaks are observed by employing a set of different broad-band filters in a survey campaign. Then objects detected in the redder bands, but undetected in the bluer bands, are selected (Shapley 2011).

The Lyα selection technique targets objects that show a large Lyα emission-line equivalent width. As we will show in the next section, this emission line is intrinsically expected to be the brightest in young, actively star-forming galaxies. Wide-area surveys targeting this emission line often employ narrow-band filters and a set of additional broad-band filters. In contrast to the Lyman-break selection, this technique preferentially selects objects that show faint continua.

However, due to the high absorption cross-section of neutral hydrogen Lyα photons cannot directly escape from a galaxy. Instead, they undergo a complex radiative transfer before they eventually can leave the galaxy. The numerous scatterings in this process increase the path length of the photons and thus also make them susceptible for destruction by dust. Currently it is not fully understood what conditions favour the escape of Lyα radiation from galaxies.

In the following Sect. 1.2 we will explain why Lyα radiation is created in all star-forming galaxies. We also outline the basics of the Lyα radiative transfer. In Sect. 1.3 we explain the structure of this thesis. For a more detailed introduction to each of the topics the reader is referred to the individual introductions.

1.2 Lyman α radiation from galaxies

Kennicutt (1998) derived, using a population-synthesis model for a galaxy with solar abundances and assuming that stars populate the main sequence according to the Salpeter (1955) initial mass function, that constant a star-formation rate (SFR) of $1\,\mathrm{M_\odot yr^{-1}}$ leads to a hydrogen-ionising photon-production rate $\dot{N}(h\nu > 13.6\,\mathrm{eV}) \approx 10^{53}\mathrm{s^{-1}}$ (h is the Planck constant – $h = 4.135\,\mathrm{eV\,s^{-1}}$ and ν denotes the frequency):

$$\mathrm{SFR}[\mathrm{M_\odot\,yr^{-1}}] = 1.08 \times 10^{-53}\,\dot{N}(h\nu > 13.6\,\mathrm{eV})\,[\mathrm{s^{-1}}] \tag{1.2}$$

Basically only luminous hot O- and B- stars with lifetimes $< 20 \times 10^6$ yr and masses $> 20\,\mathrm{M_\odot}$ contribute significantly to the ionising-photon output of such a population. In photoionisation equilibrium the hydrogen ionisations in the interstellar medium are balanced by the recombinations of electrons and protons: $\dot{N}_\mathrm{rec} \equiv \dot{N}(h\nu > 13.6\,\mathrm{eV})$.

Following a recombination the hydrogen atom is in an excited state denoted by the integral quantum numbers n (principal quantum number) and l (orbital quantum number), where always $l \leq n$. In the following we denote such a state as (n, l). The energy bound in this configuration is $-13.6\,\mathrm{eV} / n^2$ and thus does not depend[3] on l. The probability rate that the hydrogen atom with its electron in configuration (n, l) spontaneously emits a photon with energy $E_\mathrm{nm} = -13.6\,\mathrm{eV} \times (m^{-1} - n^{-2})$ is given by the Einstein coefficient $A_{nl,mk}$ for spontaneous emission. It is calculated using an overlap-integral over the wave functions of the involved states (n, l) and (m, k) with the electric dipole moment (Gordon 1929; Hoang-Binh 1990). This integral is zero if $m \neq l \pm 1$. This selection rule means that photons are only produced in transitions $(n, l) \rightarrow (m < n, l \pm 1)$. The lifetime of an excited state is given by $\tau_{nl} = (\sum_{m<n,k=l\pm1} A_{nl,mk})^{-1}$ and its typically of the order $\sim 10^{-5} \ldots 10^{-8}$ s. Hence a recombination event results in an almost instantaneous emission of a series of characteristic photons in a so called recombination cascade.

[3]Neglecting fine-structure due to the electron spin. However, the effect is minute with a correction $\sim 1/(137)^2$ (fine structure constant).

The superposition of all those photons from all hydrogen recombination events result in the characteristic hydrogen emission lines from star-forming galaxies. The transitions $m - n = \{1, 2, 3, \dots\}$ are designated by the lower case letters of the Greek alphabet $\{\alpha, \beta, \gamma, \dots\}$ and the series corresponding to the lower levels $n = 1, \dots 6$ are named in honour of the spectroscopists who first observed them: $n = 6$: *Humphreys*, $n = 5$: *Pfund*, $n = 4$: *Brackett*, $n = 3$: *Paschen*, $n = 2$: *Balmer*, and $n = 1$: *Lyman*. Only the Balmer series (abbreviated by an H) is visible with ground-based telescopes in the optical. Its first few transitions correspond to the wavelengths $\lambda_{H\alpha} = 6563$Å, $\lambda_{H\beta} = 4861$Å, $\lambda_{H\gamma} = 4340$Å, and $\lambda_{H\delta} = 4101$Å (e.g., Lang 1999). The Paschen, Brackett, Pfund, and Humphreys series are observable infrared. The Lyman series, however, is in the ultra-violet part of the electromagnetic spectrum and so it is generally not accessible from the ground unless the emission stems from a very distant galaxy whose light is redshifted according to Eq. (1.1) to wavelengths $\gtrsim 300$Å.

We now present a simple approximation why the Lyα line resulting from the transition $(2, 2) \rightarrow (1, 1)$ is expected to be the strongest line of the hydrogen recombination spectrum. Neglecting Lyβ, Lyγ, and higher Lyman transitions, two-thirds of all possible recombination cascades end up at the $(2, 2)$-state while one-third ends up at the $(2, 1)$-state. This is a direct consequence of the selection rule $(n, l) \rightarrow (m < n, l \pm 1)$. Thus also only the $(2, 2)$-state can lead to the production of a Lyα photon[4]. However, this means that in this simplified scenario two thirds of all ionising photons end up as Lyα emission.

Utilising the conversion between the rate of ionising photons and star-formation rates presented in Eq. (1.2) in this scenario, we get for the Lyα luminosity $L_{\mathrm{Ly}\alpha}$ of a star-forming galaxy:

$$L_{\mathrm{Ly}\alpha}[\mathrm{erg\,s^{-1}}] = 9.9 \times 10^{41}\,\mathrm{SFR}[\mathrm{M_\odot\,yr^{-1}}]\,. \tag{1.3}$$

This means in that under our simplifying assumptions we expect Lyα luminosities of $L_{\mathrm{Ly}\alpha} \sim 10^{42} \dots 10^{43}\,\mathrm{erg\,s^{-1}}$ from high-z galaxies that form stars at rates of $1 \dots 10\,\mathrm{M_\odot\,yr^{-1}}$. For galaxies at $z = \{3, 5, 7\}$ this corresponds to observable Lyα fluxes of $F_{\mathrm{Ly}\alpha} = \{1.3 \times 10^{-17\cdots-16}, 3.8 \times 10^{-18\cdots-17}, 1.8 \times 10^{-18\cdots-17}\}\,\mathrm{erg\,s^{-1}cm^{-2}}$. With moderate time investments these line fluxes are well within the reach of current 8–10 m class telescopes.

The above argument is essentially a quantitatively more correct version of the original Partridge & Peebles (1967) argument for why star-forming "primeval" galaxies at high-z can be optimally detected in Lyα radiation. However, our argument concerning the conversion of hydrogen-ionising photons into Lyα contains three simplifying assumptions:

1. We implicitly assumed that all possible recombinations into excited states (n, l) are equally likely.
2. We asserted that all downward transitions $(n, l) \rightarrow (m < n, l \pm 1)$ have equal probability.
3. We already noted that we neglected all other Lyman-series transitions $(n, 2) \rightarrow (1, 1)$.

Of course, the problem can be formalised without the simplifying assumptions (Dijkstra 2014). Generally, the probability rate per volume density of a recombination into a state (n, l) is expressed as the state-specific recombination coefficient $\alpha_{nl}(T)$ that depends on the temperature T of the gas. Recombination coefficients are typically given in $\mathrm{cm^3\,s^{-1}}$ and are tabulated in, e.g., Osterbrock & Ferland 2006. We can now calculate the probability that in photoionisation equilibrium an ionising photon is converted into Lyα emission as

$$P(h\nu > 13.6\,\mathrm{eV} \rightarrow \mathrm{Ly}\alpha) = \sum_{n=1\vee2}^{\infty} \sum_{l=0}^{n-1} \frac{\alpha_{nl}(T)}{\alpha_{\mathrm{tot}}(T)} P(n, l \rightarrow \mathrm{Ly}\alpha)\,. \tag{1.4}$$

[4]The one-third of recombination cascades ending up at the $(2, 1)$-state decays in forbidden transition with a typical lifetime of 0.122 s into two photons of energy $\gamma h\nu_{12}$ and $h\nu_\gamma$, with $\gamma = \nu_\gamma/\nu_{12}$.

Here $P(n, l \rightarrow \mathrm{Ly}\alpha)$ is the probability that a given state can cascade through the $(2, 2)$ level to emit a Lyα photon. This probability has to be calculated from the recursion $P(n, l \rightarrow \mathrm{Ly}\alpha) = \sum_{n'l'} P(n', l' \rightarrow \mathrm{Ly}\alpha) P(n', l' \rightarrow n, l)$. Here, $P(n', l' \rightarrow n, l)$ is the probability for a transition $(n', l') \rightarrow (n, l)$ that is the product of the Einstein coefficient with the lifetime of the (n', l')-state (see above), i.e. $P(n', l' \rightarrow n, l) = A_{n'l',nl}\tau_{n'l'} = A_{n'l',nl}(\sum_{m<n',k=l'\pm1} A_{n'l',mk})^{-1}$. The factor $\frac{\alpha_{nl}(T)}{\alpha_{\mathrm{tot}}(T)}$ in the sum of Eq. (1.4), with $\alpha_{\mathrm{tot}}(T) = \sum_{n=1\vee2}^{\infty} \sum_{l=0}^{n-1} \alpha_{nl}(T)$, can be interpreted as the probability of a particular recombination happening in a nebula with temperature T.

While we now correctly take into account the neglected effects in assumptions 1 and 2 above, we indicated with $n = 1\vee2$ as the starting value for the summation in (1.4) that we can distinguish between two cases.

- Case A: $n = 1$ - Lyman transitions are not ignored.
- Case B: $n = 2$ - Lyman transitions are ignored. In this case also all $A_{nl,11}$ Einstein coefficients have to be artificially set to 0.

For these two cases the probability for a hydrogen-ionising photon in gas of $T = 10^4$K being converted into a Lyα photon is (Dijkstra 2014):

$$P(h\nu > 13.6\,\mathrm{eV} \rightarrow \mathrm{Ly}\alpha, \mathrm{Case\,A}) = 0.41 \tag{1.5}$$

$$P(h\nu > 13.6\,\mathrm{eV} \rightarrow \mathrm{Ly}\alpha, \mathrm{Case\,B}) = 0.68 \tag{1.6}$$

Notably, in the "Case B" scenario, the value is very close to $P(h\nu > 13.6\,\mathrm{eV} \rightarrow \mathrm{Ly}\alpha \approx 2/3$ that was conjectured with all simplifying assumptions above. Considering the temperature dependence, Cantalupo et al. (2008) show that in Case B $P(h\nu > 13.6\,\mathrm{eV} \rightarrow \mathrm{Ly}\alpha)$ varies very little for T between $\sim 10^2$ to $\sim 10^5$K. Even in the "Case A" scenario almost half of the ionising photons are converted into Lyα.

However, it is indeed the "Case B" scenario that is valid in most interstellar and circumgalactic environments. The reason for this is the high absorption cross-section for Lyman series photons by neutral hydrogen. The "Case B" approximation (a terminology originally introduced by Baker & Menzel 1938, see also Zanstra 1927) states that there exits a balance between emission of Lyman-series photons and so-called resonant absorptions of those photons. Essentially this leads to a complete conversion of all higher Lyman series photons into Lyα photons.

Specifically for the resonant absorption of Lyα photons the absorption cross-section in the rest-frame of a hydrogen atom in a gas is calculated via

$$\sigma_{\mathrm{Ly}\alpha}(\nu) = \sigma_0 \times \phi(\nu) \tag{1.7}$$

with

$$\sigma_0 = 5.88 \times 10^{-14} \sqrt{T_4}\,\mathrm{cm}^2 \tag{1.8}$$

and

$$\phi(\nu) = \frac{a}{\pi} \int_{-\infty}^{+\infty} \frac{\exp(-y^2)}{(x-y)^2 + a^2}\,\mathrm{d}y\,. \tag{1.9}$$

Here $\phi(\nu)$ is the Voigt function with $x = (\nu - \nu_{\mathrm{Ly}\alpha})/\Delta\nu_D$, where $\Delta\nu_D$ is the Doppler broadening full width at half maximum: $\Delta\nu_D \propto \sqrt{T}$. The Voigt profile accounts for the Doppler broadening due to random motions of the H I particle and natural Lorentz broadening. The latter is a consequence of the *Heisenberg* uncertainty principle. In Eq. (1.8) T_4 is the temperature in 10^4K. The numerical value in Eq. (1.8), modulo some fundamental constants, is determined by the Einstein coefficient for the Lyα transition ($A_{22,11} = 6.25 \times 10^{-8}\mathrm{s}^{-1}$, e.g. Lang 1999; Osterbrock & Ferland 2006; Dijkstra 2014). Moreover, the Voigt parameter a in Eq. (1.9) is given as

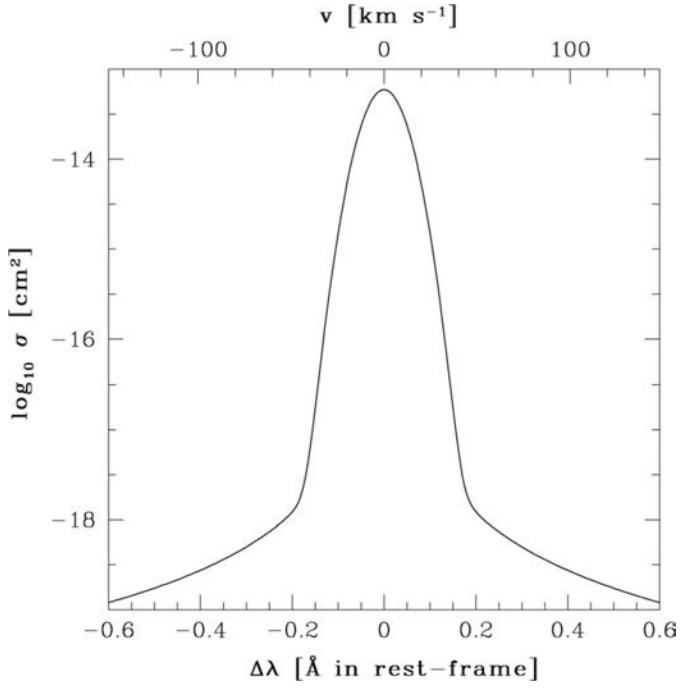

Figure 1.1: Wavelength dependence of the Lyα absorption cross-section in an atom's rest-frame for a gas with T =10^4K (from Santos 2004). The bottom axis shows $\Delta\lambda = \lambda_{\mathrm{Ly}\alpha} - \lambda$ in Å and the top axis shows the velocity difference $v = c\Delta\lambda/\lambda_{\mathrm{Ly}\alpha}$

the ratio of the Einstein coefficient to the thermal Doppler broadening width, i.e. numerically $a = 4.7 \times 10^{-4}(1/\sqrt{T_4})$. A plot of $\sigma_{\mathrm{Ly}\alpha}(\nu)$ for $T = 10^4$ K is shown in Fig. 1.1.

As can be seen from Fig. 1.1 and from Eq. (1.8) the absorption cross-section at the direct resonance is $10^{-14}\,\mathrm{cm}^2$. Assuming a typical interstellar medium with one atom per cm^3 the column density $N_{\mathrm{HI}} = 10^{14}\mathrm{cm}^2$ is already reached after 10^{-5} pc (2 AU). This means that the optical depth $\tau = N_{\mathrm{HI}} \times \sigma_{Ly\alpha}$ is 1 already after such a short path length (Hayes 2015). For typical path-lengths outwards of a galaxy the optical depth for Lyα is $\sim 10^6$. To escape a galaxy, Lyα photons have to undergo numerous scatterings until they either diffuse in space to low-density regions where they see smaller optical depths, or until they diffuse in frequency space to the wings of the absorption profile (see below). Moreover, due to the increased path length of Lyα photons in this random-walk-like process, the chance of absorption by dust grains is increased.

Diffusion of Lyα photons in frequency space is a consequence of the scatterings happening in the atoms' rest-frames. Energy conservation requires that the atom that absorbed a Lyα photon emits a photon with the same energy (except for a small recoil effect). Since the atom is moving relative to an observer, and the direction of the outgoing photon is different from the direction of the incoming Lyα photon[5], the frequency of the scattered photon changes in the frame of the observer. The result from this redistribution in frequency space is that already in static media the frequency distribution (or line profile) of the observable Lyα emission is significantly altered compared to intrinsic one. Only for simple geometries and gas distributions this problem can be treated analytically (e.g., Neufeld 1990).

[5]The angular direction to which the Lyα photon is scattered by a hydrogen atom is given by the phase probability distribution function. The polarisation of the outgoing Lyα photon depends on this angle. For an interesting observational exploitation of this effect see Hayes et al. (2011).

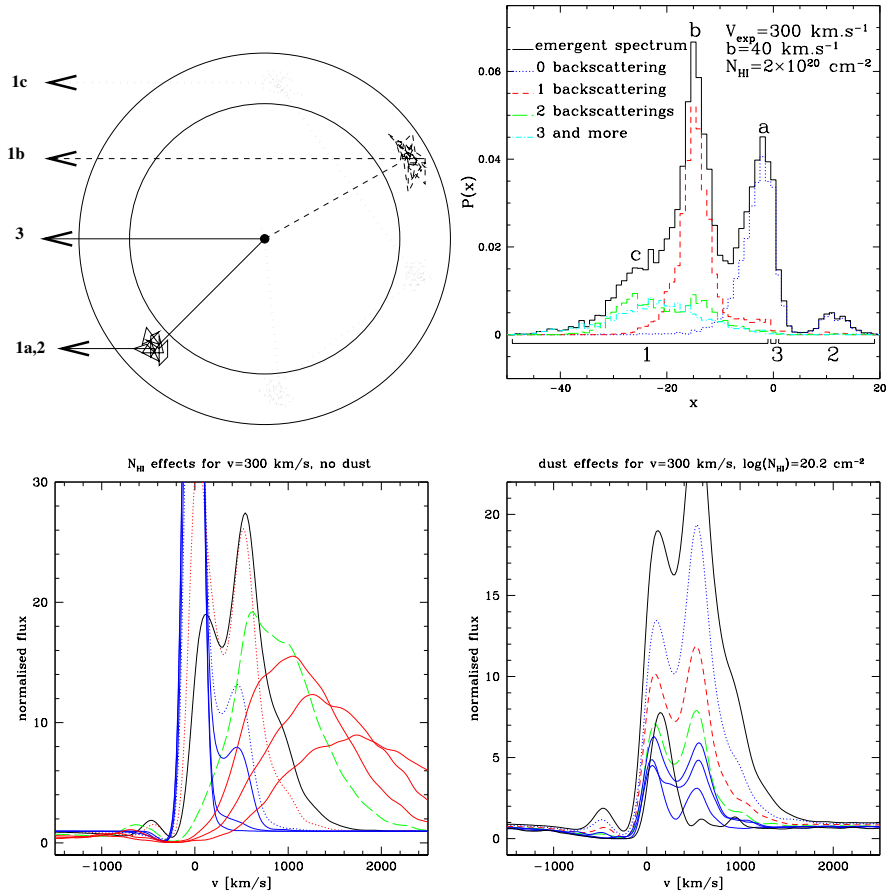

Figure 1.2: Lyα radiative transfer through expanding shell models. *Top panels* (from Verhamme et al. 2006): An illustration of the model and the scattering paths of several Lyα photons to the observer is shown in the *left panel*. The *right panel* shows a resulting spectrum from this model (shown as a probability distribution of photons in x-space, where $x = \sqrt{(\nu - \nu_0)/\Delta\nu_D}$ is the frequency shift with respect to to the line-centre ν_0 in units of the Doppler frequency width $\Delta\nu_D$ – see text). The different scattering paths of the Lyα photons correspond to different peaks of the resulting line profile. *Bottom Panels:* Illustration of the variety of Lyα line morphologies that arise in the expanding shell model (from the expanding shell model Lyα profile library of Schaerer et al. 2011). In both panels the shell is expanding with $v_{\rm exp} = 300\,{\rm km\,s^{-1}}$ and the neutral hydrogen in the shell has a velocity dispersion of $b = 30\,{\rm km\,s^{-1}}$ (corresponding to a gas temperature 5×10^4K in absence of turbulent motions). The *left panel* illustrates the effect of different neutral hydrogen column densities on the line profile. Shown is a sequence of increasing column densities $N_{\rm H} = (16., 18., 19., 19.3, 19.9, 20.2, 20.8, 21.1, 21.4, 21.7)\,{\rm cm^{-2}}$, with the solid blue lines corresponding to the three lowest- and the solid red lines corresponding to the three highest $N_{\rm H}$ values, respectively; the blue dotted, red dotted, black, and green dashed lines correspond to $N_{\rm H} = 19.3\,{\rm cm^{-2}}$, $19.9\,{\rm cm^{-2}}$, $20.2\,{\rm cm^{-2}}$, and 20.8, respectively. The *right panel* illustrates the effect of dust absorption on the line profile for the $N_{\rm H} = 20.2\,{\rm cm^{-2}}$ model, with increasing dust optical depths of $\tau_a = (0,\ 0.1,\ 0.5,\ 1.,\ 1.5,\ 2.,\ 3, 4.)$ encoded as black, blue dotted, red dashed, green dashed, solid blue and black lines, respectively (from top to bottom).

More complicated geometries already need numerical radiative transfer simulations. A popular model in this respect is the expanding-shell model (e.g. Verhamme et al. 2006; see Fig. 1.2). In this model a thin shell of expanding, contracting or static neutral gas represents the medium responsible for scattering Lyα photons. As a result from scattering in the shell complex Lyα line morphologies arise and the expansion velocity and the neutral-hydrogen column density of the shell are of pivotal importance in shaping the observable Lyα line. By introducing deviations from pure spherical symmetry Zheng & Wallace (2014) and Behrens et al. (2014) show that the observed Lyα properties also depend on the viewing angle under which a system is observed. Recently more realistic hydro-dynamic simulations of isolated galaxies have been paired with Lyα radiation-transport simulations (Verhamme et al. 2012; Behrens & Braun 2014). These studies underline again the viewing-angle dependence of the Lyα observables. In particular they show that discs observed face-on are expected to exhibit higher Lyα equivalent widths and Lyα escape fractions than if they were observed edge on. More importantly, these state-of-the-art simulations also emphasise the importance of small-scale interstellar medium structure that is not included in the simple models. Although very instructive in shaping our understanding of the Lyα-radiation transport, currently the modelling efforts can not answer the following question: What differentiates a Lyα emitting galaxy from other star-forming galaxies that do not show Lyα in emission?

As outlined in Sect. 1.1, two different methods are used to survey for high-z star-forming galaxies: Selection of galaxies via their strong Lyα line and selection of galaxies via their Lyman break. Spectroscopic observations of Lyman break selected galaxies reveal that only a fraction of those shows Lyα in emission. The overlap between Lyα selected and Lyman break selected samples is typically $\sim$ 25% (Shapley et al. 2003). However, galaxies selected via their strong Lyα emission are, on average, fainter by an order of magnitude in the UV (Ouchi et al. 2008; Shapley 2011). Therefore deep Lyα emission line searches will uncover a population of galaxies that are too faint to be detected in the UV continuum with the current and the next generation of telescopes and instruments (Windhorst et al. 2006). Unfortunately, our limited understanding of the Lyα radiative transport in realistic galactic environments does not tell us anything about the possible underlying population of galaxies that do not show Lyα in emission.

Detailed observational studies of Lyα radiative transfer in galaxies require space-based observations of nearby galaxies (see Hayes 2015 for an review). Following pioneering studies that demonstrated how a combination of the HST UV filter bands can be used to reconstruct the Lyα radiation field from local star bursts (Hayes et al. 2009; Östlin et al. 2009), a first small sample of 14 targets was observed recently (Hayes et al. 2013, 2014; Östlin et al. 2014, see Fig. 1.3). It was shown that 6 of those 14 targets could indeed be selected as Lyα emitting galaxies at high-z. The main result from this campaign is that a galaxy's morphology seen in Lyα is usually very different compared to its morphological appearance in Hα and the FUV; especially Lyα is often less centrally concentrated and so these galaxies are embedded in a faint low-surface-brightness Lyα halo (see Fig. 1.3). The different Lyα morphology compared to Hα and the extended low-surface-brightness halo are a direct result of the Lyα scattering processes (Verhamme et al. 2012; Behrens & Braun 2014; Gronke & Bird 2016). Notably, after some first tentative evidence for the existence of such a low surface-brightness halo around high-z galaxies (Steidel et al. 2011; Momose et al. 2014), Wisotzki et al. (2016) recently demonstrated that such Lyα haloes do exist around individual high-z galaxies. Moreover, for some galaxies Hayes et al. (2013) and Wisotzki et al. (2016) show that most of the Lyα emission can be attributed to the halo component. The relation between halo component and galaxy properties, as well as the effect of the halo component on the detectability of high-z galaxies require further observational studies both at high and at low redshift.

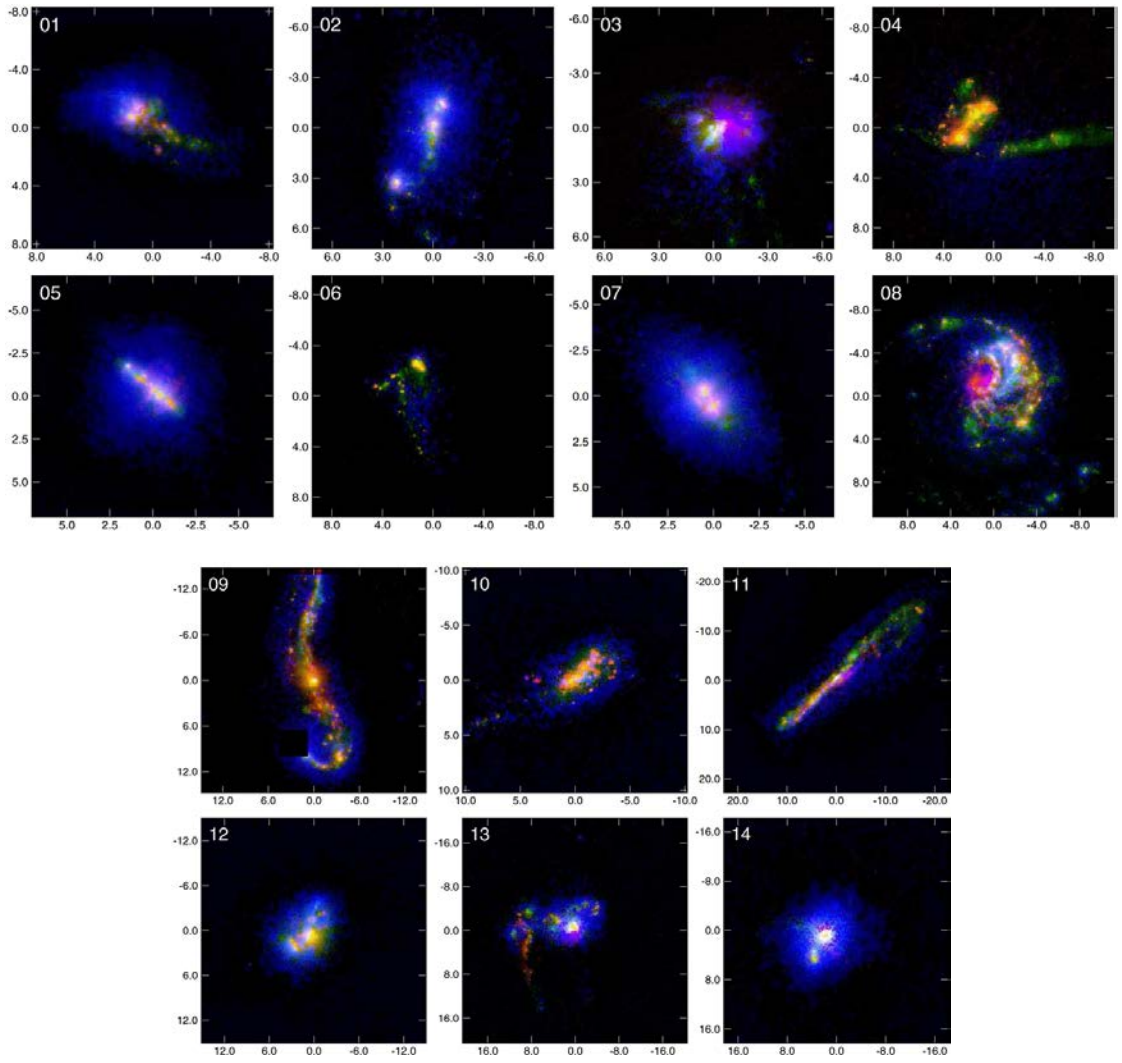

Figure 1.3: Detailed Lyα morphologies from 14 galaxies obtained with the first large-scale Lyα imaging survey (the *Lyman Alpha Reference Sample*; Hayes et al. 2013 and Östlin et al. 2014). Shown are false-colour images where green encodes the FUV continuum, red encodes continuum-subtracted Hα emission, and blue encodes continuum-subtracted Lyα emission. Due to the radiative transfer effects the Lyα morphologies bear limited resemblance to the Hα emission or the stellar UV continuum.

1.3 Structure of this thesis

In this thesis we present results from three observational projects. We employed integral-field spectroscopic observations the aim of detecting and understanding Lyα emission from galaxies. We here provide an overview over the results presented in the individual chapters.

- In Chapter 2 we present integral field spectroscopic observations of 14 nearby star-forming galaxies from the Lyman α reference sample (Fig. 1.3) in Balmer α radiation (Hα, $\lambda_{\mathrm{H}\alpha}$ = 6562.8Å). We produce 2D line-of-sight velocity maps and velocity dispersion maps from the Hα emission in our data cubes. These maps trace the spectral and spatial properties of the LARS galaxies' intrinsic Lyα radiation field. From our observations, we conjecture a causal connection between spatially resolved Hα kinematics and Lyα photometry for individual galaxies. Statistically, we find that dispersion-dominated galaxies are more likely to emit Lyα photons than galaxies where ordered gas-motions dominate. Our result indicates that turbulence in actively star-forming systems favours an escape of Lyα radiation.

- In Chapter 3 we show the results from integral-field spectroscopic observations of five radio-quiet quasars aimed at detecting possible extended emission in the Lyα line. However, in four out of five objects, we find no significant traces of this emission. But in the fifth object there is evidence for a weak and spatially quite compact Lyα excess at several kpc outside the nucleus. For all objects in our sample we estimated detection limits of 10^{-16}–10^{-17}erg s^{-1}cm^{-2}arcsec^{-2} for extended, smoothly distributed Lyα emission by adding fake nebulosities into the datacubes and trying to recover them after PSF subtraction. The faintness of these structures is consistent with the idea that radio-quiet quasars typically reside in dark matter haloes of modest masses. While we were not able to detect Lyα CGM emission, our upper limits provide constraints for the new generation of IFS instruments at 8–10m class telescopes.

- In Chapter 4 we introduce our *Line Source Detection and Cataloguing* software `LSDCat`. The aim of `LSDCat` is to build a catalogue of faint emission line sources in wide-field integral-field spectroscopic datacubes. For this purpose we utilise a 3D matched filtering approach. We will outline why `LSDCat` is well suited for surveys that will produce a large number of wide-field IFS datacubes.

- In Chapter 5 we present first results from our ongoing MUSE-Wide survey. Utilising `LSDCat` we constructed a catalogue of 831 emission line selected galaxies from a 22.2 arcmin^2 region in the CDF-S. Our sample includes 237 Lyman α emitting galaxies in the redshift range $3 \lesssim z \lesssim 6$. Only four of these galaxies had previously spectroscopic redshifts in the literature.

- We conclude this thesis in Chapter 6 by presenting first results on the Lyα luminosity function from this MUSE-Wide Lyman α emitter sample. The main conclusion of this chapter is, that extended low surface brightness emission from Lyman α emitting galaxies significantly impacts the detectability of sources near the point-source detection limit. Accounting for this statistically, we find higher number densities at the faint end of the Lyman α emitter luminosity function.

The data analysed in Chapters 2 and 3 where obtained with the Potsdam Multi Aperture Spectrophotometer at the Calar Alto 3.5 m telescope (Roth et al. 2005). The data in analysed in

Chapters 5 and Chapters 6 were obtained with the Multi Unit Spectroscopic Explorer at ESOs Very Large Telescope (Bacon et al. 2014).

Chapters 2 and 3 are versions of publications that have appeared recently in peer-reviewed journals (Herenz et al. 2015, 2016). Chapters 4 and 5 are draft versions of upcoming publications with the author of this thesis being the lead. Chapter 6 presents first result from an ongoing projects. A full list of publications where the author of this thesis was involved during the work on this thesis is given in Appendix B. Moreover, for clarity we chose to give bibliographies at the end of each chapter instead of a large bibliography at the end of the thesis.

1.4 Bibliography

Abbott, B. P., Abbott, R., Abbott, T. D., et al. 2016, Physical Review Letters, 116, 061102

Bacon, R., Vernet, J., Borisiva, E., et al. 2014, The Messenger, 157, 13

Baker, J. G. & Menzel, D. H. 1938, ApJ, 88, 52

Behrens, C. & Braun, H. 2014, A&A, 572, A74

Behrens, C., Dijkstra, M., & Niemeyer, J. C. 2014, A&A, 563, A77

Cantalupo, S., Porciani, C., & Lilly, S. J. 2008, ApJ, 672, 48

Carroll, S. M. 2001, Living Reviews in Relativity, 4

Croton, D. J. 2013, PASA, 30, 52

Dalcanton, J. J. 2009, Nature, 457, 41

Davis, T. M. & Lineweaver, C. H. 2004, PASA, 21, 97

Dijkstra, M. 2014, PASA, 31, 40

Dunlop, J. S. 2013, in Astrophysics and Space Science Library, Vol. 396, The First Galaxies, ed. T. Wiklind, B. Mobasher, & V. Bromm, 223

Ellis, R. S. 2008, Observations of the High Redshift Universe, ed. A. Loeb, A. Ferrara, & R. S. Ellis, 259–364

Gordon, W. 1929, Annalen der Physik, 394, 1031

Gronke, M. & Bird, S. 2016, ArXiv e-prints

Hayes, M. 2015, PASA, 32, 27

Hayes, M., Östlin, G., Duval, F., et al. 2014, ApJ, 782, 6

Hayes, M., Östlin, G., Mas-Hesse, J. M., & Kunth, D. 2009, AJ, 138, 911

Hayes, M., Östlin, G., Schaerer, D., et al. 2013, ApJ, 765, L27

Hayes, M., Scarlata, C., & Siana, B. 2011, Nature, 476, 304

Herenz, E. C., Gruyters, P., Orlitova, I., et al. 2016, A&A, 587, A78

Herenz, E. C., Wisotzki, L., Roth, M., & Anders, F. 2015, A&A, 576, A115

Hoang-Binh, D. 1990, A&A, 238, 449

Hogg, D. W. 1999, ArXiv Astrophysics e-prints

Hubble, E. 1929, Proceedings of the National Academy of Science, 15, 168

Jackson, N. 2015, Living Reviews in Relativity, 18

Jarosik, N., Bennett, C. L., Dunkley, J., et al. 2011, ApJS, 192, 14

Kennicutt, Jr., R. C. 1998, ARA&A, 36, 189

Lahav, O. & Suto, Y. 2004, Living Reviews in Relativity, 7

Lang, K. R. 1999, Astrophysical formulae

Loeb, A. 2013, in Astrophysics and Space Science Library, Vol. 396, The First Galaxies - Theoretical Predictions and Observational Clues, ed. T. Wiklind, B. Mobasher, & V. Bromm, 3–44

Momose, R., Ouchi, M., Nakajima, K., et al. 2014, MNRAS, 442, 110

Neufeld, D. A. 1990, ApJ, 350, 216

Oesch, P. A., Brammer, G., van Dokkum, P. G., et al. 2016, ApJ, 819, 129

Osterbrock, D. E. & Ferland, G. J. 2006, Astrophysics of gaseous nebulae and active galactic nuclei

Östlin, G., Hayes, M., Duval, F., et al. 2014, ApJ, 797, 11

Östlin, G., Hayes, M., Kunth, D., et al. 2009, AJ, 138, 923

Ouchi, M., Shimasaku, K., Akiyama, M., et al. 2008, ApJS, 176, 301

Partridge, R. B. & Peebles, P. J. E. 1967, ApJ, 147, 868

Peacock, J. A. 2013, in Astronomical Society of the Pacific Conference Series, Vol. 471, Origins of the Expanding Universe: 1912-1932, ed. M. J. Way & D. Hunter, 3

Renzini, A. 2009, in Science with the VLT in the ELT Era, ed. A. Moorwood (Springer), 3–14

Roth, M. M., Kelz, A., Fechner, T., et al. 2005, PASP, 117, 620

Salpeter, E. E. 1955, ApJ, 121, 161

Santos, M. R. 2004, MNRAS, 349, 1137

Schaerer, D., de Barros, S., & Stark, D. P. 2011, A&A, 536, A72

Shapley, A. 2009, Astrophysics in the Next Decade: The Evolution of Galaxies, ed. Thronson, H. A., Stiavelli, M., & Tielens, A., Astrophysics and Space Science Proceedings (Springer), 309

Shapley, A. E. 2011, ARA&A, 49, 525

Shapley, A. E., Steidel, C. C., Pettini, M., & Adelberger, K. L. 2003, ApJ, 588, 65

Slipher, V. M. 1917, Proceedings of the American Philosophical Society, 56, 403

Steidel, C. C., Bogosavljević, M., Shapley, A. E., et al. 2011, ApJ, 736, 160

Sumner, T. J. 2002, Living Reviews in Relativity, 5

Toomre, A. & Toomre, J. 1972, ApJ, 178, 623

Verhamme, A., Dubois, Y., Blaizot, J., et al. 2012, A&A, 546, A111

Verhamme, A., Schaerer, D., & Maselli, A. 2006, A&A, 460, 397

Windhorst, R. A., Cohen, S. H., Jansen, R. A., Conselice, C., & Yan, H. 2006, New A Rev., 50, 113

Wisotzki, L., Bacon, R., Blaizot, J., et al. 2016, A&A, 587, A98

Wright, E. L. 2006, PASP, 118, 1711

Zanstra, H. 1927, ApJ, 65, 50

Zheng, Z. & Wallace, J. 2014, ApJ, 794, 116

Zitrin, A., Labbé, I., Belli, S., et al. 2015, ApJ, 810, L12

Chapter 2

The Lyman alpha reference sample: Spatially resolved Hα kinematics

Abstract: We present integral field spectroscopic observations with the Potsdam Multi-Aperture Spectrophotometer of all 14 galaxies in the $z \sim 0.1$ Lyman Alpha Reference Sample (LARS). We produce 2D line-of-sight velocity maps and velocity dispersion maps from the Balmer α (Hα) emission in our data cubes. These maps trace the spectral and spatial properties of the LARS galaxies' intrinsic Lyα radiation field. We show our kinematic maps that are spatially registered onto the Hubble Space Telescope Hα and Lyman α (Lyα) images. We can conjecture a causal connection between spatially resolved Hα kinematics and Lyα photometry for individual galaxies. However, no general trend can be established for the whole sample. Furthermore, we compute the intrinsic velocity dispersion σ_0, the shearing velocity $v_{\rm shear}$, and the $v_{\rm shear}/\sigma_0$ ratio from our kinematic maps. In general LARS galaxies are characterised by high intrinsic velocity dispersions (54 km s^{-1} median) and low shearing velocities (65 km s^{-1} median). The $v_{\rm shear}/\sigma_0$ values range from 0.5 to 3.2 with an average of 1.5. It is noteworthy that five galaxies of the sample are dispersion-dominated systems with $v_{\rm shear}/\sigma_0 < 1$, and are thus kinematically similar to turbulent star-forming galaxies seen at high redshift. When linking our kinematical statistics to the global LARS Lyα properties, we find that dispersion-dominated systems show higher Lyα equivalent widths and higher Lyα escape fractions than systems with $v_{\rm shear}/\sigma_0 > 1$. Our result indicates that turbulence in actively star-forming systems is causally connected to interstellar medium conditions that favour an escape of Lyα radiation.

2.1 Introduction

As already envisioned by Partridge & Peebles (1967) the hydrogen Lyman α (Lyα, $\lambda_{\rm Ly\alpha}$ = 1215.67Å) line has become a prominent target in succsesful systematic searches for galaxies in the early Universe. Redshifted into the optical, this narrow high equivalent width line provides enough contrast to be effectively singled out in specifically designed observational campaigns. As of yet mostly narrow-band selection techniques have been employed (e.g. Hu et al. 1998;

A version of this chapter is published as the article "The Lyman alpha reference sample. VII. Spatially resolved Hα kinematics" in Astronomy & Astrophysics:
Edmund Christian Herenz, Pieter Gruyters, Ivana Orlitova, Matthew Hayes, Göran Östlin, John M. Cannon, Martin M. Roth, Arjan Bik, Stephen Pardy, Hector Oti-Floranes et al. (12 more), 2016, A&A Vol. 587, A78
DOI: 10.1051/0004-6361/201527373

Taniguchi et al. 2003; Malhotra & Rhoads 2004; Shimasaku et al. 2006; Tapken et al. 2006; Gronwall et al. 2007; Ouchi et al. 2008; Grove et al. 2009; Shioya et al. 2009; Hayes et al. 2010; Ciardullo et al. 2012; Sandberg et al. 2015), but multi-object and integral-field spectroscopic techniques are now also frequently used to deliver large Lyman α emitter (LAE) samples (Cassata et al. 2011; Adams et al. 2011; Mallery et al. 2012; Cassata et al. 2015; Bacon et al. 2015). Moreover, all galaxy redshift record holders in the last decade were spectroscopically confirmed by virtue of their Lyα line (Iye 2011; Ono et al. 2012; Finkelstein et al. 2013; Oesch et al. 2015; Zitrin et al. 2015) and a bright LAE at $z = 6.6$ is even believed to contain a significant amount of stars made exclusively from primordial material (so called Pop-III stars, Sobral et al. 2015).

As important as Lyα radiation is in successfully unveiling star formation processes in the early Universe, as notoriously complicated appears its correct interpretation. Resonant scatterings in the interstellar and circum-galactic medium diffuse the intrinsic Lyα radiation field in real and frequency space. These scatterings also increase the path length of Lyα photons within a galaxy and consequently Lyα is more susceptible for being destroyed by dust (see Dijkstra 2014, for a comprehensive review covering the Lyα radiative transfer fundamentals). Consequently, a galaxy's Lyα observables are influenced by a large number of its physical properties. Understanding these influences is crucial to correctly interpret high-z LAE samples. In other words, we have to answer the question: What differentiates an LAE from other star-forming galaxies that do not show Lyα in emission?

Regarding Lyα radiation transport in individual galaxies, a large body of theoretical work investigated analytically and numerically how within simplified geometries certain parameters (e.g. density, temperature, dust content, kinematics and clumpiness) affect the observed Lyα radiation field (e.g. Neufeld 1990; Ahn et al. 2003; Dijkstra et al. 2006; Verhamme et al. 2006; Laursen et al. 2013; Gronke & Dijkstra 2014; Duval et al. 2014). Commonly a spherical shell model is adopted. In this model a thin shell of expanding, contracting or static neutral gas represents the medium responsible for scattering Lyα photons. As a result from scattering in the shell complex Lyα line morphologies arise and the expansion velocity and the neutral hydrogen column density of the shell are of pivotal importance in shaping the observable Lyα line. By introducing deviations from pure spherical symmetry Zheng & Wallace (2014) and Behrens et al. (2014) show that the observed Lyα properties also depend on the viewing angle under which a system is observed. The latter result is also found in large-scale cosmological simulations that were post-processed with Lyα radiative transport simulations (e.g. Laursen & Sommer-Larsen 2007; Laursen et al. 2009; Barnes et al. 2011). Recently more realistic hydro dynamic simulations of isolated galaxies have been paired with Lyα radiation transport simulations (Verhamme et al. 2012; Behrens & Braun 2014). These studies underline again the viewing angle dependence of the Lyα observables. In particular they show, that disks observed face-on are expected to exhibit higher Lyα equivalent widths and Lyα escape fractions than if they were observed edge on. More importantly, these state of the art simulations also emphasise the importance of small-scale interstellar medium structure that was previously not included in simple models. For example Behrens & Braun (2014) demonstrate how supernova-blown cavities are able to produce favoured escape channels for Lyα photons.

Observationally, when Lyα is seen in emission, the spectral line profiles can be typified by their distinctive shapes. In a large number of LAE spectra the Lyα line often appears asymmetric, with a relatively sharp drop on the blue and a more extended wing on the red side. A significant fraction of spectra also shows characteristic double peaks, with the red peak often being stronger than the blue (e.g. Tapken et al. 2004, 2007; Yamada et al. 2012; Hong et al. 2014; Henry et al. 2015; Yang et al. 2015). Interestingly, a large fraction of double peaked and asymmetric Lyα profiles appear well explained by the spherical symmetric scenarios mentioned above. Double-

peaked profiles are successfully reproduced by slowly-expanding shells ($v_{\rm exp} \lesssim 100\,{\rm km\,s^{-1}}$) or low neutral hydrogen column densities $N_{\rm H\,I} \lesssim 10^{19}{\rm cm^{-2}}$, while high expansion velocities ($v_{\rm exp} \sim 150-300\,{\rm km\,s^{-1}}$) with neutral hydrogen column densities of $N_{\rm H\,I} \gtrsim 10^{20}{\rm cm^{-2}}$ produce the characteristic asymmetric profile with an extended red wing (Tapken et al. 2006, 2007; Verhamme et al. 2008; Schaerer et al. 2011; Gronke & Dijkstra 2014).

Further observational constraints on the kinematics of the scattering medium can be obtained by measuring the offset from non-resonant rest-frame optical emission lines (e.g. Hα or [O III]) to interstellar low-ionisation state metal absorption lines (e.g. O I λ1302 or Si II λ1304). While the emission lines provide the systemic redshift, some of the low-ionisation state metal absorption lines trace the kinematics of cold neutral gas phase. Both observables are challenging to obtain for high-z LAEs and require long integration times on 8–10 m class telescopes (e.g. Shapley et al. 2003; Tapken et al. 2004) or even additional help from gravitational lenses (e.g. Schaerer & Verhamme 2008; Christensen et al. 2012). As the continuum absorption often remains undetected, just the offset between the rest-frame optical lines and the Lyα peaks are measured (e.g. McLinden et al. 2011; Guaita et al. 2013; Erb et al. 2014). Curiously, the observed Lyα profiles also agree well with those predicted by the simple shell model, when the measured offsets (typically $\Delta v \sim 200\,{\rm km\,s^{-1}}$) are associated with shell expansion velocities in the simple shell model (Verhamme et al. 2008; Hashimoto et al. 2013; Song et al. 2014; Hashimoto et al. 2015). Only few profiles appear incompatible with the expanding shells (Chonis et al. 2013). These profiles are characterised by extended wings or bumps in the blue side of the profile (Martin et al. 2014; Henry et al. 2015). However, given aforementioned viewing angle dependencies in more complex scenarios, this overall success of the simple shell model appears surprising and is therefore currently under scrutiny (Gronke et al. 2015). Nevertheless, at least qualitatively the observations demonstrate in concert with theoretical predictions that LAEs predominantly have outflow kinematics and that such outflows promote the Lyα escape (see also Kunth et al. 1998; Mas-Hesse et al. 2003).

Kinematic information is moreover encoded in the rest-frame optical line emission alone. These emission lines trace the ionised gas kinematics and especially the hydrogen recombination lines such as Hα relate directly to the spatial and spectral properties of a galaxy's intrinsic Lyα radiation field. Therefore spatially resolved spectroscopy of a galaxy's Hα radiation field constrains the initial conditions for the subsequent Lyα radiative transfer through the interstellar, circum-galactic, and intergalactic medium to the observer. But at high z most LAEs are so compact that they cannot be spatially resolved from the ground and hence in the analysis of the integrated spectra all spatial information is lost. Resolving the intrinsic Lyα radiation of typical high-z LAEs spatially and spectrally at such small scales would require integral field spectroscopy, preferably with adaptive optics, in the near infrared with long integration times. Although large samples of continuum-selected $z \sim 2-3$ star-forming galaxies have already been observed with this method (see Glazebrook 2013, for a comprehensive review), little is known about the Lyα properties of the galaxies in those samples.

In the present manuscript we present first results obtained from our integral-field spectroscopic observations with the aim to relate spatially and spectrally resolved intrinsic Lyα radiation field to its observed Lyα properties. Therefore we targeted the Hα line in all galaxies of the $z \sim 0.03-0.18$ Lyman Alpha Reference Sample (hereafter LARS). LARS consists of 14 nearby laboratory galaxies, that have far-UV (FUV, $\lambda \sim 1500$Å) luminosities similar to those of high-z star-forming galaxies. Moreover, to ensure a strong intrinsic Lyα radiation field, galaxies with large Hα equivalent widths were selected (${\rm EW_{H\alpha}} \geq 100$Å). The backbone of LARS is a substantial program with the Hubble Space Telescope. In this program each galaxy was observed with a combination of ultra-violet long pass filters, optical broad band filters, as well as Hα and

Hβ narrow-band filters. These images were used to accurately reconstruct Lyα images of those 14 galaxies. Moreover, UV-spectroscopy with HSTs Cosmic Origins Spectrograph (COS) is available for the whole sample.

This paper is the seventh in a series presenting results of the LARS project. In Östlin et al. (2014) (hereafter Paper I) we detailed the sample selection, the observations with HST and the process to reconstruct Lyα images from the HST data. In Hayes et al. (2014) (hereafter Paper II) we presented a detailed analysis of the imaging results. We found that 6 of the 14 galaxies are indeed analogous to high-z LAEs, i.e. they would be selected by the conventional narrow-band survey selection requirement[1]: $EW_{Ly\alpha} > 20$ Å. The main result of Paper II is that a galaxy's morphology seen in Lyα is usually very different compared to its morphological appearance in Hα and the FUV; especially Lyα is often less centrally concentrated and so these galaxies are embedded in a faint low surface-brightness Lyα halo. The results in Paper II (see also Hayes et al. 2013) therefore provide clear observational evidence for resonant scattering of Lyα photons in the neutral interstellar medium. 21cm observations tracing the neutral hydrogen content of the LARS galaxies were subsequently presented in Pardy et al. (2014) (hereafter Paper III) and the results supported the complex coupling between Lyα radiative transfer and the properties of the neutral medium. In Guaita et al. (2015) (hereafter Paper IV) the morphology of the LARS galaxies was thoroughly re-examined. By artificially redshifting the LARS imaging data-products, we were able to confirm that morphologically LARS galaxies indeed resemble $z \sim 2-3$ star forming galaxies. Rivera-Thorsen et al. (2015) (herafter Paper V) then presented high-resolution far-UV COS spectroscopy of the full sample. Analysing the neutral-interstellar medium kinematics as traced by the low-ionisation state metal absorption lines, we showed that all galaxies with global Lyα escape fractions >5% appear to have outflowing winds. Finally in Duval et al. (2015, A&A submitted - hereafter Paper VI) we performed a detailed radiative transfer study of one LARS galaxy (Mrk 1468 - LARS 5) using all the observational constraints assembled within the LARS project, also including the data that is presented in this paper. In particular we show that this galaxy's spatial and spectral Lyα emission properties are consistent with scattering of Lyα photons by outflowing cool material along the minor axis of the disk.

In the here presented first analysis of our LARS integral-field spectroscopic data we focus on a comparison of results obtainable from spatially resolved Hα kinematics to results from the LARS HST Lyα imaging and 21cm H I observations. In a subsequent publication (Orlitova, in prep.) we will combine information from our 3D Hα spectroscopy with our COS UV spectra to constrain the parameters of outflowing winds.

We note, that this paper is not the first in relating observed spatially resolved Hα observations to a local galaxy's Lyα radiation field. Recently in a pioneering study exploiting MUSE (Bacon et al. 2014) science-verification data, Bik et al. (2015) showed, that an asymmetric Lyα halo around the main star-forming knot of ESO338-IG04 (Hayes et al. 2005; Östlin et al. 2009; Sandberg et al. 2013) can be linked to outflows seen in the Hα radial velocity field. Moreover, the kinematic constraints provided by our observations were already used for modelling the Lyα scattering in one LARS galaxy (Paper VI), and also here galactic scale outflows were required to explain the galaxy's Lyα radiation. With the full data set presented here, we now study whether such theoretical expected effects are indeed common among Lyα-emitting galaxies.

The outline of this chapter is as follows: In Sect. 2.2 our PMAS observations of the LARS sample are detailed. The reduction of our PMAS data is explained in Sect. 2.3. Ancillary LARS data products used in this manuscript are described briefly in Sect. 2.4. The derivation and analysis of the Hα velocity and dispersion maps is presented in Sect. 3.3. In Sect. 2.6 the results

[1] We adopt the convention established in high-z narrow-band surveys of calling galaxies with $EW_{Ly\alpha} \geq 20$Å LAEs, and galaxies with $EW_{Ly\alpha} < 20$Å non-LAEs.

Table 2.1: Log of PMAS lens array observations of the LARS sample.

LARS ID	Observing-Date	$t_{exp.}$ [s]	FoV [arcsec^2]	λ-Range $\lambda_{start} - \lambda_{end}$ [Å]	Resolving Power $\overline{R}_{FWHM}$	Seeing FWHM [″]	Observing-Conditions
1	2012-03-16	2×1800 s	16×16	5948 - 7773	5306	1.8	phot.
2	2012-03-15	2×1800 s	16×16	5752 - 7581	5205	1.1	non-phot.
3	2012-03-14	3×1800 s	16×16	5948 - 7773	5362	1.1	phot.
4	2012-03-13	3×1800 s	16×16	5752 - 7581	5883	1.0	phot.
5	2012-03-14	3×1800 s	8×8	5874 - 7700	5886	1.3	phot.
6	2012-03-13	2×1800 s	16×16	5752 - 7581	5865	1.0	phot.
7	2012-03-16	3×1800 s	16×16	5948 - 7773	3925	1.3	non-phot.
8	2012-03-15	3×1800 s	16×16	5948 - 7773	4415	0.9	non-phot.
9	2012-03-12	3×1800 s	16×16	5752 - 7581	5561	0.9	phot.
	2012-03-14	3×1800 s	16×16	5948 - 7773	4772	0.9	non-phot.
10	2012-03-14	2×1800 s	8×8	5874 - 7700	5438	1.5	phot.
11	2012-03-15	3×1800 s	16×16	5948 - 7773	4593	1.0	non-phot.
12	2012-03-14	3×1800 s	8×8	6553 - 8363	6756	0.9	phot.
13	2011-10-02	4×1800 s	8×8	6792 - 8507	7766	1.2	phot.
	2011-10-02	4×1800 s	8×8	6792 - 8507	7771	1.2	phot.
14	2012-03-13	2×1800 s	8×8	6553 - 8363	7718	0.9	phot.

See Paper I for coordinates and common names of the galaxies in the LARS sample. LARS 09 and LARS 13 were covered with two pointings each, since their extent was larger than the used FoV.

are discussed and finally we summarise and conclude in Sect. 2.7. Notes on individual objects are given in Appendix 2.A.

2.2 PMAS Observations

We observed all LARS galaxies using the Potsdam Multi-Aperture Spectrophotometer (PMAS; Roth et al. 2005) at the Calar Alto 3.5 m telescope during 4 nights from March 12 to March 15, 2012 (PMAS run212), except for LARS 13, which was observed on October 10 2011 (PMAS run197). PMAS was used in the lens array configuration, where 256 fibers are coupled to a 16×16 lens array that contiguously samples the sky. Depending on the extent of the targeted galaxy we used either the standard magnification mode, that provides an 8″×8″ field of view (FoV) or the double magnification mode[2], where the FoV is 16″×16″. The backward-blazed R1200 grating was mounted on the spectrograph. To ensure proper sampling of the line spread function the 4k×4k CCD (Roth et al. 2010) was read out unbinned along the dispersion axis. This setup delivers a nominal resolving power from $R \sim 5000$ to $R \sim 8000$ within the targeted wavelength ranges[3]. In Sect. 2.3.3 we will show that while the nominal resolving powers are met on average, the instrumental broadening varies at small amplitudes from fibre to fibre.

On-target exposures were usually flanked by 400 s exposures of empty sky near the target. These sky frames serve as a reference for removing the telluric background emission. Due to an error in our observing schedule, no sky frames were taken for LARS 4, LARS 7 and LARS 9 (2012-03-12 pointing). Fortunately, this did not render the observations unusable, since there are enough blank-sky spectral pixels (so called spaxels) within those on-target frames to provide us with a reference sky (see paragraph on sky subtraction in Sect. 2.3).

[2]The naming of the mode refers to the instruments internal magnification of the telescopes focal plane; doubling the magnification of the focal plane doubles the extent of the FoV.

[3]Values taken from the PMAS online grating tables, available at `http://www.caha.es/pmas/PMAS_COOKBOOK/TABLES/pmas_gratings.html#4K_1200_1BW`

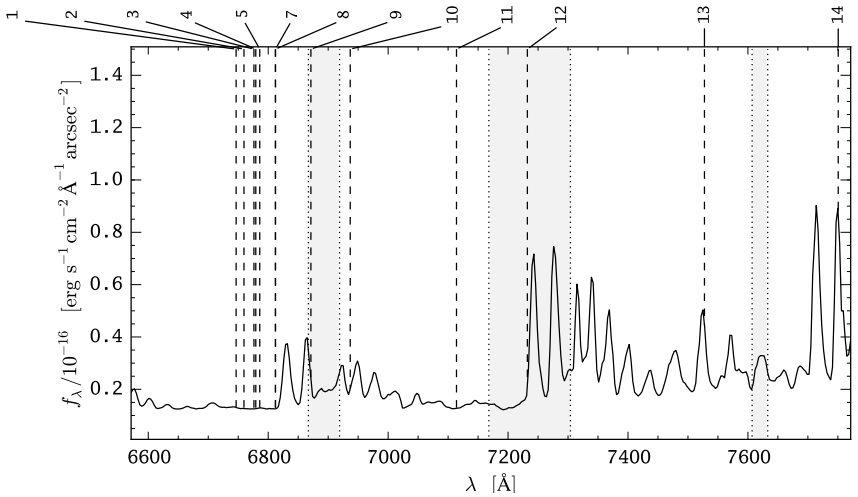

Figure 2.1: Wavelengths of the redshifted Hα lines of the LARS galaxies (vertical dashed lines) compared to the night sky emission spectrum at Calar Alto (Sánchez et al. 2007a). Grey regions indicate the telluric absorption bands (O_2 B-Band: 6887 Å - 6919 Å, O_2 A-Band: 7607 Å - 7633 Å, and H_2O a-Band: 7168 Å - 7304 Å, see e.g. Cox 2000).

Observing blocks of one hour were usually flanked by continuum and HgNe arc lamp exposures used for wavelength and photometric calibration. We obtained several bias frames throughout each night when the detector was idle during target acquisition. Spectrophotometric standard stars were observed at the beginning and at the end of each astronomical night (BD+75d325 & Feige 67 from Oke 1990, $t_{\rm exp.} = 600$ s). Twilight flat exposures were taken during dawn and dusk.

In Table 2.1 we provide a log of our observations. By changing the rotation of the grating, we adjusted the wavelength ranges covered by the detector, such that the galaxies Hα - [N II] complex is located near the center of the CCD. Note, that ±350Å at the upper/lower end of the quoted spectral ranges are affected by vignetting (a known "feature" of the PMAS detector - see Roth et al. 2010). We also quote the average spectral resolution of our final datasets near Hα. The determination of this quantity is described in Sect. 2.3.3. The tabulated seeing values refer always to the average FWHM of the guide star PSF measured during the exposures with the acquisition and guiding camera of PMAS. This value is on average $\approx 0.2''$ higher than the DIMM measurements (see also Husemann et al. 2013).

In Fig. 2.1 we show the wavelengths of the redshifted Hα line for all LARS galaxies overlaid on the typical night sky emission spectrum at Calar Alto from Sánchez et al. (2007a). As can be seen for two galaxies (LARS 13 and LARS 14) the Hα line signal is contaminated by telluric line emission and two other galaxies (LARS 9 and LARS 12) have their Hα line within an absorption band. This, however, has no effect on the presented analysis. For LARS 13 and LARS 14 we could optimally subtract the interfering sky-lines from the science exposures using the separate sky frames. Moreover, as we use only spaxels with high signal to noise Hα lines in our analysis (cf. Sect. 3.3), the high frequency changes within the telluric absorption bands do not alter the quantified features – width and peak position – of the profiles.

2.3 PMAS data reduction

2.3.1 Basic reduction with p3d

For reducing the raw data the p3d-package[4] (Sandin et al. 2010, 2012) was utilized. This pipeline covers all basic steps needed for reducing fiber-fed integral field spectroscopic data: bias subtraction, flat fielding, cosmic ray removal, tracing and extraction of the spectra, correction of differential atmospheric refraction and co-addition of exposures (see also Turner 2010). We now describe how we applied the tasks of p3d on our raw data for each of these steps[5]:

- *Bias subtraction*: Master bias frames were created by p3d_cmbias. These master bias frames were then subtracted from the corresponding science frames. Visual inspection of the bias subtracted frames showed no measurable offsets in unexposed regions between the 4 quadrants of the PMAS CCD, which attests optimal bias removal.

- *Flat fielding*: Each of the 256 fibers has its own wavelength dependent throughput curve. To determine these the task p3d_cflatf was applied on the twilight flats. The determined curves are then applied in the extraction step of the science frame (see below) to normalize the extracted spectra.

- *Cosmic ray removal*: Cosmic ray hits on the CCD were removed with p3d_cr. Visual inspections guided by the parameter study of Husemann et al. (2012) lead us to apply the L.A. Cosmic algorithm (van Dokkum 2001) with $\sigma_{\rm lim} = 5$, $\sigma_{\rm frac} = 1$, $f_{\rm lim} = 15$, a grow radius of 2 and a maximum of 4 iterations.

- *Tracing and extraction*: Spectra were extracted with the modified Horne (1986) optimal extraction algorithm (Sandin et al. 2010). The task p3d_ctrace was used to determine the traces and the cross-dispersion profiles of the spectra on the detector. Spectra were then extracted with p3d_cobjex, also using the median recentering recommended in Sandin et al. (2012).

- *Wavelength calibration*: With p3d_cdmask we obtained dispersion solutions (i.e. mappings from pixel to wavelength space) from the HgNe lamp frames using a sixth-order polynomial. The wavelength sampling of the extracted science spectra is typically 0.46 Å px^{-1}. We further improved the wavelength calibration of the science frames by applying small shifts (typically $0.1-0.3$ px) determined from the strong 6300Å and 6364Å [O I] sky lines (not available within the targeted wavelength range for LARS 12, 13, and 14)

- *Sensitivity function and flux calibration*: Using extracted and wavelength-calibrated standard star spectra, we created a sensitivity function utilizing p3d_sensfunc. Absorption bands in the standard star spectra as well as telluric absorption bands (see Fig. 2.1) were masked for the fit. Extinction curves were created using the empirical formula presented in Sánchez et al. (2007b) using the extinction in V-band as measured by the Calar Alto extinction monitor[6]. We flux-calibrated all extracted and wavelength-calibrated science frames with the derived sensitivity function and extinction curve using p3d_fluxcal.

[4] http://p3d.sourceforge.net

[5] As the amount of raw data from the observations was substantial, we greatly benefited from the scripting capabilites of p3d (Sandin et al. 2011). Our shell scripts and example parameter files can be found at https://github.com/Knusper/pmas_data_red

[6] http://www.caha.es/CAVEX/cavex.php

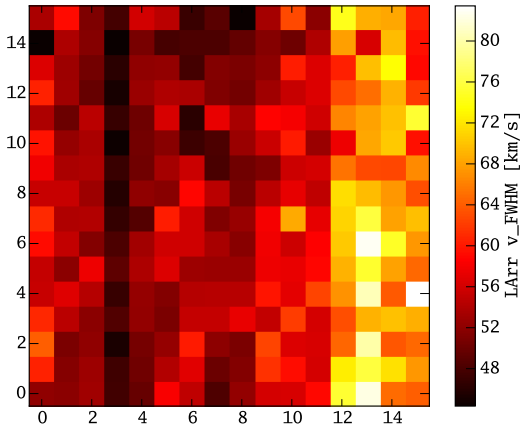

Figure 2.2: Representative resolving power map for the observation of LARS 1. The resoultion is expressed as v_{FWHM} of a 1D Gaussian fit. Black spaxels at the positions $(x, y) = (0, 14)$ and $(8, 15)$ are dead fibres.

The final data products from the `p3d`-pipeline are flux- and wavelength-calibrated data cubes for all science exposures, as well as the corresponding error cubes. From here we now perform the following reduction steps with our custom procedures written in `python`[7].

2.3.2 Sky subtraction and co-addition

- *Sky subtraction:* All sky frames were reduced like science frames as described in the previous section. These extracted, wavelength- and flux-calibrated sky frames were then subtracted from the corresponding science frames and errors were propagated accordingly. Unfortunately, no separate sky exposures were taken for three targets (LARS 4, LARS 7 and LARS 9, cf. Sect. 2.2). For these targets we created a narrow band image of the Hα-[N II] region by summing up the relevant layers in the datacube. In this image we selected spaxels that do not contain significant amounts of flux. From these spaxels then an average sky spectrum was created, which was then subtracted from all spaxels. As the spectral resolution varies across the FoV (cf. Sect. 2.3.3), this method produces some residuals at the position of the sky lines, which however do not touch the Hα lines of the affected targets.

- *Stacking:* We co-added all individual flux-calibrated and sky-subtracted data cubes using the variance-weighted mean. For this calculation the input variances were derived from squaring the error cubes. Before co-addition we ensured by visual inspection that there are no spatial offsets between individual exposures.

2.3.3 Spectral resolving power determination

To determine the intrinsic width of our observed Hα lines we need to correct for instrumental broadening by the spectrograph's line spread function (the spectrograph's resolving power, Robertson 2013). It is known that for PMAS the resolving power varies from fibre to fibre and

[7] `http://www.python.org`

with wavelength (e.g. Sánchez et al. 2012). To determine the broadening at the wavelength of the Hα line we use the HgNe arc lamp exposures, which were originally used to wavelength calibrate the on-target exposures. We first create wavelength-calibrated data cubes from these arc frames. Next we select two strong arc lamp lines which are nearest in wavelength to the corresponding galaxy's Hα line. Finally, we fit 1D Gaussians in each spaxel to each of those lines (e.g. similar as in Alonso-Herrero et al. 2009). Typically the separation from a galaxy's Hα line to one of those arc lamp lines is ~50Å. The difference between the full-width half maximum (FWHM) of the fits to the different lines is typically $\sim$ 1km s^{-1}, hence we take the average of both at the position of Hα as the resolving power for each spaxel. We point out that the arc-lamp lines FWHM is always sampled by more than 2 pixels, therfore aliasing effects can be neglected (Turner 2010).

This procedure provides us with resolving power maps. As an example we show in Fig. 2.2 a so derived map for the observations of LARS 1. We note that the spatial gradient seen in Fig. 2.2 is not universal across our observations (see Sánchez et al. 2012 for an explanation). We further note that the formal uncertainties on the resolving power determination are negligible in comparison to the uncertainties derived on the Hα profiles in Sect. 3.3.

In Table 2.1 we give the mean resolving power at the position of Hα for each galaxy as $\overline{R}_{\rm FWHM}$. Variations within the FoV typically have an amplitude of ~30 km s^{-1}. The average resolving power of all our observations is R = 5764 or 52 km s^{-1}, which is consistent with the values given in the PMAS online grating manual[8].

2.3.4 Registration on astrometric grid of HST observations

To facilitate a comparison of our PMAS observations with the HST imaging results from Hayes et al. (2014) we have to register our PMAS data cubes with respect to the LARS HST data products (cf. Sect. 2.4). As explained in Östlin et al. (2014) all HST images are aligned with respect to each other and have a common pixel scale of 0.04″px^{-1}. We use the continuum-subtracted Hα line image as a reference. From this image we create contours that highlight the most prominent morphological features in Hα. We then produce a continuum-subtracted Hα map from the PMAS data cubes by subtracting a version of the data cube that is median-filtered in spectral direction. Finally, we visually match the contours from the reference image with the PMAS Hα map. This constrains the position of the PMAS FoV relative to the HST imaging. We emphasize that we make full use of the FITS header world-coordinate representation in our method, i.e. the headers of our final data cubes are equipped with keyword value pairs to determine the position of each spaxel on the sky (Greisen & Calabretta 2002; Calabretta & Greisen 2002).

For galaxies having a single PMAS pointing we present the final result of our registration procedure in Fig. 2.5 (or Fig. 2.6 / Fig. 2.7 for the two galaxies with two PMAS pointings): For each LARS galaxy the Hα line intensity map extracted from our HST observations (cf. Sect. 2.4) is shown in the top panel and can be compared to the PMAS Hα signal-to-noise ratio (SNR) map in the panel below. SNR values for each spaxel are calculated by summation of all flux values within a narrow spectral window centred on Hα and subsequent division by the square root of the sum of the variance values in that window. The width of the summation window is taken as twice the Hα lines FWHM. Our display of the HST Hα images uses an asinh-scaling (Lupton et al. 2004) cut at 95% of the maximum value (see Section 4 and Fig. 3 of Hayes et al. 2014 for absolute Hα intensities) and we scaled our PMAS Hα SNR maps logarithmically. The inferred final position of the PMAS FoV is indicated with a white square (or two squares for the galaxies

[8] http://www.caha.es/pmas/PMAS_COOKBOOK/TABLES/pmas_gratings.html#4K_1200_1BW

having two pointings) within the Hα panel. Also shown are the Hα contours used for visual matching. As can be seen, most of the prominent morphological characteristics present in the HST Hα maps are unambiguously identifiable in the lower resolution PMAS maps, exemplifying the robustness of our registration method.

2.4 Ancillary LARS dataproducts

We compare our PMAS data to the HST imaging results of the LARS project presented in Hayes et al. (2013) and Paper II. Specifically we will use the continuum subtracted Hα and Lyα images that were presented in Paper II. These images were produced from our HST observation using the LARS extraction software LaXs (Hayes et al. 2009). Details on the observational strategy, reduction steps and analysis performed to obtain these HST dataproducts used in the present study are given in Paper II and Paper I.

We also compare with the published results of the LARS H I imaging and spectroscopy observations that were obtained with the 100m Robert C. Byrd Green Bank Telescope (GBT) and the Karl G. Jansky Very Large Array (VLA). GBT single-dish spectra are present for all systems, but for the three LARS galaxies with the largest distances (LARS 12, LARS 13 and LARS 14) the H I signal could not be detected. VLA interferometric imaging results are only available for LARS 2, LARS 3, LARS 4, LARS 8 and LARS 9. We emphasise that with beam sizes from 59″ to 72″ (VLA D-configuration) the spatial scale that is resolved within the VLA H I images is much larger than our PMAS observations. Moreover, the single-dish GBT spectra are sensitive to H I at the observed frequency range within 8′ of the beam. Full details on data acquisition, reduction and analysis are presented in Paper III.

2.5 Analysis and results

2.5.1 Hα velocity fields

We condense the kinematical information traced by Hα in our data cubes into two-dimensional maps depicting velocity dispersion and line of sight radial-velocity at each spaxel. Both quantities are derived from 1D Gaussian fits to the observed line shapes from the continuum subtracted cube (see Sect. 2.3.4). We calculate the radial velocity offset $v_{\rm LOS}$ to the central wavelength value given by the mean of all fits and the FWHM of the fitted line in velocity space $v_{\rm FWHM}$. To obtain higher signal to noise ratios in the galaxies' outskirts we use the weighted Voronoi tessellation binning algorithm by Diehl & Statler (2006), which is a generalisation of the Voronoi binning algorithm of Cappellari & Copin (2003).

We visually scrutinised the fits to the spectra and decided that lines observed at a SNR of 6 were still reliably fit. Hence, 6 defines the minimum SNR in the Voronoi binning algorithm. Furthermore, we adopted a maximum bin size of 3×3 pixels. In those calculations signal and noise are defined as in Sect. 2.3.4. In what follows, only results from the fits to bins that meet the minimum signal to noise requirement are considered. Most of the bins used are actually only a single spaxel, and very few bins in the outskirts of the galaxies meeting the minimum SNR criterion consist of 2 or 3 spaxels. In practice this means that we are typically sensitive to regions at Hα surface brightness higher than 5×10^{-16}erg s^{-1}cm^{-2}arcsec^{-2}. Using the Kennicutt (1998) conversion and neglecting extinction, this translates to an detection limit of $\sim 3\times10^{-2}$M$_\odot$yr^{-1}kpc^{-1}, more than an order of magnitude deeper than probed by high redshift integral field spectroscopy studies (~ 1M$_\odot$yr^{-1}kpc^{-1}, see e.g. Law et al. 2009).

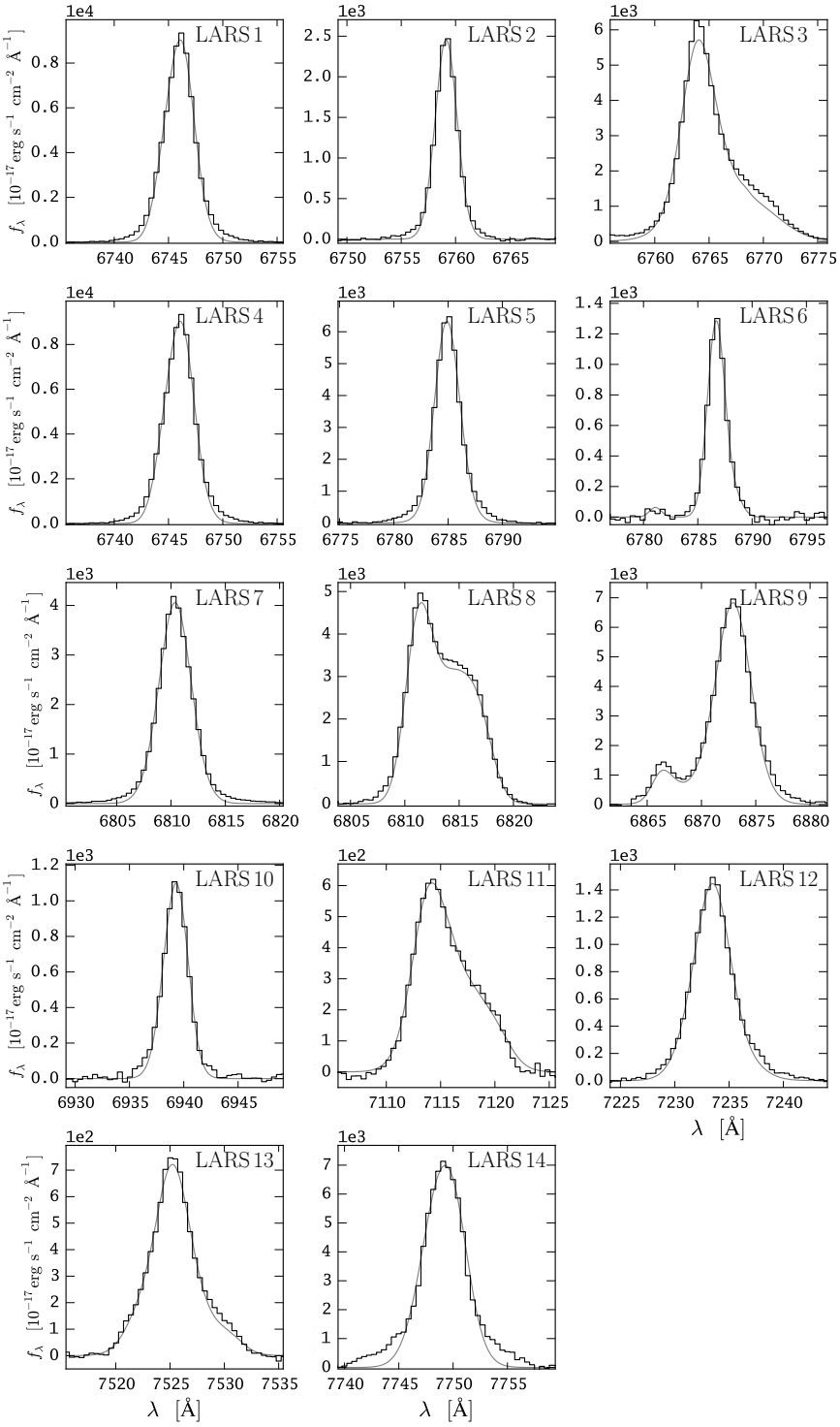

Figure 2.3: Integrated continuum-subtracted Hα profiles of the LARS galaxies (black) compared to summed 1D Gaussian model profiles (grey) from which radial-velocity and velocity-dispersion maps were generated.

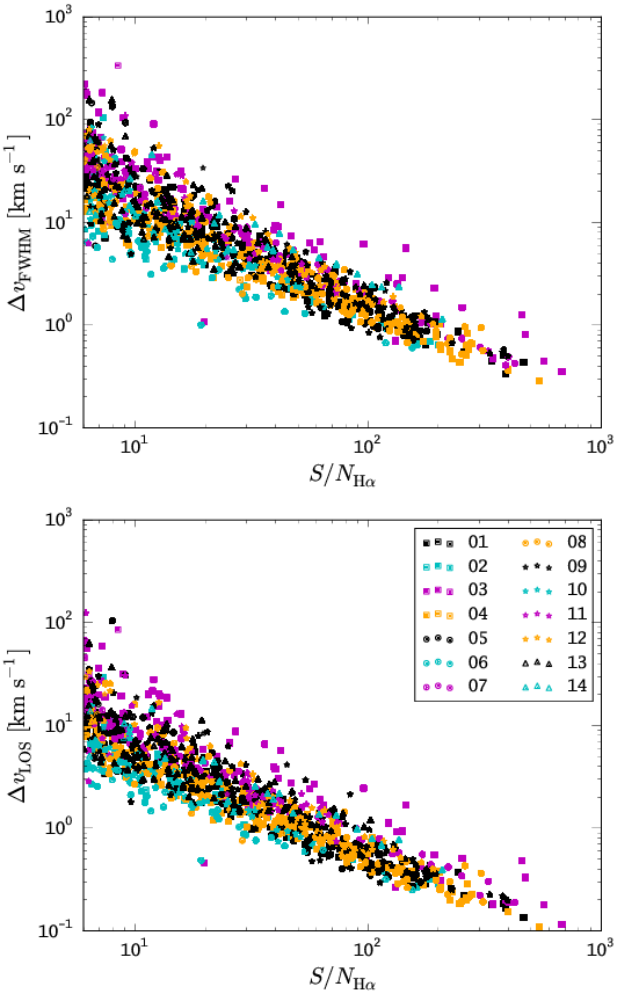

Figure 2.4: Uncertainties on derived velocity dispersions (*top panel*) and radial velocities (*top panel*) for Gaussian profile fits to Hα for all galaxies. All uncertainties for a specific galaxy have the same symbol according to the legend in the right panel.

By visual inspection we also ensured that 1D Gaussian profiles are a sufficient model of the observed Hα profiles seen in the PMAS LARS data cubes. Only in two galaxies (LARS 9 and LARS 13) we have some spaxels where a 1D Gaussian certainly fails to reproduce the complexity of the observed spectral shape. Moreover, in LARS 14 weak broad wings are visible in the individual Hα profiles. We have not attempted to model these special cases, but we describe their qualitative appearance in detail in the Appendices 2.A.9, 2.A.13 and 2.A.14 and acknowledge their existence in our interpretation in Sect. 2.6. To demonstrate the overall quality of our Hα velocity fields, we compare in Fig. 2.3 the integrated Hα profiles of the LARS galaxies to the sum of the fitted 1D Gaussians used to generate the $v_{\rm FWHM}$ and $v_{\rm LOS}$ maps. As can be seen the observed profile and the one derived from the models are largely in agreement. The strongest deviation between data and models is apparent in LARS 14, where the broad wings of the observed Hα profile are not reproduced at all by out 1D Gaussian models (cf. Sect. 2.6.1 and Appendix 2.A.14).

To estimate formal uncertainties on $v_{\rm FWHM}$ and $v_{\rm LOS}$, we use a Monte Carlo technique: We perturb our spectra 100 times with the noise from our noise cubes and then fit the 1D Gaussian profile in exactly the same way to each of these 100 realisations. The width of the distribution of all fit results characterised by their standard deviation gives a robust measure for the uncertainty on the derived quantities (see also Appendix B.4. in Davies et al. 2011). The central moment of the distribution is the final value that will be shown in our maps. In Fig. 2.4 we display for all performed fits the error on the velocity dispersion $\Delta v_{\rm FWHM}$ and on radial velocity $\Delta v_{\rm LOS}$ as a function of the lines SNR. We note, that on average our uncertainties on $v_{\rm FWHM}$ and $v_{\rm LOS}$ follow the scaling laws expected for fitting Gaussian profiles to noisy emission-line spectra $\Delta v_{\rm LOS} \propto \Delta v_{\rm FWHM} \propto v_{\rm FWHM}^{1/2} {\rm SNR}^{-1}$ (Landman et al. 1982; Lenz & Ayres 1992). For reference, at our minimum SNR = 6 we have typical errors of $\Delta v_{\rm FWHM} \approx 30\,{\rm km\,s^{-1}}$ and $\Delta v_{\rm LOS} \approx 10\,{\rm km\,s^{-1}}$, and at the median (mean) SNR of our data - ${\rm SNR_{median}} = 22$ (${\rm SNR_{mean}} = 50$) - we have $\Delta v_{\rm FWHM} \approx 7\,{\rm km\,s^{-1}}$ ($\approx 3\,{\rm km\,s^{-1}}$) and $\Delta v_{\rm LOS} \approx 3\,{\rm km\,s^{-1}}$ ($\approx 1\,{\rm km\,s^{-1}}$).

In Fig. 2.5 we show the resulting $v_{\rm FWHM}$ and $v_{\rm LOS}$ maps together with the LaXs Lyα images (lower three panels). Maps and images of the galaxies observed with two pointings are shown in Fig. 2.6 and Fig. 2.7 for LARS 9 and LARS 13, respectively. All $v_{\rm FWHM}$ maps have been corrected for instrumental broadening using the spectral resolving power maps derived in Sect. 2.3.3. In all $v_{\rm LOS}$ and $v_{\rm FWHM}$ panels we overlay contours derived from the Lyα image to emphasise distinctive morphological Lyα properties.

Individual maps are discussed in Appendix 2.A. Using the classification scheme introduced by Flores et al. (2006) (see also Sect. 3.3 in Glazebrook 2013) the LARS galaxies can be characterised by the qualitative appearance of their velocity fields:

- *Rotating Disks:* LARS 8 and LARS 11. Both galaxies show a regular symmetric dipolar velocity field with a steep gradient in the central regions. This steep gradient is also the reason for artificially broadened emission near the kinematical centre. Morphologically both galaxies also bear resemblance to a disk and the kinematical axis is aligned with the morphological axis. However, we point out in Appendix 2.A.8 that LARS 8 can also be classified as a shell galaxy, hinting at a recent merger event.

- *Perturbed Rotators:* LARS 1, LARS 3, LARS 5, LARS 7, and LARS 10. In those galaxies traces of orbital motion are still noticeable, but the maps look either significantly perturbed compared to a classical disk case (LARS 3, LARS 5, LARS 7 and LARS 10) and/or the observed velocity gradient is very weak (LARS 1, LARS 5 and LARS 10). Based solely on morphology, we previously classified two of those galaxies as dwarf edge-on disks (LARS 5 and LARS 7 - Paper II; Paper III). Moreover, LARS 3 is a member of a well

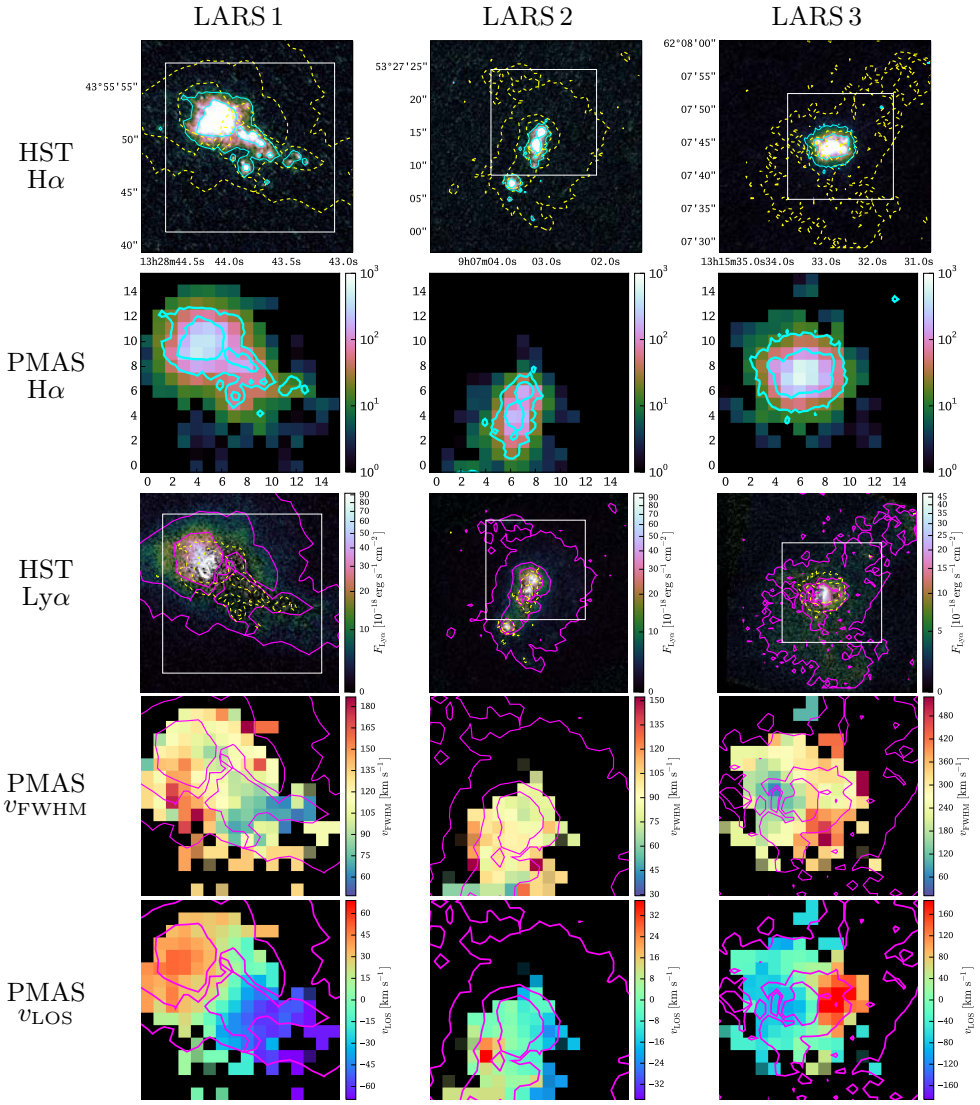

Figure 2.5: Comparison of LARS HST imaging results of the LARS sample to spatially resolved PMAS Hα spectroscopy. North is always up and east is always to the left. For each galaxy from top to bottom: The *first panel* shows the LaXs Hα line intensity map; tick labels indicate right-ascension and declination and an asinh-scaling is used cut at 95% of the maximum value. The *second panel* shows a SNR map of the continuum-subtracted Hα signal observed with PMAS. Tick labels in the PMAS SNR map are in arc-seconds, the scaling is logarithmic from 1 to 10^3 and only spaxels with $S/N > 1$ are shown. The *third panel* shows the LARS Lyα images with a colourbar indicating the flux scale in cgs-units; scaling is the same as in the Hα map. The *fourth panel* shows resolution-corrected Hα $v_{\rm FWHM}$ maps from our PMAS observations and the corresponding Hα $v_{\rm LOS}$ maps are displayed in the *fifth panel*. In the first and third panel we indicate position and extend of the PMAS field of view with a white box. Cyan contours in the HST Hα image are contours of constant surface brightness, adjusted to highlight the most prominent morphological features. Similarly, magenta contours in the HST Lyα images indicate the Lyα morphology; these contours are also shown in the fourth and fifth panel. To highlight the difference between Lyα and Hα, the Lyα and Hα panels contain as dashed yellow lines the contours from the Hα and Lyα panels, respectively.

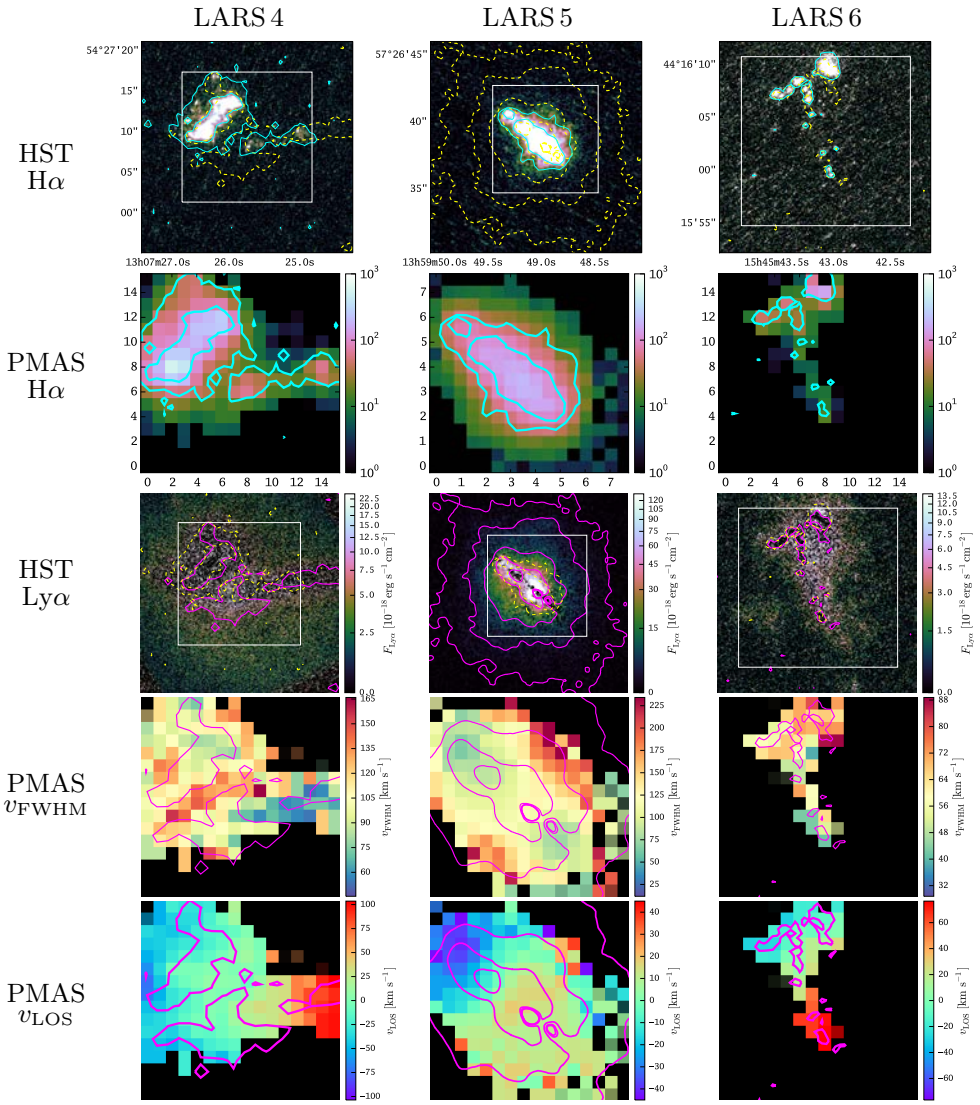

Figure 2.5: Continued.

known merger of two similar massive disks (cf. Appendix 2.A.3). From our imaging data alone LARS 7 and LARS 10 bear resemblance to shell galaxies (cf. Appendices 2.A.7 and 2.A.10).

- *Complex Kinematics:* LARS 2, LARS 4, LARS 6, LARS 9, LARS 12 LARS 13, and LARS 14. These seven galaxies are characterised by more chaotic $v_{\rm LOS}$ maps and they all have also irregular morphologies. Four of the irregulars consist of photometrically well separated components that are also kinematically distinct (LARS 4, LARS 6, LARS13 and LARS 14), while the other three each have their own individual peculiarities (LARS 2, LARS 9 and most spectacularly LARS 12 - cf. Appendices 2.A.2, 2.A.9 and 2.A.12).

These kinematic classes are also listed in Table 2.2.

Notably, in all LARS galaxies, except for LARS 6, we observe high-velocity dispersions ($v_{\rm FWHM} \gtrsim 100\,{\rm km\,s^{-1}}$); the most extreme case is LARS 3 where locally lines as broad as $v_{\rm FWHM} \sim 400\,{\rm km\,s^{-1}}$ are found. The observed width of the Hα line seen in our $v_{\rm FWHM}$ maps can

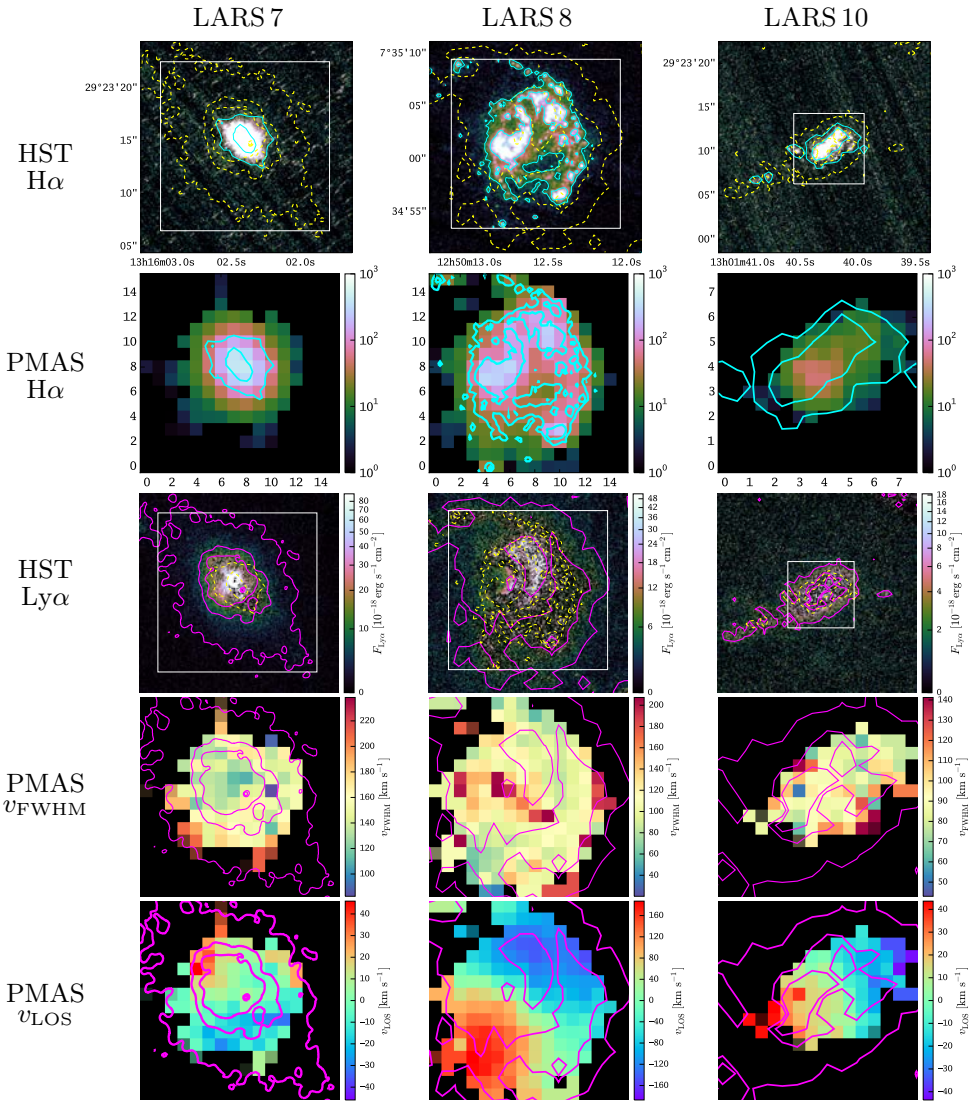

Figure 2.5: Continued.

be described as a successive convolution of the natural Hα line (7 km s^{-1} FHWM) with the thermal velocity distribution of the ionised gas (21.4 km s^{-1} FWHM at 10^4K) and with non-thermal motions in the gas (e.g. Jiménez-Vicente et al. 1999). Since all our dispersion measurements are significantly higher than the thermally broadened profile non-thermal motions dominate the observed line-widths. Non-thermal motions could be centre-to-centre dispersions of the individual H II regions and turbulent motions of the ionised gas. The latter appears to be the main driver for the observed line widths, since the observed velocity dispersions are highly supersonic (i.e. $\gtrsim 10$ km s^{-1} for H II at 10^4K, see also Sect. 5.1 in Glazebrook 2013).

2.5.2 Global kinematical properties: $v_{\rm shear}$, σ_0, $\sigma_{\rm tot}$ and $v_{\rm shear}/\sigma_0$

We now quantify the global kinematical properties of our Hα velocity fields that were qualitatively discussed in the previous section. Therefore we compute three non-parametric estimators that are commonly adopted in the literature for this purpose (e.g. Law et al. 2009; Basu-Zych

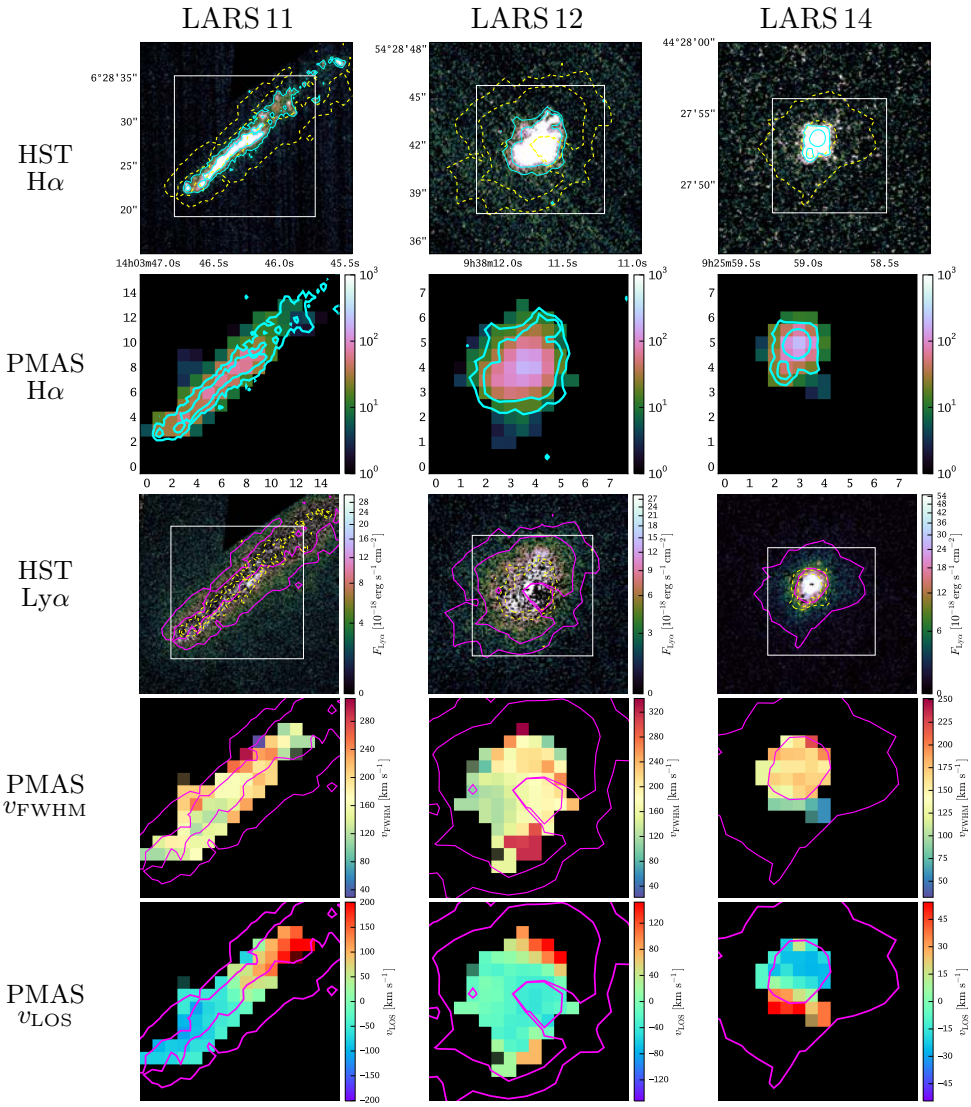

Figure 2.5: Continued.

et al. 2009; Green et al. 2010; Glazebrook 2013; Gonçalves et al. 2010; Green et al. 2014; Wisnioski et al. 2015): Shearing velocity v_{shear}, intrinsic velocity dispersion σ_0 and their ratio $v_{\mathrm{shear}}/\sigma_0$. We describe the physical meaning of those parameters and our method to determine them in the following three subsections. Furthermore, we also calculate the integrated velocity dispersion σ_{tot}. This measure provides a useful comparison for unresolved distant galaxies (cf. Sect. 2.5.2.4). Our results on v_{shear}, σ_0, σ_{tot} and $v_{\mathrm{shear}}/\sigma_0$ are tabulated in Table 2.2.

2.5.2.1 Shearing velocity v_{shear}

The shearing velocity v_{shear} is a measure for the large-scale gas bulk motion along the line of sight. We calculate it via

$$v_{\mathrm{shear}} = \frac{1}{2}\left(v_{\mathrm{max}} - v_{\mathrm{min}}\right) \ . \tag{2.1}$$

Table 2.2: Global kinematic parameters from Hα for the LARS galaxies, calculated as described in Sect. 2.5.2. For reference we also tabulate $EW_{Ly\alpha}$, Lyα/Hα and $f_{esc.}^{Ly\alpha}$ from Paper II, as well as $\xi_{Ly\alpha}$ from Hayes et al. (2013).

ID	Class	σ_0 [km s^{-1}]	σ_{tot} [km s^{-1}]	v_{shear} [km s^{-1}]	v_{shear}/σ_0	$EW_{Ly\alpha}$ [Å]	Lyα/Hα	$f_{esc.}^{Ly\alpha}$	$\xi_{Ly\alpha}$
1	P	47.5 ± 0.1	60.5	56 ± 2	1.2 ± 0.1	33.0	1.36	0.119	3.37
2	C	38.6 ± 0.9	46.0	23 ± 3	0.6 ± 0.1	81.7	4.53	0.521	2.27
3	P	99.5 ± 3.7	130.9	138 ± 3	1.4 ± 0.2	16.3	0.16	0.003	0.77
4	C	44.1 ± 0.1	55.1	74 ± 9	1.7 ± 0.1	0.00	0.00	0.000	...
5	P	46.8 ± 0.3	54.7	37 ± 4	0.8 ± 0.1	35.9	2.16	0.174	2.61
6	C	27.2 ± 0.3	58.9	52 ± 7	1.9 ± 0.2	0.00	0.00	0.000	...
7	P	58.7 ± 0.3	67.4	31 ± 3	0.5 ± 0.1	40.9	1.94	0.100	3.37
8	R	49.0 ± 0.1	111.8	155 ± 3	3.2 ± 0.1	22.3	0.67	0.025	1.12
9	C	58.6 ± 0.1	112.7	182 ± 3	3.1 ± 0.1	3.31	0.13	0.007	>2.85
10	P	38.2 ± 1.0	49.2	36 ± 3	0.9 ± 0.2	8.90	0.47	0.026	2.08
11	R	69.3 ± 3.8	114.8	149 ± 4	2.1 ± 0.3	7.38	0.72	0.036	2.27
12	C	72.7 ± 1.0	81.3	96 ± 3	1.3 ± 0.1	8.49	0.48	0.009	3.48
13	C	69.2 ± 0.7	97.3	183 ± 4	2.5 ± 0.2	6.06	0.29	0.010	1.74
14	C	67.3 ± 1.3	72.9	40 ± 1	0.6 ± 0.1	39.4	2.24	0.163	3.62

Class refers to the three kinematic classes proposed by Flores et al. (2006): C = complex kinematics, P = perturbed rotators and R = rotating disks.

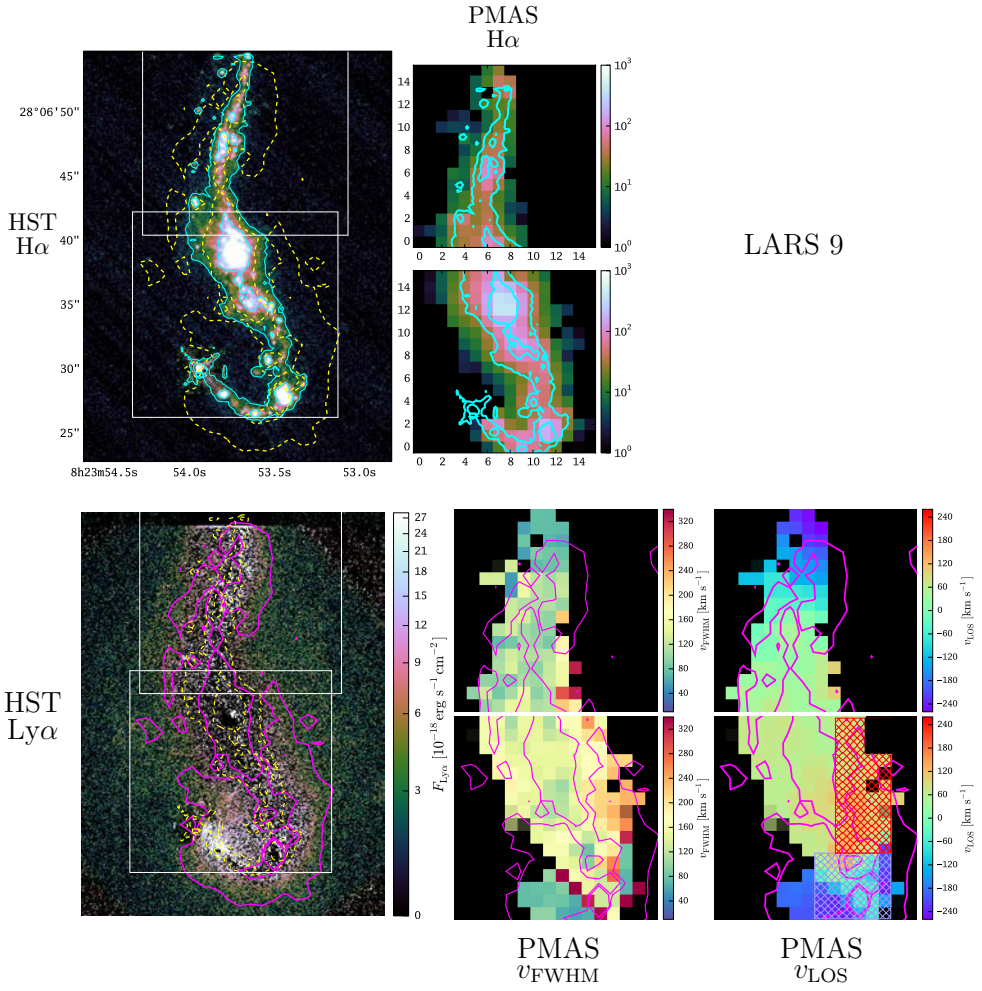

Figure 2.6: Comparison of LARS HST imaging results to spatially resolved PMAS Hα spectroscopy for LARS 9. For detailed description of individual panels see caption of Figure 2.5. This galaxy was covered with 2 PMAS pointings. Hatched regions in the $v_{\rm LOS}$ map indicate regions, where the Hα emission shows a more complex profile that could not be described by a simple Gaussian (cf. Appendix 2.A.9).

Here we take the median of the lower and upper 5 percentile of the distribution of values in the $v_{\rm LOS}$ maps for $v_{\rm min}$ and $v_{\rm max}$, respectively. This choice ensures that the calculation is robust against outliers while sampling the true extremes of the distribution. We conservatively estimate the uncertainty by propagating the full width of the upper and lower 5 percentile of the velocity map. We list our results for $v_{\rm shear}$ in the second column of Table 2.2. Our derived $v_{\rm shear}$ values for the LARS sample range from $30\,{\rm km\,s^{-1}}$ to $180\,{\rm km\,s^{-1}}$, with $65\,{\rm km\,s^{-1}}$ being the median. This is less than half the typical maximum velocity $v_{\rm max}$ of Hα rotation curves observed in spiral galaxies - e.g. $v_{\rm max} = 145\,{\rm km\,s^{-1}}$ is the median of 153 local spirals (Epinat et al. 2010). In contrast to our $v_{\rm shear}$ measurement, $v_{\rm max}$ values are inclination corrected. In a sample with random inclinations on average the correction $v_{\rm shear} = \frac{\pi}{4} v_{\rm max} \approx 0.79\, v_{\rm max}$ is expected (e.g. Law et al. 2009) but even with this correction classical disks appear still incompatible with most of our measurements by a factor larger than two. Only for the two galaxies that we classified as rotating disks in Sect. 2.5.1 we find $v_{\rm shear}$ values compatible with local rotators. Nevertheless,

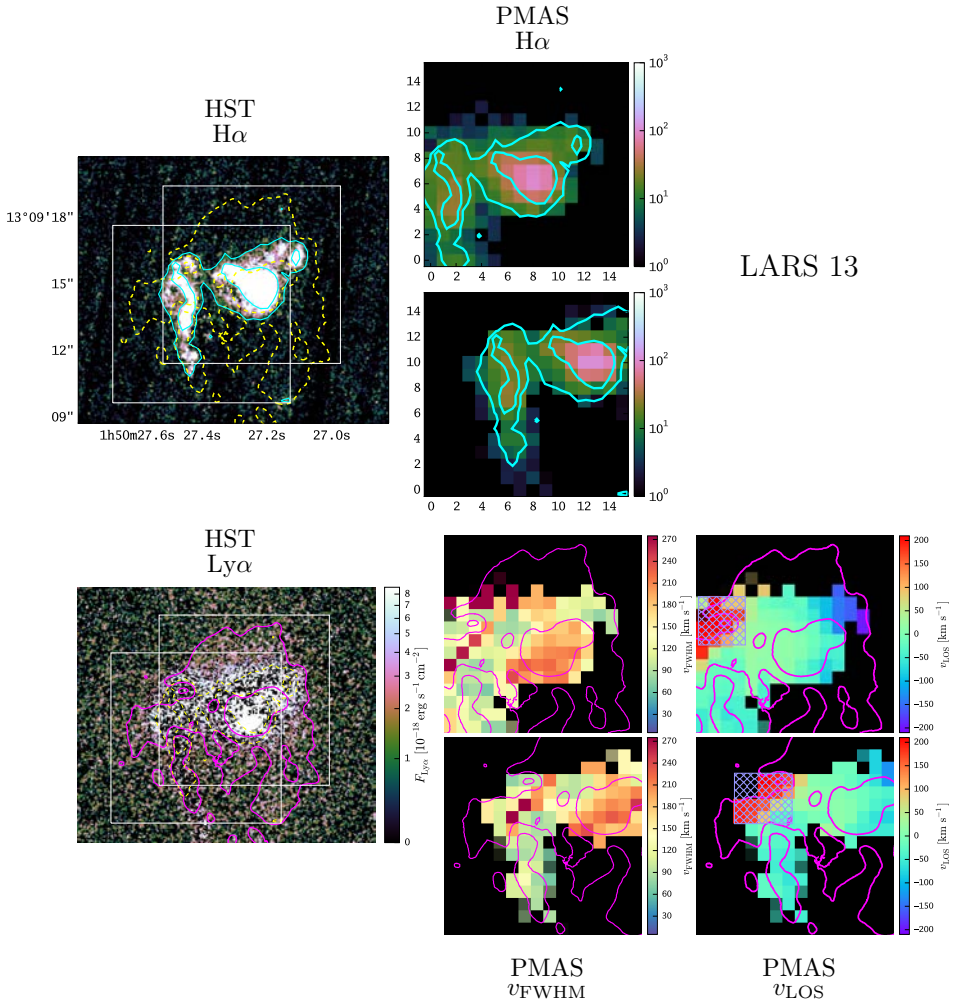

Figure 2.7: Same as Figure 2.6, but for LARS 13. Hatched region in the $v_{\rm LOS}$ map indicates the region, where the Hα emission shows a more complex profile that could not be described by a simple Gaussian (cf. Appendix 2.A.13).

high $v_{\rm shear}$ values do not necessarily imply the presence of a disk. Large-scale bulk motions at high amplitude occur also in close encounters of spatially and kinematically distinct companions (e.g. LARS 13).

Sensitivity is an important factor in the determination of the observed $v_{\rm shear}$. An observation of less depth will not detect fainter regions at larger radii, which may have the highest velocities. Indeed, for most of our galaxies the spatial positions of $v_{\rm min}$ and $v_{\rm max}$ values are in those outer lower surface-brightness regions. Hence observations of lower sensitivity will be biased to lower $v_{\rm shear}$ values. This sensitivity bias is strongly affecting high-z studies because such observations often limited only to the brightest regions (Law et al. 2009; Gonçalves et al. 2010).

2.5.2.2 Intrinsic velocity dispersion σ_0

The intrinsic velocity dispersion σ_0 (sometimes also called resolved velocity dispersion or local velocity dispersion, cf. Glazebrook 2013, Sect. 1.2.1) is in our case a measure for the typical

random motions of the ionised gas within a galaxy. We calculate it by taking the flux weighted average of the observed velocity dispersions in all spaxels:

$$\sigma_0 = \frac{\sum F^{\mathrm{H}\alpha}_{\mathrm{spaxel}} \sigma_{\mathrm{spaxel}}}{\sum F^{\mathrm{H}\alpha}_{\mathrm{spaxel}}} \,. \tag{2.2}$$

Here $F^{\mathrm{H}\alpha}_{\mathrm{spaxel}}$ is the Hα flux in each spaxel and σ_{spaxel} is the velocity dispersion measured in that spaxel; the sum runs over all spaxels with SNR $\geq$ 6 (Sect. 2.5.1). Such a flux-weighted summation σ_0 has been widely adopted in the literature to quantify the typical intrinsic velocity dispersion component (e.g. Östlin et al. 2001; Law et al. 2009; Gonçalves et al. 2010; Green et al. 2010; Glazebrook 2013; Green et al. 2014).

PSF smearing in the presence of strong velocity gradients broadens the Hα line at the position of the gradients[9]. Such a broadening could bias our calculation of the intrinsic velocity dispersion. At the distances of the LARS galaxies our typical seeing-disk PSF FWHM of 1″ corresponds to scales of 0.6 kpc to 3 kpc. In most of our observations this average PSF FWHM is comparable to the size of one PMAS spaxel (1″×1″) and most of the LARS galaxies exhibit rather weak velocity gradients. The PSF smearing effect is seen only in galaxies with strong velocity gradients (e.g. LARS 8, cf. Appendix 2.A.8), especially when observed with PMAS' 0.5″×0.5″ magnification mode (e.g. LARS 12, cf. Appendix 2.A.12). In principle the effect could be corrected by subtracting a PSF-smeared kinematical model of the v_{LOS} velocity field. Given the complexity of our observed velocity fields, however, this is not practicable. And, moreover, at $z \sim 0.1$ Green et al. (2014) find that for classical rotating disk kinematics the velocity dispersions corrected by a kinematical model are, on average, negligible. Comparison between adaptive-optics derived PSF-smearing unaffected σ_0 values to those derived from seeing-limited observations were presented by Bassett et al. (2014). They find that while for one galaxy σ_0 remains unaffected by an increase in spatial resolution, for the other galaxy σ_0 decreases by $\sim$10 km s^{-1}. Bassett et al. (2014) attribute the $\sim$10 km s^{-1} discrepancy in one of their galaxies to a strong velocity gradient that is co-spatial with the strongest emission. A similar comparison is possible for three of our LARS galaxies - LARS 12, LARS 13 and LARS 14. For these galaxies adaptive optics IFS observations were presented by Gonçalves et al. (2010) (see Appendices 2.A.12, 2.A.13 and 2.A.14). Gonçalves et al. (2010) derive $\sigma_0 = 67$ km s^{-1}, $\sigma_0 = 74$ km s^{-1} and $\sigma_0 = 71$ km s^{-1} for LARS 12, LARS 13 and LARS 14, respectively. These values are in agreement with our measurements of $\sigma_0 = 73$ km s^{-1}, $\sigma_0 = 69$ km s^{-1} and $\sigma_0 = 67$ km s^{-1} for those galaxies[10]. From all these considerations we are certain, that the adopted formalism in Eq. (2.2) gives a robust estimate of the intrinsic velocity dispersion.

We list our derived values for σ_0 in the third column of Table 2.2. In general, the ionised gas kinematics of the LARS galaxies are characterised by high intrinsic velocity dispersions ranging from 40 km s^{-1} to 100 km s^{-1} with 54 km s^{-1} being the median of the sample. Such high intrinsic dispersions are in contrast to H II velocity dispersions of $\sim 10 - 50$ km s^{-1} typically found in local spirals (e.g. Epinat et al. 2008a,b, 2010; Erroz-Ferrer et al. 2015). In high-z star-forming galaxies intrinsic dispersions $\gtrsim$ 50 km s^{-1} appear to be the norm (e.g. Puech et al. 2006; Genzel et al. 2006; Law et al. 2009; Förster Schreiber et al. 2009; Erb et al. 2014; Wisnioski et al. 2015). In the local $z \lesssim 0.1$ Universe high intrinsic velocity dispersions are also found in the studies of blue compact galaxies (BCGs, Östlin et al. 1999, 2001), local Lyman break analogues (Basu-Zych et al. 2009; Gonçalves et al. 2010) and (ultra-)luminous infrared galaxies

[9]This effect is similar to beam-smearing in radio interferometric imaging observations.

[10]We note that for LARS 13 Gonçalves et al. (2010) do not sample the entire galaxy in their observations - see Sect. 2.A.13.

(e.g Monreal-Ibero et al. 2010). Finally, σ_0 values of comparable amplitude are also common in a sample of 67 bright Hα emitters ($10^{40.6} \leq L_{\mathrm{H}\alpha} \leq 10^{42.6}$) (Green et al. 2010, 2014). Indeed, Green et al. (2010) and Green et al. (2014) show that star formation rate is positively correlated with intrinsic velocity dispersion. We will confirm this trend among our LARS galaxies and discuss its implications on Lyα observables in Sect. 2.6.3.

2.5.2.3 $v_{\mathrm{shear}}/\sigma_0$ ratio

The ratio $v_{\mathrm{shear}}/\sigma_0$ is a metric to quantify whether the gas kinematics are dominated by turbulent or ordered (in some cases orbital) motions. Our results for this quantity are listed in Table 2.2. Given the above (Sects. 2.5.2.1 and 2.5.2.2) mentioned differences to disks, it appears cogent that our $v_{\mathrm{shear}}/\sigma_0$ ratios (median 1.4, mean 1.6) are much smaller than typical disk $v_{\mathrm{shear}}/\sigma_0$ ratios $\sim 4-8$ (first to last quartile of the Epinat et al. sample).

Objects with $v_{\mathrm{shear}}/\sigma_0 < 1$ are commonly labelled dispersion dominated galaxies (Newman et al. 2013; Glazebrook 2013). - According to this criterion five galaxies of the 14 LARS sample are dispersion dominated: LARS 2, LARS 5, LARS 7, LARS 10 and LARS 14 - three perturbed rotators and two with complex kinematics. Dispersion dominated galaxies are frequently found in kinematic studies of high-z star forming galaxies. Local samples with a similar high fraction ($\sim 35\%$) of dispersion dominated galaxies are the blue compact galaxies studied by Östlin et al. (2001) or the Lyman break analogues studied by Gonçalves et al. (2010) . In Sect. 2.6.3 we will show that dispersion dominated systems are more likely to have a significant fraction of Lyα photons escaping.

2.5.2.4 Integrated velocity dispersion σ_{tot}

For reference we also compute the integrated (spatially averaged) velocity dispersion σ_{tot}. This measure provides a useful comparison for studies of unresolved distant galaxies, where no disentanglement between ordered and disordered, random motions is possible (e.g. McLinden et al. 2011; Guaita et al. 2013; McLinden et al. 2014; Rhoads et al. 2014; Erb et al. 2014).

We obtain σ_{tot} by calculating the square root of the second moment of the integrated Hα profiles shown in Fig. 2.3. The results are given in the fourth column of Table 2.2. Our integrated velocity dispersions for the LARS sample range from $46\,\mathrm{km\,s^{-1}}$ to $115\,\mathrm{km\,s^{-1}}$, with $70\,\mathrm{km\,s^{-1}}$ being the median of the sample. Given the high SNR of the integrated profiles the formal uncertainties on this σ_{tot} are very small ($\sim 10^{-2}\mathrm{km\,s^{-1}}$). As expected, when large scale motions dominate in the integrated spectrum (i.e. high $v_{\mathrm{shear}}/\sigma_0$ ratios), σ_{tot} is significantly larger than σ_0, but for dispersion dominated systems the discrepancy becomes less extreme.

2.6 Discussion: Influence of Hα kinematics on a galaxy's Lyα emission

2.6.1 Clues on Lyα escape mechanisms via spatially resolved Hα kinematics

Recent theoretical modelling of the Lyα radiative transport within realistic interstellar medium environments predicts that small scale interstellar medium physics are an decisive factor in regulating the Lyα escape from galaxies (Verhamme et al. 2012; Behrens & Braun 2014). In particular Behrens & Braun (2014) demonstrate how supernova blown outflow cavities become favoured escape channels for Lyα radiation. These cavities naturally occur in zones of enhanced star formation activity, where the input of kinetic energy from supernovae and stellar winds into

the surrounding interstellar medium is also expected to drive highly turbulent gas flows. Do we see supporting evidence for this scenario in our IFS observations of the LARS galaxies?

As described in Sect. 2.5.1, all our velocity fields are characterised by broad profiles that are best explained by turbulent flows of ionised gas. The more violent these flows are, the more likely they carve holes or bubbles through the interstellar medium through which the ionised gas eventually flows out into the galaxy's halo. Close inspection of Fig. 2.5 reveals, that in LARS 1, LARS 3 and LARS 13 (Fig. 2.7) zones of high Lyα surface brightness occur near or even cospatial to zones where for these galaxies the maximum velocity dispersions are observed. In both LARS 1 and LARS 13 these zones are also co-spatial with the regions of highest Hα surface-brightness, hence here the star formation rate density is highest. Moreover, in LARS 1 the Hα image shows a diffuse fan-like structure emanating outwards from this star-forming knot (Paper II; Paper I). Finally, also the analysis of the COS spectra in Paper V shows blue-shifted low-ionisation state interstellar absorption lines in LARS 1 and LARS 13 indicative of outflowing neutral gas. Hence for those two galaxies together with the high-resolution HST imaging data our IFS data provides further evidence for the relevance of localised outflows in shaping the observed Lyα morphology.

However, already in LARS 3 the interpretation is not as straight-forward. Here the broadest Hα lines do not occur co-spatial with the highest star formation rate density. Although also here the COS spectrum shows a bulk outflow of cold neutral gas (Rivera-Thorsen et al. 2015), the locally enhanced dispersion values seen in the PMAS maps appear not to be related to this outflow. Instead, it appears more naturally that the high turbulence within the ionised gas is not primarily driven by star formation activity, but is rather the result of the violent interaction with the north-western companion (see e.g. Teyssier et al. 2010 for theoretical support). The interpretation is further complicated by the fact, that the HST imaging data resolves the local Lyα knot on smaller scales then which we are probing with our PMAS observations.

Nevertheless, there is another example among the LARS galaxies for Lyα escape being related to an outflow: LARS 5 (cf. Duval, A&A submitted). For this galaxy we presumed already in Paper II the existence of a starburst driven wind based solely on the filamentary structure seen in the HST Hα image. Our dispersion map now reveals that these filaments fill the interior of a biconical structure, with its base confined on the most prominent star-forming clump (cf. Appendix 2.A.5) – fully in accordance with theoretical expectations for an evolved starburst driven superwind (e.g. Cooper et al. 2008). Also here Lyα photons could preferentially escape the disc through the cavity blown by the wind. The strongest Lyα enhancement is found directly above and below the main star-forming clump and the low surface brightness Lyα halo is then produced by those photons scattering on a bipolar shell-like structure of ambient neutral gas swept up by the superwind. Unfortunately, the brightest hot-spots in Lyα above and below the plane are at the base of this outflowing cone and occur at scales that we cannot resolve in our PMAS data. Similar but less spectacular examples of elevated velocity dispersions above and below a disk can be seen in LARS 7 and LARS 11, with both galaxies are also being embedded in low-surface brightness Lyα halos.

Another possible example for the importance of outflow kinematics in facilitating direct Lyα escape is the most luminous LAE in the sample: LARS 14 (cf. Appendix 2.A.14). Here the observed Hα profiles are always characterised by an underlying fainter broad component (see Fig. 2.3) that is believed to be directly related to outflowing material (e.g. Yang et al. 2015).

We conclude that while in some individual cases a causal connection between spatially resolved Hα kinematics and localised outflow scenarios might be conjectured, globally this is not a trend seen in our observations. We note further, that Hα kinematics tell only one part of the whole story, and the suggested outflow scenarios should also be traceable by gas with a high

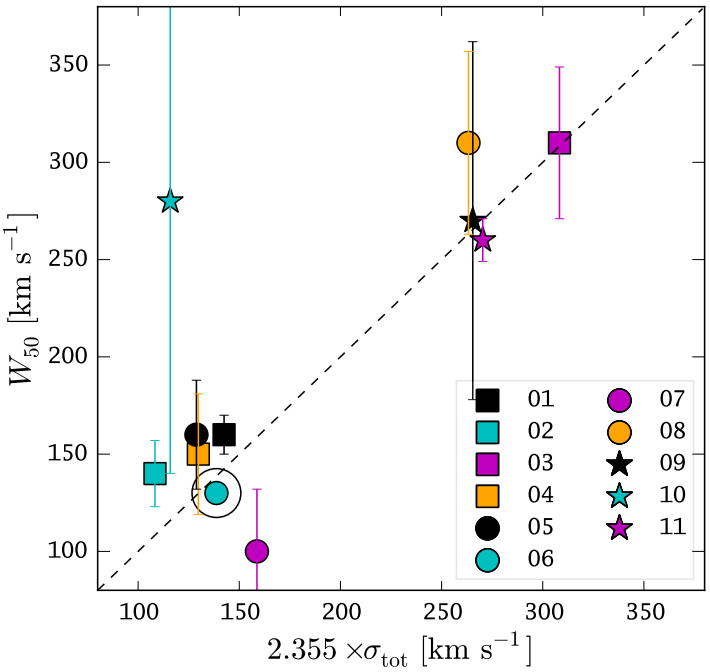

Figure 2.8: Comparison of integrated H I linewidth W_{50} to FWHM of the Hα integrated velocity dispersion $2\sqrt{2\ln 2}\times\sigma_{\rm tot}$. The dashed line indicates the one-to-one relation. We note, that for LARS 6 (encircled point) we plot as W_{50} a preliminary result based upon VLA C-configuration interferometry, as the beam of the GBT profile (used to derive W_{50} in Paper III) is too broad to separate LARS 6 from a neighbouring galaxy.

degree of ionisation. At least for one galaxy with Lyα imaging similar to the LARS galaxies, such a connection has been demonstrated: ESO338-IG04. Recently, Bik et al. (2015) analysed observations of this galaxy obtained with the MUSE integral field spectrograph (Bacon et al. 2014). They show, that the Lyα fuzz seen around the main star-forming knot of this galaxy (Hayes et al. 2005; Östlin et al. 2009) can be related to an outflow which can be traced both with Hα kinematics and by a high degree of ionisation. As a difference to our observations, Bik et al. (2015) see the fast outflowing material in their $v_{\rm LOS}$ map as significantly redshifted Hα emission. No similar prominent effect is apparent in our $v_{\rm LOS}$ maps. Nevertheless, the $v_{\rm LOS}$ fields of LARS 7 and LARS 12 display strongly localised redshifts in Hα that are spatially coincident with filamentary Hα fingers, hence here we might see also a fast outflow pointed away from the observer. But also in those galaxies, no co-spatial relation between Lyα emissivity and the suspected outflows can be established.

2.6.2 Comparison of Hα to H I observations

Radiative transfer of Lyα photons depends on the relative velocity differences between scattering H I atoms and Lyα sources. If the Lyα sources are out of resonance with the bulk of the neutral medium, they are less likely scattered, and in turn more likely to escape the galaxy. It is exactly this interplay between the ionised and neutral ISM phases that is determining the whole the Lyα radiative transfer. In Paper III we studied LARS galaxies in the H I 21 cm line, using single-dish

GBT and VLA D-configuration observations (cf. Sect. 2.4). We now attempt a comparison between the neutral and ionised gas kinematics in the LARS galaxies, cognisant of the fact that the spatial scales probed by both instruments are much larger than our PMAS H II observations.

Generally our GBT H I spectra have low SNR, and for the three most distant LARS galaxies – LARS 12, LARS 13 and LARS 14 – we could not detect any significant signal at all. The profiles are mostly single- or multiple-peaked, but rarely show a classical double-horn profile that would be expected for a flat rotation curve. Hence, qualitatively our observed GBT H I line profiles are consistent with our PMAS results that most of the LARS galaxies are kinematically perturbed or sometimes even strongly interacting systems.

In Paper III we measured the width of the H I lines at 50% of the line peak from the GBT spectra. In Fig. 2.8 we compare this quantity, W_{50}, to the FWHM of the integrated Hα velocity dispersion $\sigma_{\rm tot}$ (Sect. 2.5.2.4). Notably, two systems deviate significantly from the one-to-one relation: LARS 7 and LARS 10. LARS 10 shows the lowest SNR H I spectrum and moreover our PMAS FoV does not capture two smaller star-forming clumps in the south-east. Therefore we believe that observational difficulties are source for the $\sigma_{\rm tot}$–W_{50} difference in this galaxy. In LARS 7, however, we suspect the difference to be genuine. In this galaxy the Hα morphology is significantly puffed up and rounder compared to the disk-like continuum (cf. Appendix 2.A.7). Therefore we suspect that the smaller W_{50} measurement indicates that bulk of H I is in a kinematically more quiescent state then the ionised gas. This galaxy is one of the stronger LAEs in the sample ($f_{\rm esc.}^{\rm Ly\alpha} = 0.14$ and EW$_{\rm Ly\alpha}$=40Å). That considerable amounts of Lyα photons escape from LARS 7 was noted as peculiar in Paper V, since the metal absorption lines indicated large amounts of neutral gas sitting at the systemic velocity of the galaxy. Our observations now indicate that the intrinsic Lyα photons are produced in gas that is less quiescent than the scattering medium, which therefore is more transparent for a significant fraction of the intrinsic Lyα photons.

Spatially resolved VLA velocity fields are available for only a subset of five LARS galaxies (LARS 2, LARS 3, LARS 4, LARS 8, LARS 9). They represent rotations, disturbed by interactions with neighbours. In four of them, H I kinematical axes have similar orientations as those of the PMAS Hα velocity field. In the fifth object, the complex interacting system LARS 9, the Hα and H I velocity fields show different characteristics, but the complexities seen in the PMAS maps of this galaxy are on scales far beyond the resolving power of the VLA D-configuration (cf. Appendix 2.A.9). However, some of the LARS galaxies have already been observed with the VLA in C- and B-configuration and the analysis is currently in progress. These data will allow for the first time a comparison between Hα, H I and Lyα on meaningful physical scales. It is evident, that these comparisons will provide a critical benchmark for our understanding of Lyα radiative transfer in interstellar and circum-galactic environments.

2.6.3 Relations between kinematical properties and galaxy parameters

In Sect. 2.5.2 we quantified the global kinematical properties of the LARS galaxies using the non-parametric estimators $v_{\rm shear}$, σ_0 and $v_{\rm shear}/\sigma_0$. Before linking these observables to global Lyα properties of the LARS galaxies (cf. Sect. 2.6.4), we need to understand which galaxy parameters are encoded in them.

We find strong correlations between stellar mass $M_\star$ and $v_{\rm shear}$, as well as star formation rate (SFR) and σ_0 ($M_\star$ and SFR from Paper II). Graphically we show these correlations in Fig. 2.9 (left panel) and Fig. 2.10 (centre panel). The Spearman rank correlation coefficients (e.g. Wall 1996) are $\rho_s = 0.763$ for the $M_\star$-$v_{\rm shear}$ relation and $\rho_s = 0.829$ for the SFR-σ_0 relation. This corresponds to likelihoods of the null-hypothesis that no monotonic relation exists between the

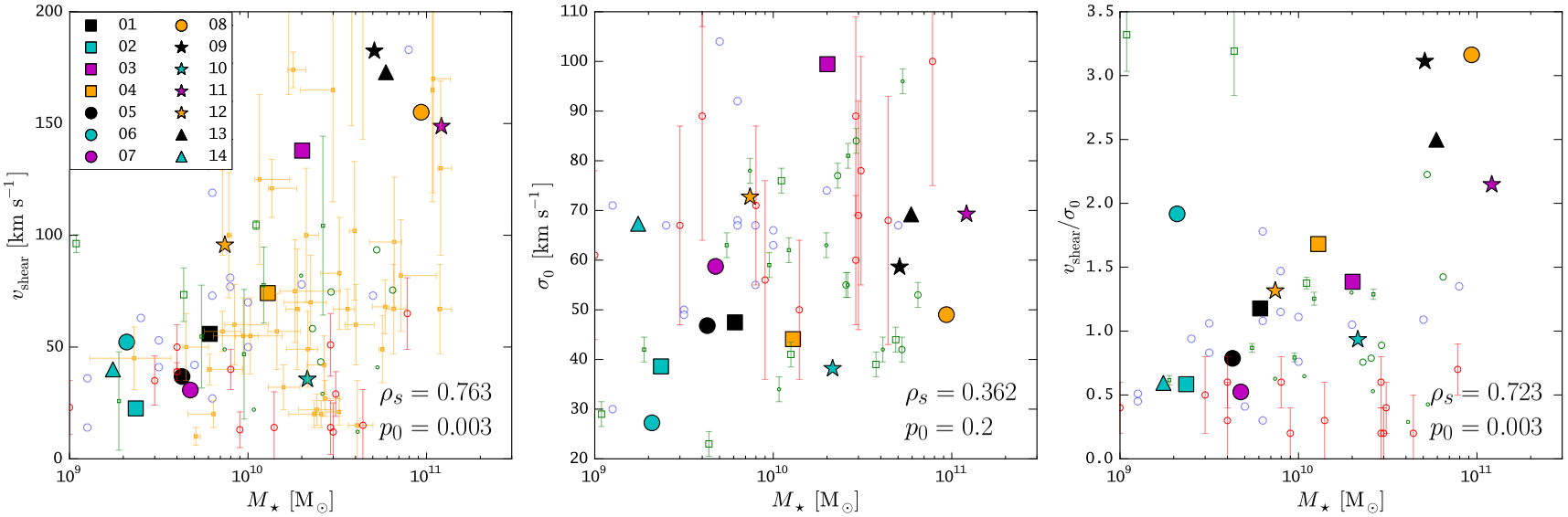

Figure 2.9: Global Hα kinematical parameters $v_{\rm shear}$ (*left panel*), σ_0 (*middle panel*) and $v_{\rm shear}/\sigma_0$ (*right panel*) in comparison to stellar mass for LARS galaxies (from Hayes et al. 2014) and in comparison to literature values: DYNAMO $z \sim 0.1$ [compact] perturbed rotators from Green et al. (2014) as *[small] green circles*; DYNAMO $z \sim 0.1$ [compact] complex kinematics from Green et al. (2014) as *[small] green squares*; Local Lyman Break Analogues from Gonçalves et al. (2010) as *blue circles*; Keck/OSIRIS resolved $z \sim 2-3$ star forming galaxies from Law et al. (2009) as *red circles*; SINS $z \sim 2-3$ galaxies from Förster Schreiber et al. (2009) as *orange squares* (only in the left panel). Uncertainties given where available. The LARS galaxies are represented by symbols according to the legend in the left panel. Spearman rank correlation coefficients ρ_s and corresponding p_0 values for the LARS galaxies are shown in each panel.

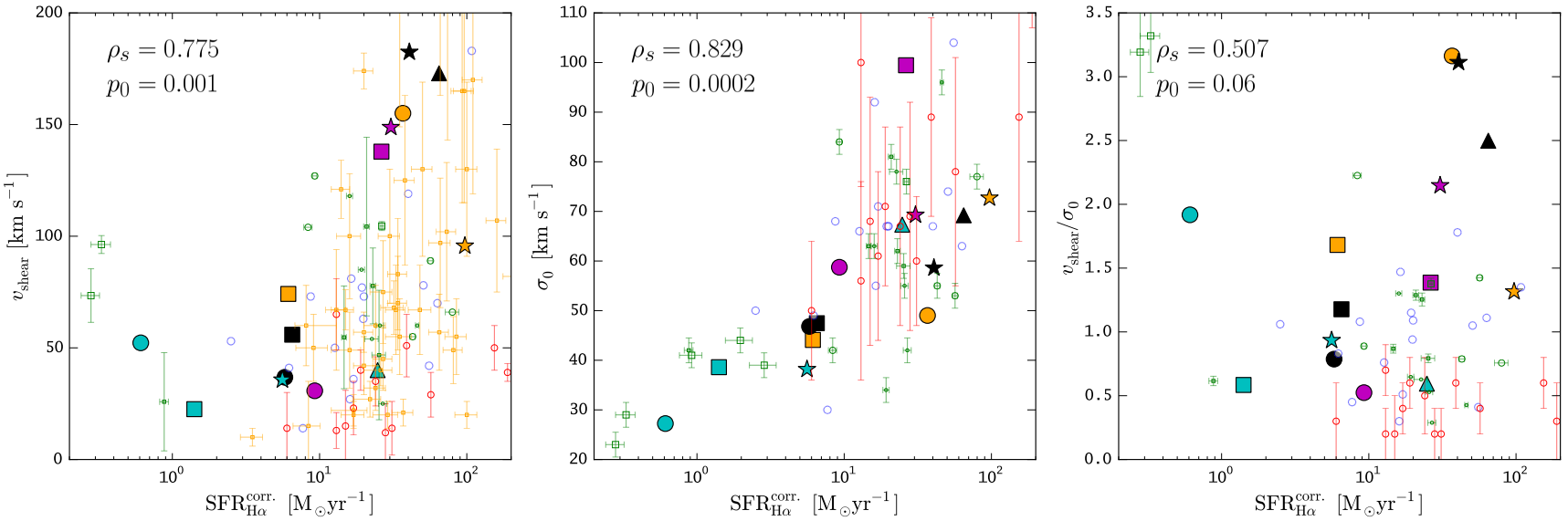

Figure 2.10: Global Hα kinematical parameters $v_{\rm shear}$ (*left panel*), σ_0 (*middle panel*) and $v_{\rm shear}/\sigma_0$ (*right panel*) in comparison to star formation rate for LARS galaxies (from Hayes et al. 2014) and in comparison to literature values (same symbols as in Fig. 2.9). Uncertainties given where available. Spearman rank correlation coefficients ρ_s and corresponding p_0 values for the LARS galaxies are shown in each panel.

two parameters of $p_0 = 0.02\%$ and $p_0 = 0.3\%$ (two-tailed test[11]) for the SFR-σ_0 and $M_\star$-$v_{\rm shear}$ relation, respectively. We discuss these two relations in more detail in Sect. 2.6.3.1 and Sect. 2.6.3.2, where we also introduce the comparison samples shown in Fig. 2.9 and Fig. 2.10.

Besides this tight correlation between SFR and σ_0, there is also a weaker correlation between SFR and $v_{\rm shear}$ in our sample ($\rho_s = 0.775$, $p_0 = 0.1\%$). We show the data in Fig. 2.10 (left panel). While not shown graphically, we note that the DYNAMO disks would scatter over the whole SFR-$v_{\rm shear}$ plane, also filling the upper left corner in this diagram. Finally, in Fig. 2.10 (right panel) we find that $v_{\rm shear}/\sigma_0$ is not significantly correlated with the SFR in LARS ($\rho_s = 0.507$, $p_0 = 6\%$).

We also check in Fig. 2.9 (centre panel) for a $M_\star$-σ_0 correlation, but with $\rho_s = 0.362$ the null-hypothesis that the variables are uncorrelated can not be rejected ($p_0 = 20\%$). Similar low correlation-coefficients are found for the comparison samples in Fig. 2.9 (centre panel). Since there is likely a monotonic relation between $M_\star$-$v_{\rm shear}$ and $M_\star$-σ_0 appear uncorrelated, the monotonic relation $M_\star$-$v_{\rm shear}/\sigma_0$ ($\rho_s = 0.723$, $p_0 = 0.3\%$) - Fig. 2.9 (right panel) - is expected.

From these results we conclude, that dispersion-dominated galaxies in our sample are preferentially low mass systems with $M_\star \lesssim 10^{10}{\rm M}_\odot$. This result is also commonly found in samples of high-z star-forming galaxies (Law et al. 2009; Förster Schreiber et al. 2009; Newman et al. 2013).

2.6.3.1 SFR-σ_0 correlation

The highly significant correlation between σ_0 and SFR has long been established for giant H II regions (Terlevich & Melnick 1981). Recently it has been shown that it extents over a large dynamical range in star formation and mass, not only locally but also at high redshifts (Green et al. 2010, 2014). The physical nature of the σ_0-SFR relation might be that star formation feedback powers turbulence in the interstellar medium. On the other hand, the processes that lead to a high SFR might also be responsible to produce a high σ_0. In particular inflows of cold gas that feed the star formation processes are expected to stir up the interstellar medium and thus lead to turbulent flows (e.g. Wisnioski et al. 2015, and references therein).

Graphically we compare in Fig. 2.10 (centre panel) the LARS SFR-σ_0 points to the values from the DYNAMO galaxies (Green et al. 2014) with complex kinematics and the DYNAMO perturbed rotators. To put this result in context with high-z studies, we also show in Fig. 2.10 the SFR-σ_0 points from the Keck/OSIRIS $z \sim 2-3$ star-forming galaxies by Law et al. (2009), and the local Lyman break analogues by Gonçalves et al. (2010). An exhaustive compilation of is presented in Green et al. (2014), and the LARS SFR-σ_0 points do not deviate from this relation.

2.6.3.2 $M_\star$-$v_{\rm shear}$ correlation

Given the complexity of the ionised gas velocity fields seen in the LARS galaxies, a tight relation between our measured, inclination-uncorrected $v_{\rm shear}$ values with stellar mass appears surprising. It indicates that, at least in a statistical sense, $v_{\rm shear}$ is tracing systemic rotation in our systems and that the scatter in our relation is dominated by the unknown inclination correction (see also Law et al. 2009).

To put our data in context to other studies, we compare our $M_\star$-$v_{\rm shear}$ data points in Fig. 2.9 (left panel) to the Green et al. (2014) DYNAMO sample and to the Gonçalves et al. (2010) local Lyman break analogues. Our high-z comparison samples are the Keck/OSIRIS $z \sim 2-3$ star-forming galaxies Law et al. and the $z \sim 1-3$ SINS sample by Förster Schreiber et al. (2009).

[11] We consider correlations as significant when the likelihood of the null-hypothesis, p_0, is smaller than 5%

We note that for the rotation-dominated and perturbed rotators in the DYNAMO sample Green et al. tabulate rotation velocity at 2.2 disc scale lengths obtained from fitting model discs to their velocity fields. We convert these to an inclination-uncorrected value by multiplication with $\sin i$. Again, for the DYNAMO sample we compare only to their objects with complex kinematics or their perturbed rotators, as they are dominant in our sample.

It is apparent from Fig. 2.9 (left panel) that while our data points line up well with the $z \sim 0.1$ galaxies, a significant number of high-z galaxies shows lower $v_{\rm shear}$ values at given stellar mass in the range 10^{10}M$_\odot$-10^{11}M$_\odot$. Reason is, that high-z studies are not sensitive enough to reach the outer faint isophotes, hence they are biased towards lower $v_{\rm shear}$ values (see Sect. 2.5.2.1). Indeed Law et al. (2009) report a detection limit of $\sim 1\,{\rm M}_\odot{\rm yr}^{-1}{\rm kpc}^{-1}$, while Förster Schreiber et al. (2009) report $\approx 0.03\,{\rm M}_\odot{\rm yr}^{-1}{\rm kpc}^{-1}$ as an average for their sample, which is comparable to our depth (Sect. 2.5.1).

2.6.4 Relations between global kinematical properties and Lyα observables

We now explore trends between global kinematical properties derived from the ionised gas in the LARS galaxies and their Lyα observables determined in Paper II, namely Lyα escape fraction $f_{\rm esc}^{{\rm Ly}\alpha}$, ratio of Ly$\alpha$ to Hα flux Lyα/Hα, and Lyα equivalent width EW$_{{\rm Ly}\alpha}$. Fore reference, we list these quantities here again in Table2.2. We recall that Lyα/Hα is the observed flux ratio, while $f_{\rm esc}$ is determined from the intrinsic luminosities, i.e. after correcting the fluxes for dust-reddening.

Regarding the qualitative classification of the $v_{\rm LOS}$ maps in Sect. 2.5.1 into rotating disks, perturbed rotators and objects showing complex kinematics there is no preference in any of the globally integrated Lyα observables. Both the maximum and the minimum of these observables occur in complex kinematics class. Therefore, just the qualitative appearance of the velocity field seems not to predict whether the galaxy is a LAE or not.

In the previous section we showed that within the LARS sample higher SFRs are found in galaxies that have higher σ_0 and higher $v_{\rm shear}$ measurements and that galaxies of higher mass show also higher $v_{\rm shear}$ values and higher $v_{\rm shear}/\sigma_0$ ratios (Fig. 2.9 and Fig. 2.10). We now compare our $v_{\rm shear}$, σ_0 and $v_{\rm shear}/\sigma_0$-ratios to the aperture integrated Lyα observables EW$_{{\rm Ly}\alpha}$, Lyα/Hα and $f_{\rm esc}^{{\rm Ly}\alpha}$ from Paper II. We do this in form of a graphical 3×3 matrix in Fig. 2.11. In each panel we include the Spearman rank correlation coefficient ρ_s and the likelihood p_0 to reject the null-hypothesis.

From the centre row in Fig. 2.11 it is obvious that none of the Lyα observables correlates with the averaged intrinsic velocity dispersion σ_0. As σ_0 correlates positively with SFR, this signifies that the observed Lyα emission is a bad star formation rate calibrator. In Fig. 2.11 it is also evident, that galaxies with higher shearing velocities ($v_{\rm shear} \gtrsim 50\,{\rm km\,s}^{-1}$) have preferentially lower EW$_{{\rm Ly}\alpha}$, lower Lyα/Hα and lower $f_{\rm esc}^{{\rm Ly}\alpha}$. Therefore, according to the above presented $M_\star$-$v_{\rm shear}$ relation (Sect. 2.6.3.2) Lyα emitters are preferentially found among the systems with $M_\star \lesssim 10^{10}$M$_\odot$ in LARS. This deficiency of strong Lyα emitters among high mass systems was already noted in Paper II. Here we see this trend now from a kinematical perspective. Also, a low $v_{\rm shear}$ value, although a necessary condition, seems not to be sufficient to have significant amounts Lyα photons escaping (e.g LARS 6). Again, this shows that Lyα escape from galaxies is a complex multi-parametric problem.

Although the LARS sample is small, the result that 7 of 8 non-LAEs have $v_{\rm shear}/\sigma_0 > 1$ and 4 of 6 LAEs have $v_{\rm shear}/\sigma_0 < 1$ signals that dispersion-dominated kinematics are an important ingredient in Lyα escape. Again, lower $v_{\rm shear}/\sigma_0$ ratios are found in lower $M_\star$ objects in our sample and σ_0 is uncorrelated with $M_\star$. Therefore the correlation between Lyα observables and

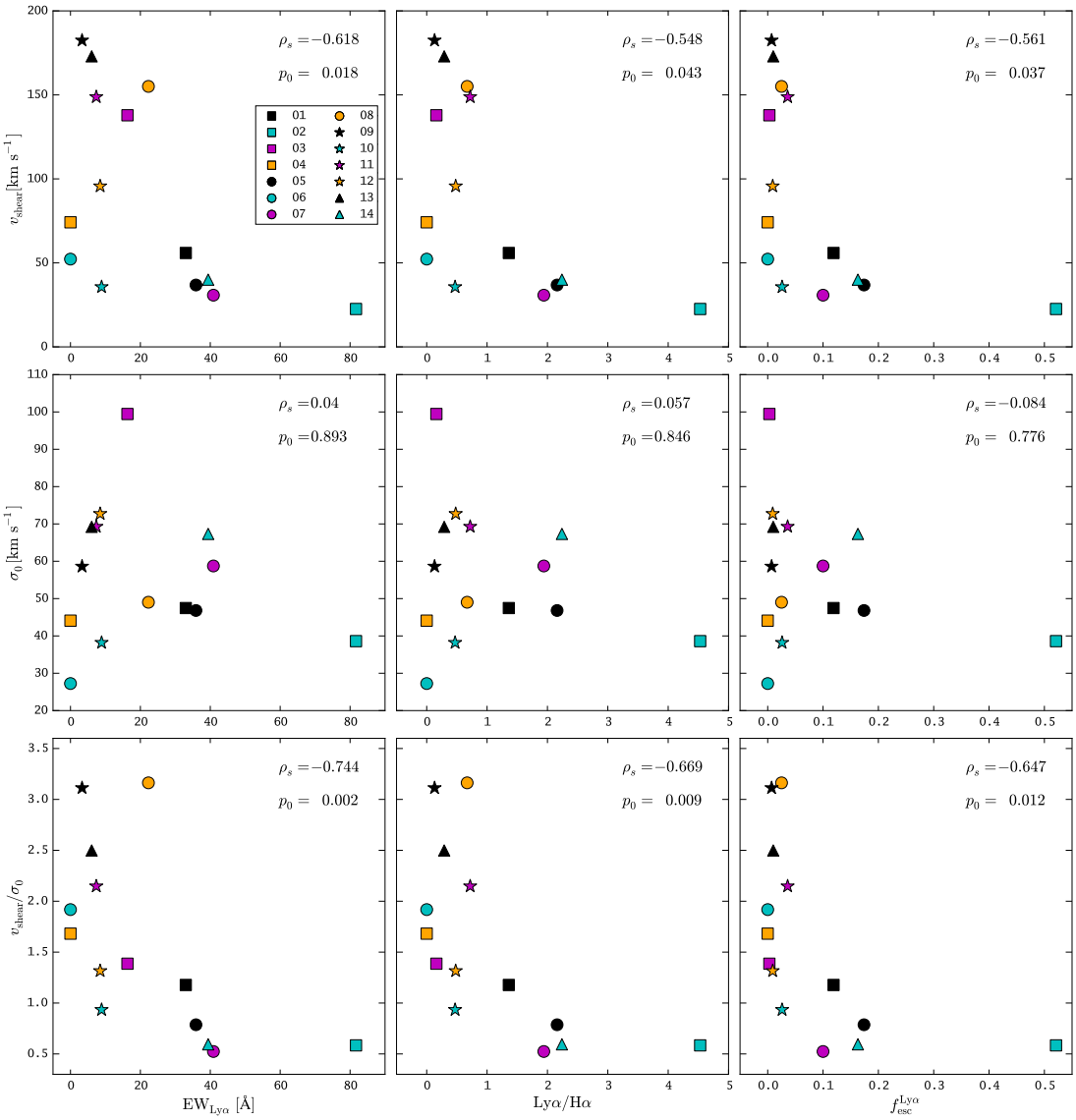

Figure 2.11: Relations between global Lyα properties of the LARS galaxies to global kinematical parameters $v_{\rm shear}$, σ_0 and $v_{\rm shear}/\sigma_0$

$v_{\rm shear}/\sigma_0$ is a consequence of the correlation between Lyα observables and $M_\star$. Nevertheless, low $v_{\rm shear}/\sigma_0$ ratios also state that the ionised gas in those galaxies must be in a turbulent state. High SFR appears to be connected to an increase turbulence, but it is currently not clear whether the processes that cause star formation or feedback from star formation are responsible for the increased turbulence (Sect. 2.6.3.1). Regardless of the causal relationship between SFR and σ_0, our results support that Lyα escape is being favoured in low-mass systems undergoing an intense star formation episode. Similarly Cowie et al. (2010) found that in a sample of UV bright $z \sim 0.3$ galaxies LAEs are primarily the young galaxies that have recently become strongly star forming. In the local Universe dispersion-dominated systems with $v_{\rm shear}/\sigma_0 < 1$ are rare, but they become much more prevalent at higher redshifts (Wisnioski et al. 2015). Coincidentally, the number density of LAEs rises towards higher redshifts (Wold et al. 2014). Therefore we speculate, that dispersion dominated kinematics are indeed a necessary requirement for a galaxy to have a significant amount of Lyα photons escaping.

2.6.5 Lyα extension and Hα kinematics

All of the LARS LAEs show a significantly more extended Lyα morphology compared to their appearance in Hα or UV continuum. These large-scale Lyα haloes appear to completely encompass the star-forming regions. LARS 1, LARS 2, LARS 5, LARS 7, LARS 12 and LARS 14 are the most obvious examples of extended Lyα emission, but the phenomenon is visible in all our objects – even for those galaxies that show Lyα in absorption (Fig. 2.5, 2.6 and 2.7; cf. Hayes et al. (2013) and Paper II). At high redshift the ubiquity of extended Lyα haloes around LAEs was recently revealed by Wisotzki et al. (2016) on an individual object-by-object basis. However, in contrast to the LARS Lyα haloes, the high-z haloes appear to have $\sim$10$\times$ larger extents at a given continuum radius (Wisotzki et al. 2016, their Fig. 12). In order to quantify the spatial extent of observed relative to intrinsic Lyα emission we defined in Hayes et al. (2013) the *Relative Petrosian Extension* $\xi_{\rm Ly\alpha}$ as the ratio of the Petrosian radii at $\eta = 20\%$ (Petrosian 1976) measured in Lyα and Hα: $\xi_{\rm Ly\alpha} = R^{\rm Ly\alpha}_{\rm P20}/R^{\rm H\alpha}_{\rm P20}$. For reference we list the $\xi_{\rm Ly\alpha}$ values of the LARS galaxies here again in Table 2.2. Based on an anti-correlation between $\xi_{\rm Ly\alpha}$ and UV slope we conjectured that smaller Lyα haloes occur in galaxies that have converted more of their circum-galactic neutral gas into forming stars and subsequently dust (Hayes et al. 2013). In such a scenario the larger extent of high-z Lyα haloes could be related to the circum-galactic gas-reservoirs being larger in the early universe.

In Fig. 2.12 we show that there are no significant correlations between $\xi_{\rm Ly\alpha}$ and the global kinematical Hα parameters $v_{\rm shear}$, σ_0 and $v_{\rm shear}/\sigma_0$. Therefore we reason that the kinematics of the interstellar medium do not strongly influence the appearance of the haloes and that the Lyα halo phenomenon is only related to the presence of a full gas-reservoir. Further 21cm HI imaging of the LARS galaxies at high spatial resolution is needed to test this scenario.

2.7 Summary and conclusions

We obtained the following results From our integral field spectroscopic observations of the Hα line in the LARS galaxies:

1. Half of the LARS galaxies show complex Hα kinematics. Only two galaxies have kinematical properties consistent with a rotating disk and in five a disturbed rotational signature is apparent. With respect to Lyα escape we find no preference of high $\rm EW_{Ly\alpha}$ or high

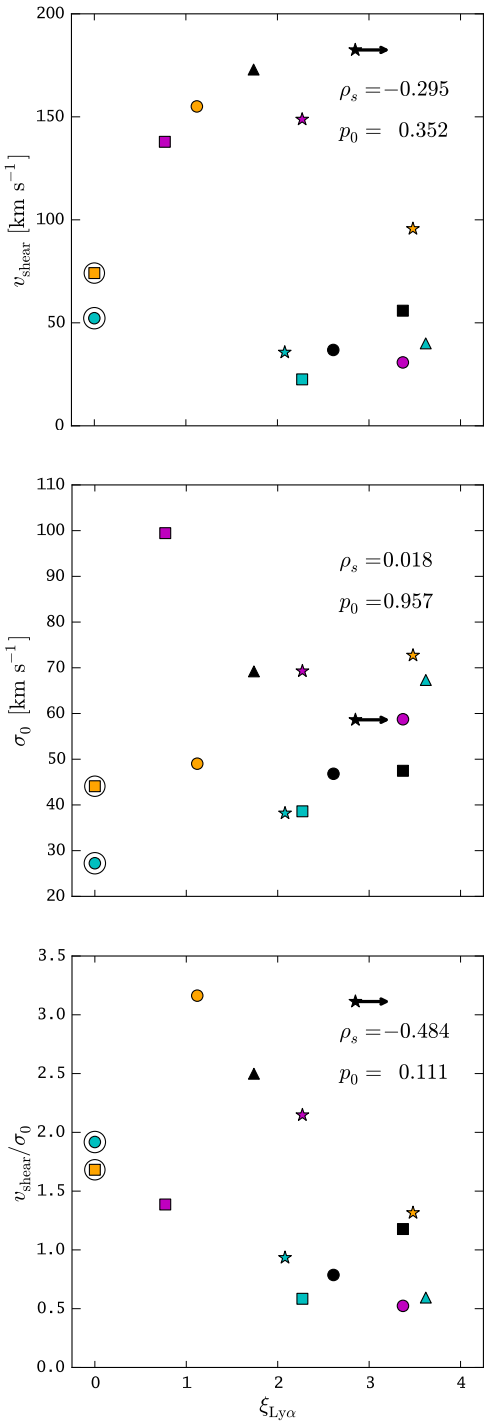

Figure 2.12: Relations between $\xi_{\rm Ly\alpha}$ – the *relative Petrosian extension of Lyα* as defined in Hayes et al. (2013) – and global kinematical parameters $v_{\rm shear}$, σ_0 and $v_{\rm shear}/\sigma_0$ with symbols according to the legend in Fig. 2.9. For galaxies with no Lyα emission (LARS 4 and LARS 6, circled symbols) $\xi_{\rm Ly\alpha}$ is defined as zero and for LARS 9 the measured $\xi_{\rm Ly\alpha}$ presents a lower limit (cf. Hayes et al. 2013). Spearman rank correlation coefficients ρ_s and corresponding p_0 values are calculated excluding the LARS 4 and LARS 6.

$f_{\rm esc.}^{{\rm Ly}\alpha}$ values towards any of those classes but the minimum and maximum values occur both in objects showing complex kinematics in our sample.

2. A common feature in all LARS galaxies are high Hα velocity dispersions. With $v_{\rm FWHM} \gtrsim 100\,{\rm km\,s^{-1}}$ our measurements are in contrast to values typically seen in local spirals, but in high-z star-forming galaxies such high values appear to be the norm.

3. While we could not infer a direct relation between spatially resolved kinematics of the ionised gas and photometric Lyα properties for all LARS galaxies, in individual cases our maps appear qualitatively consistent with outflow scenarios that promote Lyα escape from high-density regions.

4. Currently a spatially resolved comparison of our H II velocity fields to our H I data is severely limited, since the scales resolved by the radio observations are significantly larger. However, for one galaxy (LARS 7) the difference between globally integrated velocity dispersion of ionised and neutral gas offers a viable explanation for the escape of significant amounts of Lyα photons.

5. From our Hα velocity maps we derive the non-parametric statistics $v_{\rm shear}$, σ_0 and $v_{\rm shear}/\sigma_0$ to quantify the kinematics of the LARS galaxies globally. Our $v_{\rm shear}$ values range from $30\,{\rm km\,s^{-1}}$ to $180\,{\rm km\,s^{-1}}$ and our σ_0 values range from $40\,{\rm km\,s^{-1}}$ to $100\,{\rm km\,s^{-1}}$. For our ratios $v_{\rm shear}/\sigma_0$ we find a median of 1.4 and five of the LARS galaxies are dispersion-dominated systems with $v_{\rm shear}/\sigma_0 < 1$.

6. Fully consistent with other IFS studies σ_0 is positively correlated with star formation rate in the LARS galaxies. We also find strong correlations between $M_\star$ and $v_{\rm shear}$, $M_\star$ and $v_{\rm shear}/\sigma_0$, and SFR and $v_{\rm shear}$. In view of the $M_\star$-$v_{\rm shear}$ the SFR- $v_{\rm shear}$ correlation implies that more massive galaxies have higher overall star formation rates in our sample.

7. The Lyα properties EW$_{{\rm Ly}\alpha}$, Lyα/Hα and $f_{\rm esc.}^{{\rm Ly}\alpha}$ do not correlate with σ_0, but they correlate with $v_{\rm shear}$ and $v_{\rm shear}/\sigma_0$ (Fig. 2.11). We find no correlation between the global kinematical statistics and the extent of the Lyα halo.

8. 4 of 6 LARS LAEs are dispersion-dominated systems with $v_{\rm shear}/\sigma_0 < 1$ and 7 of 8 non-LAEs have $v_{\rm shear}/\sigma_0 > 1$.

Observational studies of Lyα emission in local-universe galaxies have so far focused on imaging and UV spectroscopy (for a recent review see Hayes 2015). Here we provided for the first time empirical results from IFS observations for a sample of galaxies with known Lyα observables. In our pioneering study we focused on the spectral and spatial properties of the intrinsic Lyα radiation field as traced by Hα. We found a direct relation between the global non-parametric kinematical statistics of the ionised gas and the Lyα observables $f_{\rm esc.}^{{\rm Ly}\alpha}$ and EW$_{{\rm Ly}\alpha}$, and our main result is that dispersion dominated systems favour Lyα escape. The prevalence of LAEs among dispersion dominated galaxies could be simply a consequence of these systems being the lower mass systems in our sample – a result already found in Paper II. However, the observed turbulence in actively star-forming systems should be related to ISM conditions that ease Lyα radiative transfer out of high density environments. In particular, if turbulence is a direct consequence of star formation, then the energetic input from the star formation episode might also be powerful enough to drive cavities through the neutral medium into the lower density circum-galactic environments. Of course, the kinematics of the ionised gas offer only a limited view of the processes at play and in future studies we attempt to connect our kinematic

measurements to spatial mappings of the ISMs ionisation state. The synergy between IFS data, space based UV imaging and high resolution H I observations of nearby star forming galaxies will be vital to build a coherent observational picture of Lyα radiative transport in galaxies.

Appendix

2.A Notes on individual objects

In the following we detail the observed Hα velocity fields for each galaxy. We compare our maps to the photometric Lyα properties derived from the HST images from Paper II and H I observations from Paper III (see Sect. 2.4).

2.A.1 LARS 1 (Mrk 259)

With $L_{\mathrm{Ly}\alpha} = 8 \times 10^{41}\,\mathrm{erg\,s^{-1}}$ and $\mathrm{EW}_{\mathrm{Ly}\alpha} = 33\,$Å LARS 1 is a strong Ly$\alpha$ emitting galaxy. A detailed description of the photometric properties of this galaxy was presented in Paper I. If LARS 1 would be at high-z, it would easily be selected in conventional narrow-band imaging surveys (Paper IV). The galaxy shows a highly irregular morphology. Its main feature is UV-bright complex in the north-east that harbours the youngest stellar population. As noted already in Paper II filamentary structure emanating from the north-eastern knot is seen in Hα. Towards the south-east numerous smaller star-forming complexes are found that blend in with an older stellar population.

Contrasting the irregular appearance, the line of sight velocity field of LARS 1 is rather symmetric. The velocity field is consistent with a rotating galaxy. The kinematical centre is close to centre of the PMAS FoV and the kinematical axis appears to run from the north-west to the south-east. We measure $v_{\mathrm{shear}} = 56 \pm 1\,\mathrm{km\,s^{-1}}$. The GBT single dish H I spectrum of this source is reminiscent of a classic double-horn profile, also an obvious sign of rotation, with a peak separation consistent with our v_{shear} measurement.

The highest velocity dispersions ($v_{\mathrm{FWHM}} \approx 150\,\mathrm{km\,s^{-1}}$) are found in the north-eastern region. Here LARS 1 also shines strong in Lyα. But while a fraction of Lyα appears to escape directly towards us, a more extended Lyα halo around this part is indicative of resonant scatterings in the circum-galactic gas (cf. also Östlin et al. 2014). Contrary, in the south-western part of the galaxy, where we observe the lowest velocity dispersions ($v_{\mathrm{FWHM}} \approx 70\,\mathrm{km\,s^{-1}}$), Ly$\alpha$ photons do not escape along the line of sight.

2.A.2 LARS 2 (Shoc 240)

Everywhere in LARS 2 where Hα photons are produced, Lyα photons emerge along the line of sight. LARS 2 is the galaxy with the highest global escape fraction of Lyα photons ($f_{\mathrm{esc.}}^{\mathrm{Ly}\alpha} = 52.1\%$) and the highest Ly$\alpha$/H$\alpha$ ratio (Lyα/Hα = 4.53).

With $v_{\mathrm{shear}} = 23 \pm 2\,\mathrm{km\,s^{-1}}$, LARS 2 shows the smallest v_{shear} in our sample. However, we consider this value as a lower limit since we missed in our pointing the southernmost star forming knot. Our observed velocity field appears to be disturbed, but we could envision a kinematical axis orthogonal to the photometric major axis - i.e. roughly from west to east. This idea is supported by our VLA imaging of this source (see Fig. 7 in Paper III). The H I velocity field also indicates $v_{\mathrm{shear}} \approx 30\,\mathrm{km\,s^{-1}}$, meaning that our incomplete measurement gives a sensible lower limit. Within the observed region our velocity dispersion map is rather uniform, with $v_{\mathrm{VFWHM}} \approx 100\,\mathrm{km\,s^{-1}}$.

2.A.3 LARS 3 (Arp 238)

LARS 3 is the south-eastern nucleus of the violently interacting pair of similar sized spiral galaxies Arp 238. With a global $f_{\rm esc}^{{\rm Ly}\alpha} = 0.1$ and $L_{{\rm Ly}\alpha} = 10^{41}{\rm erg\,s^{-1}}$ this dust rich luminous infrared galaxy is a relatively weak Lyα emitter. VLA H I imaging reveals an extended tail towards the west. This tidal tail is much larger than the optical dimensions of the pair Arp 238 (see also Cannon et al. 2004, for similar extended tidal H I structures around the Lyα emitting star bursts Tol 1924-416 and IRAS 08339+6517).

In Hα the main kinematical axis runs from west to east and the radial velocity field appears symmetric, although slightly disturbed towards the north and the south. We measure $v_{\rm shear} \approx 140\,{\rm km\,s^{-1}}$, a value which is in the domain of typical maximum velocities of inclination corrected Hα rotation curves of spiral galaxies (e.g. Epinat et al. 2008a, 2010; Erroz-Ferrer et al. 2015). With $v_{\rm FWHM} \gtrsim 300\,{\rm km\,s^{-1}}$ highest velocity dispersions are observed in the western part. The largest Lyα surface brightness is also observed in the western part of the nucleus. Lyα appears in absorption in the eastern region, where we also see a minimum in velocity dispersions with $v_{\rm FWHM} \approx 70\,{\rm km\,s^{-1}}$.

2.A.4 LARS 4 (SDSS J130728.45+542652.3)

Although LARS 4 is similar to LARS 1 in terms of dust content and star formation rate, globally this galaxy shows Lyα in absorption. The galaxy can be photometrically decomposed into two main components: an elongated lower surface brightness structure in the west and a more puffed up and luminous companion in the east. The eastern structure is tilted at $\approx 40^\circ$ with respect to the western one.

Compared to the highly irregular morphology in UV and Hα, the radial velocity field appears rather regular, with a moderate amplitude of $v_{\rm shear} \approx 75\,{\rm km\,s^{-1}}$ along a well defined axis from west to east. The kinematic centre appears to be right between the two photometric components, indicating that the observed shearing is the velocity difference between the merging components and not a consequence of rotation. The lack of a well defined simple and organised disk is further supported by the absence of a double-horn profile in the GBT single-dish H I profile. Nevertheless, higher sensitivity VLA imaging results show a coherent velocity field on larger scales with an amplitude comparable to $v_{\rm shear}$ (Paper III, their Fig. 9).

In the dispersion map, the two components are clearly distinguishable, with the eastern component showing higher velocity dispersions ($v_{\rm FWHM} \approx 100\,{\rm km\,s^{-1}}$) than the western ($v_{\rm FWHM} \approx 65\,{\rm km\,s^{-1}}$). In both regions, however, Lyα is seen in absorption. The highest velocity dispersions are observed at the boundary region where the two components are separated photometrically - but also here only little Lyα is escaping.

2.A.5 LARS 5 (Mrk 1486)

In the HST images LARS 5 appears as a small (i.e. projected diameter $d \approx 5\,{\rm kpc}$) highly inclined edge-on disk. Within the apparent disk Lyα appears in absorption but the galaxy shows an extended halo, which is azimuthally symmetric at low surface brightness isophotes, while brighter isophotes resemble more the elongated Hα shape. Most prominent in the Hα image are filamentary "fingers" extending below and above the disk, reminiscent of an outflowing wind.

Although the profile of our single-dish H I observations shows multiple peaks close to the noise level that might correspond to the peaks of a faint double horn profile (Paper III), our Hα kinematics appear incompatible with a typical disk scenario: Firstly, our measured $v_{\rm shear} = 37\,{\rm km\,s^{-1}}$ indicates a very low rotation curve amplitude - untypical even for a small disk (e.g.

in the largest Hα disk sample of Epinat et al. 2010, for $d \leq 5$ kpc the maximum rotation curve velocity is on average 95 km s^{-1}). Secondly, there is apparent asymmetry in the spatial distribution of the $v_{\rm LOS}$ values, i.e. a large sector in the south-west characterised by similar line of sight velocities ($v_{\rm LOS} \sim +20$ km s^{-1}), while only a small sector in the north-east shows blue-shifted Hα emission ($v_{\rm LOS} \sim -40$ km s^{-1}).

The most prominent feature in the velocity dispersion map is a biconical zone of increasing velocity dispersions (from $\sim$120 km s^{-1} to $\sim$220 km s^{-1}) with increasing distance from the centre. The base of this zone coincides the brightest region in UV and Hα in the south-western sector. We note that the seeing PSF FWHM for this observation is 1.3″, thus $\sim$2× the extend of the 0.5″×0.5″ spaxels used on LARS 5. However, as the kinematical centre is not co-spatial with the base of the cones, and since the velocity gradient around the base of the cone is very weak we are confident that this feature is real and not caused by PSF smearing effects.

2.A.6 LARS 6 (KISSR 2019)

With $\lesssim 1\,{\rm M}_\odot{\rm yr}^{-1}$ conversion of gas into stars LARS 6 shows the lowest star formation rate in the sample (Hayes et al. 2014). The main star forming knot is in the north with a tail of much smaller and less luminous knots extending to the south. In our seeing limited data cubes we can not disentangle these individual knots photometrically. Lyα is seen in absorption, even on the smallest scales.

Shearing is observed between the main component and the tail, although the amplitude is moderate ($v_{\rm shear} = 52$ km s^{-1}). The main component also shows higher velocity dispersions ($v_{\rm VFWHM} \approx 70$ km s^{-1}) than the tail ($v_{\rm VFWHM} \approx 50$ km s^{-1}). Overall this galaxy has the lowest observed velocity dispersion in the sample.

Our GBT single-dish H I measurements are severely contaminated by the nearby field spiral UGC 10028. However, newly obtained but as of yet unpublished VLA D-configuration images allow a first-order separation from LARS 6 and this companion. From these data, coherent rotation is present in the H I gas associated with LARS 6 at a level roughly consistent with the $v_{\rm shear}$ estimate we obtain from PMAS.

2.A.7 LARS 7 (IRAS F13136+2938)

In the continuum LARS 7 resembles a highly inclined disk comparable to LARS 5. But, in Hα an almost azimuthally symmetric structure emerges that is highly distended with respect to the elongated continuum morphology. Moreover, two extended low surface brightness red lobes are found at the opposite ends of the inclined disk, reminiscent of a shell like structure. This is suggestive of a recent merger event (e.g. Bettoni et al. 2011). In Lyα images LARS 7 appears even more extended, with the bright isophotes following the Hα shape and low-surface brightness isophotes resembling a more scaled up version of the apparent disk.

For similar reasons as outlined for LARS 5 in Sect. 2.A.5, our Hα kinematics argue against a typical disk scenario: We observe a low shearing amplitude; with $v_{\rm shear} = 31$ km s^{-1} even lower than in LARS 5. Moreover, the line of sight velocity maps appears disturbed compared to that expected for a classical disk. Our GBT single dish H I observations reveal a single broad (92 km s^{-1}) line. LARS 7 is the only object where the GBT line-width is incompatible to its integrated Hα linewidth (cf. Sect. 2.6.2). A main kinematical axis can be envisioned to run from north east to south west along the continuum major axis. But in the north west and south east the $v_{\rm LOS}$ values do not follow this weak gradient at all. Overall the galaxy shows high velocity dispersion in Hα ($v_{\rm FWHM} \gtrsim 160$ km s^{-1}), with the lowest values occurring in north east

($v_{\rm FWHM} \approx 120\,{\rm km\,s^{-1}}$), where the brightest fluxes in Lyα and the highest Lyα/Hα ratios are observed.

2.A.8 LARS 8 (SDSS-J125013.50+073441.5)

LARS 8 appears a face-on disk with the highest metalicity of the sample. The apparent disk also possesses a highly dust obscured nucleus. Nevertheless, there is a high degree of irregularity compared to classical disks and spiral arms are not well defined. As traces of shell-like structures are visible in the inner parts and in the outskirts of the galaxy (cf. Fig. 6 in Paper I), LARS 8 can be classified as a shell system hinting at a recent merger event (Bettoni et al. 2011, e.g.). The Lyα light distribution of LARS 8 does not resemble that seen in Hα. The brightest Lyα zone is in the north of the disk, while in the south Lyα appears only in absorption. At lower surface brightness isophotes a Lyα halo becomes visible. With an equivalent width ${\rm EW_{Ly\alpha}} = 20.3$Å this galaxy would be selected as LAE in conventional narrow-band surveys.

Our $v_{\rm LOS}$ map seems disk like. Assuming an infinitely thin disk the ellipticity of 0.2 (Guaita et al. 2015) implies an inclination of 40°, hence our observed $v_{\rm shear} = 155\,{\rm km\,s^{-1}}$ translates to $v_{\rm max} = 241\,{\rm km\,s^{-1}}$. The GBT single-dish H I profile shows a broad, possibly double peaked profile. Although these peaks are not significantly separated from the overall H I signal, the implied velocity difference of $\sim$300 km s^{-1} appears consistent with our $v_{\rm shear}$ measurement. The orientation of the velocity field from VLA interferometric H I observations is qualitatively consistent with our PMAS Hα observations, although at the VLA D-configuration beam size of 72″ LARS 8 appears only marginally resolved.

Elevated velocity dispersions with $v_{\rm FWHM} \gtrsim 160\,{\rm km\,s^{-1}}$ are apparent to extend orthogonal to the kinematical axis along the 0 km s^{-1} iso velocity contour. In the other parts of the $v_{\rm FWHM}$ map is rather flat, typically with $v_{\rm FWHM} \sim 100\,{\rm km\,s^{-1}}$ - a value that is also still commonly observed within the sample of 153 local spirals by Epinat et al. (2010). Given the strong gradient in the velocity field, the observed elevated velocity dispersions are likely a result of PSF smearing effects.

2.A.9 LARS 9 (IRAS 08208+2816)

This luminous infrared galaxy has highly irregular morphology. Numerous star forming knots are visible in Hα along two arms of large extend that are connected to central, very bright Hα nucleus. We note that at the end of the southern-tail a foreground star appears in projection; contributions from this star have been masked out in the PMAS data. In LARS 9 Lyα is almost everywhere absorbed along the line of sight towards the star forming regions. Nevertheless, this galaxy is embedded in a faint extended Lyα. Morphologically, this fuzz broadly traces a scaled up version of its optical and Hα shape. Having a globally integrated Lyα luminosity of $L_{\rm Ly\alpha} \approx 3 \times 10^{41}\,{\rm erg\,s^{-1}}$ and an equivalent width of $EW_{\rm Ly\alpha} \approx 8$Å, this galaxy would not be selected by its Lyα emission at high-z in conventional narrow-band surveys.

Since LARS 9 extends more than $\sim 0.5'$ on the sky, we needed to cover it with two PMAS 16″×16″ pointings (Fig. 2.6). The line of sight velocity field for this galaxy is very peculiar. From the north to the centre a weak ($\sim 100\,{\rm km\,s^{-1}}$) gradient from blue-shifted to systemic velocity is apparent. From the centre this weak gradient continues towards the south. The southern tail then shows an opposite gradient from red- to blue-shifts. We note that in this south- and south-western zone a single Gaussian often is not an optimal representation of the observed Hα lines. In this zone the spectral profile is sometimes asymmetric with an extended red or blue wing, but often it shows also clearly double peaked morphology (for examples see Fig. 2.13).

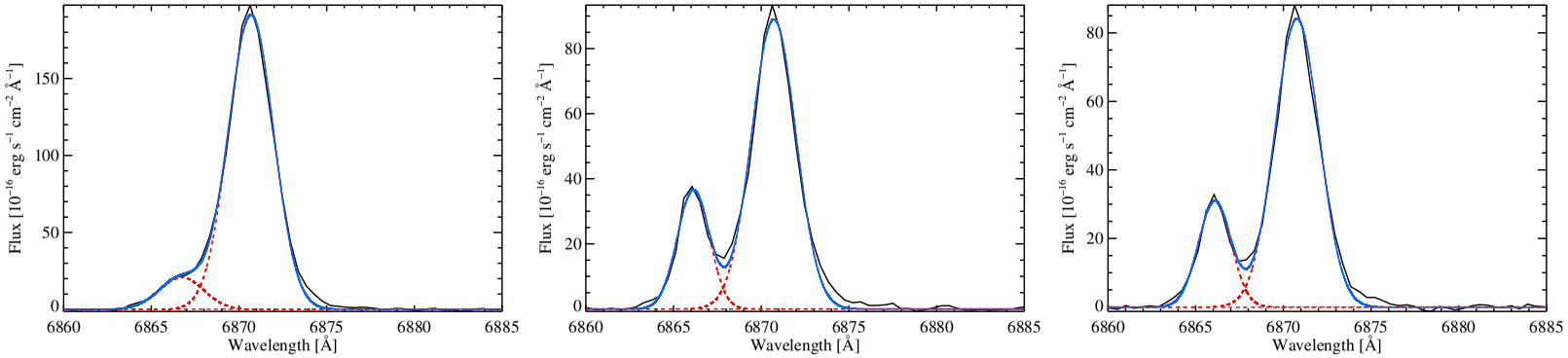

Figure 2.13: Representative LARS 9 Hα line profiles in blue hatched region of Fig. 2.6 described by a fit using two Gaussian components. The *red dashed lines* show the individual components and the *blue line* shows the sum, while the *black line* shows the profile as observed. For all profiles shown the single component fit used to create the map shown in Fig. 2.6 converged on the stronger red component.

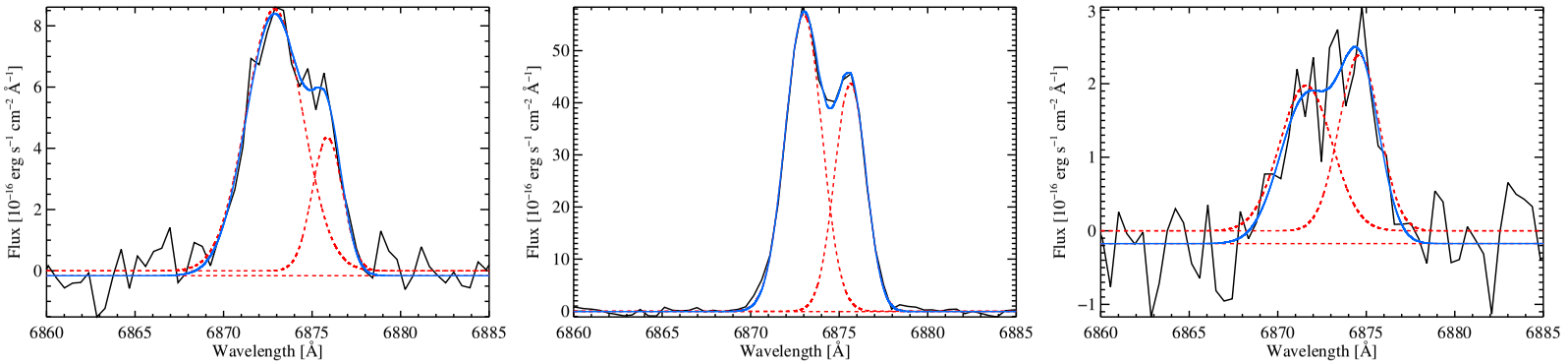

Figure 2.14: Representative LARS 9 Hα line profiles in red hatched region of Fig. 2.6, similar to Fig. 2.13. The single component fit used to create the map shown in Fig. 2.6 converged on the stronger blue component in the centre panel, but for the profiles shown in the left and right panel the single component fit is artificially broadened.

In some these regions our fit tries to capture both lines, hence the obtained line of sight velocity is centred between the peaks and the linewidth appears very broad (e.g. left and right panel of Fig. 2.14). In some other spaxels, when the secondary peak is very weak or when only an extended wing is seen, the fit converges to the stronger line. The affected zones have hatched rectangles overlaid in Fig. 2.6. These zones harbour a kinematical distinct secondary component. This secondary component does not follow the large scale motions of the northern component, to which also the nucleus belongs. We indicate by red- and blue-hatchings in Fig. 2.6 the regions of this component that are red- and blue-shifted with respect to the systemic velocity (as given by the nucleus). As a natural outcome from this qualitative analysis the emission in south-eastern tail of LARS 9 is solely coming from this secondary component. We note that also only at the end of this tail a significant fraction of Lyα photons appear to escape towards the observer.

From our PMAS observation we conclude that LARS 9 is a closely interacting pair of galaxies in an advanced stage of merging. The interaction scenario is also supported by our 21cm observations. The integrated GBT spectrum shows a broad single line, indicating that the bulk of the H I is not partaking in an ordered flat rotation. LARS 9 was only marginally resolved in our VLA H I maps (Paper III). However, as of yet unpublished VLA C configuration observations (K. Fitzgibbon, in prep.) show extended H I towards the west, enclosing the galaxy SDSS J082353.65+280622.2. For this galaxy no spectroscopic redshift is available, but the photometric redshift agrees with being associated to LARS 9. These observations therefore strongly suggests that a third system is significantly involved in the interaction. Moreover, the VLA C-configuration observations of LARS 9 show a peak in the second-moment maps that trace the random motions of H I that coincides spatially with the zones of multiple H II components in our PMAS maps . Hence, at these locations (hatched regions in Fig. 2.6) Lyα photons of both distinct kinematical components are likely scattered by H I at resonance.

2.A.10 LARS 10 (Mrk 0061)

Similar to LARS 1 this galaxy appears morphologically to be in an advanced merger state. It possesses a large UV bright core in the north-west and a spur of smaller, less luminous star forming regions towards the south-east. Several redder low-surface brightness structures are seen outside the main body of the galaxy, reminiscent of the appearance of shell galaxies (e.g. Marino et al. 2009; Bettoni et al. 2011). From the central star-forming parts Lyα is only seen in absorption, while at larger radii a faint halo emerges. When considering solely the central parts the galaxy would remain undetected in high-z LAE surveys since $\mathrm{EW}_{\mathrm{Ly}\alpha} = 8$Å. But, when integrating over the lower-surface brightness emission $\mathrm{EW}_{\mathrm{Ly}\alpha}$ rises to 31Å and with its luminosity of $L_{\mathrm{Ly}\alpha} = 2 \times 10^{41} \mathrm{erg\,s^{-1}}$ it would be within the sensitivity of the deepest contemporary LAE surveys (Rauch et al. 2008; Bacon et al. 2015).

The line of sight velocity field is symmetric and consistent with rotation and contrasts the irregular continuum morphology. The velocity gradient running from the south-east to the north-west is weak and we measure $v_{\mathrm{shear}} = 36\,\mathrm{km\,s^{-1}}$. The seeing for this observation was quite substantial (1.5″ FWHM, i.e 3× the size of the 0.5″×0.5″ spaxels). Despite the weak gradient, this leads to non-negligible PSF smearing effects in the dispersion map. Moreover, due to the short exposure time and the rather low Hα flux this galaxy has the lowest SNR per spaxel of the whole sample; this manifests in a noisy v_{FWHM} map. Both of these effects make essentially local disturbances in the velocity dispersion untraceable in our LARS 10 dataset, but our flux weighted global measurement of $\sigma_0 \approx 40\,\mathrm{km\,s^{-1}}$ is robust against these nuisances.

The GBT integrated H I spectrum shows a broad single line profile ($\sim$280 $\mathrm{km\,s^{-1}}$ FWHM), however at low signal to noise. This appears hard to reconcile with the Hα results. If real, it

might indicate that a large fraction of neutral gas in and around LARS 10 is kinematically in a different state than the gas around the galaxy's star forming regions.

2.A.11 LARS 11 (SDSS J140347.22+062812.1)

This galaxy appears as a highly inclined edge-on disk in the continuum and UV that is slightly thicker when seen in Hα. According to the Hα and UV emission, stronger star formation occurs in the south-eastern zone of the projected disk. In Lyα a mildly extended halo above and below the plane is visible, with the isophotal contours approximately preserving the axis ratio of Hα. Within the disk Lyα occurs exclusively in absorption.

Running along the disk from the north-west to the south-east a strong gradient in the $v_{\rm LOS}$ map is apparent. The observed shearing amplitude $v_{\rm shear} = 150\,{\rm km\,s^{-1}}$ is consistent with this gradient being caused by rotation (e.g. Epinat et al. 2008a, 2010; Erroz-Ferrer et al. 2015). Unfortunately the beam of our GBT single-dish H I observations is likely contaminated by other sources. Nevertheless, within the multiple peaks in the GBT spectrum a double-horn profile at a velocity separation consistent with our Hα $v_{\rm shear}$ measurement is visible. Although the projected height of the disk is similar to the PSF FWHM, the dispersion map shows traces of higher velocity dispersions above and below the disk ($v_{\rm VFWHM} \approx 200\,{\rm km\,s^{-1}}$) than within ($v_{\rm VFWHM} \approx 150\,{\rm km\,s^{-1}}$), especially around the star-forming regions in the south east. We note, however, that the elevated dispersions near the kinematic centre are caused by PSF smearing of the strong gradient in the $v_{\rm LOS}$ field.

2.A.12 LARS 12 (LEDA 27453)

Because of its modest $\mathrm{EW_{Ly\alpha}} = 13$Å this UV bright merger would not be selected as a LAE at high-z. At its brightest knot in UV and Hα the galaxy shows Lyα only in absorption. Only at larger radii, where a number of fainter star forming regions can be appreciated, Lyα appears in emission. Moreover, LARS 12 is embedded in a faint, low surface brightness Lyα halo.

The non-regular Hα velocity field indicates complex kinematics. In the north-western corner a strong $\sim 140\,{\rm km\,s^{-1}}$ gradient over $\sim 1.5''$ (~ 2.8 kpc at $d_{\rm LARS12} = 470.5$ Mpc) is observed, but from there towards the south-west the velocity field is essentially flat. The high velocity and velocity dispersion in the values seen in the south are not significant, as the low SNR of this broad line in these binned spaxels lead to a 50% error on the determined $v_{\rm LOS}$ and σ_0 value. We note that because of PSF smearing effects the strong velocity gradient is responsible for the region of elevated velocity dispersions in the north-western corner.

For LARS 12 adaptive optics Paschen α IFS observations have been presented in Gonçalves et al. (2010) - Object ScUVLG 093813 in their nomenclature. Their line-of-sight velocity field is qualitatively fully consistent with ours, but their higher resolution data allows to pinpoint the highest redshifted values directly to the two filaments that extent towards the north-west. Since they are not affected by PSF smearing their dispersion map is not contaminated by high-velocity dispersions in the north-west. Of course, our artifact in the south is also absent from their map. Nevertheless, their σ_0 value of $62\,{\rm km\,s^{-1}}$ is in good agreement with our measurement of $72\,{\rm km\,s^{-1}}$.

2.A.13 LARS 13 (IRAS 01477+1254)

Based on its highly irregular morphology this starburst system is clearly interacting. As LARS 13 shows a narrow Lyα equivalent width ($\mathrm{EW_{Ly\alpha}} = 6$ Å), it would not be selected as a LAE at

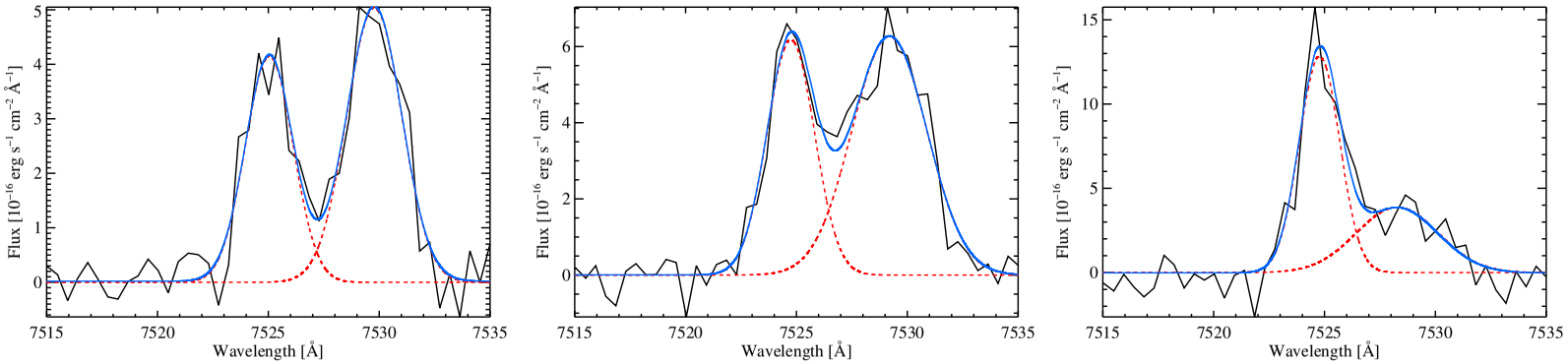

Figure 2.15: Representative LARS 13 Hα line profiles in blue hatched region of Fig. 2.7, similar to Fig. 2.13. The single component fit used to create the map shown in Fig. 2.7 converged on the stronger blue component in the right panel, but for the profiles shown in the left and canter panel the single component fit is artificially broadened.

high redshift in conventional narrow-band surveys. Overall only 1% of Lyα photons are escaping and the resulting Lyα luminosity is $L_{\mathrm{Ly}\alpha} = 7 \times 10^{41}$ erg s^{-1}.

The complex v_{LOS} map of this galaxy is characterised by a gradient from blue- to redshifts along the east-western axis for the northern component, as well as an gradient from blue-to-redshifts from south to north for the eastern component. In the north-western zone where the longitudinally aligned structure overlaps with the latitudinally aligned one, our single component Gaussian is not an optimal representation of the observed Hα line profiles. In this region the profile is often asymmetric with an extended blue wing (e.g. right panel of Fig. 2.15). Some spaxels show a double peaked Hα profile (e.g. left and centre panel of Fig. 2.15). The affected zone has a hatched rectangle overlaid in Fig. 2.7. In the region where two equally strong peaks are prominent in the spectrum, our fit tries to fit a broad line that encloses both lines; these spaxels can be seen in the east running as a diagonal line of broad velocity dispersions from north-west to south-east. Spaxels east from this demarcation show an extended blue wing. We interpret this as that we are seeing separate components of ionised gas kinematics, where one component belongs to the latitudinal elongated structure while the other belongs to the longitudinal elongated one. The spatial and spectral proximity of both regions indicates that the galaxy is still in an ongoing interaction with both progenitors not having fully coalesced.

For LARS 13 adaptive optics Paschen α IFS observations have been presented in Gonçalves et al. (2010) - object ScUVLG 015028 in their nomenclature. However, their small FoV allows them only to sample emission from the strongest star forming region in the western part, so they do not have any information on the longitudinally aligned eastern part. Consequently, their observed $v_{\mathrm{shear}} = 78\,\mathrm{km\,s^{-1}}$ is lower than our value ($v_{\mathrm{shear}} = 173\,\mathrm{km\,s^{-1}}$), since the north-eastern zone with highest v_{LOS} values in our map is not present in their data. In the zone where they have signal, there is good qualitative and quantitative agreement between our maps and their maps. In particular, they found high velocity dispersions $v_{\mathrm{FWHM}} \gtrsim 200\,\mathrm{km\,s^{-1}}$ and a weak velocity gradient in the north-western star-forming knot. We note that in this region of high velocity dispersions Lyα appears to escape directly towards the observer.

2.A.14 LARS 14 (SDSS J092600.41+442736.1)

LARS 14 is the most luminous LAE in the sample ($L_{\mathrm{Ly}\alpha} = 4.2 \times 10^{42}$erg s^{-1}). It is also classified as a green pea galaxy (Cardamone et al. 2009, see also their Fig. 7). Green pea galaxies show commonly strong Lyα emission and are also thought to be Lyman continuum leaking galaxies (Jaskot & Oey 2014; Henry et al. 2015; Yang et al. 2015). Visible in the HST images is a small companion in the south and tidal tails extending to the east and south (Cardamone et al. 2009). Our seeing limited data does not provide enough resolution to disentangle this structure photometrically from the main component within the datacube. Kinematically, however, we observe that the southern region shears at $\approx 60 - 70\,\mathrm{km\,s^{-1}}$ with respect to the northern, with not much velocity substructure seen. In the main part we observe high velocity dispersions with $v_{\mathrm{FWHM}} \approx 175\,\mathrm{km\,s^{-1}}$, dropping to $80 - 90\,\mathrm{km\,s^{-1}}$ towards the companion. Our modelling of the Hα profile with a simple 1D Gaussian did not capture the extended broad wings seen in the Hα profiles. These broad wings likely trace outflowing ionised gas, and are a feature regularly observed in pea galaxies (Yang et al. 2015).

For this galaxy adaptive optics Paschen α IFS observation have been presented in Gonçalves et al. (2010) and Basu-Zych et al. (2009) (object ScUVLG 92600 in their nomenclature). They report slightly higher values, both for the shear and the dispersion. Nevertheless, our derived $v_{\mathrm{shear}}/\sigma_0 = 0.6 \pm 0.1$ is consistent with their value of 0.51. This ratio would be lowered by about a factor of two, if only the northern main component is considered, since its velocity

offset relative to the companion dominates the shear. Noteworthy, the main component as such therefore presents the structure with the lowest $v_{\rm shear}/\sigma_0$ of our whole sample.

Acknowledgements E.C.H. especially thanks Sebastian Kamann and Bernd Husemann for teaching him how to operate the PMAS instrument. We thank the support staff at Calar Alto observatory for help with the visitor-mode observations. All plots in this paper were created using `matplotlib` (Hunter 2007). Intensity related images use the the `cubhelix` colour scheme by Green (2011). This research made extensive use of the `astropy` pacakge (Astropy Collaboration et al. 2013). M.H. acknowledges the support of the Swedish Research Council, Vetenskapsrådet and the Swedish National Space Board (SNSB) and is Academy Fellow of the Knut and Alice Wallenberg Foundation. HOF is currently granted by a Cátedra CONACyT para Jóvenes Investigadores. I.O. has been supported by the Czech Science Foundation grant GACR 14-20666P. DK is funded by the Centre National d'Études Spatiales (CNES). FD is grateful for financial support from the Japan Society for the Promotion of Science (JSPS) fund. PL acknowledges support from the ERC-StG grant EGGS-278202.

2.2 Bibliography

Adams, J. J., Blanc, G. A., Hill, G. J., et al. 2011, ApJS, 192, 5

Ahn, S.-H., Lee, H.-W., & Lee, H. M. 2003, MNRAS, 340, 863

Alonso-Herrero, A., García-Marín, M., Monreal-Ibero, A., et al. 2009, A&A, 506, 1541

Astropy Collaboration, Robitaille, T. P., Tollerud, E. J., et al. 2013, A&A, 558, A33

Bacon, R., Brinchmann, J., Richard, J., et al. 2015, A&A, 575, A75

Bacon, R., Vernet, J., Borisiva, E., et al. 2014, The Messenger, 157, 13

Barnes, L. A., Haehnelt, M. G., Tescari, E., & Viel, M. 2011, MNRAS, 416, 1723

Bassett, R., Glazebrook, K., Fisher, D. B., et al. 2014, MNRAS, 442, 3206

Basu-Zych, A. R., Gonçalves, T. S., Overzier, R., et al. 2009, ApJ, 699, L118

Behrens, C. & Braun, H. 2014, A&A, 572, A74

Behrens, C., Dijkstra, M., & Niemeyer, J. C. 2014, A&A, 563, A77

Bettoni, D., Galletta, G., Rampazzo, R., et al. 2011, A&A, 534, A24

Bik, A., Östlin, G., Hayes, M., et al. 2015, A&A, 576, L13

Calabretta, M. R. & Greisen, E. W. 2002, A&A, 395, 1077

Cannon, J. M., Skillman, E. D., Kunth, D., et al. 2004, ApJ, 608, 768

Cappellari, M. & Copin, Y. 2003, MNRAS, 342, 345

Cardamone, C., Schawinski, K., Sarzi, M., et al. 2009, MNRAS, 399, 1191

Cassata, P., Le Fèvre, O., Garilli, B., et al. 2011, A&A, 525, A143

Cassata, P., Tasca, L. A. M., Le Fèvre, O., et al. 2015, A&A, 573, A24

Chonis, T. S., Blanc, G. A., Hill, G. J., et al. 2013, ApJ, 775, 99

Christensen, L., Laursen, P., Richard, J., et al. 2012, MNRAS, 427, 1973

Ciardullo, R., Gronwall, C., Wolf, C., et al. 2012, ApJ, 744, 110

Cooper, J. L., Bicknell, G. V., Sutherland, R. S., & Bland-Hawthorn, J. 2008, ApJ, 674, 157

Cowie, L. L., Barger, A. J., & Hu, E. M. 2010, ApJ, 711, 928

Cox, A. N. 2000, Allen's astrophysical quantities

Davies, R., Förster Schreiber, N. M., Cresci, G., et al. 2011, ApJ, 741, 69

Diehl, S. & Statler, T. S. 2006, MNRAS, 368, 497

Dijkstra, M. 2014, PASA, 31, 40

Dijkstra, M., Haiman, Z., & Spaans, M. 2006, ApJ, 649, 14

Duval, F., Schaerer, D., Östlin, G., & Laursen, P. 2014, A&A, 562, A52

Epinat, B., Amram, P., Balkowski, C., & Marcelin, M. 2010, MNRAS, 401, 2113

Epinat, B., Amram, P., & Marcelin, M. 2008a, MNRAS, 390, 466

Epinat, B., Amram, P., Marcelin, M., et al. 2008b, MNRAS, 388, 500

Erb, D. K., Steidel, C. C., Trainor, R. F., et al. 2014, ApJ, 795, 33

Erroz-Ferrer, S., Knapen, J. H., Leaman, R., et al. 2015, MNRAS, 451, 1004

Finkelstein, S. L., Papovich, C., Dickinson, M., et al. 2013, Nature, 502, 524

Flores, H., Hammer, F., Puech, M., Amram, P., & Balkowski, C. 2006, A&A, 455, 107

Förster Schreiber, N. M., Genzel, R., Bouché, N., et al. 2009, ApJ, 706, 1364

Genzel, R., Tacconi, L. J., Eisenhauer, F., et al. 2006, Nature, 442, 786

Glazebrook, K. 2013, PASA, 30, 56

Gonçalves, T. S., Basu-Zych, A., Overzier, R., et al. 2010, ApJ, 724, 1373

Green, A. W., Glazebrook, K., McGregor, P. J., et al. 2010, Nature, 467, 684

Green, A. W., Glazebrook, K., McGregor, P. J., et al. 2014, MNRAS, 437, 1070

Green, D. A. 2011, Bulletin of the Astronomical Society of India, 39, 289

Greisen, E. W. & Calabretta, M. R. 2002, A&A, 395, 1061

Gronke, M., Bull, P., & Dijkstra, M. 2015, ApJ, 812, 123

Gronke, M. & Dijkstra, M. 2014, MNRAS, 444, 1095

Gronwall, C., Ciardullo, R., Hickey, T., et al. 2007, ApJ, 667, 79

Grove, L. F., Fynbo, J. P. U., Ledoux, C., et al. 2009, A&A, 497, 689

Guaita, L., Francke, H., Gawiser, E., et al. 2013, A&A, 551, A93

Guaita, L., Melinder, J., Hayes, M., et al. 2015, A&A, 576, A51

Hashimoto, T., Ouchi, M., Shimasaku, K., et al. 2013, ApJ, 765, 70

Hashimoto, T., Verhamme, A., Ouchi, M., et al. 2015, ApJ, 812, 157

Hayes, M. 2015, PASA, 32, 27

Hayes, M., Östlin, G., Duval, F., et al. 2014, ApJ, 782, 6

Hayes, M., Östlin, G., Mas-Hesse, J. M., & Kunth, D. 2009, AJ, 138, 911

Hayes, M., Östlin, G., Mas-Hesse, J. M., et al. 2005, A&A, 438, 71

Hayes, M., Östlin, G., Schaerer, D., et al. 2010, Nature, 464, 562

Hayes, M., Östlin, G., Schaerer, D., et al. 2013, ApJ, 765, L27

Henry, A., Scarlata, C., Martin, C. L., & Erb, D. 2015, ApJ, 809, 19

Hong, S., Dey, A., & Prescott, M. K. M. 2014, PASP, 126, 1048

Horne, K. 1986, PASP, 98, 609

Hu, E. M., Cowie, L. L., & McMahon, R. G. 1998, ApJ, 502, L99

Hunter, J. D. 2007, Computing In Science & Engineering, 9, 90

Husemann, B., Jahnke, K., Sánchez, S. F., et al. 2013, A&A, 549, A87

Husemann, B., Kamann, S., Sandin, C., et al. 2012, A&A, 545, A137

Iye, M. 2011, Proceeding of the Japan Academy, Series B, 87, 575

Jaskot, A. E. & Oey, M. S. 2014, ApJ, 791, L19

Jiménez-Vicente, J., Battaner, E., Rozas, M., Castañeda, H., & Porcel, C. 1999, A&A, 342, 417

Kennicutt, Jr., R. C. 1998, ARA&A, 36, 189

Kunth, D., Mas-Hesse, J. M., Terlevich, E., et al. 1998, A&A, 334, 11

Landman, D. A., Roussel-Dupre, R., & Tanigawa, G. 1982, ApJ, 261, 732

Laursen, P., Duval, F., & Östlin, G. 2013, ApJ, 766, 124

Laursen, P. & Sommer-Larsen, J. 2007, ApJ, 657, L69

Laursen, P., Sommer-Larsen, J., & Andersen, A. C. 2009, ApJ, 704, 1640

Law, D. R., Steidel, C. C., Erb, D. K., et al. 2009, ApJ, 697, 2057

Lenz, D. D. & Ayres, T. R. 1992, PASP, 104, 1104

Lupton, R., Blanton, M. R., Fekete, G., et al. 2004, PASP, 116, 133

Malhotra, S. & Rhoads, J. E. 2004, ApJ, 617, L5

Mallery, R. P., Mobasher, B., Capak, P., et al. 2012, ApJ, 760, 128

Marino, A., Iodice, E., Tantalo, R., et al. 2009, A&A, 508, 1235

Martin, D. C., Chang, D., Matuszewski, M., et al. 2014, ApJ, 786, 106

Mas-Hesse, J. M., Kunth, D., Tenorio-Tagle, G., et al. 2003, ApJ, 598, 858

McLinden, E. M., Finkelstein, S. L., Rhoads, J. E., et al. 2011, ApJ, 730, 136

McLinden, E. M., Rhoads, J. E., Malhotra, S., et al. 2014, MNRAS, 439, 446

Monreal-Ibero, A., Arribas, S., Colina, L., et al. 2010, A&A, 517, A28

Neufeld, D. A. 1990, ApJ, 350, 216

Newman, S. F., Genzel, R., Förster Schreiber, N. M., et al. 2013, ApJ, 767, 104

Oesch, P. A., van Dokkum, P. G., Illingworth, G. D., et al. 2015, ApJ, 804, L30

Oke, J. B. 1990, AJ, 99, 1621

Ono, Y., Ouchi, M., Mobasher, B., et al. 2012, ApJ, 744, 83

Östlin, G., Amram, P., Bergvall, N., et al. 2001, A&A, 374, 800

Östlin, G., Amram, P., Masegosa, J., Bergvall, N., & Boulesteix, J. 1999, A&AS, 137, 419

Östlin, G., Hayes, M., Duval, F., et al. 2014, ApJ, 797, 11

Östlin, G., Hayes, M., Kunth, D., et al. 2009, AJ, 138, 923

Ouchi, M., Shimasaku, K., Akiyama, M., et al. 2008, ApJS, 176, 301

Pardy, S. A., Cannon, J. M., Östlin, G., et al. 2014, ApJ, 794, 101

Partridge, R. B. & Peebles, P. J. E. 1967, ApJ, 147, 868

Petrosian, V. 1976, ApJ, 209, L1

Puech, M., Hammer, F., Flores, H., Östlin, G., & Marquart, T. 2006, A&A, 455, 119

Rauch, M., Haehnelt, M., Bunker, A., et al. 2008, ApJ, 681, 856

Rhoads, J. E., Malhotra, S., Richardson, M. L. A., et al. 2014, ApJ, 780, 20

Rivera-Thorsen, T. E., Hayes, M., Östlin, G., et al. 2015, ApJ, 805, 14

Robertson, J. G. 2013, PASA, 30, 48

Roth, M. M., Fechner, T., Wolter, D., et al. 2010, in Society of Photo-Optical Instrumentation Engineers (SPIE) Conference Series, Vol. 7742, High Energy, Optical, and Infrared Detectors for Astronomy IV, 774209

Roth, M. M., Kelz, A., Fechner, T., et al. 2005, PASP, 117, 620

Sánchez, S. F., Aceituno, J., Thiele, U., Pérez-Ramírez, D., & Alves, J. 2007a, PASP, 119, 1186

Sánchez, S. F., Cardiel, N., Verheijen, M. A. W., et al. 2007b, A&A, 465, 207

Sánchez, S. F., Kennicutt, R. C., Gil de Paz, A., et al. 2012, A&A, 538, A8

Sandberg, A., Guaita, L., Östlin, G., Hayes, M., & Kiaeerad, F. 2015, A&A, 580, A91

Sandberg, A., Östlin, G., Hayes, M., et al. 2013, A&A, 552, A95

Sandin, C., Becker, T., Roth, M. M., et al. 2010, A&A, 515, A35

Sandin, C., Weilbacher, P., Streicher, O., Walcher, C. J., & Roth, M. M. 2011, The Messenger, 144, 13

Sandin, C., Weilbacher, P., Tabataba-Vakili, F., Kamann, S., & Streicher, O. 2012, in Proceedings of SPIE, Vol. 8451, Software and Cyberinfrastructure for Astronomy II, ed. C. G. Radziwill N. M., Society of Photo-Optical Instrumentation Engineers (SPIE), 84510F

Schaerer, D., Hayes, M., Verhamme, A., & Teyssier, R. 2011, A&A, 531, A12

Schaerer, D. & Verhamme, A. 2008, A&A, 480, 369

Shapley, A. E., Steidel, C. C., Pettini, M., & Adelberger, K. L. 2003, ApJ, 588, 65

Shimasaku, K., Kashikawa, N., Doi, M., et al. 2006, PASJ, 58, 313

Shioya, Y., Taniguchi, Y., Sasaki, S. S., et al. 2009, ApJ, 696, 546

Sobral, D., Matthee, J., Darvish, B., et al. 2015, ApJ, 808, 139

Song, M., Finkelstein, S. L., Gebhardt, K., et al. 2014, ApJ, 791, 3

Taniguchi, Y., Shioya, Y., Ajiki, M., et al. 2003, Journal of Korean Astronomical Society, 36, 123

Tapken, C., Appenzeller, I., Gabasch, A., et al. 2006, A&A, 455, 145

Tapken, C., Appenzeller, I., Mehlert, D., Noll, S., & Richling, S. 2004, A&A, 416, L1

Tapken, C., Appenzeller, I., Noll, S., et al. 2007, A&A, 467, 63

Terlevich, R. & Melnick, J. 1981, MNRAS, 195, 839

Teyssier, R., Chapon, D., & Bournaud, F. 2010, ApJ, 720, L149

Turner, J. E. 2010, Canary Islands Winter School of Astrophysics, Vol. XVII, 3D Spectroscopy in Astronomy, ed. E. Mediavilla, S. Arribas, M. Roth, J. Cepa-Nogue, & F. Sanchez (Cambridge University Press), 87–125

van Dokkum, P. G. 2001, PASP, 113, 1420

Verhamme, A., Dubois, Y., Blaizot, J., et al. 2012, A&A, 546, A111

Verhamme, A., Schaerer, D., Atek, H., & Tapken, C. 2008, A&A, 491, 89

Verhamme, A., Schaerer, D., & Maselli, A. 2006, A&A, 460, 397

Wall, J. V. 1996, QJRAS, 37, 519

Wisnioski, E., Förster Schreiber, N. M., Wuyts, S., et al. 2015, ApJ, 799, 209

Wisotzki, L., Bacon, R., Blaizot, J., et al. 2016, A&A, 587, A98

Wold, I. G. B., Barger, A. J., & Cowie, L. L. 2014, ApJ, 783, 119

Yamada, T., Matsuda, Y., Kousai, K., et al. 2012, ApJ, 751, 29

Yang, H., Malhotra, S., Gronke, M., et al. 2015, ArXiv e-prints

Zheng, Z. & Wallace, J. 2014, ApJ, 794, 116

Zitrin, A., Labbé, I., Belli, S., et al. 2015, ApJ, 810, L12

Chapter 3

Where is the fuzz? Undetected Lyman α nebulae around quasars at z~2.3

Abstract: We observed a small sample of five radio-quiet quasars with integral field spectroscopy to search for possible extended emission in the Lyα line. We subtracted the quasar point sources using a simple point spread function (PSF) self-calibration technique that takes advantage of the simultaneous availability of spatial and spectral information. In four of the five objects we find no significant traces of extended Lyα emission beyond the contribution of the quasar nuclei itself, while in UM 247 there is evidence for a weak and spatially quite compact excess in the Lyα line at several kpc outside the nucleus. For all objects in our sample we estimated detection limits for extended, smoothly distributed Lyα emission by adding fake nebulosities into the datacubes and trying to recover them after PSF subtraction. Our observations are consistent with other studies showing that giant Lyα nebulae such as those found recently around some quasars are very rare. Lyα fuzz around typical radio-quiet quasars is fainter and less extended and is therefore much harder to detect. The faintness of these structures is consistent with the idea that radio-quiet quasars typically reside in dark matter haloes of modest masses.

3.1 Introduction

The circum-galactic medium (CGM), defined as gas outside of the main stellar body of galaxies but still within the virial radii of their dark-matter haloes, is of crucial importance in galaxy evolution. It may act as a reservoir for fuelling star formation in the galaxy, and it is also subject to feedback processes that expell material from the galaxy. If violent enough, this feedback may in turn heat up the CGM and thus prevent it from contributing further to the formation of stars. Observing the CGM at high redshifts will hence provide relevant insights about galaxy formation.

One observational approach to study the cold gas phase of the CGM ($T \lesssim 10^4$ K) at high redshift uses absorption signatures against background sources. This has provided important

A version of this chapter is published as an article in Astronomy & Astrophysics:
Herenz E.C., Wisotzki L., Roth M., and Anders F. 2015, A&A, Vol. 576, A115.
DOI: 10.1051/0004-6361/201425580

statistical constraints on several properties of the CGM (e.g. Adelberger et al. 2005; Hennawi et al. 2006; Steidel et al. 2010). However, the spatial distribution of the CGM in an individual galaxy cannot be captured with this method.

An alternative approach is to map the CGM in the Lyman α emission line. Several mechanisms have been identified that should lead to Lyα emission from the CGM: Cooling of infalling gravitationally heated gas (e.g. Haiman et al. 2000), cooling following superwind-driven shocks (e.g. Taniguchi & Shioya 2000), and – possibly most important for our investigation – Lyα fluorescence induced by exposure to UV radiation. While the metagalactic UV background alone is predicted to produce only a very faint glow that is probably out of reach for the current generation of optical instruments (e.g. Kollmeier et al. 2010), Lyα fluorescence caused by the much stronger UV radiation from a quasar should boost the emission into the detectable regime (Rees 1988; Haiman & Rees 2001; Cantalupo et al. 2005; Kollmeier et al. 2010). Searching for Lyα signatures of the CGM around luminous quasars is the topic of the present study.

Haiman & Rees (2001) estimated that a $z \sim 3$ quasar harbouring a $5 \times 10^{11} M_{\odot}$ halo should be surrounded by Lyα fuzz extending radially outwards to 2″–3″, at a surface brightness of $\sim 5 \times 10^{-17}$ erg s^{-1}cm^{-2}arcsec^{-2}. At least in this model, Lyα fuzz is predicted as a generic property of high-z quasars, where the surface brightness of this fuzz depends only on the mass of the halo. More recent theoretical work suggests, however, that a substantial fraction of gas is accreted within filamentary cold streams (Dekel et al. 2009; Faucher-Giguère & Kereš 2011; Rosdahl & Blaizot 2012, and references therein). If these streams are optically thick to ionizing radiation, they will develop a highly ionized skin in the presence of a quasar. This skin then acts like a mirror converting up to two thirds of the incident ionizing radiation into Lyα photons. In this scenario the expected surface brightness then depends on the ionizing photon flux produced by the quasar and the projected spatial configuration of the streams (Kollmeier et al. 2010; Hennawi & Prochaska 2013).

Revealing extended Lyα structures around quasars requires a proper subtraction of the PSF-broadened nuclear component, which will outshine – even under good seeing conditions – the expected CGM signal close to the quasar. Observationally, this makes the detection of circum-quasar Lyα fuzz much harder than searching for Lyα blobs, now routinely found in large-area narrow-band surveys (Steidel et al. 2000; Matsuda et al. 2004; Saito et al. 2006; Ouchi et al. 2009; Matsuda et al. 2011; Erb et al. 2011; Prescott et al. 2012, 2013). Many of these blobs have no obvious central source of ionizing photons (e.g. Nilsson et al. 2006), which might make them physically distinct from circum-quasar Lyα fuzz. On the other hand, some Lyα blobs may also be powered by AGN that are highly obscured along the line of sight (e.g. Basu-Zych & Scharf 2004; Geach et al. 2007; Hayes et al. 2011; Martin et al. 2014b); such blobs would be physically linked to the fuzz we want to observe (see also Baek & Ferrara 2013).

As of yet, sizeable samples of extended Lyα emission around quasars exist only for radio-loud objects (Heckman et al. 1991a,b), for which such emission seems to be a generic property at $z \sim 2$–3, with detections reported up to $z \sim 6$ (Roche et al. 2014). However, it appears likely that a large fraction of extended Lyα emission around radio loud quasars is driven by interaction with the radio jets. Evidence for this stems from an observed spatial correlation between radio and Lyα morphology (e.g. Heckman et al. 1991b; Humphrey et al. 2007) and a frequent occurrence of similar morphologies in extended C IV and He II emission (Humphrey et al. 2006; Sánchez & Humphrey 2009).

In order to search for the CGM in quasars unaffected by radio jets, one obviously has to resort to radio-quiet objects. For this class, however, mostly single object discoveries have been published so far (Bergeron et al. 1999; Bunker et al. 2003; Weidinger et al. 2004, 2005; Francis & McDonnell 2006; Willott et al. 2011; Goto et al. 2012; Rauch et al. 2013; Cantalupo et al. 2014;

Martin et al. 2014a), and only one single-object study reported a non-detection at a faint surface-brightness detection limit (Francis & Bland-Hawthorn 2004). Very few programmes aimed at observing (however small) samples (Christensen et al. 2006; Courbin et al. 2008; North et al. 2012), and these reported high detection frequencies of circum-quasar Lyα-fuzz: Christensen et al. (2006) found Lyα fuzz around 4 of 6 radio-quiet quasars, while North et al. (2012), by extending the sample of Courbin et al. (2008), found Lyα fuzz around 4 of 6 targets. So the literature suggests that Lyα fuzz is indeed a rather generic feature and not a peculiarity around high-redshift radio-quiet quasars, even if the number of systematically observed quasars appears still too low for certainty.

A major increase in sample size was recently achieved as a result of the work of Hennawi & Prochaska (2013). In a long-slit campaign on 8m-class telescopes they observed 29 close quasar-quasar pair sightlines, where Lyman-limit absorption in the background quasar spectrum indicated the presence of optically thick hydrogen clouds in the CGM of the foreground $z \sim 2$ radio-quiet quasars. The a priori known presence of such gas clouds implies that the sample would be positively biased for detecting 'mirrored' Lyα fuzz converted from the quasars ionizing photons (see above). They find a single quasar surrounded by a large scale nebula and 10 objects surrounded by small scale Lyα fuzz. Surprisingly, none of their spectra showed Lyα fuzz with the properties expected for optically thick 'Lyα mirrors'.

For a survey on circum-quasar Lyα fuzz, integral-field spectroscopy is an excellent observational method since it has continuous spatial and spectral coverage. This technique allows an optimal subtraction of the PSF-broadened nuclear emission. Moreover, since spatial and spectral information are obtained simultaneously in case of a detection, more inferences on the physical state of the CGM gas can be made. Given the previous success of a Calar-Alto 3.5m PMAS IFU campaign where 4 extended Lyα nebulae were detected around 6 radio-quiet quasars (Christensen et al. 2006) (hereafter CJW06), we initiated a new targeted PMAS IFU campaign to extend this sample.

The outline of this paper is as follows: In Sect. 3.2 we describe our PMAS observations and how we reduced the raw data. In Sect. 3.3 we explain how we remove the quasar emission from the datacubes to unveil possible extended Lyα nebulae. We detail how we estimate surface brightness upper limits in Sect. 3.3.3 and present the results of those calculations. We summarize our conclusions in Sect. 3.4.

Conversions of observed to physical quantities always assume standard ΛCDM cosmology with $\Omega_\Lambda = 0.7$, $\Omega_M = 0.3$ and $\mathrm{H}_0 = 70\,\mathrm{km\,s^{-1}Mpc^{-1}}$.

3.2 Observations & Data Reduction

3.2.1 Sample selection & observations

Our sample was selected to be at redshifts around $z \sim 2.3$ so that, in the case of a successful detection of extended Lyα fuzz, spectroscopic follow-up observations of rest-frame optical emission lines would be possible. Starting from the Véron-Cetty & Véron (2010) catalogue with this constraint, we browsed through all bright ($m_\mathrm{V} > 19$ as in Véron-Cetty & Véron (2010)) radio-quiet quasars at approximatly the above redshift. In the end we were able to observe five of these targets with the Potsdam Multi-Aperture Spectrophotometer (PMAS; Roth et al. 2005) at Calar Alto Observatory during three consecutive cloudless dark to grey-time nights in October 2011. Table 3.1 lists the redshifts and the SDSS u and g band magnitudes of our observed quasars.

We used PMAS in its 16×16 lens array (LArr) configuration, giving an $8''\times8''$ field of view (FoV), (i.e. at $0.5''\times0.5''$ spatial sampling). Motivated by the increased sensitivity and larger

Table 3.1: Observed radio-quiet quasars: Properties, exposure Times & observing conditions.

Quasar	z_{VC}	z_{SDSS}	u_{SDSS}	g_{SDSS}	t_{exp} [s]	Seeing [″]	Airmass	Conditions
Q0027+0103	2.310	2.313	19.27	18.50	7×1800	0.9-1.3	1.2-1.6	photometric / grey
Q0308+0129	2.335	–	19.21	18.45	7×1800	1.0-1.4	1.2-1.5	mainly clear / dark
Q0256−0003	2.381	2.385	20.13	19.41	8×1800+1×900	0.9-1.1	1.3-1.6	photometric / dark
Q2243+0141	2.314	–	18.48	17.98	8×1800	0.9-1.2	1.3-1.5	photometric / grey
UM 247	2.333	2.333	18.85	18.10	5×1800	0.9-1.1	1.2-1.4	photometric / dark

Redshifts from Véron-Cetty & Véron (2010) (z_{VC}); and Pâris et al. (2012) (z_{SDSS}). Photometry from Ahn et al. (2012).

spectral coverage of the upgraded PMAS detector (Roth et al. 2010), we mounted the V1200 grating to obtain the highest possible spectral resolution within the targeted wavelength range. The CCD was read out unbinned in dispersion direction. Exposure times, seeing, airmasses and observing conditions of our observations are listed in Table 3.1. To ensure the best possible spectral tracing and wavelength calibration we flanked each on-target exposure by continuum and HgNe lamp exposures. At the beginning and end of each night we observed an Oke (1990) spectrophotometric standard star (BD+24d4655 and G191B2B, respectively). We obtained skyflats during twilight and several bias frames during the night in idle time (e.g. while performing acquisitions).

3.2.2 Data reduction with p3d

To reduce the observations we employed the p3d-pipeline[1] (Sandin et al. 2010, 2012). We briefly outline in this section how we applied the different tasks of the pipeline to our data.

For every observing night a masterbias was created with the routine `p3d_cmbias`. The `p3d_ldmask` task then produced dispersion solutions for every arc-lamp frame, fitting 5th order polynomials for the mapping from pixel- to wavelength space; measured residuals for all arc lines were $\lesssim 10^{-1}$px. To determine spectrum traces and cross-dispersion profiles we applied the `p3d_ctrace` method to every continuum lamp frame. We created wavelength calibrated flatfields using `p3d_cflatf`. The `p3d_cobjex` task then performed extraction, flat-fielding, and subsequent wavelength calibration of every target and standard star exposure. As detailed by Sandin et al. (2010), the best signal-to-noise for PMAS LArr spectra is achieved by using the modified optimal extraction (MOX) algorithm (Horne 1986). Because of the large separation of LArr fibre traces on the CCD, cross-talk correction between fibres is not needed. Sandin et al. (2012) advises correcting for small spectra trace shifts between continuum-lamp and on-target exposures for achieving highest fidelity with MOX extraction, therfore we switched on median recentring in `p3d_cobjex`. Compared to extractions where we experimentally turned off this feature, we saw a clear improvement in signal-to-noise, even though the determined offset was typically less than half a pixel. Cosmic-ray hit removal was implemented within `p3d_cobjex`, utilizing the `PyCosmic` (Husemann et al. 2012) algorithm. We also chose the option to subtract a scattered light model before extraction, as advised for PMAS LArr data (Sandin et al. 2012). Next, the `p3d_sensfunc` routine was utilized to create sensitivity functions. Here we first created a 1D standard star spectra with the `p3d_sensfunc` GUI using the extracted standard star observations. Then these sensitivity functions were applied to every extracted target exposure using the `p3d_fluxcal` task. For correction of atmospheric extinction we used values from the empirical Calar Alto extinction curve model (Sánchez et al. 2007).

[1] `http://p3d.sourceforge.org`

The final data products resulting from the `p3d` pipeline are flux calibrated datacubes for all target exposures; `p3d` also produces the corresponding error cubes, containing the standard-deviation of each volume pixel (called a voxel). After trimming regions affected by vignetting on the detector (Roth et al. 2010), the cubes cover a wavelength range from 3600 – 4600 Å sampled on identical wavelength grids ($\Delta\lambda = 0.75\,\text{Å}\,\text{px}^{-1}$). Their spectral resolution, determined from fitting 1D Gaussian profiles to several lines in the spectra of the extracted arc-lamp frames, is $v_{\text{FWHM}} \approx 160\ \text{km}\,\text{s}^{-1}$ ($R \approx 1850$). We note there is a spatial and spectral dependence of R in PMAS (see also Sánchez et al. 2012, Sect. 6.2), and the value reported here is the median near the centrum of our wavelength range.

3.2.3 Sky subtraction

To remove night sky emission from the datacubes, we created for each target a median spectrum from the ring of spaxels bracketing the FoV (ignoring low-transmission fibres) and subtracted this from every spaxel. Even though the median is more robust against contamination of signal from the target than the mean, it is still possible that we subtracted a fraction of the nebular emission if this emission extended out into and beyond the FoV. However, we note that most of the known extended Lyα regions[2] around RQQs have projected maximum extents of $\lesssim 65\,\text{kpc}$, corresponding to $\lesssim 8''$ (the PMAS FoV) at the redshifts of our objects. Nevertheless, we first visually inspected all datacubes if any obvious extended emission features were present, and then checked the individual outer-ring median spectra if they contain spikes not attributable to sky lines. Both tests were negative, so we are certain at this point not having accidentally removed very bright extended nebular emission. Still, we will return to this point in our analysis in Sect. 3.3.5, showing that for special cases of large-scale extended emission our observing strategy may have been less than optimal.

3.2.4 Stacking the individual exposures for each quasar

To increase the signal-to-noise of faint emission we stacked the individual sky-subtracted and flux-calibrated datacubes. During the observations the quasar was centred in the LArr FoV using the acquisition and guiding (A&G) system of PMAS. No dithering scheme was intended, to avoid cross-correlation of neighbouring spaxels on the sky. Unfortunately the filter wheel of the A&G camera was set to V-Band, causing the quasars centroid point source to move around within our bluer wavelength range owing to differential atmospheric refraction, even though the guide star observed with the A&G system remained steady. We corrected for these unintended dither offsets by spatial integer pixel shifts before stacking. Integer pixel shifts were preferred over fractional shifts to avoid interpolation effects and thus keeping the original observational information as unaffected as possible.

In practice, we first determined the quasars centroid position in the individual exposures using images created from summing up datacube layers around $\lambda_{\text{Ly}\alpha}(z_{\text{QSO}})$. If a centroid was shifted more than a half pixel along a spatial axis, this cube was then shifted by a pixel along this axis in the opposite direction. No exposure needed to be shifted by more than one pixel in x or y direction. Because of the varying sky background (and different exposure times in the case of Q0256−0003) we employed a variance-weighted mean for stacking, using the error cubes generated by the pipeline.

[2]Using the compilation in Fig. 3 of Cantalupo et al. (2014) and 10 additional detections reported by Hennawi & Prochaska (2013).

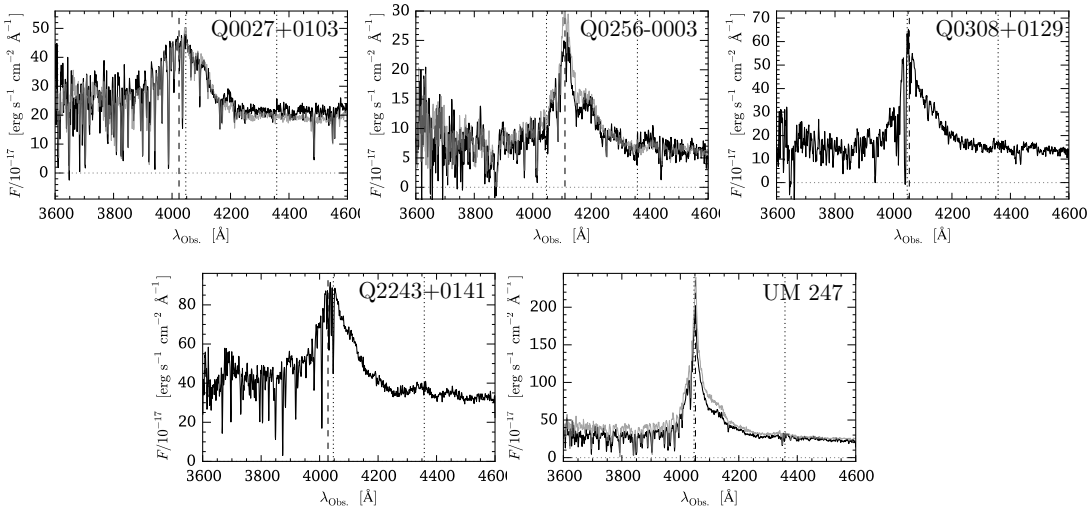

Figure 3.1: Extracted spectra from the PMAS datacubes in a 3″diameter aperture. For those objects where available (Q0027+0103, Q0256−0003 & UM 247) SDSS DR9 spectra have been over-plotted in grey to illustrate the quality of our flux calibration. The vertical dashed line shows the wavelength of Lyα at the quasars redshift and the vertical dotted lines indicate the wavelengths of the artificial telluric Hg I (4047 Å & 4358 Å) emission-lines.

Having reduced the raw data as described, we were now left with five datacubes containing voxels $F_{x,y,z}$, where (x, y) are the spatial indices, and z is the index for the spectral layers, in units of 10^{-17} erg s^{-1}cm^{-2}Å.

3.3 Analysis and results

3.3.1 Quasar spectra

We show spectra of our five quasars in Fig. 3.1. These spectra were extracted in a 3″ diameter aperture centred on the highest S/N spectral pixel (spaxel). Where available, we overlay SDSS DR9 (Ahn et al. 2012) spectra. Our spectra differ to SDSS by $\lesssim 10$ % for Q0027+0103 and Q0308+0129; for UM 247 there is a systematically offset by $\lesssim 20$ % in the blue. Quasar variability, spectrophotometric uncertainties in the SDSS or imperfections in our flux calibration could be reasons for these differences. We note that for Q0308+0129 the observing conditions were not photometric, thus our fluxes of this object are likely somewhat too low.

The night sky emission line spectrum in Calar Alto shows significant man-made contributions, arising from tropospheric scattering of high-pressure street lamps in nearby populated areas. In our wavelength range the Hg I 4047 Å and 4358 Å emission lines are prominent. Wavelengths of these lines and the expected Lyα wavelength $\lambda^{\rm Obs.}_{{\rm Ly}\alpha} = (1 + z_{\rm QSO}) \cdot \lambda_{{\rm Ly}\alpha}$ are indicated in Fig. 3.1. As can be seen, the λ4047 line is located unfavourably close near the expected peak of the Lyα emission for 4 of our quasars. We had not anticipated the strength of this anthropic line in the planning of our observations. This unresolved line has an average surface brightness of $F^{\rm Hg\,I}_{4047} = 3.5 \times 10^{-16}$ erg s^{-1}cm^{-2}arcsec^{-2} (Sánchez et al. 2007) and thus, by amplifying the background noise in a narrow-band window around $\lambda^{\rm Obs.}_{{\rm Ly}\alpha}$, contributes negatively to our efforts in uncovering extended Lyα emission. The sensitivity in this narrow-band is further decreased

by residuals from sky subtraction, resulting from the varying spectral resolution across the FoV (Sect. 3.2.2).

3.3.2 Subtraction of quasar emission from the datacubes

Because of the PSF broadening, spectra at radial distances $\lesssim 2''$ from the quasar centre are visibly contaminated by the nuclear spectrum. Thus, in order to reveal possible extended Lyα emission around the quasar, we had to remove this contamination. CJW06 experimented with three algorithms to achieve this *deblending* in PMAS LArr datacubes:

- *On- minus scaled off-band method*: An on- and off-band image is created from the datacube. The latter is then scaled and subtracted from the former, thereby revealing possible contribution of extended emission in the on-band. Here the *on-band* is obtained as a summation in wavelength direction over all datacube layers expected to contain the extended-emission signal, while the *off-band* is a sum over nearby layers not being affected by extended emission. Asserting that the extended emission contributes only a few percentage points to the on-bands peak intensity (i.e. quasar+extended emission), the ratio between the peak intensities in on- and off-band is a sufficient scale factor for the subtraction.

- *Analytical PSF Extraction*: An analytical PSF model is fitted and subtracted from every datacube layer, thereby creating a datacube which should only contain non-nuclear emission. Then an iterative scheme is employed, where in a second iteration positional and shape parameters of the PSF function are fixed, using values from the first iteration with the constraint of allowing them to vary only smoothly with wavelength (see e.g. Wisotzki et al. 2003; Kamann et al. 2013, for more elaborate versions of this technique involving multiple point-sources within the FOV). According to CJW06 the analytical PSF extraction produces unsatisfying results in PMAS in terms of quasar residuals, so we did not consider applying this method to our data.

- *Empirical PSF Subtraction*: By summation over datacube layers expected to be unaffected by extended emission, an empirical PSF image is created. It is then scaled and subtracted from every layer, thus creating a residual datacube containing extended emission. To find the scaling the PSF image with respect to the datacube layers, a spectrum is aperture-extracted from the datacube, with every spaxel in the aperture having weights assigned via the PSF image. An iterative scheme is employed to remove contamination in the scaling spectrum from extended emission possibly covering parts of the aperture: the datacube resulting from the deblending is subtracted from the undeblended datacube from which in turn the next scaling spectrum is extracted. A variant of this method was developed by Husemann et al. (2013), where in subsequent iterations the correction is achieved using an annulus-extracted spectrum from the deblended datacube.

We emphasize the methodological similarity between the *on- minus scaled off-band method* and the *empirical PSF subtraction* deblending: If the PSF image in the latter is created from the same layers as the off-band in the former, every layer in the deblended datacube can be thought of as an 'on-band' having a scaled 'off-band' subtracted. If, moreover, no iterative corrections are applied, the image resulting from the *on- minus scaled off-band method* is identical to the image resulting from summation over the on-band defining layers in the empirical PSF subtracted datacube. We note that the iterative correction only increases the fidelity of an extended

emission signal when it is measurably present after the first deblending iteration; otherwise only noise is shuffled around in subsequent iterations.

Because of this similarity we applied solely the *empirical PSF subtraction* method to our datacubes. As PSF image we take ∼ 40 layers (∼ 30 Å) beginning ∼10 Å redwards of $\lambda_{\mathrm{Ly}\alpha}(z_{\mathrm{QSO}})$. We found this choice to produce the best results in terms of subtraction residuals for the following reasons: Firstly, for the red side of $\lambda_{\mathrm{Ly}\alpha}(z_{\mathrm{QSO}})$, a redward band gives a better signal-to-noise ratio for the PSF image because of $z_{\mathrm{abs}} \approx z_{\mathrm{em}}$ Lyα absorbers appearing bluewards of $\lambda_{\mathrm{Ly}\alpha}(z_{\mathrm{QSO}})$ (see Fig. 3.1). Secondly, as we did not correct for differential atmospheric refraction, the position and shape of the PSF changes with λ, thus selecting layers further away would produce a non-optimal representation of the PSF at the expected position of Lyα fuzz, resulting in stronger residuals from the subtraction. This is also the reason why we chose the spectral window to be relatively narrow.

We experimented with different extraction apertures for the scaling spectrum. Visual inspection revealed no extended emission after the first iteration in all objects. As expected (see above), performing more iterations does not improve upon this. We thus decided to use the smallest possible aperture for scaling, i.e. the single spaxel with the highest S/N. Despite this, we could not find any evidence for extended Lyα fuzz around any of our targets, except a small-scale feature to the north of UM 247.

To visualize our findings, we show in Fig. 3.2 narrow-band images centred on $\lambda_{\mathrm{Ly}\alpha}(z_{\mathrm{QSO}})$ created by summing over 20 layers (15Å) of the residual datacubes. Instead of using physical units, the scale on the colour bar uses multiples of the standard-deviation per pixel. This colour bar scaling simplifies the judgment whether features seen in this image are actually significant, and it also makes the comparison between the panels straightforward. Except for UM 247, none of these images shows any significant feature.

In Fig. 3.3 we show spectra from the residual datacubes extracted within a small circular aperture consisting of 20 spaxels (aperture with outer radius $r_C = 1.25''$, cf. Sect. 3.3.3) centred around the scaling spectrum. Again, only UM 247 displays a distinct spectral line that seems inconsistent with noise. We discuss this feature further in Sect. 3.4.2.

3.3.3 Estimation of detection limits

From our visual inspection of the residual datacubes (see also Figs. 3.2 & 3.3) we conclude that in 4 out of 5 objects we have no significant detections. We now want to constrain an upper limit in surface brightness for extended Lyα nebulae around those quasars. To do so, we define confidence limits for rejecting the null hypothesis, which states that there is no extended Lyα emission present in the data. The upper limit is then given as the minimum surface brightness for which we would not be able to confidently reject the null hypothesis anymore.

We adopted circular apertures centered on the scaling spectrum. In absence of morphological information for the non-detections, this simplification appears reasonable, although it is known that quasar CGM Lyα nebulae can be asymmetric (e.g. Weidinger et al. 2004; Rauch et al. 2013). For such nebulae the average surface brightness within a circular aperture will generally be lower than a surface brightness obtained within an isophote.

We explored successively larger apertures around the central scaling spectrum by adding annuli with a width of one pixel. This defined eight circular apertures C_k ($k = 1 \ldots 8$) with outer radii of $r_c = (2k + 1)/4''$. The numbers of spaxels N_C in those apertures are then N_{C_k} = (8, 20, 36, 68, 96, 136, 176).

The assessment was performed on the residual datacube $F'_{x,y,z}$ after PSF subtraction. The

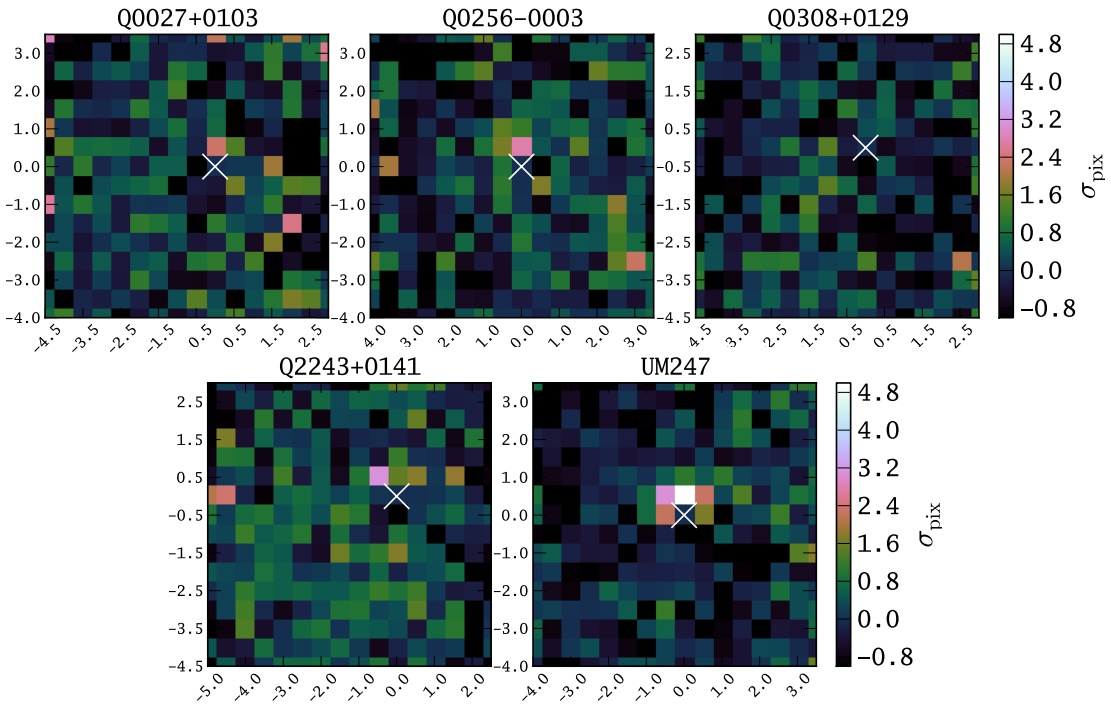

Figure 3.2: Narrow-band images (15Å wide, centred on $\lambda_{\mathrm{Ly}\alpha}(z_{\mathrm{QSO}})$) for our 5 quasars. These images were created from the quasar-subtracted datacubes using the empirical PSF subtraction method. The position of the spaxel used for scaling the PSF image is indicated by a cross; this position corresponds to the centroid of the quasar nucleus. Colours indicate multiples of the standard-deviation per pixel σ_{pix}, calculated for each image. The values of σ_{pix} are (2.3, 1.4, 2.7, 2.6, 3.5)$\times 10^{-17}$erg s^{-1} cm^{-2}, from top left to bottom right. North is up, and east is to the left. Axes ticks are $\Delta\delta$ and $\Delta\alpha$ in arcseconds with respect to the quasar centroid.

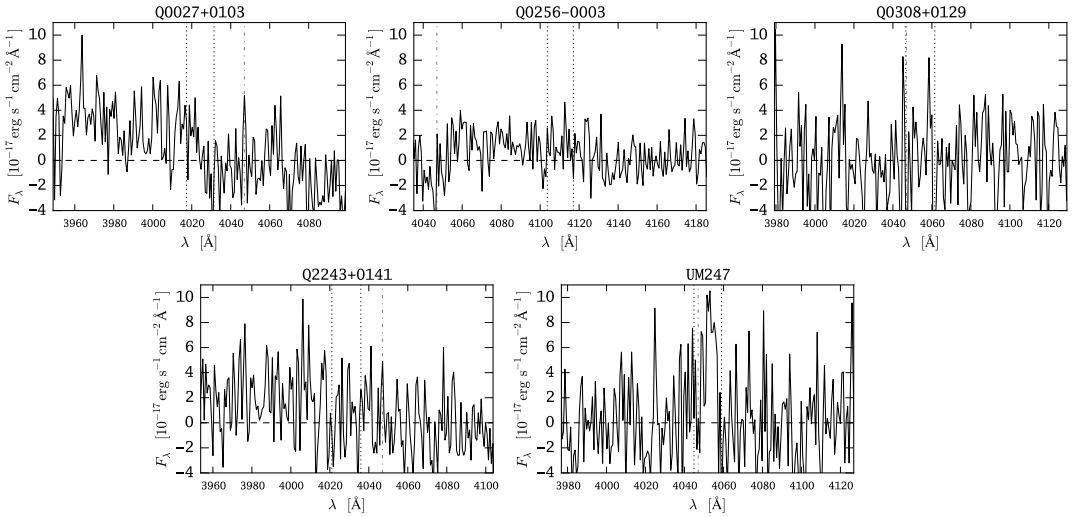

Figure 3.3: Residual spectra for our 5 quasars from the quasar-subtracted datacubes, extracted within the $r_c = 1.25''$ aperture (cf. Sect. 3.3.3) around the scaling spectrum. The *vertical dotted lines* indicate the boundaries of the narrow-band image (15 Å = 20 layers), shown in Fig. 3.2. The *vertical dashed-dotted lines* show the position of the Hg I-sky line (Sect. 3.3.1).

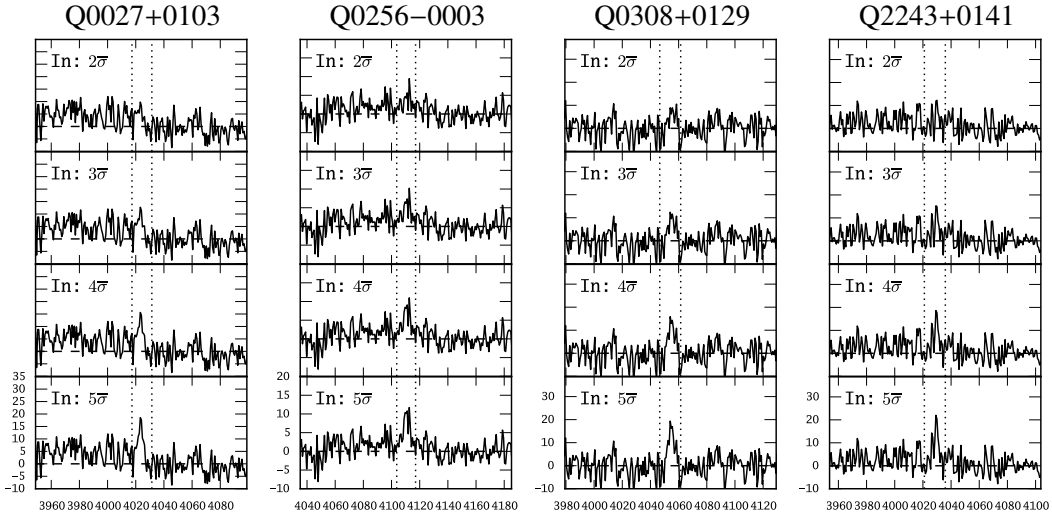

Figure 3.4: Examples of recovered spectra after adding artificial nebulae into the datacube prior to the empirical PSF subtraction. The surface brightness of the artificial nebulae was scaled with integer values of $n_{\rm spatial}$ according to Eq. (3.4). After empirical PSF subtraction the spectrum was extracted from the residual datacube using the $r_C = 1.25''$ aperture (i.e. the same as in Fig. 3.3). The spectra are shown in units of 10^{-17}erg s^{-1}cm^{-2}Å^{-1}. We note that artificial nebulae with $n_{\rm spat} \geq 5$ can be unambiguously discriminated from the background for all objects.

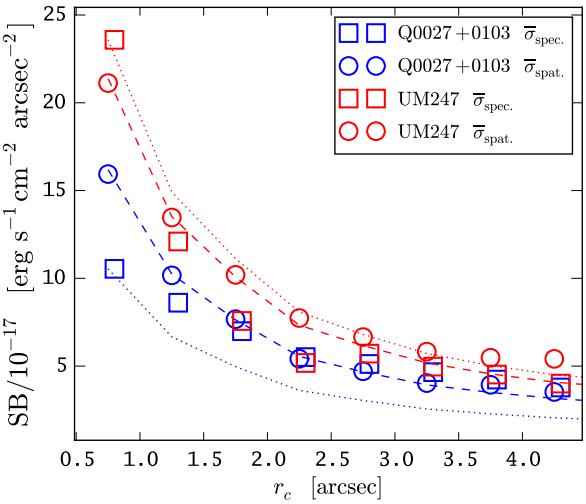

Figure 3.5: Comparison of formal 5σ surface brightness detection limits as a function of aperture radius using the different noise estimators $\overline{\sigma}_{\rm spat}$ and $\overline{\sigma}_{\rm spec}$, exemplarily shown for two objects (Q0027+0103 - *blue* symbols, UM 247 - *red* symbols panel). The agreement between $\overline{\sigma}_{\rm spat}$ and $\overline{\sigma}_{\rm spec}$ is similarly good for the other objects.

residual signal S_k within the relevant spectral layers and inside each circular aperture C_k can be written as

$$S_k = \sum_{(x,y)\in C_k} I_{x,y} \ , \tag{3.1}$$

where $I_{x,y} = \sum_{z\in \rm NB} F'_{x,y,z}$ is the value of a pixel in the narrow-band images shown in Fig. 3.2. For the sake of brevity, we do not explicitly state units and conversions in our equations.

Assuming for the moment that we had reliable variance estimates $\sigma^2_{x,y}$ for every pixel of the pseudo narrow-band image $I_{x,y}$ (or equivalently $\sigma^2_{x,y,z}$ for every voxel of the residual datacube), the noise in C_k could be written as

$$\sigma_k = \frac{1}{N_{C_K}} \sqrt{\sum_{(x,y)\in C_k} \sigma^2_{x,y}} \ . \tag{3.2}$$

Combining now Eqs. (3.1) and (3.2), we could express the signal S_k within C_k in amounts of the noise σ_k being present in C_K, i.e.

$$S_K = n \cdot \sigma_k \ , \tag{3.3}$$

where, under assumption of pure Gaussian noise, n would directly translate into a probability of the null hypothesis – no nebular emission detected – being false (e.g. Wall 1979).

However, neither of the above made assumptions – having reliable variance estimates for every voxel and pure Gaussian noise – are met by our data: The quasar subtraction introduces non-Gaussian residuals, as does the background subtraction (Sect. 3.2.3), which are not captured by the formal variances. There may also be further unknown systematics. We therefore replaced the formal variances by two empirical proxies for $\sigma_{x,y}$:

- $\overline{\sigma}^{\rm spat}_k$: The standard deviation (relative to an expectation value of zero) per pixel of the narrow-band image $I_{x,y}$ outside of the circular aperture C_k.

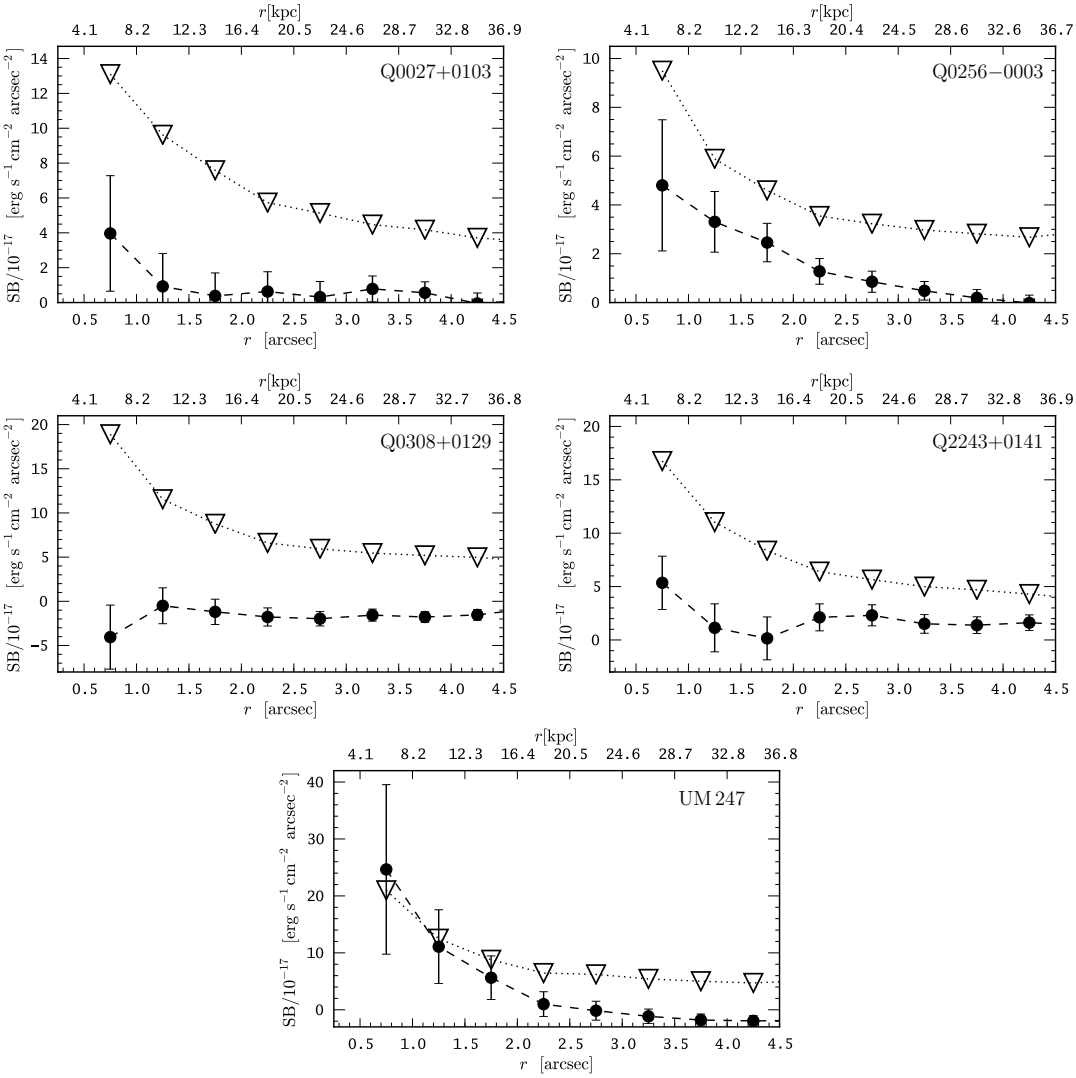

Figure 3.6: Surface brightness upper limits (triangles) for circularly symmetric extended Lyα emission around our 5 quasars as a function of radial angular (bottom abscissa) or physical extent (top abscissa). The integrated observed signal within each apertures is shown by the black points, where the error bars indicates the standard deviation within the aperture, as a measure of the irregularity of the flux distribution within the aperture.

- $\overline{\sigma}_k^{\rm spec}$: The standard deviation (relative to an expectation value of zero) per spaxel within the circular aperture C_k, calculated from spectral layers not contributing to the narrow-band images. The calculation is limited to wavelengths not further than 75Å away from $\lambda(z_{\rm QSO})$, since here the empirical PSF subtraction starts to produce strong residuals because of differential atmospheric refraction.

We note that both noise estimators depend on the aperture C_k.

With these proxies we then set $\sigma_{x,y} \approx \overline{\sigma}_k^{\rm spat}$ or $\sigma_{x,y} \approx \overline{\sigma}_k^{\rm spec}$ for all x, y in Eq. (3.2) and obtain

$$S_k = n_{\rm spat} \cdot (\overline{\sigma}_k^{\rm spat} / \sqrt{N_{C_k}}) \,, \tag{3.4}$$

$$S_k = n_{\rm spec} \cdot (\overline{\sigma}_k^{\rm spec} / \sqrt{N_{C_k}}) \,. \tag{3.5}$$

We show below that $n_{\rm spec} \approx n_{\rm spat}$ (or equivalently $\overline{\sigma}_k^{\rm spec} \approx \overline{\sigma}_k^{\rm spat}$) holds.

The question is, which $n_{\rm spec}$ or $n_{\rm spat}$ is required, in each quasar, for a detection? We addressed this problem by adding simulated extended emission into our datacubes before subtracting the quasar. Specifically we used circular nebulae of an extent that would fill a particular aperture C_k. These simulated nebulae had a flat surface brightness profile and a Gaussian line profile with 300 km s^{-1} FWHM (approximately twice the spectral resolution) centred around $\lambda_{{\rm Ly}\alpha}(z_{\rm QSO})$. We emulated seeing effects by convolving those nebulae with 2D Gaussians of the average seeing FWHM of the particular observation. Using the above defined noise proxies we scaled the surface brightness of the nebulae by integer multiples $n_{\rm spat}$ according to Eq. (3.4). We downsampled our simulated nebulae to the grid of our datacubes and added them before the final step of empirical PSF subtraction. By visual inspection of the residual cubes we found that nebulae with $n_{\rm spat} = 5$ can be unambiguously discriminated from the background. Exemplarily we show in Fig. 3.4 the results of this numerical experiment for nebulae covering the $r_C = 1.25''$ aperture. Results for other aperture sizes were similar, i.e. a $5\overline{\sigma}^{\rm spat}$ input according to Eq. (3.4) yielded an unambiguous visual detection after PSF subtraction.

We now demonstrate that both noise proxies yield similar results for our surface brightness limits, defined as the minimum surface brightness that a circular nebulae with a particular radius could have before it would fall below our detection criterion. For this purpose we show in Fig. 3.5 the surface brightness limits exemplarily for two objects, as a function of aperture radius. These limits were calculated using either Eq. (3.4) or Eq. (3.5) with $n_{\rm spat} = 5$ or $n_{\rm spec} = 5$. Figure 3.5 shows the trend expected for a noise estimate independent of aperture, obtained by scaling the curve for the smallest aperture ($r_C = 0.75''$) by aperture area $\propto N_{C_k}^{-1/2}$. We note that indeed $\overline{\sigma}^{\rm spec}$ and $\overline{\sigma}^{\rm spat}$ have similar values, and that there is only a mild dependence on aperture size. For the cases not shown, the agreement is similar. Since also no a priori distinction can be made as to which of the two proxies is better, we quote the average $(\overline{\sigma}^{\rm spec} + \overline{\sigma}^{\rm spat})/2$ as our detection limits in surface brightness.

3.3.4 Surface brightness limits on extended emission

The resulting surface brightness upper limits for extended Lyα emission surrounding the observed quasars, calculated by applying the method presented in the previous section, are shown in Fig. 3.6. For reference, the obtained upper limits for Lyα fuzz with 2.5″ (20.5 kpc) radial extend – the typical extent of circum-quasar Lyα fuzz predicted by Haiman & Rees (2001) – are (5.4, 3.4, 6.5, 6.0, 6.3) $\times$ 10^{-17} erg s^{-1} cm^{-2} arcsec^{-2} for the quasars Q0027+0103, Q0256−0003, Q0308+0129, Q2243+0141, and UM 247, respectively.

In Fig. 3.6 we also show the integrated signal with a circular aperture, i.e. Eq. (3.1) transformed to surface brightness units. Here the error bar on the integrated signal indicates the

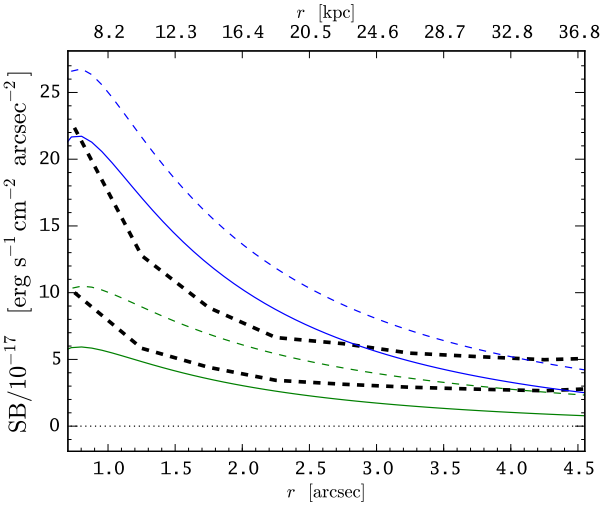

Figure 3.7: Expected average surface brightness profiles for exponential nebulae $SB_{Ly\alpha}(r) = \Sigma_0 \times \exp(-r/r_0)$, measured within circular apertures and compared to the our surface brightness upper limits (*dashed lines*, indicating the range of our limits shown in Fig. 3.6). Coloured *solid lines* show the expectations including the effect of our sky subtraction procedure, while the *dashed* lines ignore it (*blue*: $\Sigma_0 \approx 10^{-16}$erg s^{-1} cm^{-2}arcsec^{-2} and $r_0 = 2''$; *green*: $\Sigma_0 = 5 \times 10^{-17}$erg s^{-1} cm^{-2}arcsec^{-2} and $r_0 = 4''$).

standard deviation within the aperture. In our case, this is a measure for how asymmetric possible signal is distributed within the aperture; e.g. for UM 247, a bright spot appears only to the north of the object, thus the error bar on the integrated signal within the circular aperture is large. We note that for all objects except UM 247 the integrated signal is always below our detection limits, thus confirming the visual impression gained from Figs. 3.2 and 3.3. We discuss the fuzz around UM 247 further in Sect. 3.4.2.

Background offsets, positive or negative, can be seen in the integrated signal for Q0308+0129 or Q2243+0141; however, we note that we incorporated these systematics in the calculation of our detection significances by forcing the expectation value to zero for our noise proxies (see above). There also appears a hint of possible extended emission in Q0256−0003, which is however below our detection threshold and not confidently separable from noise in the residual

3.3.5 Effect of sky subtraction on large-scale Lyα fuzz.

Recently, two nebulae were discovered that have sizes significantly larger than our field of view (Cantalupo et al. 2014; Martin et al. 2014a, see Table 3.2). As explained in Sect. 3.2.3, we subtracted a median spectrum generated from the outer spaxels framing our field of view to remove emission by the night sky. Would giant nebulae as the above mentioned still leave a detectable signal in our observations?

From the intensity map presented in Cantalupo et al. (2014) we see that at a distance of $r \approx 5''$ to the quasar UM 287, their nebula has a mean surface brightness of $\approx 5 \times 10^{-17}$ erg s^{-1} cm^{-2} arcsec^{-2}. At a similar distance to their central quasar, Martin et al. (2014a) measured a surface brightness of $\approx 9 \times 10^{-18}$ erg s^{-1} cm^{-2} arcsec^{-2}. If the surface brightness profile increases towards the centre, the central parts might still leave a significant detectable signal in our datacubes. If, however, the central surface brightness profile is rather flat, the significance of the recoverable signal will be substantially reduced. Unfortunately, currently no information

on the central parts of the surface brightness profile in UM 287 is available (Cantalupo, priv. comm.).

We investigated the recoverability of the nebula in UM 287 assuming two different exponential surface brightness profiles, $SB_{Ly\alpha}(r) = \Sigma_0 \times \exp(-r/r_0)$ with $r_0 = 2''$ and $r_0 = 4''$, which are fixed to UM 287's surface brightness of 10^{-17}erg s^{-1} cm^{-2}arcsec^{-2} at $r = 5''$. The central surface brightness of the $r_0 = 2''$ profile is then $\Sigma_0 \approx 10^{-16}$erg s^{-1} cm^{-2}arcsec^{-2} and for the $r_0 = 4''$ profile $\Sigma_0 = 5 \times 10^{-17}$erg s^{-1} cm^{-2}arcsec^{-2}. Our sky subtraction procedure would subtract a constant surface brightness of $SB(4'') \approx 1.5 \times 10^{-17}$ from both profiles. We note that such a faint signal would not have been seen in the visual inspection of the subtracted sky spectra.

Applying our detection criterion in Fig. 3.7, the $r_0 = 2''$ profile would still permit a significant detection of the nebula. However, for the flatter $r_0 = 4''$ profile the recovered signal would fall below the detection threshold. And obviously we would always underestimate the true extent of the nebula. We emphasize that our observations were originally not designed with such large scale nebulae in mind and their recent discovery came as a surprise.

3.4 Discussion

3.4.1 Comparison with observations from the literature

How do our upper limits in surface brightness for extended Lyα emission around radio-quiet quasars compare with previous investigations of this phenomenon? Most of the studies reporting a successful attempt in detecting circum-quasar Lyα fuzz (sometimes serendipitous discoveries) have focused on single objects. We compiled a list of such investigations in Table 3.2. Beyond these single-object results, very few studies aimed at constructing actual samples (which were always small). We list the relevant publications in Table 3.3.

Substantial methodological differences between the studies listed in Tables 3.2 and 3.3 have to be kept in mind when comparing those results with our non-detections. The sizes in Table 3.2 often refer to the maximum extent at which the authors were able to detect Lyα emission. This quantity obviously depend on the depth of the observations and, in the case of long-slit spectroscopy, the orientation of the slit. For the latter case, fluxes are also affected by significant slit-losses, since only a fraction of the nebula is usually captured. Finally, line emission from the central quasar might contaminate the fluxes of the nebular component in some cases, especially since a subtraction of the quasar point source was not performed in some cases (e.g. Bergeron et al. 1999; Martin et al. 2014a; Rauch et al. 2013).

The quoted values for the surface brightness limits of the samples in Table 3.3 are also very rough estimates, as the actual limits depends on the assumed size of the fuzz (see our derivation in Sect. 3.3.3 and also the derivation in Sect. 4.3 of Hennawi & Prochaska 2013) and, moreover, they differ from target to target because of differences in the used instruments and observing strategies. Unfortunately, CJW06 did not quantify the depth of their observations. Since they also used PMAS (although in a different setup than we) and knowing the typical instrumental and atmospheric parameters, we estimated that their detection sensitivity was similar to that in our study.

We next considered whether the Lyα fuzz detected by the studies listed in Tables 3.2 and 3.3 would have been recovered if 'implanted' into our quasars. For this exercise we selected only objects for which the reported maximum extent (after de-redshifting) would be covered by our field of view. The Martin et al. (2014a), Cantalupo et al. (2014) and Bergeron et al. (1999) objects do not fulfill this criterion (see also Sect. 3.3.5). We also excluded the Rauch et al. (2013) object, since their flux value is contaminated by quasar Lyα emission. We then circularized

Table 3.2: Compilation of observational results from the literature on extended Lyα emission around radio-quiet quasars (single-object investigations).

Reference	Quasar	Redshift	Extent	Flux	Method
Bergeron et al. (1999)	Q 2233-606	2.238	9.2″×12.1″	3.2×10^{-15}	narrow-band imaging
Bunker et al. (2003)	PC 0953+4749	4.46	≈5″	3.6×10^{-17}	long-slit spectrum
Weidinger et al. (2005)	Q 1205-30	3.041	≈10″	7×10^{-16}	narrow-band & long-slit
Francis & McDonnell (2006)	PSS 2155+1358	4.28	≲0.7″	1.7×10^{-17}	integral field spectroscopy
Goto et al. (2012)	CFHQS J2329-0301	6.417	∼1.3 -1.5″	8×10^{-17}	long-slit spectrum
Rauch et al. (2013)	Q J0332-2751	3.045	2.2″	5.4×10^{-17}	long-slit spectrum
Cantalupo et al. (2014)	UM 287	2.28	≈55″	5.5×10^{-15}	narrow-band imaging
Martin et al. (2014a)	HS 1449+19	2.843	≳30″	2.0×10^{-13}	integral-field spectroscopy

Flux is given in erg s^{-1}cm^{-2}.
Measurements on the fuzz around CFHQS J2329-0301 have also been published by Willott et al. (2011), who obtained similar results. No flux has been reported by Bunker et al. (2003) for the flux of the extended Lyα emission surrounding PC 0953+4749, but this object is also part of the CJW06 sample. The flux for the nebula around HS 1449+19 is from Table 3 in Martin et al. (2014a). See text for possible caveats considering the comparability of the presented values on flux and extent.

Table 3.3: Compilation of observational results from the literature on extended Lyα emission around radio-quiet quasars (samples).

Reference	Radio-Quiet Quasars		Redshift	SB limit	Instrument - Method
	Targeted	Fuzz detected			
CJW06 [(a)]	6	4	$2.7 \lesssim z \lesssim 4.5$	$\sim 10^{-17}$	PMAS – integral-field spectroscopy
North et al. (2012) [(b)]	6	4	$z \sim 4.5$	$\sim 5\times10^{-19}$	FORS2 - slit spectroscopy
Hennawi & Prochaska (2013)	29	11	$z \sim 2$	$\sim 5\times10^{-18}$	LRIS & GMOS - slit spectroscopy
This study	5	1	$z \sim 2.3$	$\sim 5.5\times10^{-17}$	PMAS – integral-field spectroscopy

(a) Surface brightness limit for CJW06 estimated by us.
(b) North et al. (2012) is an extension of Courbin et al. (2008). Surface brightness limit in erg s^{-1}cm^{-2}arcsec^{-2}.

the nebulae, i.e. we assumed the flux to be distributed symmetrically around the quasar with a radius defined as half the maximum extent. After calculating de-redshifted radii and surface brightness levels, we determined the integrated signals within circular apertures covering the whole nebulae. We note that only Weidinger et al. (2005) provided a surface brightness profile, so that only for this object we could calculate the integrated signal at various radii.

In Fig. 3.8 we plot the results from this exercise and compare them to our surface brightness limits: Out of 11 nebula used in this calculation, 3 would be detected in all our observations, further 4 would yield a 5σ detection only in our deepest dataset, and 4 would not be recoverable at all. We note, however, that the circularization is actually reducing the signal from sources that have significantly asymmetric flux distributions. Thus a nebula yielding a 5σ detection only in our deepest dataset might have been recovered at a higher significance if the area over which the signal was integrated was better matched to the light distrubution of the nebula.

We note that half of the points in Fig 3.8 are at radii less than 10 kpc and 8 out of 10 are below 25 kpc. Small scale Lyα fuzz appears to be quiet frequent around radio-quiet quasars. This is also supported by the high recovery rate of this phenomenon in Hennawi & Prochaska (2013), although their detections are generally fainter. We argue in the next section that the signal we find around UM 247 also falls into this category.

Finally, we point out that most of the reported detections of bright Lyα fuzz are typically at $z \gtrsim 3$. Our recovery rate of this phenomenon at $z \approx 2.3$ (20%) is lower compared to CJW06 (66%). Moreover, Hennawi & Prochaska (2013) report a recovery rate of 38% at $z \sim 2$. Observations are insufficient at this stage to infer a redshift evolution of circum-quasar Lyα fuzz properties. It is nevertheless intriguing that Zirm et al. (2009) find that Lyα nebulae enshrouding radio-loud quasars decline in size and luminosity with decreasing redshift. If real, such a decline could indicate a depletion of the cool gas content of the CGM (at least on average). Extending such a trend to radio-quiet quasars would however require much larger and more homogenous samples over a range of redshifts.

3.4.2 Small-scale Lyα fuzz near UM 247

UM 247 is the only object in our sample with a formally significant residual at Lyα after PSF subtraction. To assess whether this residual is real and not an artefact caused by a fault (e.g. an undetected cosmic) in a single exposure, we repeated the stacking of the individual exposures (Sect. 3.2.4) 5 times, each time with one exposure excluded from the stack. We then performed the empirical PSF subtraction in exactly the same manner as described above (Sect. 3.3.2) for each of those stacks. The feature remained, hence we assert that it is genuine.

This basically unresolved excess emission is located at a distance of $d \lesssim$4-8 kpc (0.5-1″) north of UM 247. The line has a flux of $\sim 5.6 \times 10^{-16}$ erg s^{-1}cm^{-2}, corresponding to a Lyα luminosity of $L_{\mathrm{Ly}\alpha} \approx 2.4 \times 10^{43}$ erg s^{-1}.

If the Lyα emission of this feature was powered purely by star formation, ignoring ionization of the nearby quasar as well as radiative transfer effects, this would correspond to a star formation rate of $\sim$ 10–20 M$_\odot$ yr^{-1} (with the exact value being dependent on the metallicity of the underlying stellar population, see Schaerer 2003). This Lyα luminosity is the bright end of the Lyα emitter luminosity function for $z \sim 2.3$ (Blanc et al. 2011). Given the small field of view of our observations, the detection of such a bright Lyα emitter in close vicinity to a quasar would appear rather coincidental.

In an opposing scenario we consider the possibility that the Lyα radiation is produced purely by fluorescence of a compact nearby cloud, devoid of internal star formation and optically thick to ionizing radiation from the quasar. This cloud will behave as a special mirror, converting

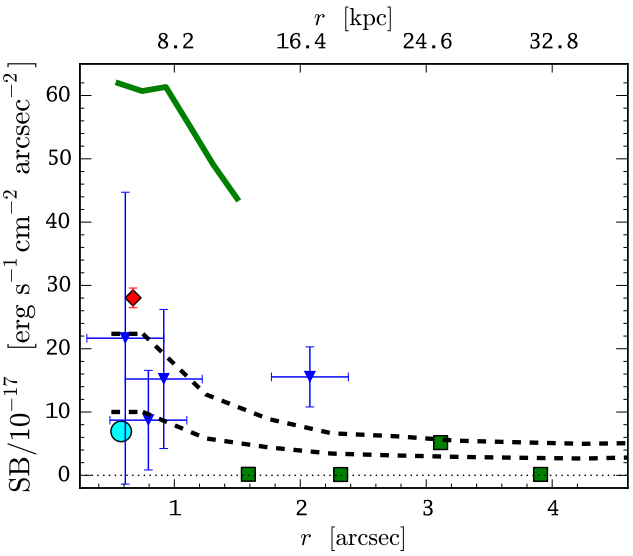

Figure 3.8: Comparison of our surface brightness upper limits as a function of radius (thick dashed lines) to the reported literature detections of circum-quasar Lyα emission, de-redshifted to $z = 2.3$, and assuming that the reported maximum extent defines the radius of the detection aperture. The symbols feature results from the CJW06 sample (*blue triangles* with error bars), from the North et al. (2012) sample (*green squares*), the nebula from Goto et al. (2012) (*red diamond*) and the fuzz from Francis & McDonnell (2006) (*cyan circle*). We also show the integrated signal at various radii from the de-redshifted Weidinger et al. (2005) surface brightness profile (*solid green line*).

~66% of all impinging hydrogen-ionizing photons into Lyα. Thus, given the quasar ionizing luminosity and the size of the cloud one can predict its Lyα luminosity (e.g. Francis & Bland-Hawthorn 2004; Adelberger et al. 2006; Kollmeier et al. 2010; Hennawi & Prochaska 2013). Since the cloud is unresolved, we adopt as an upper limit of its size the extent of one PMAS spaxel. Thus the physical surface extent of the Lyα emitting cloud is $R^2_{\rm cloud} \lesssim 16$ kpc^2. From a measured quasar flux density of $f_\lambda = 2.5 \times 10^{-16}\,{\rm erg\,s^{-1}cm^{-2}\AA^{-1}}$ for UM 247 at 4500Å, we estimate a quasar luminosity at the Lyman edge of $L_{\nu_{\rm LL}} = 8.0 \times 10^{29}\,{\rm erg\,s^{-1}Hz^{-1}}$, assuming a power-law index of $\alpha_1 = 0.44$ ($f_\nu \propto \nu^{-\alpha}$) for the quasar continuum redwards of the Lyman edge (Vanden Berk et al. 2001), and $\alpha_2 = 1.57$ bluewards of 912Å (Telfer et al. 2002). We also corrected for galactic extinction ($A_\lambda = 0.08$ at 4500Å for UM 247), although that is a small effect. Assuming isotropic radiation, this results in an ionizing photon number flux of $\Phi = 4 \times 10^{10}$ s^{-1} cm^{-2} (1×10^{10} s^{-1} cm^{-2}) at a distance of $d = 4$ kpc (8 kpc). The expected Lyα luminosity of a spherical cloud at this location follows as

$$L_{{\rm Ly}\alpha} = 4\pi \times f_{\rm gm} \times \eta_{\rm thick} \times h\nu_{{\rm Ly}\alpha} \times R^2_{\rm cloud} \times \Phi\,, \tag{3.6}$$

where $\eta_{\rm thick}$ is the fraction of ionizing continuum photons converted to Lyα photons, i.e. $\eta_{\rm thick} = 0.66$. With $f_{\rm gm}$ we denote the geometric reduction factor – a free parameter that accounts for the inhomogeneous illumination of the cloud and subsequent redistribution of Lyα photons over a wide solid angle. Radiative transfer simulations suggest that for a transversely illuminated cloud $f_{\rm gm} = 0.5$ (Kollmeier et al. 2010). For our upper limit on the cloud radius, Equation (3.6) then provides an upper limit on its Lyα luminosity of $L_{{\rm Ly}\alpha} \lesssim 4 \times 10^{44}$ erg s^{-1} (1×10^{44} erg s^{-1}) at $d = 4$ kpc (8 kpc). This is almost an order of magnitude higher then the observed value. In reality, however, the cloud size might be much smaller than our instrumentally imposed upper limit, and it might also be further away than the projected transverse distance. Hence this order of magnitude estimate of Lyα radiation emanating from the surface of an optically thick cloud in the vicinity of the quasar is still consistent with what we observe.

3.4.3 Comparison with models

Haiman & Rees (2001) presented a strongly idealized model to predict the luminosity of Lyα fuzz around radio-quiet quasars. Specifically, they assumed a spherical symmetric 2-phase gas distribution in pressure equilibrium within a collapsed dark-matter halo and predicted extended Lyα emission as a generic property of high-z quasars. The phases are a hot tenuous virialized plasma (i.e. $T_{\rm hot} \sim T_{\rm vir}$ of the halo) and colder neutral gas that has cooled down to $T_{\rm cold} \sim 10^4$ K during the age of the system. If in such an environment the quasar emits radiation isotropically and ionizes the whole nebula, its Lyα luminosity depends only on the total gas mass and thus on the total halo mass. In this framework, the absence of significant Lyα fuzz in our quasars might suggest that the hosting haloes are not overly massive. However, as already pointed out by Haiman & Rees (2001) and also Alam & Miralda-Escudé (2002), small deviations from this idealized scenario might alter the surface brightness of the Lyα fuzz substantially. Currently, the observations do not provide strong constraints on the basic assumptions in these models.

State-of-the-art numerical simulations in a cosmological framework predict that the spatial distribution of the CGM gas shows filamentary structure, with cold gas accreting along streams towards the centre of the halo (e.g. Dekel et al. 2009; Faucher-Giguère & Kereš 2011; Rosdahl & Blaizot 2012). Those streams have high column densities and their surfaces will therefore reflect up to 2/3 of incoming ionizing photons as Lyα photons. Although Lyα cooling radiation from those streams alone might already produce a detectable signal in extremely massive haloes, the presence of a central quasar should enhance the contrast of the filamentary structures by

boosting their Lyα emissivity by up to 2 orders of magnitude (Cantalupo et al. 2005; Kollmeier et al. 2010). While the giant Lyα nebulae around some quasars may well be explained by such fluorescently glowing accretion streams, these are by no means typical. More high-resolution simulations will be required in order to predict robustly the luminosities and sizes of Lyα fuzz for the lower-mass haloes typical for radio-quiet quasars.

3.5 Conclusions

It seems that on average, radio-quiet quasars are rather unspectacular sources of spatially extended Lyα emission. The non-detection of such Lyα fuzz in 4 of our objects and the marginal detection in one case are all fully consistent with the results of other recent investigations, although even the combined samples are still small.

The spectacularly bright and extended Lyα nebulae discovered around a few quasars (Weidinger et al. 2005; Martin et al. 2014a; Cantalupo et al. 2014) must be probably considered very rare cases. The rarity of this phenomenon may be explained if giant Lyα nebulae are seen only around quasars that reside in extraordinarily massive haloes.

The observing techniques used to search for Lyα fuzz around quasars are quite divers, encompassing narrow-band imaging, long-slit spectroscopy, and now also integral field spectrocopy (IFS). In principle, IFS should surpass the other methods by a large margin; in fact, any IFS datacube allows the user to explore both the narrow-band imaging as well as the spectral domain. The limiting factor for most existing optical IFS studies – including the present investigation – is sensitivity and light-collecting area of the available telescopes. This is however about to change, as a new generation of efficient IFS systems is being deployed at 8–10m class telescopes. Of particular interest for the topic of this study is the MUSE instrument, recently commissioned at the ESO Very Large Telescope (Bacon et al. 2014). Its unprecedented sensitivity will make it an optimal discovery machine for Lyα fuzz around quasars. Moreover, the large field of view of MUSE will ensure that there is no longer a danger of sky subtraction removing physical signal from very extended nebulae with flat radial profiles. It is to be expected that within a relatively short time, the statistics of observed Lyα fuzz around quasars will improve dramatically, turning the emphasis from discovery to the detailed dissection of physical properties.

Acknowledgments: We thank the support staff at Calar Alto observatory for help with the visitor-mode observations. E.C.H. especially thanks Sebastian Kamann and Bernd Husemann for teaching him how to operate the PMAS instrument. For all visual inspections of IFS datacubes mentioned in this paper we used the software `QFitsview`[3] by Ott (2012). All plots were made with `matplotlib` (Hunter 2007). The colour scheme in Fig. 3.2 is the `cubehelix` colour scheme by Green (2011). We thank Sebastiano Cantalupo for sharing unpublished details about the nebula around UM 287 with us. Finally, we thank the anonymous referee for constructive input.

3.6 Bibliography

Adelberger, K. L., Shapley, A. E., Steidel, C. C., et al. 2005, ApJ, 629, 636

Adelberger, K. L., Steidel, C. C., Kollmeier, J. A., & Reddy, N. A. 2006, ApJ, 637, 74

Ahn, C. P., Alexandroff, R., Allende Prieto, C., et al. 2012, ApJS, 203, 21

Alam, S. M. K. & Miralda-Escudé, J. 2002, ApJ, 568, 576

[3] `http://www.mpe.mpg.de/~ott/QFitsView/`

Bacon, R., Vernet, J., Borisiva, E., et al. 2014, The Messenger, 157, 13

Baek, S. & Ferrara, A. 2013, MNRAS, 432, L6

Basu-Zych, A. & Scharf, C. 2004, ApJ, 615, L85

Bergeron, J., Petitjean, P., Cristiani, S., et al. 1999, A&A, 343, L40

Blanc, G. A., Adams, J. J., Gebhardt, K., et al. 2011, ApJ, 736, 31

Bunker, A., Smith, J., Spinrad, H., Stern, D., & Warren, S. 2003, Ap&SS, 284, 357

Cantalupo, S., Arrigoni-Battaia, F., Prochaska, J. X., Hennawi, J. F., & Madau, P. 2014, Nature, 506, 63

Cantalupo, S., Porciani, C., Lilly, S. J., & Miniati, F. 2005, ApJ, 628, 61

Christensen, L., Jahnke, K., Wisotzki, L., & Sánchez, S. F. 2006, A&A, 459, 717

Courbin, F., North, P., Eigenbrod, A., & Chelouche, D. 2008, A&A, 488, 91

Dekel, A., Birnboim, Y., Engel, G., et al. 2009, Nature, 457, 451

Erb, D. K., Bogosavljević, M., & Steidel, C. C. 2011, ApJ, 740, L31

Faucher-Giguère, C.-A. & Kereš, D. 2011, MNRAS, 412, L118

Francis, P. J. & Bland-Hawthorn, J. 2004, MNRAS, 353, 301

Francis, P. J. & McDonnell, S. 2006, MNRAS, 370, 1372

Geach, J. E., Smail, I., Chapman, S. C., et al. 2007, ApJ, 655, L9

Goto, T., Utsumi, Y., Walsh, J. R., et al. 2012, MNRAS, 421, L77

Green, D. A. 2011, Bulletin of the Astronomical Society of India, 39, 289

Haiman, Z. & Rees, M. J. 2001, ApJ, 556, 87

Haiman, Z., Spaans, M., & Quataert, E. 2000, ApJ, 537, L5

Hayes, M., Scarlata, C., & Siana, B. 2011, Nature, 476, 304

Heckman, T. M., Lehnert, M. D., Miley, G. K., & van Breugel, W. 1991a, ApJ, 381, 373

Heckman, T. M., Miley, G. K., Lehnert, M. D., & van Breugel, W. 1991b, ApJ, 370, 78

Hennawi, J. F. & Prochaska, J. X. 2013, ApJ, 766, 58

Hennawi, J. F., Prochaska, J. X., Burles, S., et al. 2006, ApJ, 651, 61

Horne, K. 1986, PASP, 98, 609

Humphrey, A., Villar-Martín, M., Fosbury, R., et al. 2007, MNRAS, 375, 705

Humphrey, A., Villar-Martín, M., Fosbury, R., Vernet, J., & di Serego Alighieri, S. 2006, MNRAS, 369, 1103

Hunter, J. D. 2007, Computing In Science & Engineering, 9, 90

Husemann, B., Kamann, S., Sandin, C., et al. 2012, A&A, 545, A137

Husemann, B., Wisotzki, L., Sánchez, S. F., & Jahnke, K. 2013, A&A, 549, A43

Kamann, S., Wisotzki, L., & Roth, M. M. 2013, A&A, 549, A71

Kollmeier, J. A., Zheng, Z., Davé, R., et al. 2010, ApJ, 708, 1048

Martin, D. C., Chang, D., Matuszewski, M., et al. 2014a, ApJ, 786, 106

Martin, D. C., Chang, D., Matuszewski, M., et al. 2014b, ApJ, 786, 107

Matsuda, Y., Yamada, T., Hayashino, T., et al. 2004, AJ, 128, 569

Matsuda, Y., Yamada, T., Hayashino, T., et al. 2011, MNRAS, 410, L13

Nilsson, K. K., Fynbo, J. P. U., Møller, P., Sommer-Larsen, J., & Ledoux, C. 2006, A&A, 452, L23

North, P. L., Courbin, F., Eigenbrod, A., & Chelouche, D. 2012, A&A, 542, A91

Oke, J. B. 1990, AJ, 99, 1621

Ott, T. 2012, QFitsView: FITS file viewer, astrophysics Source Code Library

Ouchi, M., Ono, Y., Egami, E., et al. 2009, ApJ, 696, 1164

Pâris, I., Petitjean, P., Aubourg, É., et al. 2012, A&A, 548, A66

Prescott, M. K. M., Dey, A., & Jannuzi, B. T. 2012, ApJ, 748, 125

Prescott, M. K. M., Dey, A., & Jannuzi, B. T. 2013, ApJ, 762, 38

Rauch, M., Becker, G. D., Haehnelt, M. G., Carswell, R. F., & Gauthier, J.-R. 2013, MNRAS, 431, L68

Rees, M. J. 1988, MNRAS, 231, 91P

Roche, N., Humphrey, A., & Binette, L. 2014, MNRAS, 443, 3795

Rosdahl, J. & Blaizot, J. 2012, MNRAS, 423, 344

Roth, M. M., Fechner, T., Wolter, D., et al. 2010, in Society of Photo-Optical Instrumentation Engineers (SPIE) Conference Series, Vol. 7742, High Energy, Optical, and Infrared Detectors for Astronomy IV, 774209

Roth, M. M., Kelz, A., Fechner, T., et al. 2005, PASP, 117, 620

Saito, T., Shimasaku, K., Okamura, S., et al. 2006, ApJ, 648, 54

Sánchez, S. F., Aceituno, J., Thiele, U., Pérez-Ramírez, D., & Alves, J. 2007, PASP, 119, 1186

Sánchez, S. F. & Humphrey, A. 2009, A&A, 495, 471

Sánchez, S. F., Kennicutt, R. C., Gil de Paz, A., et al. 2012, A&A, 538, A8

Sandin, C., Becker, T., Roth, M. M., et al. 2010, A&A, 515, A35

Sandin, C., Weilbacher, P., Tabataba-Vakili, F., Kamann, S., & Streicher, O. 2012, in Proceedings of SPIE, Vol. 8451, Software and Cyberinfrastructure for Astronomy II, ed. C. G. Radziwill N. M., Society of Photo-Optical Instrumentation Engineers (SPIE), 84510F

Schaerer, D. 2003, A&A, 397, 527

Steidel, C. C., Adelberger, K. L., Shapley, A. E., et al. 2000, ApJ, 532, 170

Steidel, C. C., Erb, D. K., Shapley, A. E., et al. 2010, ApJ, 717, 289

Taniguchi, Y. & Shioya, Y. 2000, ApJ, 532, L13

Telfer, R. C., Zheng, W., Kriss, G. A., & Davidsen, A. F. 2002, ApJ, 565, 773

Vanden Berk, D. E., Richards, G. T., Bauer, A., et al. 2001, AJ, 122, 549

Véron-Cetty, M.-P. & Véron, P. 2010, A&A, 518, A10

Wall, J. V. 1979, QJRAS, 20, 138

Weidinger, M., Møller, P., & Fynbo, J. P. U. 2004, Nature, 430, 999

Weidinger, M., Møller, P., Fynbo, J. P. U., & Thomsen, B. 2005, A&A, 436, 825

Willott, C. J., Chet, S., Bergeron, J., & Hutchings, J. B. 2011, AJ, 142, 186

Wisotzki, L., Becker, T., Christensen, L., et al. 2003, A&A, 408, 455

Zirm, A. W., Dey, A., Dickinson, M., & Norman, C. J. 2009, ApJ, 694, L31

Chapter 4

LSDCat
Detection and cataloguing of emission line sources in integral-field spectroscopy datacubes

Abstract: This paper accompanies the release of our *Line Source Detection and Cataloguing* software LSDCat. The aim of LSDCat is to build a catalogue of faint emission line sources in wide-field integral-field spectroscopic datacubes. LSDCat detects emission lines via thresholding in signal-to-noise utilising a 3D matched filtered version of the datacube. The catalogue produced by the software contains positions, extents, and fluxes of the detected emission lines. We implemented LSDCat's algorithms in Python with a focus on fast processing of datacubes of large size. In this paper we also provide guidelines for the use of LSDCat based on our experience from emission line searches in MUSE datacubes. Our LSDCat software is available for download at http:/muse-vlt.eu/science/tools[1].

4.1 Introduction

One motivating driver for the construction of the current generation of optical wide-field integral-field spectrographs such as the Multi Unit Spectroscopic Explorer at (MUSE - since 2014 in operation; Bacon et al. 2014; Kelz et al. 2015) or the Keck Cosmic Web Imager (KCWI - under construction; Martin et al. 2010) is the detection of faint emission lines from high-redshift galaxies. The high-level data-products from those instruments are so called datacubes – three-dimensional (3D) arrays containing intensity related values with two spatial axes and one wavelength axis. So far an efficient, robust and user-friendly detection and cataloguing software for faint line emitting sources in such datacubes is not available. To remedy this situation we developed the *Line Source Detection and Cataloguing* (LSDCat) tool.

Automatic detection of faint astronomical sources in 2D imaging data is a well studied problem. Various methods to tackle it have been implemented in software packages that are widely

This chapter is a draft version of a paper (Authors: E. C. H and Lutz Wisotzki) that will accompany the public release of the LSDCat software.

[1]This webpage will link to the LSDCat software when it is publicly released. In the meantime the code is available on request.

adopted in the astronomical community (see reviews by Bertin 2001 and Masias et al. 2012, or the comparison of two frequently used tools by Annunziatella et al. 2013). A conceptually simple approach consists of two steps: In the first step the observed imaging data is transformed in order to highlight objects while simultaneously reducing the background noise. A particular transformation that satisfies both requirements is the matched filter (MF) transform. Here the image is convolved with a 2D template that matches the expected light-distribution of the sources to be detected. Mathematically it can be proven that for stationary noise the MF maximises the signal-to-noise ratio (S/N) of a source that is optimally represented by the template (e.g. Schwartz & Shaw 1975; Das 1991; Zackay & Ofek 2015; Vio & Andreani 2016). In the second step the MF-transformed image is segmented into objects via thresholding, i.e. each pixel is set to one if it is above the threshold or zero otherwise. Connected 1-valued pixels then define the objects on which further measurements (e.g. centroid coordinates, brightnesses, ellipticities etc.) can be performed. Other image transformations (e.g. multi-scale methods) and detection strategies (e.g. histogram-based methods) have been used, but especially in optical (or near-infrared) imaging surveys for faint extragalactic objects the "MF + thresholding"-approach is most frequently employed. This wide spread adoption can be partly attributed to the conceptual simplicity and robustness of the method that is able to meet the specifications of most scientific programs. However, it is also caused by the availability of a stable and user-friendly implementation of a source detection and extraction software based on this approach (Shore 2009): `SExtractor` (Bertin & Arnouts 1996).

The detection and cataloguing of astronomical sources in 3D datasets has so far mostly been of interest in the realm of radio astronomy. Similar to integral-field spectroscopy these observations result in 3D datacubes containing intensity values with two spatial and one frequency axis. Here especially surveys for extragalactic 21 cm H I emission are faced with the challenge to discover faint emission line sources in such datacubes. The current generation of those surveys utilises custom tailored software for this task and also relies heavily on manual inspection of the datacubes. Notably, the approach of Saintonge (2007) tries to minimise such error-prone interactivity by employing a search technique based on matched filtering, although only in spectral direction. More recently, driven mainly by the large data volumes expected from the next generation of large radio surveys with the Square Kilometre Array, development and testing of new 3D source finding techniques has started (e.g. Koribalski 2012; Popping et al. 2012; Serra et al. 2012; Jurek 2012). Currently, two software packages implementing some of these techniques are available to the community: DUCHAMP (Whiting 2012) and SoFiA (Serra et al. 2015). While in principle these programs could be adopted for source detection purposes in optical integral field spectroscopic datasets, in practice there are limitations that necessitated the development of a dedicated IFS source finder. For example, in contrast to the uniform noise properties of radio datacubes, the noise properties of long exposure IFS datacubes are dominated by telluric line- and continuum emission and are therefore varying with wavelength. Moreover, the search strategies implemented in the radio 3D source finders are tuned to capture the large variety of signals expected in future and ongoing radio surveys. But, as we show in this paper, the emission line signature from compact high-redshift sources in IFS data is well described by a simple template that needs, however, an IFS-specific parameterisation. Finally, the input data as well as the parameterisation of detected sources is different in the radio domain compared to the requirements in integral field spectroscopy: typically radio datacubes have their spectral axis expressed as frequency and flux-densities are measured in Jansky, while in IFS cubes the spectral axis is in wavelengths and flux-densities are measured in $\mathrm{erg\,s^{-1}cm^{-2}\AA^{-1}}$.

`LSDCat` is part of a long-term effort, initially motivated by the construction of MUSE, to develop source detection algorithms for wide-field IFS datasets (e.g. Bourguignon et al. 2012).

As part of this effort Meillier et al. (2016) recently released the *Source Emission Line FInder* SELF. This software is based on a Baysian scheme utilising a reversible jump Monte Carlo by Markov Chain algorithm. While this mathematical sophisticated machinery is powerful in unearthing faint emission line objects in a datacube, the execution time of the software is too long for practical use. In contrast the algorithm of `LSDCat` is rather simple. It is also robust, as it is based on the matched-filtering method that has long been successfully utilised for detecting sources in imaging data. Moreover, the execution time is fast on state-of-the art workstations. `LSDCat` is therefore well suited for upcoming surveys that will produce a large number of wide-field IFS datacubes. Additionally, the fast execution time also permits additional fake source insertion experiments for empirically reconstructing the selection function of those surveys.

The remainder of this article is structured as follows: In Sect. 4.2 we describe the search technique in implemented in `LSDCat` to build a catalogue of emission line objects from a wide field IFS datacube. In Sect. 4.3 we give guidelines for an optimal choice of the free parameters in the detection procedure. We discuss possible future improvement in the concluding Sect. 4.4.

4.2 Method Description & Implementation

The high-level data product of an integral field unit (IFU) observing campaign is a datacube $\boldsymbol{F}$ (e.g. Allington-Smith 2006; Turner 2010). The purpose of `LSDCat` is to detect and parameterise emission line sources in $\boldsymbol{F}$. More specifically $\boldsymbol{F}$ is set of volume pixels (commonly referred to as voxels) $F_{x,y,z}$ with intensity related values, for example flux densities in units of erg s^{-1}cm^{-2}Å^{-1}. The indices x, y are spatial indexing the spatial pixels (so-called spaxels), and z indexes the spectral layers of the datacube. Moreover, unique mappings between x, y and sky position (right ascension and declination), as well as between z and wavelength λ can be included in the metadata (Greisen & Calabretta 2002; Greisen et al. 2006). In `LSDCat` we currently require that the mapping between z and λ is linear, i.e. $\lambda = \lambda_0 + \Delta\lambda \times z$ with $\Delta\lambda$ being the wavelength sampling and λ_0 the wavelength associated with $z \equiv 0$. In the new generation of wide-field IFUs based on image-slicers, such as MUSE or KCWI the sky is sampled contiguously and typical dimensions of the datacube are $x_{\max}, y_{\max}, z_{\max} \simeq a \times 10^2, b \times 10^2, c \times 10^3$, with $a \approx b \sim 3$ and $c \sim 4$, i.e. the datacubes consist of $\sim 10^8$ voxels.

For MUSE the datacube $\boldsymbol{F}$ is the result of resampling the raw CCD data of the IFU observational campaign with a dedicated data reduction system (Weilbacher et al. 2012, 2014). Such a data reduction system also ensures that the atmospheric background line and continuum emission have been subtracted from $\boldsymbol{F}$ (Streicher et al. 2011, see also Soto et al. 2016). Moreover, to achieve a unique mapping between x, y and sky position for each spectral layer z the MUSE pipeline accounts in the resampling step for the wavelength-dependent lateral off-set along the parallactic angle induced by the atmosphere (the so called differential atmospheric refraction, see e.g. Filippenko 1982). Finally, also the noise term from each CCD pixel is propagated to its corresponding voxel in the data reduction process, so that a variance datacube $\boldsymbol{\sigma}^2$ is available.

Source detection is essentially a decision process based on a test statistic to either reject or accept features in the data as genuine astronomical source signals (e.g. Schwartz & Shaw 1975; Wall 1979; Hong et al. 2014; Zackay & Ofek 2015; Vio & Andreani 2016). This decision is usually based on a comparison with the noise statistics of the dataset under scrutiny. Consequently an accurate knowledge of those noise statistics is desired for deciding on meaningful thresholds, e.g. in terms of false-alarm probability. In `LSDCat` we assume that $\boldsymbol{\sigma}^2$ contains a good estimate of the variance. However, in the resampling process carried out by the data reduction pipelines the co-variance terms are usually neglected due to the large number of voxels

Table 4.1: Routines of LSDCat with the required input parameters.

Processing step	LSDCat Routine	Input parameters
Spatial filtering	`lsd_cc_spatial.py`	– PSF functional form: Moffat or Gaussian – p_0,p_1,p_2 and λ_0 for FWHM(λ) [$''$] = $p_0 + p_1(\lambda - \lambda_0) + p_2(\lambda - \lambda_0)^2$ – (Moffat β, if Moffat PSF)
Spectral filtering	`lsd_cc_spectral.py`	– FWHM of Gaussian profile: v_{FWHM} [km s^{-1}]
Thresholding	`lsd_cat.py`	– Detection threshold: S/N$_{\mathrm{det.}}$
Measurements	`lsd_cat_measure.py`	– Analysis threshold: S/N$_{\mathrm{ana.}}$

in a datacube. Accordingly any noise statistics calculated from $\boldsymbol{\sigma}^2$ could underestimate the true noise. In Sect. 4.3.1 we show how a user could test this and we describe a possible workaround if this is the case.

We also assume in LSDCat that, as a preparatory step, galaxies and stars with a bright continuum (i.e. sources with significant signal in the majority of spectral bins) have been subtracted in $\boldsymbol{F}$. In principle the presence of such sources does not render the detection and cataloguing algorithm unusable. However, continuum bright sources will lead to a a number of catalogue entries unrelated to actual emission line objects. We give some guidance for subtraction of continuum bright sources prior to a LSDCat run in Sect. 4.3.2.

In Fig. 4.1 we depict in a flowchart the processing steps of LSDCat that lead from the input datacube $\boldsymbol{F}$ and its associated variances $\boldsymbol{\sigma}^2$ to a catalogue of emission lines. Each processing step is implemented as a standalone Python[2] program. The file format of the input data- and variance cubes have to conform to the FITS standard (Pence et al. 2010). LSDCat requires routines provided by NumPy[3] (van der Walt et al. 2011), SciPy[4] (Jones et al. 2001), and Astropy[5] (Astropy Collaboration et al. 2013). For processing $300 \times 300 \times 4000$ datacubes with intensity values stored in as 32-bit floating point numbers a computer with at least 16 GB of random access memory is recommended. The names of the individual LSDCat routines implementing the various processing steps are listed in Table 4.1 together with the main input parameters that influence the detection and cataloguing process. In the following we describe each of the processing steps with its routines in more detail.

4.2.1 3D matched filtering for compact emission line sources

The optimal detection statistic of an isolated signal in a dataset with additive white Gaussian noise is given by the matched filter transform of the dataset (e.g. Schwartz & Shaw 1975; Das 1991; Bertin 2001; Zackay & Ofek 2015; Vio & Andreani 2016). This transform cross-correlates the dataset with a template that matches the properties of the signal to be detected.

We utilise the matched filtering approach in LSDCat to obtain a robust detection statistic for isolated emission line sources in wide-field IFS datacubes. Therefore $\boldsymbol{F}$ needs to be convolved with a 3D template $\boldsymbol{T}$:

$$\tilde{\boldsymbol{F}} = \boldsymbol{F} * \boldsymbol{T} \ . \tag{4.1}$$

[2]Python Software Foundation. Python Language Reference, version 2.7. Available at `http://www.python.org`

[3]NumPy version 1.10.1. Available at `http://www.numpy.org/`.

[4]SciPy version 0.16.1, available at `http://scipy.org/`

[5]AstroPy version 1.0.1, available at `http://www.astropy.org/`

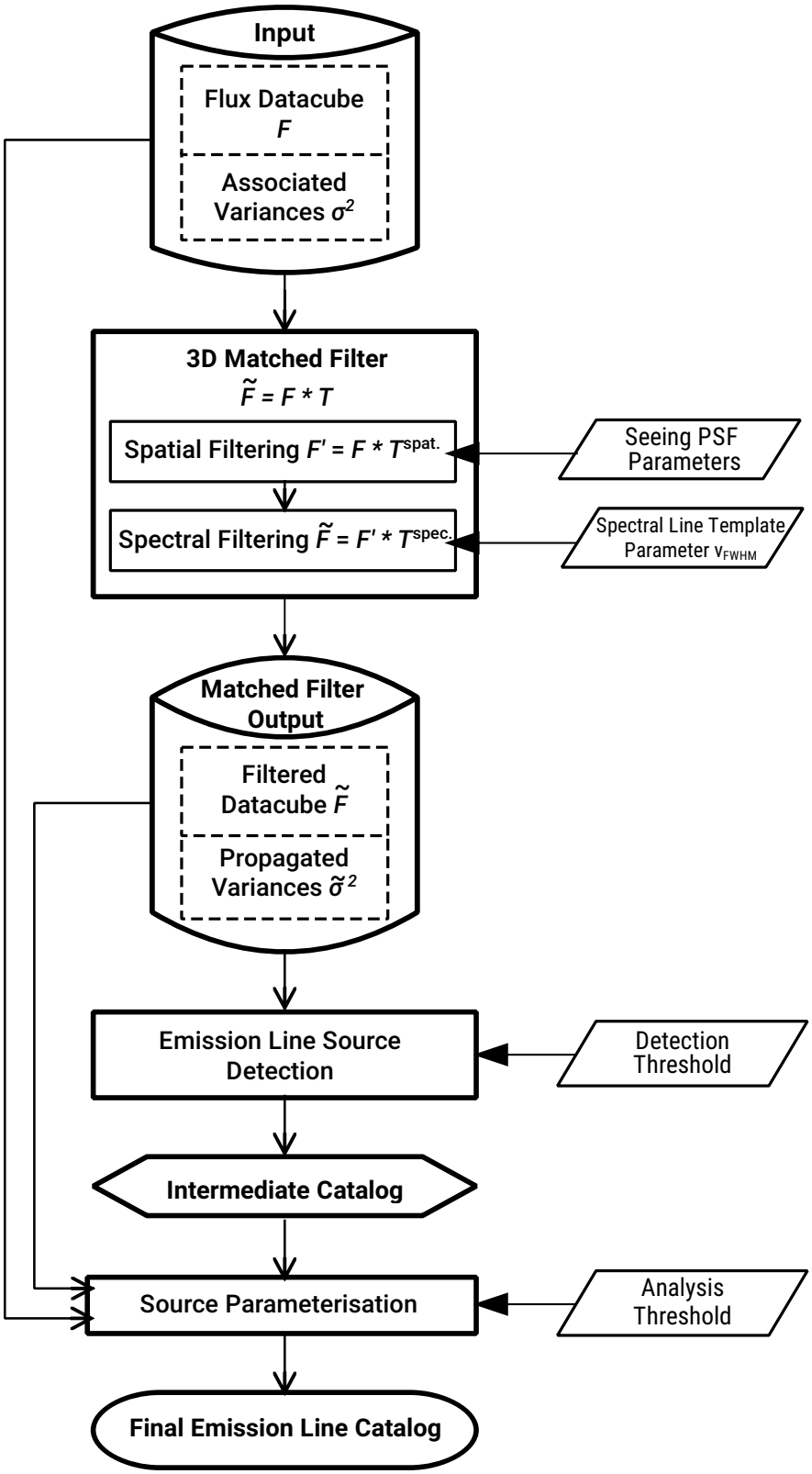

Figure 4.1: Flowchart illustrating the processing steps of `LSDCat` from an input datacube to a catalogue of positions, shape parameters and fluxes of emission line sources.

Here $*$ denotes the (discrete) convolution operation, i.e. every voxel of $\tilde{\boldsymbol{F}}$ is given by

$$\tilde{F}_{x,y,z} = \sum\nolimits_{i,j,k} F_{i,j,k}\, T_{x-i,y-j,z-k} = \sum\nolimits_{i,j,k} T_{i,j,k}\, F_{x-i,y-j,z-k} \ . \tag{4.2}$$

In principle the summation runs over the whole dimensions of the datacube, in practice terms where $T_{i,j,k} \approx 0$ can be neglected. Propagating the variances from $\boldsymbol{\sigma}^2$ through Eq. (4.2) yields the voxels of $\tilde{\boldsymbol{\sigma}}^2$:

$$\tilde{\sigma}^2_{x,y,z} = \sum_{i,j,k} T^2_{i,j,k}\, \sigma^2_{x-i,y-j,z-k} \ . \tag{4.3}$$

We require that $\boldsymbol{T}$ matches the spectral and spatial properties of an expected emission line source in $\boldsymbol{F}$. `LSDCat` is optimised for the search of faint compact emission line sources. For those sources it is a reasonable assumption that their spatial and spectral properties are independent. We can therefore write $\boldsymbol{T}$ as a product

$$\boldsymbol{T} = \boldsymbol{T}^{\mathrm{spec}} \boldsymbol{T}^{\mathrm{spat}} \ , \tag{4.4}$$

where $\boldsymbol{T}^{\mathrm{spat}}$ is the expected spatial- and $\boldsymbol{T}^{\mathrm{spec}}$ is its expected spectral profile. The voxels of $\boldsymbol{T}$ are thus given by

$$T_{x,y,z} = T^{\mathrm{spat}}_{x,y}\, T^{\mathrm{spec}}_{z} \ . \tag{4.5}$$

So the convolution from Eq. (4.2) yielding $\tilde{\boldsymbol{F}}$ can be performed as a two successive convolutions, in no particular order, one in each spectral layer with the appropriate $\boldsymbol{T}^{\mathrm{spat}}$, and one along the spectral direction at each spaxel x, y with $\boldsymbol{T}^{\mathrm{spec}}$:

$$\tilde{F}_{x,y,z} = \textstyle\sum_k T^{\mathrm{spec}}_k \left(\sum_{i,j} T^{\mathrm{spat}}_{i,j}\, F_{x-i,y-j,z-k} \right) \tag{4.6}$$

$$= \textstyle\sum_{i,j} T^{\mathrm{spat}}_{i,j} \left(\sum_k T^{\mathrm{spec}}_k\, F_{x-i,y-j,z-k} \right) \ . \tag{4.7}$$

For the spatial template $\boldsymbol{T}^{\mathbf{spat}}$ the `LSDCat` user has currently the choice between utilising a circular Gaussian profile

$$T_{x,y} = \frac{1}{2\pi\sigma^2_{\mathrm{G}}} \exp\left(-\frac{x^2+y^2}{2\sigma^2_{\mathrm{G}}} \right) \tag{4.8}$$

with standard deviation σ_{G}, or utilising a Moffat (1969) profile

$$T_{x,y} = \frac{\beta-1}{\pi r^2_{\mathrm{d}}} \left[1 + \frac{x^2+y^2}{r^2_{\mathrm{d}}} \right]^{-\beta} \tag{4.9}$$

with the width parameter r_{d} and the kurtosis parameter β. Both functions[6] are commonly used as approximation of the seeing induced point spread function (PSF) in ground based optical and near-IR observations (e.g. Trujillo et al. 2001a,b) and therefore represent an ideal spatial template in the search for compact emission line sources.

Typically the parameter used to characterise the PSF is its full width at half maximum (FWHM). In Eq. (4.8) it is at

$$\mathrm{FWHM} = 2\ \sqrt{2\ln 2}\,\sigma \tag{4.10}$$

and in for the Moffat in Eq. (4.9) it is at

$$\mathrm{FWHM} = 2\ \sqrt{2^{1/\beta}-1}\, r_{\mathrm{d}} \ . \tag{4.11}$$

[6] In the limiting case $\beta \to \infty$ Eq. (4.9) is equal to Eq. (4.8); cf. Trujillo et al. (2001b).

However, the seeing FWHM usually depends on wavelength[7]. In the framework of the standard (Kolmogorov) turbulence model of the atmosphere it is expected that the seeing FWHM decreases with wavelength at FWHM $\propto \lambda^{-1/5}$, where the constant of proportionality depends on airmass (see e.g. review by Hickson 2014). We account for this FWHM(λ) dependency in a model independent way within `LSDCat` by using a polynomial

$$\mathrm{FWHM}(\lambda)[''] = p_0 + p_1(\lambda - \lambda_0) + p_2(\lambda - \lambda_0)^2 \tag{4.12}$$

with the coefficients $p_0['']$, $p_1['''/\text{Å}]$, and $p_2['''/\text{Å}^2]$ being input parameters supplied by the user. In Sect. 4.3 we explain how an optimal choice for these coefficients can be determined.

In `LSDCat` we adopt as a spectral template a simple 1D Gaussian

$$T_z = \frac{1}{\sqrt{2\pi}\sigma} \exp\left(-\frac{z^2}{2\sigma^2}\right) , \tag{4.13}$$

where the width is parameterised by the standard deviation σ. The Gaussian function is an adequate model for the emission lines of unresolved distant galaxies where often no spatial disentanglement between ordered motions and unordered motions is possible. Neglecting ordered motions, the intrinsic emission line profile can be seen as a convolution of the natural line width of the element ($\sigma_{\text{nat.}} \sim 1\,\mathrm{km\,s^{-1}}$) with the thermal ($\sigma_{\text{th.}} \sim 10\,\mathrm{km\,s^{-1}}$) and non-thermal ($\sigma_{\text{nt.}} \gtrsim 10^2\,\mathrm{km\,s^{-1}}$) motions of the line-emitting gas. For a flat rotation curve above line width of an unresolved galaxy is additionally broadened by $\sigma_{\text{rot.}} \propto v_c/\sqrt{2}$, where v_c is the velocity in the flat part of the rotation curve and the constant of proportionality depends on the inclination under which the system is observed. On these grounds a velocity broadening σ_v appears as the natural choice in parameterising the Gaussian template. Since the mapping between λ and z is assumed to be linear, i.e. $\lambda = \lambda_{z=0} + \Delta\lambda \cdot z$, with $\Delta\lambda$ being the wavelength sampling and $\lambda_{z=0}$ being the wavelength of the first layer, σ in Eq. (4.13) depends on z when parameterised by σ_v:

$$\sigma \equiv \sigma_z = \frac{\sigma_v}{c}\left(\frac{\lambda_{z=0}}{\Delta\lambda} + z\right) . \tag{4.14}$$

The input parameter supplied by the `LSDCat` user is the velocity FWHM of the Gaussian profile $v_{\text{FWHM}} = 2\sqrt{2\ln 2}\,\sigma_v$ in $\mathrm{km\,s^{-1}}$. In Sect. 4.3.4 we provide guidelines for the optimal choice of this parameter.

As every layer z of the datacube is convolved with a different PSF and with a varying spectral response, mathematically the equivalence between Eq. (4.6) and Eq. (4.7) is only an approximation. However, the deviation is small since the decrease of spatial FWHM with increasing λ is much slower than the rapid response of the spectral profile of an emission line and the width of spectral response also increases slowly (considering that typically $\lambda_{z=0}/\Delta\lambda > 1000$).

In `LSDCat` the spatial convolution is performed by the routine `lsd_cc_spatial.py` and the spectral convolution is performed by `lsd_cc_spectral.py`. The output of a subsequent run of those routines is a FITS file with two header and data units; one storing $\tilde{\boldsymbol{F}}$ and the other one storing $\tilde{\boldsymbol{\sigma}}^2$. If available, both routines are able to fully leverage multiple processor cores to process several datacube layers or spaxels simultaneously. We optimise the computation time of `lsd_cc_spatial.py` by using the fast Fourier transform convolution method provided by SciPy to convolve the individual layers. However, since the spectral kernel varies with wavelength we can not utilise the fast Fourier transform method in `lsd_cc_spectral.py`. But since the discrete 1D convolution operation can be written as a matrix-vector product with the convolution

[7]For the Moffat parametrisation the FWHM(λ) dependence appears to be mainly driven by a variation in r_d, with β being almost constant (e.g. Husser et al. 2016).

matrix being a sparse banded matrix (e.g. Das 1991, Sect. 3.3.6), we achieve a substantial acceleration of the computational speed by utilising SciPy's sparse matrix multiplication algorithm. Typical execution times of `lsd_cc_spatial.py` or `lsd_cc_spectral.py` on a 300×300×4000 data- and variance cube, including reading and writing of the data, are ∼ 5 minutes on an Intel Core-i7 workstation with 8 cores or ∼ 2 minutes on a workstation with 2× AMD Opteron 6376 processors with 32 cores.

4.2.2 Thresholding: Generation of an intermediate catalogue

To decide on the presence or absence of an emission line in $\boldsymbol{F}$ at a position x, y, z we use the statistic

$$\mathrm{S/N}_{x,y,z} = \frac{\tilde{F}_{x,y,z}}{\tilde{\sigma}_{x,y,z}} \,, \tag{4.15}$$

with $\tilde{F}_{x,y,z}$ from Eq. (4.2) and $\tilde{\sigma}_{x,y,z}$ being the square root of Eq. (4.3). The voxels $\mathrm{S/N}_{x,y,z}$ constitute the signal-to-noise cube $\mathbf{S/N} \equiv \tilde{\boldsymbol{F}}/\tilde{\boldsymbol{\sigma}}$ that can be computed after the matched filtering has been performed. In principle the values on the left side of Eq. (4.15) translate into a probability for rejecting the null-hypothesis of no source being present at position x, y, z in $\boldsymbol{F}$. This is commonly referred to as the detection significance of a source. However, in a strict mathematical sense this direct translation is only valid for sources that are exactly described by the matched-filtering template $\boldsymbol{T}$ in a dataset where the variance terms on the right-side of Eq. (4.3) are stationary and fully uncorrelated. Nevertheless, even if these strict requirements are not met by the IFS datacube, filtering with $\boldsymbol{T}$ will always reduce high-frequency noise while enhancing the presence of sources that are similar in appearance with $\boldsymbol{T}$. Thus Eq. (4.15) can still be used as a robust empirical measure to decide with an detection threshold $\mathrm{S/N}_{\mathrm{det.}}$ whether or not a source is present at a position x, y, z in $\boldsymbol{F}$. We illustrate this for a faint high-z Lyman α emitting galaxy seen in a one hour observation with MUSE in Fig. 4.2; this source has a peak value above 10 in this particular $\mathbf{S/N}$ cube.

We now construct a catalogue of emission line sources by performing thresholding in the $\boldsymbol{S/N}$-cube, i.e. we create a datacube $\boldsymbol{L}$ whose voxels are given by

$$L_{x,y,z} = \begin{cases} 1 & \text{if } \mathrm{S/N}_{x,y,z} \geq \mathrm{S/N}_{\mathrm{det.}} \,, \\ 0 & \text{otherwise.} \end{cases} \tag{4.16}$$

The detection threshold $\mathrm{S/N}_{\mathrm{det.}}$ is the principal input parameter to be set by the `LSDCat` user. Each cluster of non-zero neighbouring voxels in $\boldsymbol{L}$ (6-connected topology) constitutes a detection. For each detection we record the coordinates x_{peak}, y_{peak},z_{peak} of the peak in the $\boldsymbol{S/N}$-cube, its value $\mathrm{S/N}_{\mathrm{peak}} \equiv \mathrm{S/N}_{x_{\mathrm{peak}},y_{\mathrm{peak}},z_{\mathrm{peak}}}$ and the number of voxels $N_{det.}$ constituting the detection. These values form an intermediate catalogue of sources. In this catalogue each entry also gets assigned a unique identifier (a so called running ID). Of course, the lower the detection threshold the higher the rate of spurious detections in the catalogue. We give guidelines on the choice of the detection threshold based on our experience with MUSE data in Sect. 4.3.

The `LSDCat` routine `lsd_cat.py` creates this intermediate catalogue from the output of the matched filtering process. We implemented the thresholding and catalogue building step by using routines from SciPy's `ndimage.measurements` package. The intermediate catalogue is written to disk in the FITS binary table format. The actual execution time depends not only on the dimensions of the input datacube but also on the detection threshold that determines the number of objects. As an example, running `lsd_cat.py` on an optimally matched filtered $\boldsymbol{S/N}$ datacube obtained in the MUSE-Wide survey (Chapter 5) with $\mathrm{S/N}_{\mathrm{det.}} = 8$ takes typically

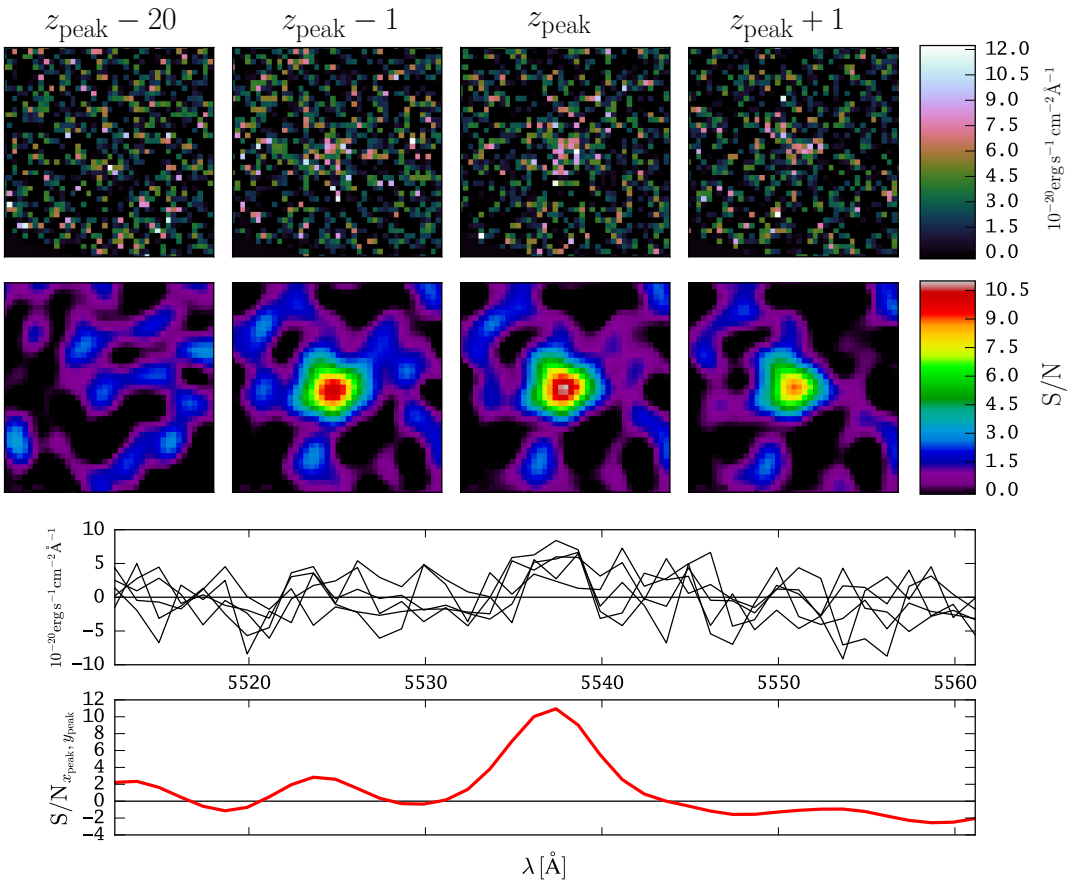

Figure 4.2: Example of the impact of the matched filtering on the detectability of a faint compact emission line source in a MUSE dataset of one hour integration time. Shown is a Lyman α emitting galaxy at redshift 3.6 with $F_{\mathrm{Ly}\alpha} = 1.5 \times 10^{-17}\,\mathrm{erg\,s^{-1}}$. The panels in the first row display four different layers of the datacube $\boldsymbol{F}$. The panels in the second row show the same layers in the $\mathbf{S/N}$-cube (Eq. 4.15) that is used to build the catalogue of emission line sources via thresholding (Eq. 4.16). In both rows the right panel shows a layer significantly away from the emission line peak (at 5020Å). The three panels on the right are the layers at $z_{\mathrm{peak}} - 1$, z_{peak}, and $z_{\mathrm{peak}} + 1$, respectively, where z_{peak} designates the layer containing the highest S/N value of the source. In the third row the flux density spectrum in the spaxels at x_{peak}, y_{peak} and $x_{\mathrm{peak}} \pm 1$, $y_{\mathrm{peak}} \pm 1$ are shown, where x_{peak} and y_{peak} is the spatial coordinate of the highest S/N value. The last row shows a S/N spectrum extracted from the $\boldsymbol{S/N}$-cube at x_{peak} and y_{peak}.

40 seconds on the Intel Core-i7 or AMD Opteron 6376 workstation described at the end of Sect. 4.2.1 — these catalogues contain typically $\sim$ 60–100 entries, with most of the entries being caused by genuine line emission from distant galaxies.

4.2.3 Measurements

Table 4.2: Output parameters for each `LSDCat` detection.

Source Parameters	`LSDCat` Name	Description
$x_{\rm peak}$, $y_{\rm peak}$, $z_{\rm peak}$	`{X,Y,Z}_PEAK_SN`	$\mathrm{S/N}_{\rm peak.}$ coordinate; see Sect. 4.2.2
$N_{\rm pix.}$	`NPIX`	Number of voxels above $\mathrm{S/N}_{\rm det.}$; see Sect. 4.2.2
$\mathrm{S/N}_{\rm peak}$	`DETSN_MAX`	S/N value at $x_{\rm peak}, y_{\rm peak}, z_{\rm peak}$; see Sect. 4.2.2
$x^{\rm COM}_{\boldsymbol{S/N}}$, $y^{\rm COM}_{\boldsymbol{S/N}}$, $z^{\rm COM}_{\boldsymbol{S/N}}$	`{X,Y,Z}_SN`	$\boldsymbol{S/N}$ centroid; see Eq. (4.17)
$x^{\rm COM}_{\boldsymbol{F}}$, $y^{\rm COM}_{\boldsymbol{F}}$, $z^{\rm COM}_{\boldsymbol{F}}$	`{X,Y,Z}_FLUX`	$\boldsymbol{F}$ centroid; Eq. (4.17) with $\mathrm{S/N}_{x,y,z} \rightarrow F_{x,y,z}$
$x^{\rm COM}_{\tilde{\boldsymbol{F}}}$, $y^{\rm COM}_{\tilde{\boldsymbol{F}}}$, $z^{\rm COM}_{\tilde{\boldsymbol{F}}}$	`{X,Y,Z}_SFLUX`	$\tilde{\boldsymbol{F}}$ centroid; Eq. (4.17) with $\mathrm{S/N}_{x,y,z} \rightarrow \tilde{F}_{x,y,z}$
$z^{\rm NB}_{\rm min}$, $z^{\rm NB}_{\rm max}$	`Z_NB_{MIN,MAX}`	Min. or max. z coordinate above $\mathrm{S/N}_{\rm ana.}$ in $\boldsymbol{S/N}$
$x^{(1)}, y^{(1)}$	`{X,Y}_1MOM`	2D $\mathrm{NB}^{\tilde{\boldsymbol{F}}}_{x,y}$-centroid; see Eq. (4.18) and Eq. (4.19)
$x^{(2)}, y^{(2)}, [xy]^{(2)}$	`{X,Y,XY}_2MOM`	Second central $\mathrm{NB}^{\tilde{\boldsymbol{F}}}_{x,y}$ moments; see Eq. (4.20), Eq. (4.21), and Eq. (4.22)
R_σ	`R_SIGMA`	$R_\sigma = \sqrt{(x^{(2)} + y^{(2)})/2}$
$R_{\rm Kron}$	`R_KRON`	Kron radius Eq. (4.20)
$F(k \cdot R_{\rm Kron})$	`FLUX_{k}KRON`	Integrated flux in $k \cdot R_{\rm Kron}$ aperture; see Eq. (4.24)
$\Delta F(k \cdot R_{\rm Kron})$	`ERR_FLUX_{k}KRON`	Uncertainty on $F(k \cdot R_{\rm Kron})$

A comma separated list within curly braces in the second column indicate the set of corresponding `LSDCat` output column names.
For each x, y coordinate there is also a corresponding right ascension and declination value available and for each z coordinate a corresponding wavelength can be tabulated if a corresponding world coordinate system (Greisen & Calabretta 2002) is specified.

`LSDCat` provides a set of basic parameters for each detection in the intermediate catalogue using the datacubes $\boldsymbol{F}$, $\boldsymbol{\sigma}^2$, $\tilde{\boldsymbol{F}}$ and $\boldsymbol{S/N}$. The parameters are chosen to be robust and independent from a specific scientific application. For more complex measurements, involving e.g. fitting of the sources flux distributions, the `LSDCat` measurement capability can serve as a starting point.

Parameterisation of sources is the final processing step in `LSDCat`. In Table 4.2 we list the various output parameters that can be generated for each detection. The routine performing the parameterisation task that writes out the final catalogue is called `lsd_cat_measure.py`. Of course, the final catalogue contains also the parameters $x_{\rm peak}$, $y_{\rm peak}$,$z_{\rm peak}$, $\mathrm{S/N}_{\rm peak}$, and $N_{\rm pix.}$ from the intermediate catalogue. Running the routine `lsd_cat_measure.py` on an intermediate catalog with $\sim 10^2$ entries takes typically 100 seconds on the machines mentioned before, with reading of the input data costing most of the time.

As positional parameters `lsd_cat_measure.py` provides weighted 3D centroid coordinates. For example the 3D $\boldsymbol{S/N}$-weighted centroid is given by the first moments

$$\left(x^{\rm COM}_{\boldsymbol{S/N}}, y^{\rm COM}_{\boldsymbol{S/N}}, z^{\rm COM}_{\boldsymbol{S/N}}\right) = \left(\frac{\sum_{x,y,z} x \cdot \mathrm{S/N}_{x,y,z}}{\sum_{x,y,z} \mathrm{S/N}_{x,y,z}} , \frac{\sum_{x,y,z} y \cdot \mathrm{S/N}_{x,y,z}}{\sum_{x,y,z} \mathrm{S/N}_{x,y,z}} , \frac{\sum_{x,y,z} z \cdot \mathrm{S/N}_{x,y,z}}{\sum_{x,y,z} \mathrm{S/N}_{x,y,z}} \right) . \quad (4.17)$$

Here for each detection the summation runs over all non-zero ($x_{\rm peak}$, $y_{\rm peak}$,$z_{\rm peak}$)-neighbouring voxels in a thresholded datacube similar to $\boldsymbol{L}$ (Eq. 4.16), but with voxels set to one if they are above an analysis threshold $\mathrm{S/N}_{\rm ana.}$. This analysis threshold, which must be smaller or equal than $\mathrm{S/N}_{\rm ana.}$, is the required input parameter for `lsd_cat_measure.py`. A reasonable way of choosing $\mathrm{S/N}_{\rm ana.}$ is discussed in Sect. 4.3.5. Other than the $(x^{\rm COM}_{\boldsymbol{S/N}}, y^{\rm COM}_{\boldsymbol{S/N}}, z^{\rm COM}_{\boldsymbol{S/N}})$ 3D centroid coordinates we provide 3D centroid coordinates weighted with the voxels of $\boldsymbol{F}$ and $\tilde{\boldsymbol{F}}$ — ($x^{\rm COM}_{\boldsymbol{F}}$, $y^{\rm COM}_{\boldsymbol{F}}$, $z^{\rm COM}_{\boldsymbol{F}}$) and ($x^{\rm COM}_{\tilde{\boldsymbol{F}}}$, $y^{\rm COM}_{\tilde{\boldsymbol{F}}}$, $z^{\rm COM}_{\tilde{\boldsymbol{F}}}$). For those $\mathrm{S/N}_{x,y,z}$ in Eq. (4.17) is substituted by $F_{x,y,z}$ and $\tilde{F}_{x,y,z}$, respectively.

As spatial coordinates `lsd_cat_measure.py` furthermore provides 2D weighted centroids for each detection. These are calculated from a narrow-band image created from $\tilde{\boldsymbol{F}}$:

$$\mathrm{NB}^{\tilde{\boldsymbol{F}}}_{x,y} = \sum_{z=z^{\rm NB}_{\rm min}}^{z^{\rm NB}_{\rm max}} \tilde{F}_{x,y,z} \; . \tag{4.18}$$

Here the boundaries $z^{\rm NB}_{\rm min}$ and $z^{\rm NB}_{\rm max}$ of each narrow-band image are the minimum and maximum z-coordinate of the voxels of a detection that are above $\mathrm{S/N}_{\rm ana.}$ in the $\boldsymbol{S/N}$-cube. Now the 2D weighted centroid coordinates are the first moments

$$(x^{(1)}, y^{(1)}) = \left(\frac{\sum_{x,y} x \cdot \mathrm{NB}^{\tilde{\boldsymbol{F}}}_{x,y}}{\sum_{x,y} \mathrm{NB}^{\tilde{\boldsymbol{F}}}_{x,y}}, \frac{\sum_{x,y} y \cdot \mathrm{NB}^{\tilde{\boldsymbol{F}}}_{x,y}}{\sum_{x,y} \mathrm{NB}^{\tilde{\boldsymbol{F}}}_{x,y}} \right) \; . \tag{4.19}$$

In this equation the summation runs over all pixels x, y of $\mathrm{NB}^{\tilde{\boldsymbol{F}}}_{x,y}$ that belong to the detection and are above the analysis threshold $\mathrm{S/N}_{\rm ana.}$ in its $z_{\rm peak.}$ layer of the $\boldsymbol{S/N}$-cube.

We also calculate in `lsd_cat_measure.py` the second central moments from a detection in $\mathrm{NB}^{\tilde{\boldsymbol{F}}}_{x,y}$, i.e.

$$x^{(2)} = \frac{\sum_{x,y} x^2 \cdot \mathrm{NB}^{\tilde{\boldsymbol{F}}}_{x,y}}{\sum_{x,y} \mathrm{NB}^{\tilde{\boldsymbol{F}}}_{x,y}} - (x^{(1)})^2 \tag{4.20}$$

$$y^{(2)} = \frac{\sum_{x,y} y^2 \cdot \mathrm{NB}^{\tilde{\boldsymbol{F}}}_{x,y}}{\sum_{x,y} \mathrm{NB}^{\tilde{\boldsymbol{F}}}_{x,y}} - (y^{(1)})^2 \tag{4.21}$$

$$[xy]^{(2)} = \frac{\sum_{x,y} x^2 \cdot y^2 \cdot \mathrm{NB}^{\tilde{\boldsymbol{F}}}_{x,y}}{\sum_{x,y} \mathrm{NB}^{\tilde{\boldsymbol{F}}}_{x,y}} - x^{(1)} \cdot y^{(1)} \; . \tag{4.22}$$

These second central moments are measures for the extent or non-circularity of a detection. For example $[xy]^{(2)} \equiv 0$ for a circular symmetric distribution of $\mathrm{NB}^{\tilde{\boldsymbol{F}}}_{x,y}$ for which $R_\sigma = \sqrt{(x^{(2)} + y^{(2)})/2}$ is the radius encircling 68% of $\sum_{x,y} \mathrm{NB}^{\tilde{\boldsymbol{F}}}_{x,y}$.

While in principle the original fluxcube $\boldsymbol{F}$ could be used in Eqs. (4.18) to (4.22), in practice such moments are quite susceptible to errors especially for low signal-to-noise sources. On the other hand, using the $\boldsymbol{S/N}$-cube could bias the result by neglecting layers in the narrow-band image that, due to the presence of a telluric line, have a higher background noise.

For a reasonable choice of $\mathrm{S/N}_{\rm ana.}$ the boundaries $z^{\rm NB}_{\rm min}$ and $z^{\rm NB}_{\rm max}$ enclose the emission line completely in $\boldsymbol{F}$. Therefore the pixels of the narrow-band image $\mathrm{NB}^{\boldsymbol{F}}_{x,y}$ created by summation from $z^{\rm NB}_{\rm min}$ to $z^{\rm NB}_{\rm max}$ over $F_{x,y,z}$ analogue to Eq. (4.18) can be used for flux integration. In `LSDCat`

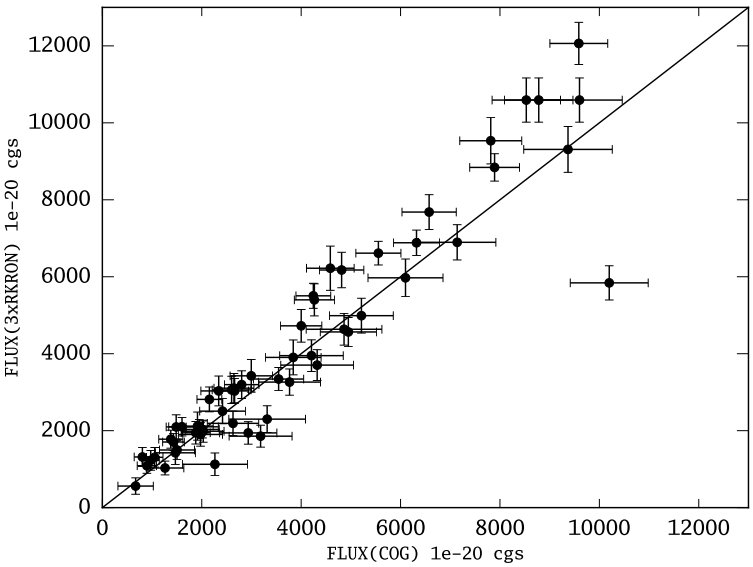

Figure 4.3: Comparison of a manual flux measurement approach to the automatic flux measurement done by `LSDCat` for a sample of 60 Lyman α emission lines in MUSE datacubes. The manual measurements F_{COG} utilise a curve-of-growth integration to turnover on a manually determined narrow band window. The automatic measurements are extracted in circular apertures of radius $3R_{\mathrm{Kron}}$ according to Eq. (4.24), with $z^{\mathrm{NB}}_{\mathrm{min}}$ and $z^{\mathrm{NB}}_{\mathrm{max}}$ being minimum and maximum z-coordinate of the voxels of a above $\mathrm{S/N}_{\mathrm{ana.}} = 3.5$ in the $\boldsymbol{S/N}$-cube.

we provide fluxes integrated over circular apertures. The radii of these apertures are defined as multiples k of the detections Kron radii (Kron 1980), i.e. $F(k \cdot R_{\mathrm{Kron}})$ with

$$R_{\mathrm{Kron}} = \frac{\sum_{x,y} \mathrm{NB}^{\tilde{\boldsymbol{F}}}_{x,y} \sqrt{(x - x^{(1)})^2 + (y - y^{(1)})^2}}{\sum_{x,y} \mathrm{NB}^{\tilde{\boldsymbol{F}}}_{x,y}} \,. \tag{4.23}$$

The factor k can be set by the `LSDCat` user, and multiple choices of k result in multiple columns of the output catalogue. The flux $F(k \cdot R_{\mathrm{Kron}})$ of is the given by the sum

$$F(k \cdot R_{\mathrm{Kron}}) = \sum\nolimits_{x,y} \sum\nolimits_{z=z^{\mathrm{NB}}_{\mathrm{min}}}^{z^{\mathrm{NB}}_{\mathrm{max}}} F_{x,y,z} \tag{4.24}$$

with the first sum running over all x, y satisfying $\sqrt{(x - x^{(1)})^2 + (y - y^{(1)})^2} \leq R_{\mathrm{Kron}}$.

For compact sources, whose light-profile is dominated by the broadening of the PSF, it can been shown that the $F(2.5\,R_{\mathrm{Kron}})$ aperture contains up to 94% of the total flux. This requires, however, that the determination of the Kron radius in Eq. (4.23) sums over pixels at large enough radii (e.g. Graham & Driver 2005). We therefore follow a similar approach as adopted in `SExtractor` (Bertin & Arnouts 1996) by summing in Eq. (4.23) over all x, y satisfying $\sqrt{(x - x^{(1)})^2 + (y - y^{(1)})^2} \leq 6 \times R_{\sigma}$. Finally, the uncertainty $\Delta F(k \cdot R_{\mathrm{Kron}})$ on this flux measurement is obtained by propagating the errors through Eq. (4.24) using the voxels $\sigma^2_{x,y,z}$ from the variance cube. To demonstrate the quality of the so obtained fluxes we compare in Fig. 4.3 fluxes from `LSDCat` measured in apertures of $R = 3R_{\mathrm{Kron}}$ according to Eq. (4.24) with fluxes that were manually measured on a sample of 60 Lyman α emitting galaxies. As can be

seen for all except one emission line LSDCat $R = 3R_{\mathrm{Kron}}$ fluxes are in good agreement with those determined manually. The line for which the flux is underestimated by the automatic method is characterised by a very pronounced Lyα double peak (e.g. Yamada et al. 2012; Hong et al. 2014), for which the automatically determined narrow-band window captures only one peak.

4.3 Guidelines for the usage of LSDCat

Here we provide some guidelines for using LSDCat on wide-field IFS datacubes. These guidelines are based on our experience of running the algorithm on MUSE datacubes in searches for faint emission lines from high-redshift galaxies (Bacon et al. 2015, Bina et al. 2016, and Chapter 5 of this thesis). Therefore these guidelines are meant to be instructive for the potential LSDCat user, but they should not be understood as recipes.

4.3.1 Effective variances

In Sect. 4.2 we stated the requirement that the variance cube $\boldsymbol{\sigma}^2$ must contain good estimates of the true variances. However, the values of $\boldsymbol{\sigma}^2$ may in fact be an underestimate since co-variance terms are often neglected when resampling raw CCD pixels from several exposures to datacube voxels. In this case the $\boldsymbol{S/N}$ cube will be biased to higher values that do not permit a translation into probabilities for rejecting spurious detections. To use meaningful detection thresholds it is therefore recommended to check if the values of $\boldsymbol{\sigma}^2$ are representative of the true variances and, if not, to correct them. To perform this check or correction we suggest to use an empirical estimate of the variances that can be obtained directly from the datacube.

As a possible empirical estimate we propose the creation of an effective variance spectrum $\sigma^2_{\mathrm{eff.}}(z)$ by analysing the pixel statistics in each layer of regions not affected by emission from objects. These regions could be identified e.g. on a white-light image created by summation over all datacube layers or on deep imaging data from other instruments using conventional 2D image detection algorithms (e.g. SExtractor, Bertin & Arnouts 1996). Instead of using the distribution of values from single pixels it is favourable to analyse the distribution of averages obtained in small apertures, as covariance terms are especially expected to affect neighbouring pixels. The so obtained effective variance spectrum can then be compared to the average variance in each layer of the pipeline reduced variance cube. If a significant difference between the two is found, then it is advised to rescale the pipeline produced variance accordingly. However, as a caveat, by construction the so created variance spectrum does not account for spectral co-variances.

4.3.2 Dealing with bright continuum sources in the datacube

Even in relatively empty regions on the sky there will be objects that have a detectable continuum signal within the datacube. These objects can be easily identified in a so-called white-light image that results from averaging over all layers in the datacube (see e.g. Fig. 3 in Bacon et al. 2015). Hence, conventional 2D source detection algorithms are sufficient to catalogue these sources. In principle their presence within the datacube does not render LSDCat's detection algorithm unusable. Nevertheless, since in the detection process pure emission line signals are assumed, we recommend to remove continuum signal from objects beforehand. Especially, it is only after such a continuum removal that LSDCat can correctly catalogue the emission lines from galaxies that are bright in the continuum.

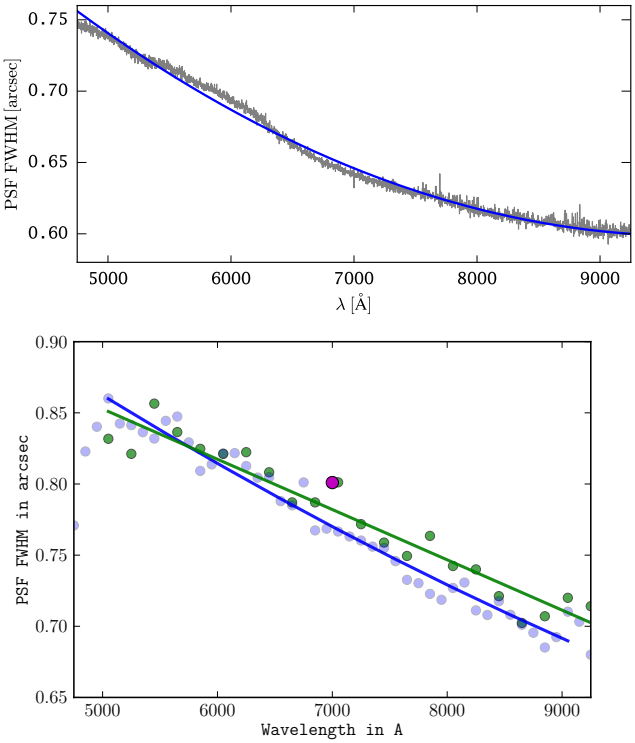

Figure 4.4: *Top:* Polynomial fits to the PSF FWHM as a function of wavelength derived from a Moffat fits to the brightest star in the MUSE *Hubble* Deep Field South datacube (Bacon et al. 2015). The grey curve shows the FWHM fit results in each individual layer, the blue curve shows a polynomial fit of degree two to these values. The coefficients of this polynomial fit are the input parameters for `lsd_cc_spatial.py`. *Bottom:* Comparison of the PSF FWHM(λ) determination utilising a bright star or a set of compact galaxies within the datacube. The shown example is taken from a 1h MUSE observation in a CANDELS/Deep field (Herenz et al., in prep.). The green points are the result of minimising the χ^2-difference between images of compact galaxies as seen in the datacube (binned over ~150 layers) and resmpled, PSF convolved HST images of those galaxies. The green line is a linear fit through these points, whose coefficients can be used as input parameters in `lsd_cc_spatial.py`. The blue points and curve a the result of direct PSF fitting to a star in the field. The red point marks the average auto guider seeing.

To perform the continuum subtraction we recommend to create a datacube median-filtered in spectral direction. The width of the median filter should be much broader than the width of the expected emission lines and it should be narrow enough to correctly subtract a slowly varying continuum. From our experience filter widths of ~ 150 Å–200 Å serve these goals. This spectrally median-filtered datacube is then subtracted from the original datacube. The median-filter subtracted datacube can then be used as input $\boldsymbol{F}$ for `LSDCat`.

4.3.3 Parameterising the PSF

As explained in Sect. 4.2.1 the FWHM(λ) dependency of the matched filter in `LSDCat` is modelled via FWHM(λ)[″] = $p_0 + p_1(\lambda - \lambda_0) + p_2(\lambda - \lambda_0)^2$. The coefficients p_0[″], p_1[″/Å], and p_2[″/Å^2] are free input parameters for `lsd_cc_spatial.py` that have to be determined by the user in advance. A mismatch between the true and the used PSF FWHM results in reduced

$S/N_{peak.}$ values for point-like sources. However, it can be shown, assuming that a Gaussian with FWHM $\equiv$ $FWHM_{true}$ is representative of the true PSF, that $S/N_{peak.}$ decreases only as $2k/(k^2+1)$ when a matched filter of incorrect width $FWHM_{incorrect} = k \times FWHM_{true}$ is used (Zackay & Ofek 2015). Hence a small differences up to 20% between the used and the correct PSF FWHM result in insignificant reduction of sensitivity. Nevertheless, in many cases an accurate measurement of the FWHM(λ) dependency is possible from the datacube.

In case an isolated and reasonably bright star is within the datacube, the FWHM(λ) determination is achieved by fitting a Gaussian or Moffat function to this star in each spectral layer, or within bins of layers. Next the p_i's are found via a polynomial fit to those values. Exemplarily we show in Fig. 4.4 the results from this procedure for the brightest star in the MUSE *Hubble* Deep Field South datacube (Bacon et al. 2015). In case an isolated but not sufficiently bright star is present additional binning of datacube layers is recommended for the fitting. A reliable method for performing PSF fits in IFS datacubes was presented in Kamann et al. (2013). This method can also be used if two or more nearby stars are present within the field of view.

Of course, the fortunate situation of having a star within the datacube is not always given. If the observations were performed in fields where deep space-based broadband data is available, it is possible to utilise compact galaxies to measure the PSF in the datacube. To this aim the compact galaxies have to be convolved with a set of PSFs with different FWHMs before being resampled to the spatial scale of the IFS observations. The FWHM where the χ^2-difference between the actual data and the convolved and resampled high-resolution images is minimised is then taken as the best estimate. This process has to be carried out over a set of binned layers covering the whole wavelength range of the datacube. Since the χ^2 curve is very smooth around the minimum, the results on the individual FWHM determinations are usually noisier then when directly fitting a PSF model to a well defined point source. Therefore it is recommended to fit just a line instead of a polynomial to the resulting values (i.e. forcing $p_2 \equiv 0$ in `LSDCat`). Exemplarily we show the result of the outlined procedure in Fig. 4.4. To demonstrate the robustness of this approach we also compare in this figure to the FWHM(λ) determination from a star within the same field.

If both above methods are not applicable to the data, an analytic expression describing the FWHM(λ) dependency could be fitted with the polynomial to determine the p_i's. In particular, Tokovinin (2002) provide a set of equations that can be used to predict FWHM(λ) given a differential image motion monitor seeing FWHM measurement. At least for single, relatively short exposures ($\lesssim$10 min) under good seeing conditions (FWHM $< 1''$) the so predicted FWHM(λ) curve are in good agreement with the observed one (S. Kamann, priv. comm.). However, for longer exposures or datacubes that consist of multiple exposures taken under different seeing conditions the the choice of the free parameters in the Tokovinin-equations can not be well motivated.

4.3.4 Choosing a spectral filter width

As detailed in Sect. 4.2.1 the width of the Gaussian used for the spectral filtering is parameterised by its FWHM in velocity space. For a 1D Gaussian profile it can be shown[8] that S/N_{peak} decreases as $\sqrt{2k/(k^2+1)}$ if an incorrect width of $v_{\mathrm{FWHM,\,incorrect}} = k \times v_{\mathrm{FWHM,\,correct}}$ is chosen, when $v_{\mathrm{FWHM,\,correct}}$ is the actual width of the emission line. Hence, the maximum reachable detection significance reduces by approximately 10%, if the filter width is chosen half or twice as wide as the original emission line. Therefore a good choice of this parameter can be motivated by analysing the distribution of typical line widths of the targeted emission line objects from

[8]Following Appendix D Zackay & Ofek (2015) with insertion of a 1D Gaussian.

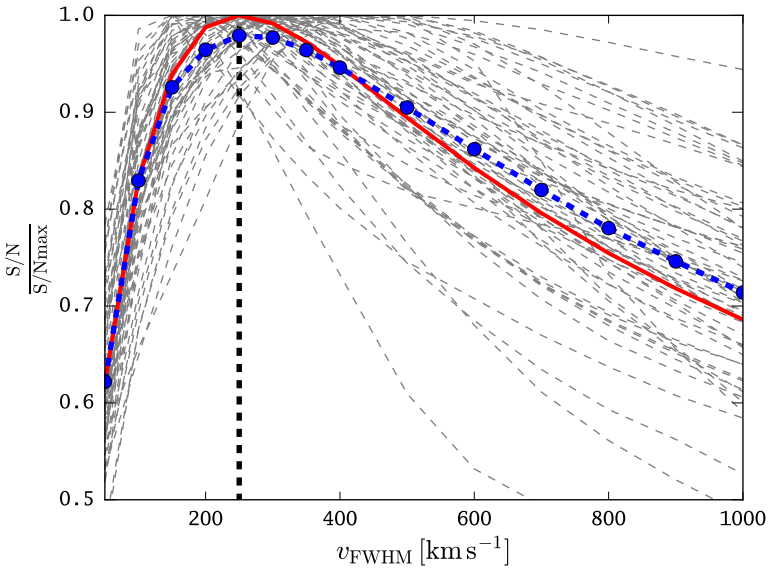

Figure 4.5: Ratio $(S/N)/(S/N_{max})\%$ for all Lyman α emitting sources in the *Hubble* Deep Field South MUSE datacube from Bacon et al. (2015). S/N_{max} is the maximum S/N_{peak} of a source over all filter widths. The grey lines denote the individual emitters and the blue curve shows the average over those curves. The dashed black vertical line indicates the filter width $v_{\rm FWHM} = 250\,{\rm km\,s^{-1}}$, where almost all Lyman α line emitters have $(S/N)/(S/N_{max}) > 90\%$. The red curve shows the theoretically expected $(S/N)/(S/N_{max}) \propto \sqrt{2k/k^2+1}$ ratio for an assumed Gaussian emission line with $v^{\rm correct}_{\rm FWHM} = 250\,{\rm km\,s^{-1}}$ filtered with an incorrect filter width of $v_{\rm FWHM,\,incorrect} = k \times v_{\rm FWHM,\,correct}$.

previous surveys. If the distribution is narrow, i.e. most of the line-widths are expected to lie within the interval $[0.5 \times v^{\rm peak}_{\rm FWHM}\,,\, 2 \times v^{\rm peak}_{\rm FWHM}]$, with $v^{\rm peak}_{\rm FWHM}$ being the peak of the distribution, then $v^{\rm peak}_{\rm FWHM}$ is a good choice. If the distribution is broader, it may be advisable to generate two filtered datacube with different $v_{\rm FWHM}$s, thereby essentially creating two catalogues that have later to be merged. For making the above choice it should be kept in mind that intrinsic line width of the objects under scrutiny is always additionally broadened by a convolution with spectrograph's line spread function. Approximating both the emission line and the line spread function with a Gaussian leads to the well known result that the observed line width is given by $\sigma_{\rm obs.} = \sqrt{\sigma^2_{\rm int.} + \sigma^2_{\rm LSF}}$, where $\sigma_{\rm int.}$ is the intrinsic line width and $\sigma_{\rm LSF}$ is the width of the line spread function.

Moreover, it is also possible to use of a published reference catalogue created from a wide-field IFS dataset to determine good $v_{\rm FWHM}$ values. However, this catalogue should not have been created using only the `LSDCat` detection algorithm, as in this case the argument for the optimal $v_{\rm FWHM}$ choice would be circular. A continuum-selected reference catalogue meeting this requirement is provided by Bacon et al. (2015) for the 27h MUSE exposure of the *Hubble* Deep Field South. Exemplarily, we show in Fig. 4.5 the dependence of the ratio $(S/N)/(S/N_{max})$ for all Lyman α line emitters from this catalogue as a function of $v_{\rm FWHM}$. For this experiment the datacube was filtered with the PSF as described in the previous section and then spectrally convolved with a set of Gaussians with different values of $v_{\rm FWHM}$. S/N_{max} denotes the maximum S/N_{peak} of a source over all those filter widths. As can be seen, nearly all emitters reach 90% of their maximum possible detection significance for a filter-width of $v_{\rm FWHM} = 250\,{\rm km\,s^{-1}}$. Hence, this value could define an 'optimal' filter width for Lyman α emission line searches in

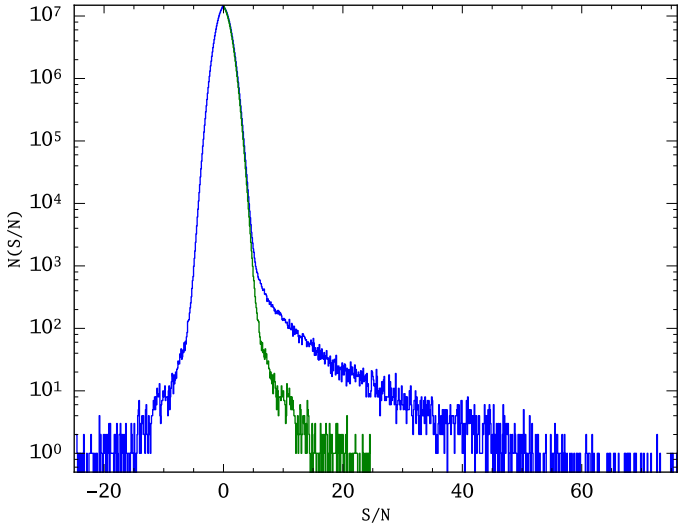

Figure 4.6: Histogram of $S/N_{x,y,z}$ values after matched-filtering a continuum-subtracted MUSE datacube (1h total exposure time). The blue curve shows the actual histogram, while the green curve is an idealised empty field, where the distribution of negative $S/N_{x,y,z}$ values is mirrored on the positive side.

other datacubes of similar spectral resolution. Moreover, it is also apparent that the mean over all $(S/N)/(S/N_{max})$ ratios follow the theoretically predicted trend for matched filtering of an expected Gaussian emission line with $v_{FWHM} = 250\,\mathrm{km\,s^{-1}}$.

4.3.5 On choosing the detection- and analysis thresholds

The voxels $S/N_{x,y,z}$ of the signal-to-noise cube defined in Eq. (4.15) can be interpreted as detection significances for an emission line matching the template at position x, y, z in the datacube. Therefore the false-alarm probability is related to the detection threshold $S/N_{det.}$. Since a wide-field datacube consists of $\sim 10^8$ voxels it is desirable to have very low false alarm probabilities. After matched filtering with typical templates the number of independent voxels reduces by a factor of $\sim 10^2$. Therefore, assuming perfect Gaussian noise, even thresholding for 5σ-detections still would result on average in ~ 10 spurious detections.

However, above interpretation is only valid if the variance datacube $\boldsymbol{\sigma}^2$ is representative of the true variances and if there are no systematic offsets to positive or negative values in $\boldsymbol{F}$. Although we explained in Sect. 4.3.1 a possible method to check and correct for biases in the variance cube, this empirical estimator can not account for systematic non-Gaussian noise or offsets in the datacube. For example, such systematics are frequently found around strong night-sky emission lines in MUSE datacubes, although their amplitude can be significantly reduced by utilising the principle component analysis sky-subtraction algorithm of Soto et al. (2016).

For the outlined reasons we strongly recommend a visual check of the $\boldsymbol{S/N}$ cube before deciding on a detection threshold instead of relying only on theoretical expected false alarm properties. A good choice for a visual checks is the QFitsView tool (Ott 2012). Additionally, an inspection of the $S/N_{x,y,z}$ value distribution is recommended. In Fig. 4.6 we show such a histogram of $S/N_{x,y,z}$ values exemplarily from a real MUSE survey datacube. As can be seen, the distribution is significantly skewed to positive values due to signal from actual objects. Compar-

ing to an idealised empty field distribution, which we generate by mirroring the distribution of negative values to the positive side, the actual tail of object signals becomes apparent at $S/N \geq 5$. However, according to the distribution of the idealised empty field, at this threshold there is still a high contamination of false alarms expected. Contrary, the number of non-object containing voxels above a detection threshold of $S/N_{\mathrm{det.}} = 8$ is reduced to $\lesssim 10^2$. A visual inspection of this particular $\boldsymbol{S/N}$-datacube then revealed, that all those voxels that can be attributed to above mentioned sky-subtraction residuals. Hence, in this particular case, we decided to generate the catalogue of emission lines utilising $S/N_{\mathrm{det.}} = 8$, since no false detections had to be wielded out from the final catalogue.

The choice of the analysis threshold $S/N_{\mathrm{ana.}}$ used in the measurement routine (Sect. 4.2.3) again depends on the noise characteristics and thus should also be motivated by a visual inspection of the detected sources. Consider exemplarily the faint emission line source presented in Fig. 4.2. Comparing the left panel, where no source is present, to the right panel with the source, we find that non-source voxels can obtain S/N-values as high as three. Therefore S/N-values above 3.5 around a source are likely linked to its presence in the datacube. Hence, in this particular datacube an analysis threshold $S/N = 3.5$ appears reasonable.

4.4 Conclusion and outlook

We presented in this paper `LSDCat`, a conceptually simple but robust and efficient detection package for emission lines in wide-field IFS datacubes. The detection utilises a 3D matched-filtering approach for compact single emission line objects. Furthermore, the software measures fluxes and extents of detected lines. `LSDCat` is implemented in Python, with a focus on fast processing of the large data-volumes of typical wide-field IFS datacubes. The software package is available for download. In this paper we also provided some instructive guidelines for optimal usage of `LSDCat`.

The fast execution speed of `LSDCat` is of great advantage when working with a large set of datacubes or when performing selection function estimates using fake-source experiments. However, there are still areas where we see room for future improvements. Currently, `LSDCat` does not perform a deblending of merged detections, nor does it merge close by detections belonging to a single source. Indeed, in our searches for faint emission lines in MUSE datacubes we encountered a few cases of extended line emitting galaxies that fragmented into several sources. We aim at addressing this problem in a future version, employing a similar scheme as implemented by Bertin & Arnouts (1996) in `SExtractor`. Currently these sources have to be merged or deblended manually in the resulting output catalogue. Another improvement planned for a future release is an automatic object classification for objects where multiple lines are detected. To this aim the combination of spectral lines found at the same position on the sky must match a known combination of redshifted galaxy emission line peaks (Garilli et al. 2010). Nevertheless, despite these missing features `LSDCat` can be regarded as a complete software package and we hope that it will be of value to the community.

Acknowledgments: We thank Maria Werhahn for valuable help with the parameter study shown in Fig. 4.5 and Joseph Caruana for providing us with curve-of-growth flux integrations of 60 Lyα emitters shown in Fig. 4.3. We also thank the MUSE-consortium lead by Roland Bacon for constructive feedback during the `LSDCat` development. Moreover, this chapter is dedicated to *Cosmos*, my friends' cute fat cat.

4.5 Bibliography

Allington-Smith, J. 2006, New A Rev., 50, 244

Annunziatella, M., Mercurio, A., Brescia, M., Cavuoti, S., & Longo, G. 2013, PASP, 125, 68

Astropy Collaboration, Robitaille, T. P., Tollerud, E. J., et al. 2013, A&A, 558, A33

Bacon, R., Brinchmann, J., Richard, J., et al. 2015, A&A, 575, A75

Bacon, R., Vernet, J., Borisiva, E., et al. 2014, The Messenger, 157, 13

Bertin, E. 2001, in Mining the Sky, ed. A. J. Banday, S. Zaroubi, & M. Bartelmann, 353

Bertin, E. & Arnouts, S. 1996, A&AS, 117, 393

Bina, D., Pelló, R., Richard, J., et al. 2016, A&A, 590, A14

Bourguignon, S., Mary, D., & Éric Slezak. 2012, Statistical Methodology, 9, 32 , special Issue on Astrostatistics + Special Issue on Spatial Statistics

Das, P. K. 1991, Optical Signal Processing (Springer Science + Business Media)

Filippenko, A. V. 1982, PASP, 94, 715

Garilli, B., Fumana, M., Franzetti, P., et al. 2010, PASP, 122, 827

Graham, A. W. & Driver, S. P. 2005, PASA, 22, 118

Greisen, E. W. & Calabretta, M. R. 2002, A&A, 395, 1061

Greisen, E. W., Calabretta, M. R., Valdes, F. G., & Allen, S. L. 2006, A&A, 446, 747

Hickson, P. 2014, A&A Rev., 22, 76

Hong, S., Dey, A., & Prescott, M. K. M. 2014, PASP, 126, 1048

Husser, T.-O., Kamann, S., Dreizler, S., et al. 2016, A&A, 588, A148

Jones, E., Oliphant, T., Peterson, P., et al. 2001, SciPy: Open source scientific tools for Python, [Online; accessed 2016-01-15]

Jurek, R. 2012, PASA, 29, 251

Kamann, S., Wisotzki, L., & Roth, M. M. 2013, A&A, 549, A71

Kelz, A., Kamann, S., Urrutia, T., et al. 2015

Koribalski, B. S. 2012, PASA, 29, 359

Kron, R. G. 1980, ApJS, 43, 305

Martin, C., Moore, A., Morrissey, P., et al. 2010, in Society of Photo-Optical Instrumentation Engineers (SPIE) Conference Series, Vol. 7735, Society of Photo-Optical Instrumentation Engineers (SPIE) Conference Series, 0

Masias, M., Freixenet, J., Lladó, X., & Peracaula, M. 2012, MNRAS, 422, 1674

Meillier, C., Chatelain, F., Michel, O., et al. 2016, A&A, 588, A140

Moffat, A. F. J. 1969, A&A, 3, 455

Ott, T. 2012, QFitsView: FITS file viewer, astrophysics Source Code Library

Pence, W. D., Chiappetti, L., Page, C. G., Shaw, R. A., & Stobie, E. 2010, A&A, 524, A42

Popping, A., Jurek, R., Westmeier, T., et al. 2012, PASA, 29, 318

Saintonge, A. 2007, AJ, 133, 2087

Schwartz, M. & Shaw, L. 1975, Signal processing: discrete spectral analysis, detection, and estimation (Tokyo: McGraw-Hill Kogakusha, Ltd.)

Serra, P., Jurek, R., & Flöer, L. 2012, PASA, 29, 296

Serra, P., Westmeier, T., Giese, N., et al. 2015, MNRAS, 448, 1922

Shore, S. N. 2009, A&A, 500, 491

Soto, K. T., Lilly, S. J., Bacon, R., Richard, J., & Conseil, S. 2016, MNRAS, 458, 3210

Streicher, O., Weilbacher, P. M., Bacon, R., & Jarno, A. 2011, in Astronomical Society of the Pacific Conference Series, Vol. 442, Astronomical Data Analysis Software and Systems XX, ed. I. N. Evans, A. Accomazzi, D. J. Mink, & A. H. Rots, 257

Tokovinin, A. 2002, PASP, 114, 1156

Trujillo, I., Aguerri, J. A. L., Cepa, J., & Gutiérrez, C. M. 2001a, MNRAS, 321, 269

Trujillo, I., Aguerri, J. A. L., Cepa, J., & Gutiérrez, C. M. 2001b, MNRAS, 328, 977

Turner, J. E. 2010, Canary Islands Winter School of Astrophysics, Vol. XVII, 3D Spectroscopy in Astronomy, ed. E. Mediavilla, S. Arribas, M. Roth, J. Cepa-Nogue, & F. Sanchez (Cambridge University Press), 87–125

van der Walt, S., Colbert, S. C., & Varoquaux, G. 2011, Computing in Science & Engineering, 13, 22

Vio, R. & Andreani, P. 2016, A&A, 589, A20

Wall, J. V. 1979, QJRAS, 20, 138

Weilbacher, P. M., Streicher, O., Urrutia, T., et al. 2012, in Society of Photo-Optical Instrumentation Engineers (SPIE) Conference Series, Vol. 8451, Society of Photo-Optical Instrumentation Engineers (SPIE) Conference Series, 84510B

Weilbacher, P. M., Streicher, O., Urrutia, T., et al. 2014, in Astronomical Society of the Pacific Conference Series, Vol. 485, Astronomical Data Analysis Software and Systems XXIII, ed. N. Manset & P. Forshay, 451

Whiting, M. T. 2012, MNRAS, 421, 3242

Yamada, T., Matsuda, Y., Kousai, K., et al. 2012, ApJ, 751, 29

Zackay, B. & Ofek, E. O. 2015, ArXiv e-prints

Chapter 5

A catalogue of emission line selected galaxies in the MUSE-Wide survey

Abstract: Using the integral-field spectrograph MUSE on ESO's Very Large Telescope we are conducting a blind spectroscopic survey named MUSE-Wide. When completed, MUSE-Wide will have covered a total area of $\sim 100\,\mathrm{arcmin}^2$ with 1 hour exposures for each 1 arcmin^2 MUSE pointing at locations in the CANDELS/Deep region of the *Chandra* Deep Field South (CDF-S) and in the CANDELS COSMOS field. As a first result we here provide a catalogue of 831 emission line selected galaxies from a 22.2 arcmin^2 region in the CDF-S using a dedicated line source detection software. For the classification of the detected emission lines we follow a semi-automatic approach: galaxies detected with multiple emission lines are automatically classified, single line detections are classified by visual inspection. Our sample includes 237 Lyman α emitting galaxies in the redshift range $3 \lesssim z \lesssim 6$, of which spectroscopic redshifts existed only for four previously in the literature. At lower redshifts 351 galaxies are detected primarily by their [O II] emission line ($0.3 \lesssim z \lesssim 1.5$), 189 by their [O III] line ($0.21 \lesssim z \lesssim 0.85$), and 46 by their H$\alpha$ line ($0.04 \lesssim z \lesssim 0.42$). Comparing the spectroscopically determined redshifts to photometrically determined redshifts by the 3D-HST survey, we find a systematic difference of $\Delta z \sim 0.1 \ldots 0.2$ for the $z > 3$ Lymanα emitting galaxies.

5.1 Introduction

The new large wide-field integral field spectrograph MUSE (Multi Unit Spectroscopic Explorer, Bacon et al. 2004, 2006, 2009, 2010, 2014) at the ESO Very Large Telescope is a powerful instrument for discovering and characterising high-redshift galaxies, even beyond the reach of current deep imaging surveys. Recently its discovery potential was strikingly demonstrated in a 27 hour integration on the *Hubble* Deep Field South (HDF-S, Bacon et al. 2015). Remarkably, the analysis of this dataset revealed 26 Lyman α emitting galaxies (LAEs) for which not even a stacking of deep HST imaging data showed any detectable signal. Multi-slit spectroscopic surveys target objects based on deep-field photometric pre-selection (e.g. Noll et al. 2004; Le Fèvre et al. 2005; Vanzella et al. 2006, 2008; Popesso et al. 2009; Balestra et al. 2010; Mallery

This chapter is a draft version of a paper to be submitted to a journal with E.C.H as first author. The work presented contains contributions by Lutz Wisotzki (Project PI, ESO proposals, emission line classification), Josephine Kerutt (PSF determination, emission line classification, Lyα emitter redshift measurements, qtClassify programming), Tanya Urrutia (data reduction, emission line classification), and Maria Werhahn (redshift measurements).

et al. 2012; Le Fèvre et al. 2013, 2015; Tasca et al. 2016), and therefore missed this population of continuum-faint, except when such sources serendipitously fall on the spectroscopic slit centred on a continuum selected primary target (Cassata et al. 2011; Le Fèvre et al. 2013). On the other hand building a spectroscopic sample over a contiguous area on the sky without any photometric pre-selection is a task perfectly suited for integral field spectroscopy (van Breukelen et al. 2005; Adams et al. 2011; Blanc et al. 2011). MUSE, because of its $1'\times1'$ field of view (FoV), its high spatial resolution ($0.2''\times0.2''$ per spatial pixel), and its wide simultaneous spectral range (4750Å – 9300Å) resolved at a relatively high spectral resolution ($R \simeq 3000$) is a unique instrument for such blind integral field spectroscopic surveys.

As part of the MUSE Guaranteed Time Observations we have started to perform such a "spectroscopic survey of everything" in the CANDELS fields for which the deepest space- and ground-based panchromatic datasets are publicly available (Grogin et al. 2011; Koekemoer et al. 2011). Similar to the CANDELS survey our strategy follows a three-tiered "wedding cake" approach: A wide-field but relatively shallow programme that yields robust statistics for relatively bright but rarer targets, a small area deep programme that uncovers numerous faint targets, and an ultra-deep pencil-beam programme that pushes the sensitivity to the faintest flux levels reachable with the current class of 10m telescopes.

In the present manuscript we detail an analysis of a first batch of data-products obtained for the wide-field component of our survey, baptised MUSE-Wide. In particular we provide a catalogue of 831 galaxies selected on basis of their emission lines in a 22.2 arcmin^2 region in the CANDELS/Deep region in the GOODS-South. When completed the MUSE-Wide survey will have covered a total area of $\sim$100 arcmin^2 at one hour depth in the CDFS and CANDELS COSMOS regions.

The main science driver for MUSE-Wide is the accumulation of a substantial sample of $\sim$ 1000 relatively bright LAEs that have deep complementary multi-wavelength data to allow detailed and statistically robust studies of their physical properties. In addition, our spectroscopic survey of everything approach in the well studied CANDELS/Deep and CANDELS/COSMOS fields has also an immense legacy value. We plan to provide a first release of the full MUSE-Wide dataset to the public in a subsequent publication (Urrutia et al., in prep.).

The structure of this paper is as follows: In Sect. 5.2 we outline how we obtained and reduced the observational dataset that is the foundation of the presented catalogue. We then describe in Sect. 5.3 how we detect, parameterise and classify emission line sources in our datacubes. In the following Sects. 5.4 we detail the redshift determination of the detected emission line galaxies. In this section we also provide a comparison with existing photometric and spectroscopic redshifts. Finally, we present our source catalogue in Sect. 5.5. We conclude with an outlook of future results from MUSE-Wide in Sect. 5.6.

5.2 Observations and data reduction

Our current dataset is based on the analysis of 24 adjacent $1'\times1'$ MUSE pointings in the CANDELS/Deep region in the GOODS-South field (Grogin et al. 2011; Koekemoer et al. 2011). In Fig. 5.1 we show a footprint of the survey area and in Table 5.1 we provide a log of our observations. We integrated 1 hour on each pointing. The integration was split into 4 exposure of 15 minutes. In between exposures small dither offsets were applied and the spectrograph was rotated by 90 degrees. With the exception of pointing 08 all exposures for a pointing where obtained in immediate succession. Pointing 08 was split into two exposure sequences in two subsequent nights. The seeing values in Table 5.1 are the average values of the VLT autoguider

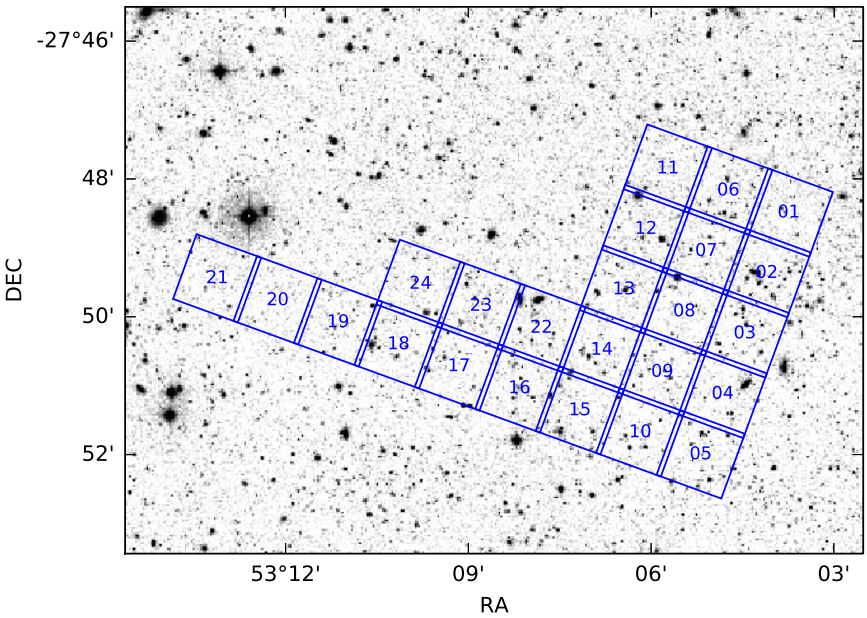

Figure 5.1: Footprint of the first 24 1′×1′ pointings of the MUSE-Wide survey in the CANDELS Deep region of GOODS-South (overlaid over R-Band Image from GaBoDS – Erben et al. 2005; Hildebrandt et al. 2006).

Table 5.1: Log of Observations

Pointing	Pointing centre		Date	AG Seeing	Air-	Conditions
	α_{J2000}	δ_{J2000}		["]	mass	
CDFS-01	$03^h32^m15.04^s$	-27°48′29.4″	2014-10-20	0.86	1.087	phot.
CDFS-02	$03^h32^m16.48^s$	-27°49′21.5″	2014-09-20	1.05	1.076	clear
CDFS-03	$03^h32^m17.80^s$	-27°50′13.6″	2014-11-17	0.93	1.061	clear
CDFS-04	$03^h32^m19.67^s$	-27°51′07.1″	2014-11-17	0.76	1.041	clear
CDFS-05	$03^h32^m20.70^s$	-27°51′59.8″	2014-11-19	1.03	1.017	clear
CDFS-06	$03^h32^m18.91^s$	-27°48′10.7″	2014-11-18	0.84	1.021	clear
CDFS-07	$03^h32^m20.36^s$	-27°49′02.6″	2014-11-19	0.92	1.026	phot.
CDFS-08	$03^h32^m21.89^s$	-27°49′55.3″	2014-11-19+20	1.00	1.034	phot.
CDFS-09	$03^h32^m23.25^s$	-27°50′47.9″	2014-11-26	0.87	1.044	phot.
CDFS-10	$03^h32^m24.68^s$	-27°51′40.8″	2014-11-27	0.90	1.071	phot.
CDFS-11	$03^h32^m22.91^s$	-27°47′50.9″	2014-11-28	0.95	1.104	phot.
CDFS-12	$03^h32^m24.35^s$	-27°48′43.2″	2014-11-27	1.02	1.144	phot.
CDFS-13	$03^h32^m25.88^s$	-27°49′36.2″	2014-11-27	1.07	1.193	phot.
CDFS-14	$03^h32^m27.21^s$	-27°50′28.9″	2014-11-28	0.88	1.229	phot.
CDFS-15	$03^h32^m28.66^s$	-27°51′21.5″	2014-12-25	0.83	1.241	phot.
CDFS-16	$03^h32^m32.62^s$	-27°51′02.1″	2014-11-28	0.83	1.228	phot.
CDFS-17	$03^h32^m36.60^s$	-27°50′43.8″	2014-12-23	0.80	1.191	clear.
CDFS-18	$03^h32^m40.58^s$	-27°50′24.3″	2014-12-21	0.89	1.191	phot.
CDFS-19	$03^h32^m44.60^s$	-27°50′04.6″	2014-12-21	0.82	1.223	phot.
CDFS-20	$03^h32^m48.61^s$	-27°49′46.0″	2014-12-23	0.82	1.288	clear
CDFS-21	$03^h32^m52.54^s$	-27°49′26.1″	2014-12-23	0.72	1.388	clear
CDFS-22	$03^h32^m31.19^s$	-27°50′09.8″	2014-12-22	0.79	1.338	clear
CDFS-23	$03^h32^m35.23^s$	-27°49′50.3″	2014-12-24	0.86	1.266	phot.
CDFS-24	$03^h32^m39.14^s$	-27°49′31.5″	2014-12-26	0.81	1.168	phot.

seeing over all four exposures, and the airmass in Table 5.1 similarly refers to the average over all four exposures.

Adjacent pointings have an overlap by 4″. Taking this overlap and the exact geometry of the MUSE field of view into account, the total area exposed with MUSE is 22.2 arcmin^2. We matched the position angle of our pointings to the 70° position angle (east of north) of the CANDELS/Deep region.

For the reduction of the individual pointings we used version 1.0 of the MUSE data reduction system[1] (Weilbacher et al. 2006, 2012, 2014, and in prep.), in combination with custom developed `python`[2] routines and the ZAP tool of Soto et al. (2016). An in-depth description and validation of the data reduction procedure will be given in the publication complementing the full data release (Urrutia et al., in prep.), in the following we only provide a brief overview.

We used the set of calibration exposures taken close in time to the actual observations to create master biases, master flats, dispersion solutions, and trace tables. Using standard-star exposures taken at the beginning and at the end of each night we constructed response curves for flux-calibration. Then we applied these calibration products to all 24 CCD images belonging to one science exposure. The result of this process is a so-called pixel table that contains all calibrated CCD flux values, errors, wavelengths, and information on their location on the sky. It is known that the current version of the MUSE pipeline sky-subtraction routine (Streicher et al. 2011) leaves significant systematic residuals behind that hamper the detection of faint object signals (Soto et al. 2016). For this reason we developed our own sky-subtraction routine that work on the pixel tables[3]. Our method exploits the similarity of the spectrographs line-spread function over all 24 detectors within a so called spectral-slice. Therefore we can create a master per-slice sky spectrum for each of the 48 slices by averaging over the same slice on all 24 detectors with aggressive sigma-clipping and masking of heavily object-contaminated regions. This master per-slice sky spectrum is then scaled to the corresponding slice on each detector before being subtracted. Finally, we apply the self-calibration method described in Sect. 3.1 of Bacon et al. (2015) to remove systematic mean zero-flux level offsets between slices. For each exposure then the pipeline routine `MUSE_SCIPOST` resamples the sky-subtracted and self-calibrated pixel tables into a datacube and propagates the errors into a corresponding variance datacube. These datacubes are stored in multiple header-data-units within a FITS file (Pence et al. 2010). The datacubes are corrected for differential atmospheric refraction using the formula by Filippenko (1982). Remaining sky-subtraction residuals were then purged from the cubes using the ZAP-software of Soto et al. (2016). We then create white-light images from the datacubes by summation over the spectral axis. These images are used to determine the reference registration to the CANDELS HST astrometry by 2D Gaussian fits to compact objects (compact galaxies, or stars when available). Lastly, by averaging the four exposure cubes with rejection of 3σ outliers we created the final flux datacube for each each pointing.

Each of the 24 flux datacubes contains 3.5×10^8 exposed volume-pixels (so called voxels) and is ~3GB on disk. The spatial sampling of these cubes is $0.2''\times0.2''$, the spectral sampling is 1.25Å, and the wavelength range extends from 4750Å to 9350Å. The wavelength axis is given in air wavelengths in the barycentric reference frame. For each cube the astrometry is such that the east-west and south-north axes are parallel to the spatial coordinate axes. Complementary to the flux datacubes we produced a final variance datacube by propagating the individual variance

[1] Available from ESO via `http://www.eso.org/sci/software/pipelines/muse/muse-pipe-recipes.html`.

[2] `http://www.python.org`

[3] The `Python`-routines of our sky-subtraction procedure: "YASSA" (Yet Another Sky Subtraction Approach) are available on request.

values. We also created exposure-map cubes, where we track the number of individual single exposures that went into a voxel of the final datacube.

5.3 Emission line source detection and classification

5.3.1 Detection and parameterisation

After having reduced the observational dataset we were equipped with 24 flux-calibrated datacubes, corresponding variance cubes, and exposure map cubes. We then performed the following tasks to build a catalogue of emission line source candidates:

1. Empirical estimation and correction of the pipeline propagated variance cubes.
2. Removal of continuum bright sources from the datacube.
3. Cross-correlation of the datacube with a 3D matched filter for compact emission line sources.
4. Thresholding and cataloguing of emission line source candidates.
5. Position, size, and flux measurements of the emission line source candidates.

These tasks are applied to each datacube. For the tasks 3 to 5 we have developed the emission line source detection and cataloguing tool `LSDCat`. For an in-depth description of `LSDCat` we refer to Chapter 4. In the following subsections we describe the above tasks and our application of the `LSDCat` routines on our MUSE-Wide dataset.

5.3.1.1 Empirical estimation and correction of the pipeline propagated noise cubes

Source detection in astronomical datasets is essentially a decision process utilising a test statistic to reject or accept features in the data as genuine source signals (e.g. Wall 1979; Masias et al. 2012; Vio & Andreani 2016). As we outline below, we detect emission lines in matched-filter transformed datacubes via thresholding in signal-to-noise (S/N). Therefore we require an accurate characterisation of the noise of our datacubes. In the resampling process carried out by the MUSE pipeline co-variance terms are neglected. This means that the variance cubes provided by the MUSE pipeline are likely to underestimate the true variance.

In order to quantify this deviation from the pipeline propagated variance we determine an empirical variance estimate from the datacubes. For this we place 100 circular apertures of five pixel radius (2″ diameter) at random positions within each pointing. Using the CANDELS GOODS-S photometric catalogue by Guo et al. (2013) we ensure that our apertures sample blank sky by requiring no overlap with sources having $m_{F814} < 25\,\mathrm{mag}$. The width of the distribution of flux values in those apertures, characterised by its standard deviation, can be used as an estimate of the noise for each spectral layer. This method is similar to the estimation of background noise in wide-field imaging surveys (e.g. Furusawa et al. 2008; Matthee et al. 2015). Since we are limited by a relatively small number of apertures that can be placed within the 1′×1′ MUSE FoV, we obtain a robust estimate of the width of the distribution for each layer via $\sigma_{\mathrm{emp.}} = (q_{75} - q_{25})/(2\sqrt{2}\mathrm{erf}^{-1}(1/2)) \approx 0.7413\,(q_{75} - q_{25})$, where erf^{-1} is the inverse error function and $q_{75} - q_{25}$ is the interquartile range of the distribution (e.g., Sect. 3.2.2 in Ivezić et al. 2014). We now compare the so obtained empirical noise values $\sigma^2_{\mathrm{emp.}}$ to the an average value of the pipeline propagated variance in each layer – this process is illustrated in Fig. 5.2.

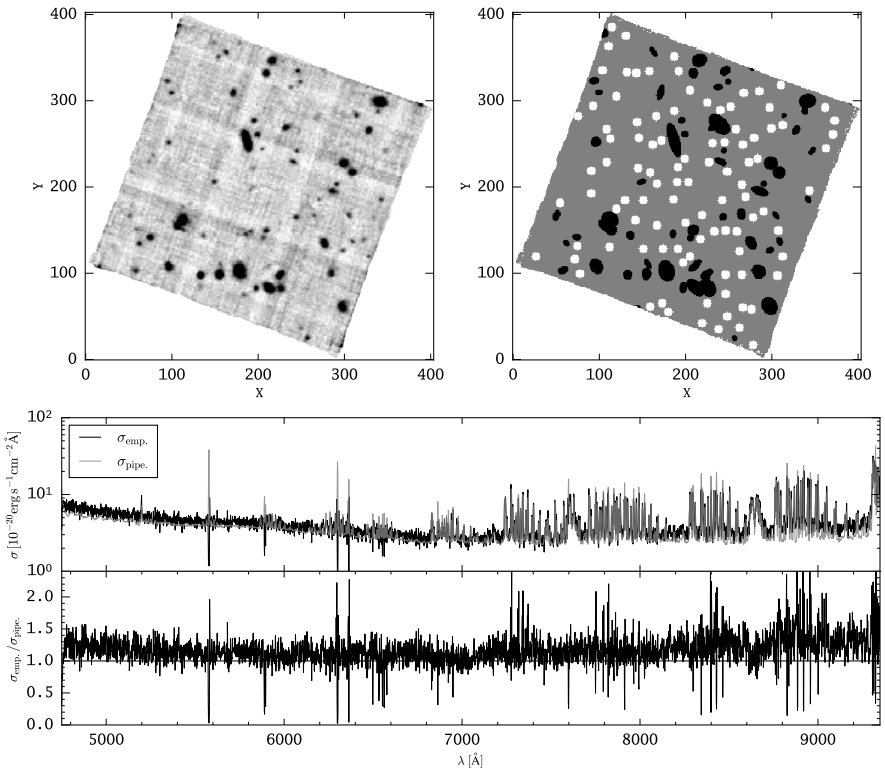

Figure 5.2: Empirical noise calculation procedure, exemplarily shown in the MUSE-Wide pointing CDFS-08. The *top left panel* shows a white-light image created by summation over all spectral layers in the datacube. In the *top right panel* we show the 100 random 2″ diameter apertures (white) and the avoided regions (black) because of the presence of continuum bright objects (sources with $m_{F814} < 25$ mag in Guo et al. 2013). In the *bottom panels* we compare the width of the distribution of the flux values extracted in the 100 apertures for each spectral layer $\sigma_{\rm emp.}$ normalised to one spectral pixel to the corresponding average value from the pipeline produced variance cube $\sigma_{\rm pipe.}$.

As can be seen in the bottom panel of Fig. 5.2 the ratio $\sigma_{\rm emp.}/\sigma_{\rm pipe}$ is greater than one in almost all datacube layers. For all cubes we find typically $\sigma_{\rm emp.} = 1.15 \ldots 1.20\,\sigma_{\rm pipe.}$. These finding is consistent with an empirical noise estimate made in MUSE datacubes obtained with a similar observing strategy (Borisova et al., in prep.). However, as can be also seen in Fig. 5.2 there is a small number of layers where the ratio $\sigma_{\rm emp.}/\sigma_{\rm pipe}$ is smaller than one. The affected layers are typically in the cores of telluric emission lines, and we attribute the low empirical variance to an over-subtraction of the high-frequency noise in this layer by the ZAP routine.

In order to correct the by the pipeline propagated variance underestimated noise, we replaced the values in the variance cubes with our empirical noise estimate $\sigma^2_{\rm emp.}$. In layers where $\sigma_{\rm emp.}/\sigma_{\rm pipe} < 1$ we use the average value from the pipeline. Moreover, we take the exposure map cubes in our replacement procedure into account by rescaling the replaced variance values with $4/N_{\rm exp.}$ in all voxels that have less than $N_{\rm exp.} = 4$ exposures contributing to them (these voxels are mostly on the border of the FoV).

There are two caveats in our empirical noise estimation. First, due to the small number of apertures our noise estimate is itself noisy. This can be seen when comparing the smooth

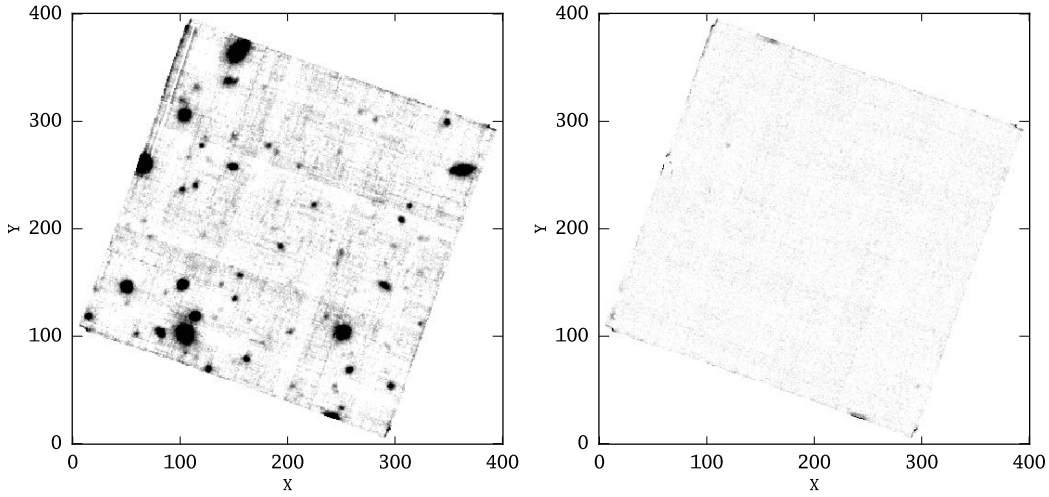

Figure 5.3: Example demonstrating the effectiveness of subtracting an in spectral direction median filtered version of the datacube to remove signal from bright continuum sources. *Left*: White-light image created by summation over all spectral layers in the MUSE-Wide pointing CDFS-15. *Right*: White-light image of the median filter subtracted version of the same cube.

$\sigma_{\text{pipe.}}$-curve to the noisier $\sigma_{\text{emp.}}$-curve in Fig. 5.2. Second, our estimate does not take correlated noise in the spectral direction into account. We plan to adress these issues in more detail when providing the first release of the MUSE-Wide data (Urrutia et al. in prep.).

5.3.1.2 Removal of continuum bright sources

We removed signal from continuum-bright sources in each datacube by subtracting an in spectral direction median-filtered version of the datacube. The width of the median-filter was chosen to be 151 spectral layers (188.75Å), much broader than the width of the expected emission lines and narrow enough to robustly subtract a slowly varying continuum. The remaining residuals in the datacube are either real emission lines or features from rapidly varying continua (e.g. cold stars). We demonstrate the effectiveness of our median-filter subtraction method in Fig. 5.3 for an example pointing.

5.3.1.3 Cross-correlation with matched filter

The detection algorithm of `LSDCat` is based on matched filtering (e.g. Schwartz & Shaw 1975; Das 1991; Bertin 2001; Zackay & Ofek 2015; Vio & Andreani 2016). The 3D matched filter employed is a 3D Gaussian tailored to the detection of compact emission line sources. Spatially this filter approximates the seeing-induced point-spread function. Spectrally, the filter is an adequate model for the emission lines of unresolved distant galaxies where often no spatial disentanglement between ordered motions and unordered motions is possible. By cross-correlating the datacube with this filter the S/N ratio of faint compact emission lines within the datacube is maximised.

The spatial width of this filter was taken as the wavelength-dependent full width at half-maximum (FWHM) of the seeing induced point-spread function. The input-parameters for `LSDCat` describing this width and its wavelength dependence are the coefficients p_0, p_1, and p_2 of the polynomial function $\text{FWHM}(\lambda)[''] = p_0 + p_1(\lambda - 7000\text{Å}) + p_2(\lambda - 7000\text{Å})^2$. In

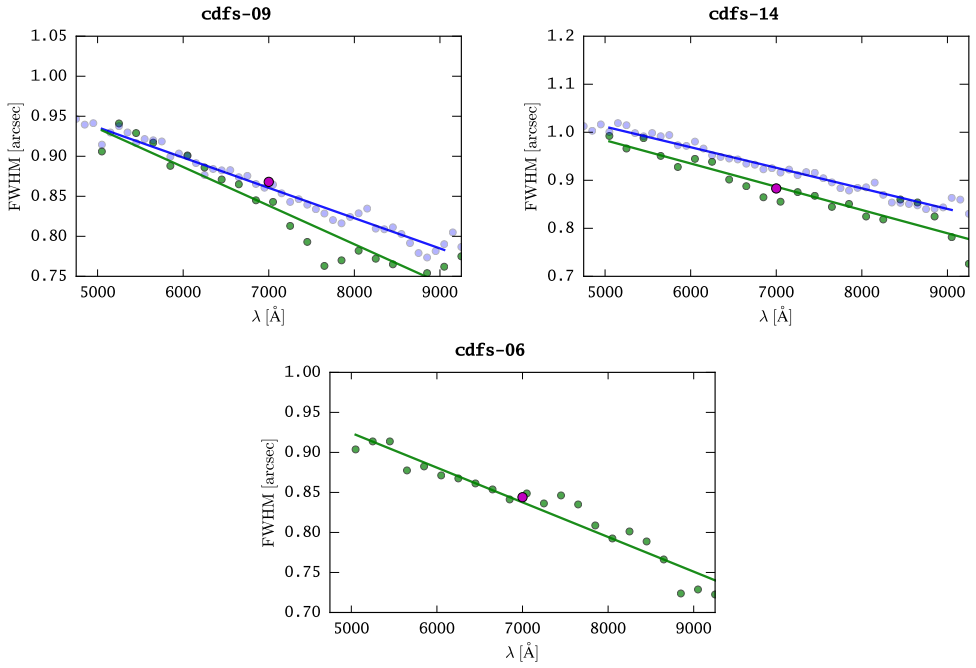

Figure 5.4: Examples for the determination of the wavelength dependence of the seeing PSF FWHM in three MUSE-Wide pointings (CDFS-06, CDFS-09, and CDFS-14). *Blue points* show the FWHM values obtained from fitting a 2D Gaussian to images of a star within the datacube. The used images are created by summing over 100 Å along the spectral axis. *Green points* show the results from minimising the χ^2 difference between MUSE images of several compact galaxies within a pointing to 2D Gaussian-convolved and to MUSE resolution resampled HST images of those galaxies. For each image the FWHM of the 2D Gaussian kernel minimising χ^2 is displayed. Here the used images are created by summing over 200 Å along the spectral axis. The green and the blue lines are the linear fits $\mathrm{FWHM}(\lambda) = p_0 + p_1(\lambda - 7000\,\text{Å})$ to the individual data points of the FWHM determination using a star or several compact galaxies, respectively. The purple point at 7000 Å is the value inferred from the VLT auto guider probe. In CDFS-06 no sufficiently bright star was available, but in CDFS-09 and CDFS-14 there was. However, in CDFS-14 the linear fit to the FWHM values derived using the compact galaxies is closer to the auto guider value, so that here these coefficients where chosen as input parameters for `LSDCat`.

principle, the determination of the coefficients can be achieved by fitting a 2D Gaussian function to a reasonably bright star in each spectral layer of the datacube. However, by choice the CANDELS fields are devoid of bright stars. Selecting objects from the Guo et al. (2013) CANDELS GOODS-S photometric catalogue with `CLASS_STAR` > 0.95 results for numerous of our pointings only in objects with $m_{F814} > 23$ mag. Even when binning 100 spectral layers of the datacube, the S/N-ratio of these stars was not sufficient for a reliable 2D Gaussian fit. However, for stars brighter than $m_{F814} \lesssim 22$ mag such fits converged. Because of the binning and the relatively low S/N of the stars we then fitted the so determined FWHM values only with a linear function (i.e. setting $p_2 \equiv 0$) to infer p_0 and p_1. Complementary to this direct point-source fit we also employed a minimisation scheme utilising compact galaxies. For this we visually selected compact galaxies within the FoV of a pointing from the CANDELS F814W image. We then convolved these galaxies with 2D Gaussians of different FWHMs and resampled these convolved images to the spatial resolution of MUSE. In a series of $\sim 100 - 200$ binned layers we then

Table 5.2: Coefficients p_0 and p_1 of FWHM(λ) = p_0 + $p_1(\lambda - 7000\,\text{Å})$ used as input parameters in `LSDCat` for the datacubes corresponding to the 24 pointings.

Pointing No.	p_0 [″]	p_1 [10^{-5} ″/Å]	Method
01	0.836	-4.429	fit to 10548, 22.18
02	0.940	-3.182	compact galaxies, no star
03	0.944	-4.460	fit to 8374, 19.39
04	0.747	-4.219	compact galaxies, no star
05	1.026	-3.003	compact galaxies, no star
06	0.835	-4.332	compact galaxies, no star
07	0.935	-3.966	compact galaxies, no star
08	0.991	-5.007	compact galaxies, closer to AG
09	0.833	-8.069	fit to 68879, 19.73
10	0.890	-3.051	compact galaxies, closer to AG
11	0.989	-3.771	compact galaxies, closer to AG
12	1.020	-4.123	compact galaxies, no star
13	1.063	-5.285	compact galaxies, closer to AG
14	0.884	-4.844	compact galaxies, closer to AG
15	0.702	-4.441	fit to 5744, 20.3
16	0.859	-3.784	fit to 6475, 18.86
17	0.780	-3.534	compact galaxies, closer to AG
18	0.929	-3.479	compact galaxies, no star
19	0.814	-3.524	compact galaxies, no star
20	0.713	-5.196	compact galaxies, no star
21	0.836	-4.255	fit to 9801, 21.92
22	0.788	-3.253	fit to 7813, 20.23
23	0.777	-3.019	compact galaxies, no star
24	0.728	-4.232	compact galaxies, no star

The ID and the F814 magnitude from the Guo et al. (2013) catalogue are given in the method column if the coefficients were derived using a star within the pointing. We indicate with "compact galaxies, closer to AG" in the method column, when the minimisation utilising compact galaxies provided a p_0 value closer to the AG Seeing and we therefore used p_0 and p_1 from this method. We remark with "compact galaxies, no star" when no sufficiently bright star was present within the datacube, and we had to rely on the minimisation scheme utilising compact galaxies.

determined the χ^2 of the differences between the convolved and resampled images to the real data. Finally, we fitted the so determined sequence of FWHM values at different wavelengths with a linear function to obtain p_0 and p_1. Obviously this method does not rely on the presence of stars in the field. For pointings that have a star in the field both methods agreed within 10% on the derived FWHM(λ) dependence. We adopted as the final input parameters for `LSDCat` the set of coefficients from the method where p_0 was closest to the measured auto guider seeing. In Fig. 5.4 we show three examples of the FWHM(λ) determination procedure outlined above

and in Table 5.2 we list the p_0 and p_1 values that we used as input for the matched filtering in LSDCat.

The width in spectral direction needs to be specified in LSDCat as the velocity FWHM – v_{FWHM} – in $\mathrm{km\,s^{-1}}$. We fixed this parameter in our emission line search to $v_{\mathrm{FWHM}} = 250\,\mathrm{km\,s^{-1}}$ as the best single value for achieving the highest S/N for LAEs by using the reference catalogue of emission line selected galaxies in the MUSE observations of the HDF-S (Bacon et al. 2015). For this we cross-correlated the MUSE HDF-S datacube with a set of different v_{FWHM} widths. The subsequent analysis of the resulting S/N-ratio distributions as a function of v_{FWHM} widths reveals, that all except one of the 89 LAEs in the Bacon et al. (2015) catalogue reach 90 % of their maximum possible S/N when $v_{\mathrm{FWHM}} = 250\,\mathrm{km\,s^{-1}}$ is used. This value is also consistent with the expectations from the distributions of LAE FWHMs in the literature that peak around $250\,\mathrm{km\,s^{-1}}$ (Dawson et al. 2007; Mallery et al. 2012).

Being equipped with a set of carefully vetted parameters for the cross-correlation with the matched filter, we then applied the relevant LSDCat-tasks (Chapter 4). These tasks also propagate our empirically estimated variances accordingly (Sect. 5.3.1.1). As a result we obtained 24 new datacubes that contained in each voxel the detection significance of an emission line being present at this position in terms of S/N.

5.3.1.4 Thresholding and cataloguing of emission line source candidates

LSDCat collects emission line candidates by thresholding the S/N-cubes from the matched-filtering procedure. This means that we created a binary datacube with voxels set to one if they are above a certain threshold $\mathrm{S/N_{thresh}}$, or set to zero otherwise. Connected regions of non-zero neighbouring voxels in this binary cube formed the detection clusters. LSDCat collects these detection clusters in form of a catalogue containing their peak S/N value, the 3D coordinate of the peak, and the numbers of voxels constituting the detection cluster.

In theory, i.e. for perfect data without artifacts, the voxel values of the matched-filter processed cubes are directly related to the probability of rejecting the null hypothesis of no source signal being present at a voxel position (Vio & Andreani 2016). Under thisassumption the choice of $\mathrm{S/N_{thresh}}$ can directly be related to the number of expected false detections in a datacube. From this an optimal threshold can be motivated that minimises the number of false detections while maximising the number of sources in the catalogue. In practice, however, we have to face the difficulties of possible unknown systematics in the data and the limitations of our empirical noise estimate (Sect. 5.3.1.1). As we describe in Sect. 5.3.2, our source classification scheme is semi-automatic, requiring visual inspection of most sources. This requires a low ratio of spurious to real detections.

By experimenting we found that the number of unclassifiable sources increased rapidly when we lowered S/N threshold below eight. Hence, we chose this value for the present analysis. This resulted in a total of 2603 line detections over all 24 fields in our intermediate catalogue. We describe how we classified these line detections into sources below in Sect. 5.3.2. From this classification we found that only 74 of the line detections were spurious detections or resulting from systematics in the data (e.g. from strong telluric residuals or the edges of the FoV). Hence, the fraction of real to spurious detections is 3%. Further 636 of detections were associated with high-frequency residuals from continuum bright objects (24% of all detections).

5.3.1.5 Position, extent, and flux measurements

LSDCat also determines positions, extents, and fluxes of the detected emission lines. The algorithms for this are explained in detail in Chapter 5. For the positions we use primarily first

central moments which are determined in a smoothed pseudo narrow band image. The bandwidth of this image is given by the spectral coordinates of voxels that are above a certain analysis threshold $S/N_{ana.}$. After visual inspection of the line profiles, we found that setting $S/N_{ana.} = 3$ delivers a band that is optimally suited for almost all objects. However, since `LSDCat` currently does not offer an algorithm to deblend emission lines that are close by in real- and wavelength space, above first central moments can be ambiguous for such cases. For these emission lines we tabulate as primary coordinate the S/N-peak position introduced in Sect. 5.3.1.4. More details on the available coordinates per source are given in Sect. 5.5 where we describe the contents of the source catalogue.

In the same narrow bands where we determined the first central moments we measure the spatial extents in the emission lines. As extent we calculated the characteristic light distribution weighted radius introduced by Kron (1980). In calculating the Kron-radius R_{Kron} our algorithm follows closely the `SExtractor` implementation (Bertin & Arnouts 1996). We then integrated the flux in an unsmoothed narrow-band image of the same bandwidth within an $k \times R_{\mathrm{Kron}}$ aperture. With $k = 3$ this aperture is expected to contain $> 95\%$ of the total flux for compact sources whose light-profile is mainly determined by PSF broadening (e.g. Graham & Driver 2005). For comparison purposes we measured all emission lines fluxes in $k = 1$, $k = 2$, $k = 3$, and $k = 4$ apertures. We show in the publication describing `LSDCat` (Herenz et al., in prep.) that these automatically measured fluxes in $k = 3$ apertures compare well with manually determined fluxes based on a curve-of-growth method.

5.3.2 Classification and cleaning

After running `LSDCat` on the 24 MUSE-Wide datacubes we were left with 24 catalogues with 2603 emission line candidates in total. The process of assigning line identifications to those individually detected lines was the obvious next step.

To classify the detections we first grouped lines located at nearly the same position on the sky. Setting the maximal allowed radial distance between lines to $0.8''$ resulted in 374 line groups consisting of two or more lines and 642 spatially isolated single line detections. We then inspected those groups and single line detections with the toool *qtClassify* that we developed especially for the classification of emission line galaxies in wide-field IFS datasets. In Fig. 5.5 we show a screenshot of this tool. The software is developed in Python[4] and depends on NumPy (van der Walt et al. 2011), SciPy (Jones et al. 2001–), Astropy (Astropy Collaboration et al. 2013), and pyqtgraph[5]. qtClassify works as follows: Detections with multiple peaks above the detection threshold (i.e. quality A objects in the terminology of Sect. 5.3.2) are automatically classified by anchoring a redshift solution to the peak positions of the detected emission lines (cf. Garilli et al. 2010). The remaining single line detections have than to be manually classified. For this purpose the program takes as input a guess for the detected line, and then displays in several panels data at the positions of possible other emission lines from the original datacube and the S/N-datacube from `LSDCat`. These panels are interactive, i.e. the cut levels of the images can be changed and the spectral position can be shifted. Moreover, the aperture radius for the displayed spectrum can be altered interactively. The spectrum itself can be smoothed with kernels of different sizes. Within the spectrum vertical lines indicate the position of additional lines corresponding to the current guess. Additionally, an image cutout of the region of interest from an HST band can be displayed. Having evaluated all this information, the user then decides on an emission line or flags the detection as spurious. This decision has to be accompanied by

[4] `http://www.python.org/`
[5] `http://pyqtgraph.org/`

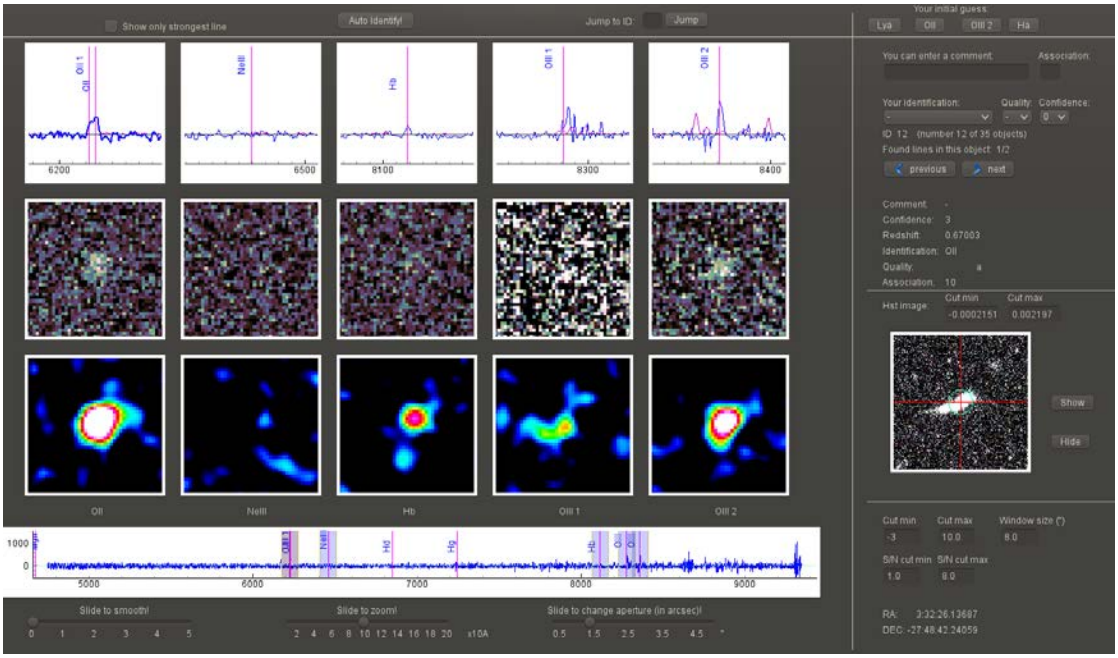

Figure 5.5: Screenshot of qtClassify. All graphical panels are interactive. The top row panels display sections of a spectrum extracted from the datacube at the position of the detected emission line under scrutiny. The aperture radius for extraction, the limits of the y-axis, as well as the degree of smoothing of the spectrum can be changed interactively. The positions of displayed sections are adjusted to show regions around possible veto lines under the users guess for the nature of the detected emission line. Below the spectra pseudo-narrow band images at the veto line positions are displayed. Here the cut-levels as well as the width of the narrow-band window can be altered interactively. The bottom row of panels displays the corresponding layers from `LSDCat`'s S/N-cube. Both the spectral position of the center-row panels and the bottom-row panels can be changed simultaneously with a slider or by moving the pointer in the top-row panels. On the bottom of the window an overview over the whole extracted spectrum is displayed, and at the right side of the window a cut-out from an HST image can be shown.

the assignment of a quality and confidence tag. There exists also a text field, that allows the input of free-form comments. When closing the *qtClassify* session, all information entered by the user is saved as a FITS table (Pence et al. 2010) to disk.

All groups and single line detections, including the ones that had automatically assigned classifications, were inspected with *qtClassify* by three investigators independently (ECH, JK, and TU). Afterwards this group plus a fourth investigator (LW) consolidated these individual classifications into a final one. In these consolidation sessions we also assign quality and confidence values to the individual detections. Our quality value indicates the amount of objective information from the datacube that could be used to classify the line(s):

- *Quality A*: Multiple emission lines were detected at the same position and it was possible to anchor a unique redshift solution for the object. These unambiguous identifications were assigned automatically but were also confirmed by visual cross-checks in *qtClassify*. We show an example of a quality A classified object in Fig. 5.6. There 288 objects "Quality A" objects in our catalogue.

- *Quality B*: Only one emission line was detected above the detection threshold. However,

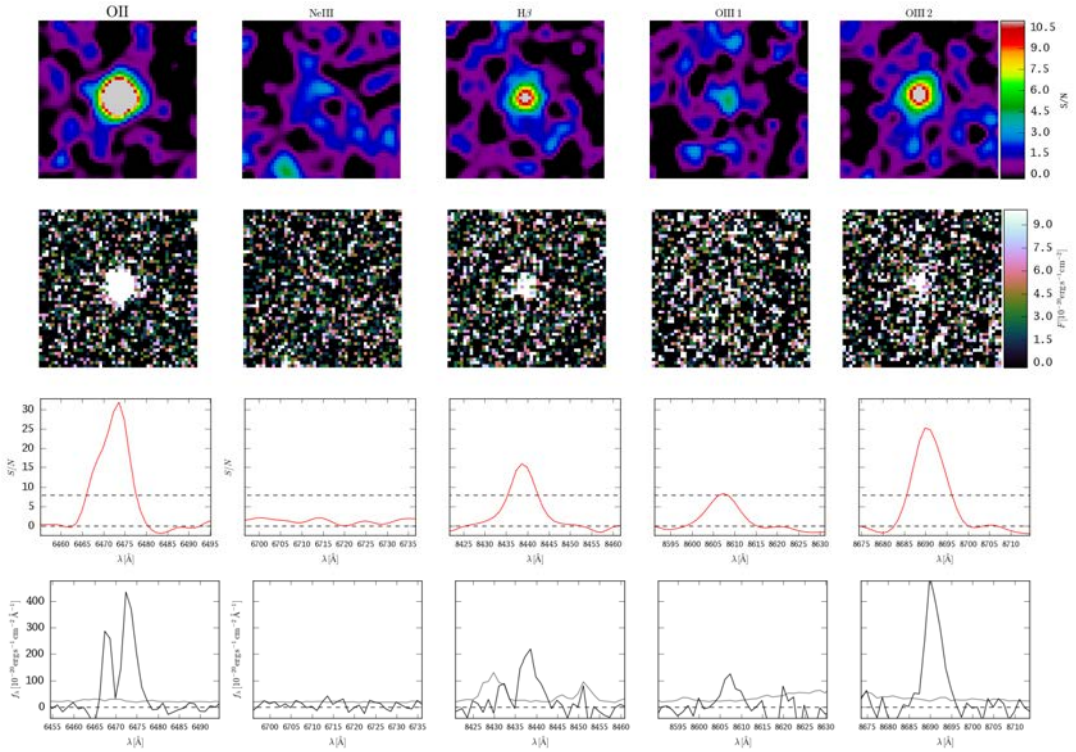

Figure 5.6: Example of a quality A object (MUSE-Wide ID 10825145 at $z = 0.73584$, strongest line in S/N is O II). Multiple emission lines from this galaxy are detected above the detection threshold $S/N_{thresh} = 8$. *First row*: Individual layers from the S/N cube after matched filtering with `LSDCat`. The position of the layers is chosen to match the classified redshift of the object. *Second row*: Pseudo narrow-band images created by summation over four layers around the expected position of the emission lines. *Third Row:* Corresponding segments of the spaxel from the `LSDCat` generated S/N cube with the highest S/N peak. *Fourth Row:* Corresponding segments of an aperture extracted spectrum (aperture diameter = 1.4″) from the flux datacube.

several other lines below the detection threshold would also be seen. These mostly unambiguous identifications were assigned manually in *qtClassify*. We show an example of a quality B classified object in Fig. 5.7. There are 117 "Quality B" objects in our catalogue.

- *Quality C*: Only one emission line was detected with no veto lines being visible. The identification was then based on the visual appearance of the line (e.g. double peak matches O II $\lambda\lambda$3726,3728 profile, characteristic Lyα profile shape), and the appearance of the object in the HST CANDELS images. Prior information on the photometric redshifts was *not* employed, however. We show an example of a quality C classified object in Fig. 5.8. There are 426 "Quality C" objects in our catalogue.

Confidence is a more subjective measure, indicating how sure the team of classifiers is on a certain classification:

- *Confidence 3*: All classifiers agreed without any doubt on the classification. By definition all quality A and mostly all quality B identifications have confidence 3. In total we have 578 objects marked with a confidence value 3.
- *Confidence 2*: These objects were discussed among the classifiers in the consolidation

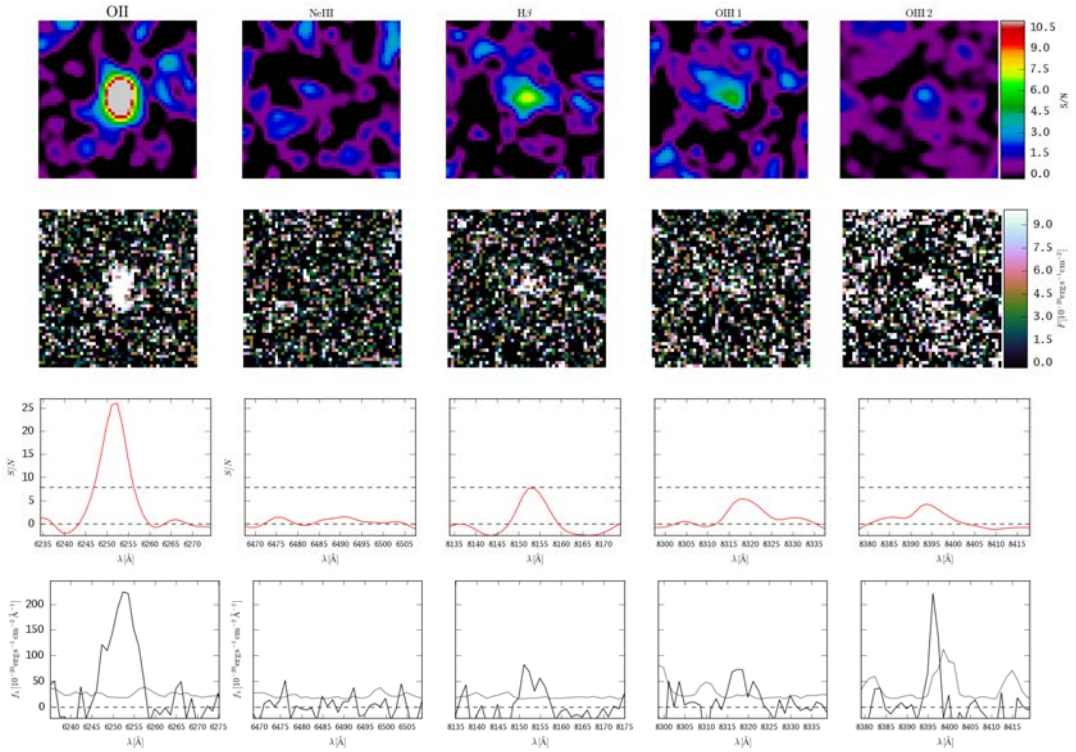

Figure 5.7: Similar to Fig. 5.6, but for a quality B object (MUSE-Wide ID 10721114 at z = 0.6770, strongest line in S/N is O II). Only one emission line is detected above the detection threshold, but other lines are clearly visible in the `LSDCat` generate S/N and flux datacube. We note, that since the [O III] λ5007 line falls on a telluric emission line, its S/N ratio is lower compared to the stronger [O III] λ4959 line.

process. Often the line profile had to be evaluated in detail. In some cases CANDELS images and photometry were consulted in the consolidation process. 210 objects in the catalogue are marked with confidence 2.

- *Confidence 1*: The classifiers initially disagreed on the classification. Inspection of the line-profile and HST imaging data did not resolve possible conflicts. These lines usually show the lowes S/N-ratios. Only 43 objects in our catalogue are in this category.

In Fig. 5.10 we display exemplarily lines classified as Lyα for the different confidence categories.

After having consolidated classifications for all entries in the per-pointing catalogues we went through several cleaning steps in order to build the final object catalogue. First, detections classified as spurious, e.g. telluric line residuals or continuum emission residuals, were purged. Second, superpositions, e.g two objects at different redshifts on nearly the same position on the sky and thus had to be split into separate objects. Related to this point, some low-z galaxies tended to fragment into detections of, e.g., multiple H II regions. Such fragmented detections were manually merged into a single object. Finally, due to the overlap of pointings, some sources were detected in two pointings. In the final catalogue we report for such a source only the quantities determined for the detections in that pointing where the source is located further away from the edge. After these cleaning step we finally arrived at a set of 831 emission line galaxies from which in total 1656 emission lines were detected.

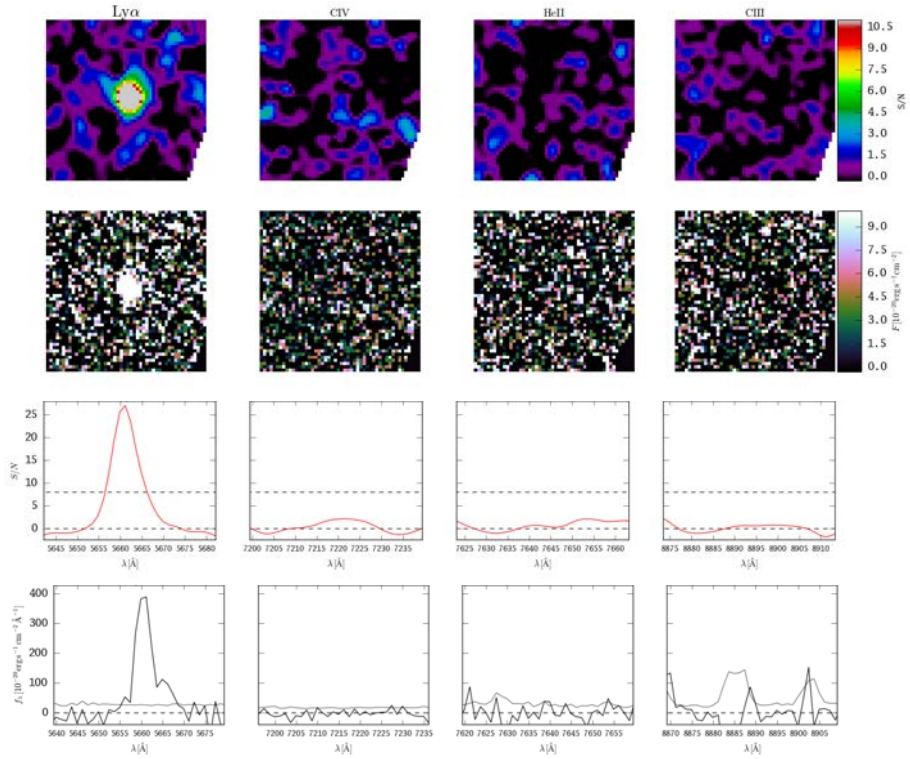

Figure 5.8: Similar to Fig. 5.6, but for a quality C object (MUSE-Wide ID 10415052 at z = 3.6570, only one detected line). No other lines were found in the datacube. Also no veto lines were found if would assume that detected line is an O II emission line. Based on the characteristic profile of the emission line we classified it as Lyα.

Table 5.3: Emission lines used for redshift determination

Line	Air Wavelength [Å]	Vacuum Wavelength [Å]
Lyα	...	1215.670
C IV	...	1548.203
[O II]	3726.032, 3728.815	3727.048, 3729.832
Hβ	4861.325	4862.650
[O III]	4958.911, 5006.843	4960.263, 5008.208
Hα	6562.800	6564.589

Wavelengths are from the "Atomic Line List" compiled by P. van Hoof: `http://www.pa.uky.edu/~peter/atomic/`. Wavelengths longward of 2000 Å are tabulated in air and converted to vacuum with formula used in the Vienna atomic line database (Ryabchikova et al. 2015): `http://www.astro.uu.se/valdwiki/Air-to-vacuum\%20conversion`.

5.4 Redshifts

To measure redshifts of the 831 emission line galaxies in our sample we first extracted 1D spectra for each of our objects. To achieve a S/N-optimised extraction for compact we performed a PSF-

weighted extraction on each source position. We adopted the PSF parameterisation previously used for the cross-correlation with the matched filter explained in Sect. 5.3.1.3. Depending whether the source is a high-z LAE or a low-z galaxy detected by its rest-frame optical emission line we employed different emission line fitting strategies. We explain the fitting in Sects. 5.4.1 and 5.4.2 for the high-z LAEs and low-z galaxies, respectively. In Fig. 5.9 we show a histogram of the redshift-distribution obtained from these fits. We have 595 galaxies at $z < 2$ detected by their rest-frame optical emission lines and 238 $z > 2.95$ galaxies. In Sect. 5.4.3 we compare our redshifts with the compilation of redshifts in the CANDELS/Deep region of the GOODS-South given by Momcheva et al. (2015) and with the redshifts from the first data release of the VIMOS Ultra Deep Survey (Le Fèvre et al. 2015; Tasca et al. 2016).

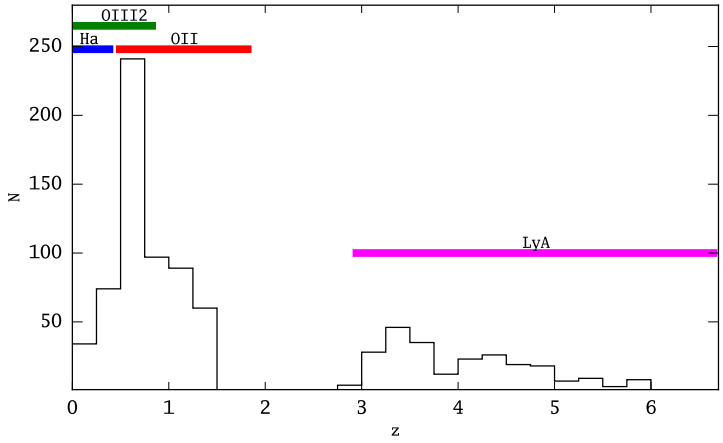

Figure 5.9: Histogram showing the redshifts of 833 emission line selected galaxies in the MUSE-Wide CDF-S sample. The bin size is $\Delta z = 0.25$. Horizontal bars indicate the redshift range of MUSE's wavelength coverage for the strongest emission lines of star-forming galaxies.

5.4.1 High-redshift Lyman α galaxies

To determine the redshifts of the LAEs we fitted the Lyα line profiles with the formula

$$f(\lambda) = A \times \exp\left\{-\left(\frac{\lambda - \lambda_0}{a_{\mathrm{asym}}(\lambda - \lambda_0) + d}\right)^2\right\} \tag{5.1}$$

which describes an asymmetric Gaussian profile (Shibuya et al. 2014). For objects showing a double peak, only the red peak is fitted. The free parameters A, λ_0, a_{asym}, and d in our fit to Eq. (5.1) are the amplitude, the peak wavelength, the asymmetry parameter, and the typical width of the line, respectively. An LAE with a profile skewed to the red (blue) side has $a_{\mathrm{asym}} > 0$ ($a_{\mathrm{asym}} < 0$), while a symmetric profile is characterised by $a_{\mathrm{asym}} = 0$. Shibuya et al. (2014) argue that Eq. (5.1) provides a more robust peak wavelength for the typical LAE profiles than a simple Gaussian. However, it is known and commonly attributed to the complex Lyα radiative transfer physics that the Lyα-peak redshift is systematically offset by $\sim 100-200\,\mathrm{km\,s^{-1}}$ with respect to the systemic redshift determined from rest-frame optical emission lines (e.g. McLinden et al. 2011; Chonis et al. 2013; Shibuya et al. 2014; Erb et al. 2014; Song et al. 2014; Hashimoto et al. 2015). No correction for such offsets was applied here.

Practically the fitting was performed in a window around the peak where all flux values are greater than 10 % of the peak flux. For 11 objects we had to adjust the window size manually to

avoid strong sky-subtraction residuals[6]. We accounted for a possible continuum by subtracting a running median from the 1D spectrum. To demonstrate the quality of our fits we show in Fig. 5.10 twelve representative Lyα profiles from our sample with the fitted profiles according to Eq. (5.1). The λ_0 values from the fit were then converted to vacuum wavelengths[7] before being transformed to redshifts using the laboratory wavelength of Lyα (Table 5.3). Finally, we determined the error on each redshift by repeating the fitting procedure 100 times on random realisations of the spectra generated by perturbing each pixel according to the noise statistics from the error spectrum.

5.4.2 $z \lesssim 1.5$ galaxies

Emission line galaxies at $z \lesssim 1.5$ are detected in MUSE datacubes by their rest-frame optical emission lines. For those galaxies the most common transitions found in our catalogue are [O II] $\lambda\lambda$3276,3278 (472 detections), [O III] $\lambda\lambda$4958, 5006 (310 detections), Hβ (184 detections), and Hα λ6563 (73 detections). These are typically the strongest emission lines of star-forming galaxies (e.g. Kennicutt 1992). In Table 5.3 we list the air wavelengths and the vacuum wavelengths of these transitions. We fitted 1D Gaussians to these spectral lines. For these fits we subtracted a continuum determined in small spectral windows around the position of the line. Since the datacube wavelengths are given in air we converted the peak position of those fits to vacuum wavelengths[7] before transforming them to redshift. The error on the redshift was determined again by repeating the fitting procedure 100 times on realisations of the spectra generated by perturbing each pixel according to the noise statistics from the error spectrum. For objects having several detected emission lines we computed the S/N-weighted mean of all emission line fits.

5.4.3 Comparision with literature redshifts

We now compare the redshifts of our 833 emission line selected galaxies to literature redshifts within our survey area. Recently, Momcheva et al. (2015) presented a redshift catalogue of $\sim 10^5$ sources in all CANDELS fields containing grism redshifts from the 3D-HST survey (Brammer et al. 2012; Momcheva et al. 2015), photometric redshifts from 3D-HST/CANDELS photometry (Skelton et al. 2014), as well as a compilation of ground-based spectroscopic redshifts also presented in Skelton et al. (2014). For the CDF-S region ground-based redshifts in this compilation are in-turn taken from a compilation by Wuyts et al. (2008; see their Table 3 for individual spectroscopic campaigns). To compare the redshifts with this catalogue we first performed a cross-match on source positions, discarding all entries separated by $\geq 0.5''$ radial distance. 687 sources match this criterion. We then visually checked the positions of these within the HST images to identify cases where the association between the two catalogues is unclear. These cases are characterised by several objects located in close proximity to the MUSE-Wide detection. After this screening we removed 18 objects from the comparison. 141 of the remaining 669 objects have a ground based spectroscopic redshift (139 at $z \lesssim 2$ / 2 at $z \gtrsim 3$), 184 have a grism redshift (182 at $z \lesssim 2$ / 2 at $z \gtrsim 3$), and 344 have a photometric redshift (241 at $z \lesssim 2$ / 103 at $z \gtrsim 3$).

In Fig. 5.11 we compare for the 669 objects the MUSE-Wide redshifts to the redshifts from the 3D-HST compilation. Following the literature (e.g. Skelton et al. 2014) we define a catas-

[6]The MUSE-Wide IDs of the objects requiring manual intervention are 10105016, 10130050, 10924083, 11101001, 11504089, 11018062, 11705019, 11902002, 12104014, 12212068, and 12403012.

[7] Using the formula from the Vienna atomic line database (Ryabchikova et al. 2015): `http://www.astro.uu.se/valdwiki/Air-to-vacuum\%20conversion`.

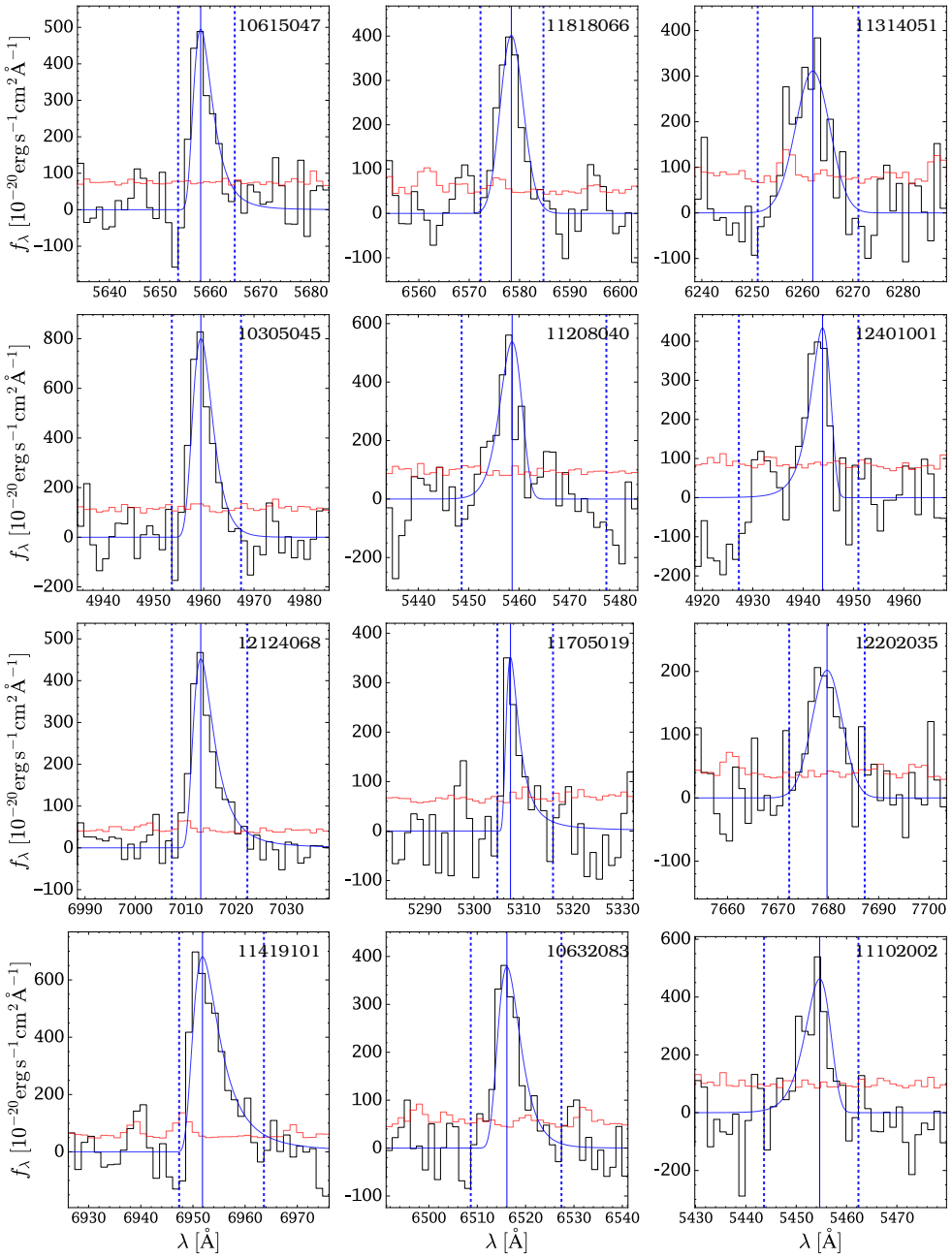

Figure 5.10: 12 representative Lyα line profiles from our sample. The first, second, and third column include only objects with confidence flag 3, 2, and 1, respectively. In each panel we show the PSF-extracted and continuum subtracted spectra in black, their corresponding variances from our effective noise determination in red, and the fitted profile according to Eq. (5.1) in blue. The blue vertical line marks the position of the peak wavelength λ_0 from the fitted profile that, after conversion to a vacuum wavelength, is used to measure the redshift.

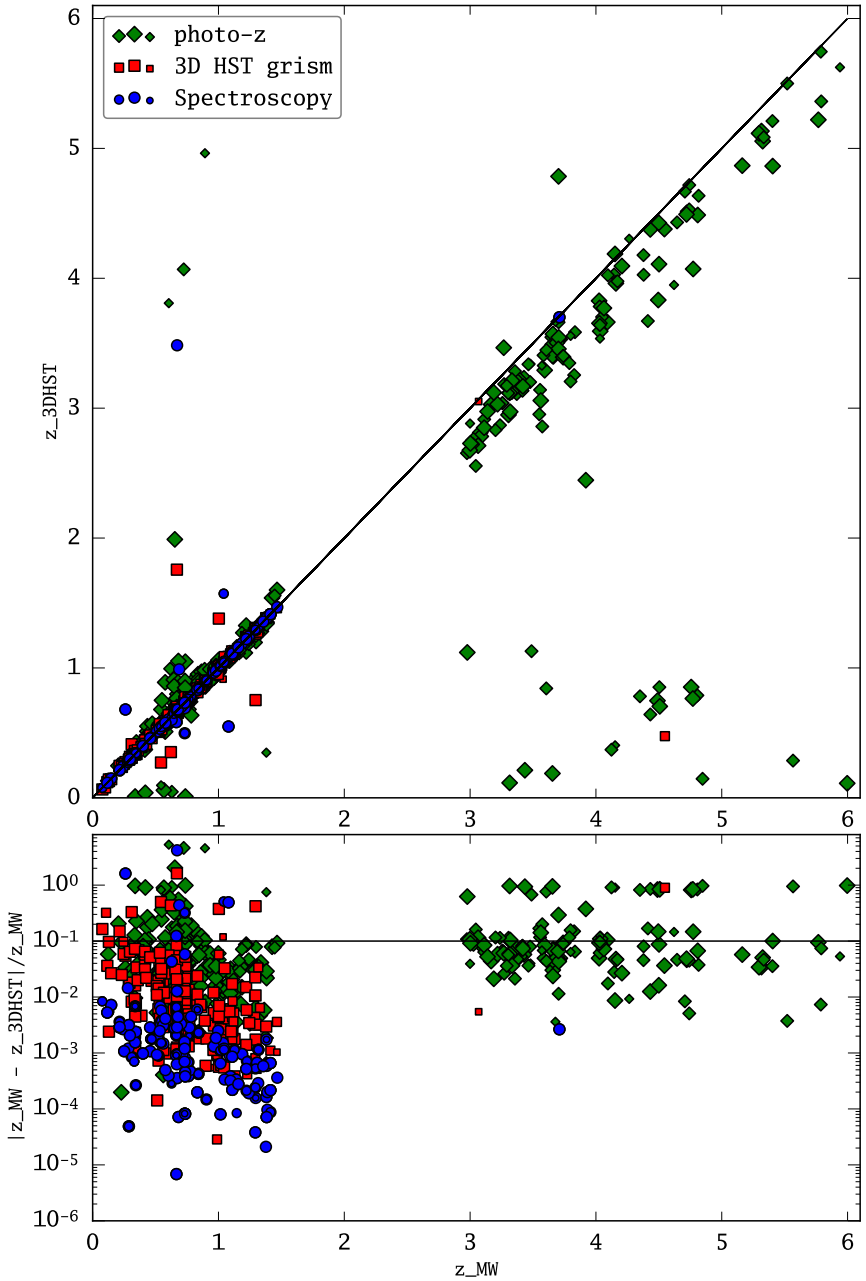

Figure 5.11: Redshift comparison between our MUSE-Wide emission line selected galaxy sample and the 3D-HST redshift compilation presented by Momcheva et al. (2015). *Top panel*: 3D-HST redshifts ($z_{\rm 3DHST}$) versus MUSE-Wide redshifts ($z_{\rm MW}$). Symbol size encodes the confidence on the MUSE-Wide emission line classification (Sect. 5.3.2), with the largest symbols representing "Confidence 3" sources. The different symbols encode the source of the catalogue redshifts according to the legend. *Bottom panel:* Relative difference between 3D-HST and MUSE-Wide redshifts as a function of MUSE-Wide redshifts. The horizontal line indicates a relative difference of 10%.

Table 5.4: Catastrophic redshift missmatches with 3D-HST redshift compilation

Source	$z \lesssim 2$	$z \gtrsim 3$
spectroscopy	7 (5%)	0 (0%)
3D-HST grism	6 (3%)	1 (50%)
photo-z	19 (7%)	31 (30%)
total	32 (5%)	32 (29%)

Percentages of total sources in a particular category are given in brackets.

trophic redshift mismatch as one with $|z_{\rm MW} - z_{\rm 3DHST}|/(1 + z_{\rm MW}) > 10\%$. Overall we have 64 of these catastrophic mismatches. In Table 5.4 we separate this number into low- and high-redshift galaxies and by the source of the comparison redshift. With 30% we find a high rate of catastrophic mismatches amongst photometrically determined redshifts at $z \gtrsim 3$. Moreover, for all high-z LAEs in our sample we see a systematic offset between photometric and spectroscopic redshifts with $|z_{\rm MW} - z_{\rm 3DHST}|/(1 + z_{\rm MW}) \sim 10^{-1.5}$, i.e. $\Delta z = |z_{\rm MW} - z_{\rm 3DHST}| \sim 0.1 \ldots 0.2$. This systematic offset is much larger then the known systematic offset of the Lyα line to the systemic redshift explained in Sect. 5.4.1. These systematic offsets therefore point at a systematic mismatch between high-z LAEs spectral energy distributions and the templates used in the photometric redshift determination by Skelton et al. (2014).

We also cross-matched our objects with the first data release of the VIMOS Ultra Deep Survey (Le Fèvre et al. 2015; Tasca et al. 2016). We find 10 of our objects in their spectroscopic redshift catalogue; seven $z < 2$, and three $z \gtrsim 3$ galaxies. All their redshifts are in excellent agreement with ours as characterised by $|z_{\rm MW} - z_{\rm VUDS}|/(1 + z_{\rm MW}) < 10^{-3}$.

5.5 Source catalogue

5.5.1 Object Table

In Table 5.5 we present the catalogue of all 831 detected emission line galaxies in the here analysed 22.2 arcmin^2 of MUSE-Wide. We show in print only the first 100 entries of this catalogue to give guidance on its form and content[8]. We now explain the columns of this object table.

Column (1) contains a unique MUSE-Wide ID. This ID is composed of five digits `ABBCCDDD`. Here `A` indicates to the MUSE-Wide survey-area (1≙ECDF-S CANDELS/Deep, 2≙COSMOS CANDELS, or other numbers for future MUSE-Wide regions), `BB` indicates the pointing number (here 01–24, see Fig. 5.1), `CC` refers to the per-pointing object ID, and `DDD` to the running ID of the strongest line. These last two identifiers relate to the emission-line table explained in the following Sect. 5.5.2.

Columns (2) and (3) contain the position of the galaxy as right-ascension $\alpha_{\rm J2000}$ and declination $\delta_{\rm J2000}$. As explained in Sect. 5.3.1.5, for most sources this position is given as first central moments determined in an adaptive narrow-band image. However, for 40 sources this position differed by more than 0.4″ to the peak S/N position found in the initial thresholding step (Sect. 5.3.1.4). Visual inspection revealed that these cases are often affected by blends with neighbouring sources. Since the peak S/N-coordinate is less affected by blending, we replace for

[8]The entire table will become available as a FITS table with the publication of this paper.

those 40 cases the first central moment coordinate with the peak S/N coordinate. `LSDCat` offers more positional parameters per emission line detection – these are explained in the following Sect. 5.5.2.

Column (4) contains the redshift z for each galaxy and column (5) contains the error on this quantity. The redshift determination and error estimation was explained in Sect. 5.4.

In column (6) we list the lead line for each galaxy. The lead line is defined as the galaxies line that has the strongest S/N after the matched-filtering process (Sect. 5.3.1.3). The lead-line is therefore not necessarily the line with the strongest flux. Column (7) contains the S/N of the lead-line.

In column (8) and column (9) we list the quality and confidence values indicating the robustness of the object classification and line identification. The meaning of the individual values was explained in Sect. 5.3.2.

Finally, we provide in column (10) a list of all other emission lines that were detected at a lower S/N than the lead line. This column is empty in case of a single line detection.

Table 5.5: Catalog of emission line selected galaxies in MUSE-Wide CDF-S Pointings 1 – 24

(1) MUSE-Wide ID	(2) α_{J2000} [hh:mm:ss.ss]	(3) δ_{J2000} [±dd:ss:mm.mm]	(4) z	(5) Δz	(6) Lead Line	(7) S/N	(8) Quality	(9) Confidence	(10) Other Lines Detected
10101006	03:32:14.44	-27:48:48.47	0.310564	1.8e-05	Hα	76.11	a	3	O II,Hγ,Hβ,O III,O III,S II
10102010	03:32:12.43	-27:48:10.04	0.348878	3.3e-05	O III	25.0	a	3	O II,Hβ,Hα
10103014	03:32:14.92	-27:48:03.14	0.363892	0.000119	Hα	13.49	a	3	O II,Hβ
10105016	03:32:16.56	-27:48:52.60	3.25748	0.001	Lyα	8.44	c	2	
10106018	03:32:12.96	-27:48:36.60	0.416752	4.7e-05	O III	26.35	a	3	O II,Hα
10108022	03:32:15.48	-27:48:26.41	0.076361	8e-06	Hα	39.54	a	3	O III,S II
10109024	03:32:12.66	-27:48:27.61	3.47936	0.0009	Lyα	8.6	c	1	
10110025	03:32:15.76	-27:48:50.77	3.70334	0.00062	Lyα	9.7	c	2	
10111026	03:32:14.70	-27:48:17.07	3.79441	0.00034	Lyα	18.03	c	2	
10112027	03:32:12.96	-27:48:13.42	3.82689	0.00025	Lyα	15.88	c	2	
10113028	03:32:14.96	-27:48:34.00	0.624856	6.5e-05	O II	23.03	a	3	O III
10114030	03:32:14.67	-27:48:15.58	0.666994	0.00023	O II	11.91	c	3	
10115031	03:32:13.57	-27:48:47.65	4.27553	0.00036	Lyα	15.83	c	3	
10116032	03:32:13.04	-27:48:40.98	4.29585	0.00033	Lyα	15.49	c	3	
10117033	03:32:16.80	-27:48:13.51	0.730218	0.0003	O II	10.87	b	3	
10118034	03:32:16.06	-27:48:16.73	0.73159	0.000583	O II	8.34	c	2	
10120036	03:32:17.47	-27:48:38.54	0.737494	7e-06	O II	52.75	a	3	Hγ,Hβ,O III,O III
10121041	03:32:14.89	-27:48:15.88	0.736698	0.000403	O II	9.29	c	2	
10122042	03:32:14.14	-27:48:11.77	0.75107	0.000157	O II	16.32	c	2	
10123043	03:32:16.24	-27:48:44.01	4.43189	0.00079	Lyα	10.95	c	3	
10124044	03:32:16.16	-27:48:44.49	4.54431	0.00018	Lyα	31.28	c	3	
10125045	03:32:16.45	-27:48:25.08	4.54833	0.00033	Lyα	12.23	c	2	
10126046	03:32:12.23	-27:48:12.49	4.74834	0.00026	Lyα	14.15	c	2	
10127047	03:32:15.29	-27:48:16.45	4.81602	0.00069	Lyα	9.62	c	2	
10128048	03:32:17.27	-27:48:23.39	0.953781	0.000171	O II	9.57	c	1	
10129049	03:32:13.17	-27:48:21.67	0.546511	3.6e-05	O III	11.37	b	3	
10130050	03:32:14.75	-27:47:59.01	5.93967	0.00063	Lyα	13.91	c	1	
10131051	03:32:16.35	-27:48:24.03	1.294314	0.000119	O II	26.27	c	2	
10132052	03:32:16.13	-27:48:06.42	1.298433	4.1e-05	O II	18.29	c	2	
10133053	03:32:12.76	-27:48:23.34	1.317507	0.000197	O II	8.78	c	3	
10202010	03:32:16.98	-27:49:30.31	0.260775	4e-06	Hα	106.34	a	3	Ne III,Hβ,O III,O III,S II,S II
10203017	03:32:18.93	-27:49:29.28	0.330341	1.5e-05	O III	59.31	a	3	O II,Hγ,Hβ,O III,Hα,S II

(1)	(2)	(3)	(4)	(5)	(6)	(7)	(8)	(9)	(10)
10205037	03:32:17.57	-27:49:41.05	0.337523	2e-06	O III	1651.47	a	3	O II,Ne III,Ne III,Hδ,Hγ,O III,Hβ,O III,O I,Hα,N II,S II,S II
10206048	03:32:15.64	-27:49:33.25	0.337535	4e-06	O III	178.29	a	3	O II,Hγ,Hβ,O III,Hα,N II,S II
10207068	03:32:17.07	-27:49:21.64	0.337584	0.000121	N II	39.35	a	3	O II,N III,O III,O III,Hα
10208071	03:32:17.47	-27:49:19.64	0.338015	9.1e-05	N II	19.64	a	3	O II,Hα
10209072	03:32:15.00	-27:49:20.70	0.337698	1.3e-05	O II	32.94	a	3	Hβ,O III,O III,Hα
10210079	03:32:15.32	-27:49:27.29	0.338025	3.3e-05	O III	25.26	a	3	O II,Hβ,Hα
10211084	03:32:16.71	-27:49:34.89	0.337758	4.4e-05	O III	31.62	a	3	O II,Hβ,O III
10212085	03:32:17.95	-27:49:30.19	3.16729	0.00022	Lyα	14.56	c	3	
10213086	03:32:15.95	-27:49:40.50	3.25527	0.00021	Lyα	18.01	c	3	
10214087	03:32:19.20	-27:49:37.04	3.25491	0.00057	Lyα	8.69	c	1	
10215088	03:32:16.57	-27:48:52.89	3.25692	0.00038	Lyα	8.1	c	2	
10216089	03:32:14.94	-27:49:41.03	1.358569	0.000192	O II	11.29	b	3	
10219097	03:32:18.39	-27:49:35.44	3.37243	0.00044	Lyα	11.11	c	3	
10221103	03:32:17.81	-27:49:26.42	0.246619	2e-06	Hα	156.37	a	3	Hγ,Hβ,O III,O III,N II,S II,S II
10222112	03:32:14.60	-27:49:13.15	0.468833	2.1e-05	O III	137.27	a	3	O II,Ne III,Hγ,Hβ,O III
10223113	03:32:15.90	-27:49:19.59	0.545595	0.000395	O II	8.13	b	3	
10226124	03:32:17.39	-27:49:44.47	0.576592	0.000136	O III	16.32	a	3	O II
10227126	03:32:17.83	-27:49:15.97	1.127736	1.6e-05	O II	55.41	a	3	Mg II,Ne III,Hζ,Ne III,Hδ,Hγ
10228132	03:32:18.68	-27:49:20.48	1.379417	0.000291	O II	12.03	c	2	
10230136	03:32:14.31	-27:49:20.64	0.665421	4e-06	O II	63.96	a	3	Hγ,Hβ,O III,O III
10231144	03:32:16.16	-27:49:41.81	0.665374	0.000122	O III	33.81	a	3	O II,Ne III,O III
10232148	03:32:15.07	-27:49:17.75	0.665519	1.1e-05	O III	51.56	a	3	O II,Hβ,O III
10233149	03:32:15.11	-27:49:51.57	0.665896	4.4e-05	O II	22.66	a	3	Hβ
10234151	03:32:16.47	-27:49:45.34	0.665098	0.000158	O II	8.15	c	3	
10235152	03:32:14.14	-27:49:17.41	0.669521	0.000469	O II	8.51	c	2	
10236153	03:32:15.54	-27:49:36.64	0.723836	0.000283	O II	8.01	c	2	
10237154	03:32:16.05	-27:48:59.44	1.412876	0.000425	O II	8.5	c	1	
10238155	03:32:14.72	-27:49:15.28	0.729054	0.000328	O II	17.49	b	3	
10240161	03:32:16.55	-27:49:34.51	0.732011	1.2e-05	O II	51.07	a	3	Hβ,O III,O III
10241165	03:32:16.22	-27:48:53.70	0.732951	0.000177	O II	12.94	c	2	
10242166	03:32:17.14	-27:49:25.13	0.840128	0.000269	O II	9.8	b	3	
10243169	03:32:15.61	-27:49:21.03	0.841056	1.5e-05	O III	26.05	a	3	O II,O III
10244170	03:32:14.47	-27:49:25.31	0.864384	0.000346	O II	8.71	b	3	
10245171	03:32:18.52	-27:49:14.11	1.219471	4.5e-05	O II	27.62	c	3	
10246172	03:32:17.08	-27:49:06.03	4.81535	0.00134	Lyα	10.47	c	2	
10247173	03:32:14.15	-27:49:15.57	0.963078	1.8e-05	O II	46.25	a	3	Hγ

(1)	(2)	(3)	(4)	(5)	(6)	(7)	(8)	(9)	(10)
10248175	03:32:18.70	-27:49:31.83	0.964064	1.9e-05	O II	43.5	b	3	
10249176	03:32:17.87	-27:49:12.88	5.10303	0.00051	Lyα	14.45	c	2	
10250177	03:32:15.24	-27:49:10.98	1.004142	9e-06	O II	72.94	a	3	Ne III,Hδ,Hγ
10251181	03:32:18.71	-27:49:19.83	1.036665	0.000552	O II	13.54	c	2	
10252182	03:32:14.87	-27:49:12.60	1.079899	7.6e-05	O II	24.47	c	2	
10253183	03:32:18.15	-27:49:00.68	1.080194	0.000321	O II	9.4	c	1	
10254184	03:32:14.93	-27:49:07.95	1.096482	0.000338	O II	14.03	c	2	
10255185	03:32:18.12	-27:49:27.70	0.576617	3.7e-05	O III	8.74	b	3	
10301001	03:32:19.19	-27:50:20.07	2.97467	0.00074	Lyα	10.68	c	2	
10302002	03:32:16.13	-27:50:04.11	3.04522	0.00044	Lyα	13.09	c	2	
10304043	03:32:17.15	-27:49:47.87	0.330533	1.3e-05	Hα	72.7	a	3	O II,Hβ,O III,O III,S II
10305045	03:32:16.88	-27:50:37.07	3.0807	0.00031	Lyα	10.79	c	3	
10306046	03:32:16.62	-27:50:02.99	3.08488	0.00028	Lyα	13.26	c	3	
10308055	03:32:18.22	-27:49:44.22	3.36296	0.00046	Lyα	10.5	c	2	
10309056	03:32:17.93	-27:50:18.66	3.37083	0.00051	Lyα	10.62	c	2	
10310057	03:32:17.01	-27:50:46.52	3.42957	0.00037	Lyα	10.69	c	2	
10311058	03:32:18.41	-27:50:00.04	3.57094	0.00167	Lyα	9.53	c	2	
10312059	03:32:19.72	-27:50:23.60	0.56074	8.3e-05	O II	78.43	a	3	Hγ,Hβ,O III,O III
10313064	03:32:16.75	-27:50:20.70	0.560494	5.9e-05	O II	21.51	a	3	Hβ,O III,O III
10314071	03:32:18.03	-27:50:32.04	0.561173	8e-05	O III	43.12	a	3	O II,Hβ,O III
10315072	03:32:19.42	-27:50:34.05	0.561336	0.000381	O II	8.05	b	3	
10317080	03:32:18.21	-27:49:47.38	0.227555	7e-06	Hα	39.98	a	3	Hβ,O III,O III
10318081	03:32:19.14	-27:49:56.64	3.91963	0.00052	Lyα	10.1	c	3	
10319082	03:32:19.18	-27:50:01.04	4.0252	0.00045	Lyα	10.87	c	3	
10320083	03:32:16.85	-27:50:07.39	0.665234	0.000257	O II	14.82	a	3	O III
10321085	03:32:15.12	-27:50:02.75	0.667928	0.000103	O II	15.74	b	3	
10322086	03:32:18.03	-27:49:53.05	0.670301	0.000218	O II	32.07	a	3	Hβ
10323093	03:32:16.55	-27:50:38.35	0.670205	8.9e-05	O III	21.91	a	3	O II,Hβ
10323091	03:32:16.58	-27:50:38.79	0.678631	0.000442	O II	8.85	c	3	
10324094	03:32:16.04	-27:50:15.84	0.670501	0.00023	O II	19.62	a	3	Hβ
10325096	03:32:19.63	-27:49:56.17	0.246265	0.000107	O III	8.67	b	3	
10326097	03:32:18.77	-27:50:33.29	4.28395	0.00025	Lyα	14.24	c	2	
10328100	03:32:18.69	-27:50:24.15	0.296767	2.1e-05	Hα	14.09	a	3	O III

Note: Only the first 100 of 830 entries are shown in print. The full table is availble electronically on request from the author.

Table 5.6: Columns of the Emission Line Table

Column	Unit(s)	Description
UNIQUE_ID	—	Unique MUSE-Wide ID from Table 5.5.
POINTING_ID	—	Pointing Number (see Fig. 5.1).
OBJ_ID	—	Object ID – only unique per pointing.
RID	—	Running ID – only unique per pointing.
IDENT	—	Line identification.
COMMENT	—	Free-form comment added during classification and cleaning (Sect. 5.3.2).
SN	—	Detection significance (Sect. 5.3.1.3)
{RA,DEC,LAMBDA}_SN	deg / Å	3D S/N-weighted position.
{RA,DEC,LAMBDA}_PEAK_SN	deg / Å	S/N-peak position
LAMBDA_NB_{MIN,MAX}	Å	Minimum- and maximum wavelength of optimal narrow band image.
R_KRON	arcsec	Kron-Radius (see Sect. 5.3.1.5).
F_KRON,F_{2,3,4}KRON	erg s^{-1} cm^{-2}	Flux extracted in ($k\times$) R_KRON aperture within narrow band defined by LAMBDA_NB_MIN,MAX.
F_KRON,F_{2,3,4}KRON_ERR	erg s^{-1} cm^{-2}	Error on the extracted flux.

Comma separated list within curly braces in the first column indicate the set of similar columns.

5.5.2 Emission Line Table

For each of the 1656 detected emission lines listed in column (6) and column (10) of Table 5.5 LSDCat provides a set of measurements (Herenz et al., in prep.). Supplementing the object catalogue we provide a table that contains for all emission lines these measurements and additional information. This table is available only in electronic format as a FITS table. In Table 5.6 we list the entries that are available for each emission line.

The link between the source catalogue (Table 5.5) and the emission line table can be established via the UNIQUE_ID column that uniquely indexes the galaxies found in our survey. Moreover, OBJECT_ID is a unique identifier for each galaxy per pointing and RID uniquely indexes each detected emission line per pointing. The identification of each line which was established in the classification process (Sect. 5.3.2) is given in the column IDENT. During classification with qtClassify we sometimes also entered a free-form comment. These comments are stored in the COMMENT column. All remaining columns are produced by LSDCat.

5.6 Conclusions and outlook

We presented first results from our on-going blind-spectroscopic survey MUSE-Wide. Using a novel 3D source detection approach for wide-field IFS data based on matched filtering – LSDCat – we constructed a catalogue of 1656 emission lines from 831 galaxies. The discovery potential of our survey technique is demonstrated by the fact that only four of our 237 LAEs at $z \gtrsim 3$ had previously ground based spectroscopic redshifts (Wuyts et al. 2008; Skelton et al. 2014; Momcheva et al. 2015; Tasca et al. 2016). As shown by the histogram in Fig. 5.12, most of the LAEs have very faint continuum magnitudes. Previous spectroscopic surveys in the CDF-S targeted primarily brighter galaxies (typically $i_{\mathrm{AB}} \lesssim 25$ mag, e.g. Vanzella et al. 2006; Popesso

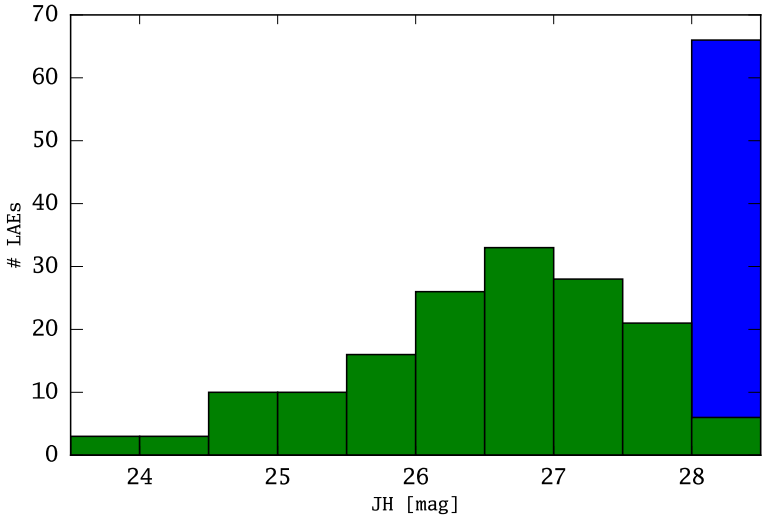

Figure 5.12: Counts of MUSE-Wide LAEs versus 3D-HST JH-magnitude (taken from the Momcheva et al. 2015 catalogue). 157 LAEs have a photometric counterpart within 0.5″ search radius (green histogram). For 66 LAEs we find no catalogue counterpart, so we artificially assign them to the JH =28.5 mag bin (blue histogram). 14 LAEs with unclear photometric association have been excluded from the analysis (see Sect. 5.4.3).

et al. 2009; Le Fèvre et al. 2013, 2015), hence these continuum faint galaxies were missed. However, spectroscopic confirmation and flux-measurements are essential to characterise this continuum-faint population of galaxies that dominate the build-up of stellar mass at this early cosmic epochs (e.g., Salvadori et al. 2010; Dayal & Libeskind 2012). When completed our MUSE-Wide survey will deliver ∼1000 of these galaxies offering an unprecedented dataset for statistical studies of this important population of star-forming galaxies.

In a forthcoming publication based on the present sample (Kerutt et al., in prep.) we will demonstrate that there is indeed photometric signal for a significant fraction of so far not catalogued LAEs in the CANDELS imaging data. Some of these objects are characterised by extreme Lyα equivalent widths, hinting at very metal-poor stellar populations (Schaerer 2003; Raiter et al. 2010; Schaerer 2013). Moreover, we also detect for a significant fraction in our LAEs extended Lyα halo emission (Saust et al., in prep.). The most extreme Lyα nebula in our sample is seen in the vicinity of a quasar (Urrutia et al., in prep.). Finally, our data allows us to construct a luminosity function of the LAEs (Herenz et al., in prep.). This analysis will allow for the first time to take the effects of extended Lyα emission onto the LAE luminosity function into account. From these examples it is evident that the here presented catalogue accompanied by the future release of the datacubes (Urruttia et al., in prep.) will provide a valuable resource for high-z studies. Nevertheless, also the spatially resolved spectroscopy for the 351 $z < 2$ emission line galaxies catalogued will provide valuable resource for future studies.

5.7 Bibliography

Adams, J. J., Blanc, G. A., Hill, G. J., et al. 2011, ApJS, 192, 5

Astropy Collaboration, Robitaille, T. P., Tollerud, E. J., et al. 2013, A&A, 558, A33

Bacon, R., Accardo, M., Adjali, L., et al. 2010, in Society of Photo-Optical Instrumentation Engineers (SPIE) Conference Series, Vol. 7735, Society of Photo-Optical Instrumentation Engineers (SPIE) Conference Series

Bacon, R., Bauer, S., Böhm, P., et al. 2006, The Messenger, 124, 5

Bacon, R., Bauer, S., Brau-Nogué, S., et al. 2009, in Science with the VLT in the ELT Era, ed. A. Moorwood, 331

Bacon, R., Bauer, S.-M., Bower, R., et al. 2004, in Society of Photo-Optical Instrumentation Engineers (SPIE) Conference Series, Vol. 5492, Society of Photo-Optical Instrumentation Engineers (SPIE) Conference Series, ed. A. F. M. Moorwood & M. Iye, 1145–1149

Bacon, R., Brinchmann, J., Richard, J., et al. 2015, A&A, 575, A75

Bacon, R., Vernet, J., Borisiva, E., et al. 2014, The Messenger, 157, 13

Balestra, I., Mainieri, V., Popesso, P., et al. 2010, A&A, 512, A12

Bertin, E. 2001, in Mining the Sky, ed. A. J. Banday, S. Zaroubi, & M. Bartelmann, 353

Bertin, E. & Arnouts, S. 1996, A&AS, 117, 393

Blanc, G. A., Adams, J. J., Gebhardt, K., et al. 2011, ApJ, 736, 31

Brammer, G. B., van Dokkum, P. G., Franx, M., et al. 2012, ApJS, 200, 13

Cassata, P., Le Fèvre, O., Garilli, B., et al. 2011, A&A, 525, A143

Chonis, T. S., Blanc, G. A., Hill, G. J., et al. 2013, ApJ, 775, 99

Das, P. K. 1991, Optical Signal Processing (Springer Science + Business Media)

Dawson, S., Rhoads, J. E., Malhotra, S., et al. 2007, ApJ, 671, 1227

Dayal, P. & Libeskind, N. I. 2012, MNRAS, 419, L9

Erb, D. K., Steidel, C. C., Trainor, R. F., et al. 2014, ApJ, 795, 33

Erben, T., Schirmer, M., Dietrich, J. P., et al. 2005, Astronomische Nachrichten, 326, 432

Filippenko, A. V. 1982, PASP, 94, 715

Furusawa, H., Kosugi, G., Akiyama, M., et al. 2008, ApJS, 176, 1

Garilli, B., Fumana, M., Franzetti, P., et al. 2010, PASP, 122, 827

Graham, A. W. & Driver, S. P. 2005, PASA, 22, 118

Grogin, N. A., Kocevski, D. D., Faber, S. M., et al. 2011, ApJS, 197, 35

Guo, Y., Ferguson, H. C., Giavalisco, M., et al. 2013, ApJS, 207, 24

Hashimoto, T., Verhamme, A., Ouchi, M., et al. 2015, ApJ, 812, 157

Hildebrandt, H., Erben, T., Dietrich, J. P., et al. 2006, A&A, 452, 1121

Ivezić, Ž., Connelly, A. J., VanderPlas, J. T., & Gray, A. 2014, Statistics, Data Mining, and Machine Learningin Astronomy

Jones, E., Oliphant, T., Peterson, P., et al. 2001–, SciPy: Open source scientific tools for Python, [Online; accessed 2016-01-15]

Kennicutt, Jr., R. C. 1992, ApJS, 79, 255

Koekemoer, A. M., Faber, S. M., Ferguson, H. C., et al. 2011, ApJS, 197, 36

Kron, R. G. 1980, ApJS, 43, 305

Le Fèvre, O., Cassata, P., Cucciati, O., et al. 2013, A&A, 559, A14

Le Fèvre, O., Tasca, L. A. M., Cassata, P., et al. 2015, A&A, 576, A79

Le Fèvre, O., Vettolani, G., Garilli, B., et al. 2005, A&A, 439, 845

Mallery, R. P., Mobasher, B., Capak, P., et al. 2012, ApJ, 760, 128

Masias, M., Freixenet, J., Lladó, X., & Peracaula, M. 2012, MNRAS, 422, 1674

Matthee, J., Sobral, D., Santos, S., et al. 2015, MNRAS, 451, 400

McLinden, E. M., Finkelstein, S. L., Rhoads, J. E., et al. 2011, ApJ, 730, 136

Momcheva, I. G., Brammer, G. B., van Dokkum, P. G., et al. 2015, ArXiv e-prints

Noll, S., Mehlert, D., Appenzeller, I., et al. 2004, A&A, 418, 885

Pence, W. D., Chiappetti, L., Page, C. G., Shaw, R. A., & Stobie, E. 2010, A&A, 524, A42

Popesso, P., Dickinson, M., Nonino, M., et al. 2009, A&A, 494, 443

Raiter, A., Schaerer, D., & Fosbury, R. A. E. 2010, A&A, 523, A64

Ryabchikova, T., Piskunov, N., Kurucz, R. L., et al. 2015, Phys. Scr, 90, 054005

Salvadori, S., Dayal, P., & Ferrara, A. 2010, MNRAS, 407, L1

Schaerer, D. 2003, A&A, 397, 527

Schaerer, D. 2013, in Astrophysics and Space Science Library, Vol. 396, Astrophysics and Space Science Library, ed. T. Wiklind, B. Mobasher, & V. Bromm, 345

Schwartz, M. & Shaw, L. 1975, Signal processing: discrete spectral analysis, detection, and estimation (Tokyo: McGraw-Hill Kogakusha, Ltd.)

Shibuya, T., Ouchi, M., Nakajima, K., et al. 2014, ApJ, 788, 74

Skelton, R. E., Whitaker, K. E., Momcheva, I. G., et al. 2014, ApJS, 214, 24

Song, M., Finkelstein, S. L., Gebhardt, K., et al. 2014, ApJ, 791, 3

Soto, K. T., Lilly, S. J., Bacon, R., Richard, J., & Conseil, S. 2016, MNRAS, 458, 3210

Streicher, O., Weilbacher, P. M., Bacon, R., & Jarno, A. 2011, in Astronomical Society of the Pacific Conference Series, Vol. 442, Astronomical Data Analysis Software and Systems XX, ed. I. N. Evans, A. Accomazzi, D. J. Mink, & A. H. Rots, 257

Tasca, L. A. M., Le Fevre, O., Ribeiro, B., et al. 2016, ArXiv e-prints

van Breukelen, C., Jarvis, M. J., & Venemans, B. P. 2005, MNRAS, 359, 895

van der Walt, S., Colbert, S. C., & Varoquaux, G. 2011, Computing in Science & Engineering, 13, 22

Vanzella, E., Cristiani, S., Dickinson, M., et al. 2008, A&A, 478, 83

Vanzella, E., Cristiani, S., Dickinson, M., et al. 2006, A&A, 454, 423

Vio, R. & Andreani, P. 2016, A&A, 589, A20

Wall, J. V. 1979, QJRAS, 20, 138

Weilbacher, P. M., Roth, M. M., Pécontal-Rousset, A., & Bacon, R. 2006, New A Rev., 50, 405

Weilbacher, P. M., Streicher, O., Urrutia, T., et al. 2012, in Society of Photo-Optical Instrumentation Engineers (SPIE) Conference Series, Vol. 8451, Society of Photo-Optical Instrumentation Engineers (SPIE) Conference Series, 84510B

Weilbacher, P. M., Streicher, O., Urrutia, T., et al. 2014, in Astronomical Society of the Pacific Conference Series, Vol. 485, Astronomical Data Analysis Software and Systems XXIII, ed. N. Manset & P. Forshay, 451

Wuyts, S., Labbé, I., Förster Schreiber, N. M., et al. 2008, ApJ, 682, 985

Zackay, B. & Ofek, E. O. 2015, ArXiv e-prints

Chapter 6

Outlook: Towards a Lyman α emitter luminosity function from the MUSE-Wide survey

6.1 Introduction

One of the fundamental statistical tools to characterise a population of galaxies is the luminosity function (LF). The differential LF is the probability density $\phi(L)$ that describes the relative number density of galaxies with different luminosities, such that the observed number density of galaxies $\mathrm{d}N/\mathrm{d}V$ within a differential luminosity interval $\mathrm{d}L$ can be written as $\mathrm{d}N/\mathrm{d}V = \phi(L)\,\mathrm{d}L$. Determining the evolution of the LF with cosmic look-back time provides an essential benchmark for theoretical models of structure formation in our universe (see Johnston 2011, for a historical and methodological review). Especially the UV ($\lambda \approx 1500\,\text{Å}$) luminosity density given by the integral $\rho_{\mathrm{UV}} = \int_L^\infty L_{\mathrm{UV}}\Phi(L_{\mathrm{UV}})\,\mathrm{d}L_{\mathrm{UV}}$ can be directly linked to the star-formation rate density. From ρ_{UV} the density of ionising photons can be inferred. However, the latter requires an extrapolation to faint luminosities where the UV continuum is out of reach for the current and even the next generation of telescopes and instruments (e.g. Windhorst et al. 2006; Dunlop et al. 2012; Bouwens et al. 2015). This is especially unsettling, since these low-luminosity galaxies are expected to provide the majority of the ionising photon budget in the universe.

Selecting high-z galaxies via there Lyman α (Lyα) emission line provides substantial samples of galaxies that have extremely faint or undetected UV continua, even in the deepest space-based imaging datasets (Bacon et al. 2015 and Chapter 5). Since the Lyα equivalent width (EW) establishes a direct conversion between UV luminosity and Lyα luminosity, Lyα selected samples provide an opportunity to constrain the faint end of the UV LF. In principle the intrinsic Lyα EW of a star-forming galaxy is determined by the star-formation history and by its metallicity (Schaerer 2003; Raiter et al. 2010). However, due to the complex Lyα radiative transfer in typical interstellar environments, the observed Lyα EW is influenced by a large number of physical quantities, with their exact order of precedence not being well understood (e.g., Hayes 2015; Herenz et al. 2016). Nevertheless, observationally the Lyα EW distribution can be constrained

Rikke Saust contributed to the results shown in this chapter with setting up the and running the source insertion experiments. Lutz Wisotzki helped with the calculation of the binned and cumulative luminosity functions.

at least for the UV-detected part of the LAE population. Using large LAE samples it will become feasible to probe if and how these distributions depend on the UV luminosity (Nilsson et al. 2009). With these EW distributions and an accurate determinations of the LAE LF it, then is possible to constrain the faint end of the UV LF. For example, Gronke et al. (2015) shows that probing the LAE LF to luminosities $L_{\mathrm{Ly}\alpha} \sim 10^{41}\,\mathrm{erg\,s^{-1}}$ enables us to determine the UV LF down to $M_{\mathrm{UV}} \sim 15$.

So far most of the large $z \gtrsim 2$ LAE samples that were used to construct luminosity functions were obtained via narrow-band imaging techniques (e.g. Taniguchi et al. 2003; Westra et al. 2006; Tapken et al. 2006; Gronwall et al. 2007; Ouchi et al. 2008; Grove et al. 2009; Shioya et al. 2009; Ouchi et al. 2010). Integral-field spectroscopic LAE LF determinations were performed by van Breukelen et al. (2005) and Blanc et al. (2011). Cassata et al. (2011) used the whole area covered by the VVDS slits to construct a LAE LF. At lower redshifts LAEs are only observable from space. Here, Wold et al. (2014) constructed a $z \sim 1$ LAE LF using GALEX grism data. The main result from all these surveys is that the LAE LF appears to be non-evolving between $z \sim 3$ and $z \sim 6$. At higher redshifts there is currently no consensus if there is an evolution between $z \sim 6$ and $z \sim 6.5$ (Ouchi et al. 2010; Matthee et al. 2016), but there seems to be a sudden decrease in the number density of LAEs at $z \gtrsim 7$ (e.g., Ota et al. 2008; Caruana et al. 2014). On the other hand, at $z \sim 2$ LAEs become fainter on average compared to higher redshifts and from $z \sim 2$ to $z \sim 1$ the LAE luminosity density decreases by a factor of ~ 20. Moreover, in the low-redshift ($z \sim 0.1 \ldots 0.5$) universe LAEs with $L_{\mathrm{Ly}\alpha} \sim 10^{42} \ldots 10^{41}\,\mathrm{erg\,s^{-1}}$ – as encountered frequently at high-z – are very rare (Cowie et al. 2010). While the evolution at low-z is commonly attributed to more evolved stellar populations, increased dust-contents, and an overall decrease in the cosmic star-formation rate density, the LAE LF evolution at $z \sim 7$ might indicate that the re-ionisation of the universe was not complete at this epoch. In the present chapter, we construct a LF from the catalogue of LAEs at $3 \lesssim z \lesssim 6$ from the first data set of the ongoing MUSE-Wide survey. MUSE-Wide is the wide, but relatively shallow part, of our three-tiered wedding-cake survey strategy. By construction it does not probe the faint end of the LF. However, when complete, it delivers a large sample of ~ 1000 LAEs with $L_{\mathrm{Ly}\alpha} \sim 10^{42}\,\mathrm{erg\,s^{-1}}$. This sample will allow to perform both an accurate measurement of the LAE LF and the LAE EW distribution.

This chapter is structured as follows: In Sect. 6.2 we give a brief overview of the LAE sample and the MUSE-Wide survey. We then continue by describing our method to construct a realistic selection function for LAEs in the MUSE-Wide survey (Sect. 6.3.1). Next, we contrast this selection function with one that is obtained under the assumption that LAEs are point-like objects without extended structures (Sect. 6.3.2). Finally, in Sect. 6.4 we use these selection-functions to construct the LAE luminosity function. Since this chapter, in contrast to the previous chapters, presents results of a work-in-progress project, we conclude with an outlook on future work in Sect. 6.5.

6.2 Data and catalogue

A complete overview over the MUSE-Wide dataset is used in this chapter is presented in Chapter 5. Here we use the sample of 237 $z \lesssim 3 \lesssim 6$ LAEs from our catalogue of emission line selected galaxies. A complete list of the LAEs, as well as a spectral atlas are provided in Appendix A of this thesis. We exclude two bona-fide X-Ray detected AGN from this sample: MUSE-Wide ID (MW #) 11503085 and MW #2 10414050 (Urrutia et al., in prep).

Our total survey area is 22.2 arcmin^2. The MUSE wavelength range corresponds to a redshift

range for LAEs from $z_{\rm min} = 2.9$ to $z_{\rm max} = 6.7$. Integrating the comoving volume element over this redshift range and dividing by the survey area gives a total comoving survey volume of $2.3{\times}10^5{\rm Mpc}^3$.

6.3 The LAE selection function of MUSE-Wide

The selection function is needed to correct for the *Malmquist* bias – the preferential selection of intrinsically bright objects at greater distances – in our catalogue when constructing the LF. In our integral-field spectroscopic LAE survey it is the probability $f_C(F_{{\rm Ly}\alpha}, \lambda)$ that a LAE with a given flux $F_{{\rm Ly}\alpha}$ at a given wavelength λ is contained in in our catalogue. Equivalently $f_C(F_{{\rm Ly}\alpha}, \lambda)$ corresponds to the fraction of the total survey area where we are complete for a given $(F_{{\rm Ly}\alpha}, \lambda)$-pair. Since we can transform uniquely[1] between $(F_{{\rm Ly}\alpha}, \lambda)$ and $(L_{{\rm Ly}\alpha}, z)$, we can construct from $f_C(F_{{\rm Ly}\alpha}, \lambda)$ the completeness correction $f_C(L_{{\rm Ly}\alpha}, z)$. Using this, our maximum survey volume $V_{{\rm max},i}$ for an LAE with given $L_{{\rm Ly}\alpha,i}(F_{{\rm Ly}\alpha,i}, \lambda_i)$ in our sample is calculated via

$$V_{{\rm max},i} = \omega \int_{z_{\rm min}=2.9}^{z_{\rm max}=6.7} f_C(L_{{\rm Ly}\alpha,i}, z) \frac{{\rm d}V}{{\rm d}z} {\rm d}z \; . \tag{6.1}$$

Here ${\rm d}V/{\rm d}z$ is the comoving volume element (per unit solid angle, e.g. Hogg 1999) and $\omega = 22.2\,{\rm arcmin}^2$ is our total survey area.

In order to construct $f_C(F_{{\rm Ly}\alpha}, \lambda)$ for MUSE-Wide, we study the success rate of recovering artificially-implanted implanted LAEs as a function of their fluxes and wavelength positions in the MUSE-Wide datacubes. In Sect. 6.3.1 we perform this experiment with real LAEs in order to cover the variety of observed spatial and spectral profiles. We contrast these results in Sect. 6.3.2 with a similar experiment where we assume point-like emitters with a Gaussian spectral profiles.

6.3.1 Selection function from source recovery experiment with rescaled MUSE HDF-S LAEs

We perform a source insertion and recovery experiment using the 10 highest S/N LAEs from the MUSE HDF-S (Bacon et al. 2015) catalogue (MUSE HDF-S ID 43, 92, 95, 112, 139, 181, 246, 325, 437, and 547 – all have fluxes measured at signal-to-noise ratios >10). These sources represent realistic test sources for our recovery experiment: On the one hand, they show a range of different surface-brightness profiles: E.g., while the LAEs #43, #92, and #95 are fairly extended, the LAEs #181, #325, and #542 show more compact surface brightness profiles (Wisotzki et al. 2016). On the other hand, these LAEs represent also a range in fluxes and redshifts that overlap well with the fainter part our sample (see Fig. 6.1).

To determine the recovery rate as a function of flux in our experiment, we have to rescale the total flux of the fake sources. For this purpose we first measure the fluxes from the MUSE HDF-S LAEs by utilising LSDCat's flux-measurement routine with circular apertures of $3R_{\rm Kron}$ radius (Chapter 4). This is the same flux measurement that was used for the MUSE-Wide LAEs in Chapter 5. We cut out mini cubes from the MUSE HDF-S datacube centred on the LAEs. These are then re-scaled to reach the desired flux levels. In particular we re-scale the LAEs to 20 different flux levels between $\log F_{{\rm Ly}\alpha} = -17.5$ to $\log F_{{\rm Ly}\alpha} = -15.5$ in steps of 0.1 dex, where $F_{{\rm Ly}\alpha}$ is in units of ${\rm erg\,s^{-1}cm^{-2}}$.

These 20×10 (flux samples × source samples) "fake-source" mini cubes are now inserted into each of our 24 MUSE-Wide datacubes at five different wavelengths λ_i. These wavelengths

[1] As mentioned in Sect. 1.1, throughout this thesis we use a 737-cosmology: $\Omega_\Lambda = 0.7$, $\Omega_M = 0.3$, and $h = 0.7$.

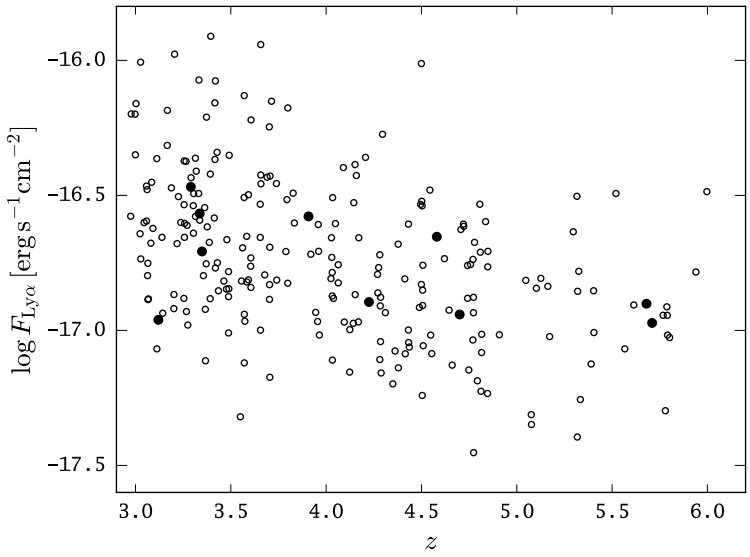

Figure 6.1: Lyα fluxes and redshifts of our LAE sample (circles) compared to the fluxes and redshifts of the 10 highest S/N LAEs from the MUSE HDF-S LAE sample (filled circles; Bacon et al. 2015; Wisotzki et al. 2016) that are used for the construction of the selection function.

are λ_1 =5000Å, λ_2 =6861.25Å, λ_3 =7100Å, λ_4 =7242.5Å, and λ_5 =8292.5Å. They are chosen to sample representative regions of the noise background spectrum (see Fig. 6.2). The regions around 5000Å and 7100Å are devoid of telluric line emission, 6861.25Å is in the wing of such a line, and the 7242.5Å and 8292.5Å positions are chosen to lie right between such lines.

At each of those wavelengths we insert the "fake source" at $N_{\mathrm{total}} = 64$ different spatial positions. Instead of placing the sources on a regular grid, we use a quasi-random grid based on a Sobol-sequence (Sect. 7.7 of Press et al. 1992). We do this to avoid placing the sources in regions that have similar distances to the edges of the MUSE slicer-stacks which are arranged in a rectangular grid.

Moreover, when inserting the flux-rescaled mini cubes into the MUSE-Wide data we account for the difference between the point-spread functions (PSF) in MUSE-Wide and in the MUSE HDF-S observations. Since in all MUSE-Wide datacubes the PSF-FWHM is larger compared to the HDF-S we have to degrade the PSF of the mini cubes. We do this by assuming a Gaussian PSF which represents a good approximation for the core of the PSF. Under this assumption we convolve the spatial layers of the "fake datacubes" with a 2D Gaussian with dispersion $\sigma_{2D}(\lambda) = \sqrt{\sigma_{\mathrm{MW}}(\lambda)^2 - \sigma_{HDFS}(\lambda)^2}$, where $\sigma_{\mathrm{MW}}(\lambda)$ and $\sigma_{HDFS}(\lambda)$ are the wavelength dependent PSF dispersions of the MUSE-Wide datacube and the MUSE HDF-S datacube, respectively. The determination of $\sigma_{\mathrm{MW}}(\lambda)$ for the 24 MUSE-Wide datacubes is extensively described in the first MUSE-Wide Chapter 5 of this thesis (Sect. 5.3.1.3). In brief, we model the $\sigma_{\mathrm{MW}}(\lambda)$-dependency as a linear function that is determined from fits to stars or compact galaxies in the field. The MUSE HDF-S PSF is determined in a similar manner from fits to the brightest star in the field (cf. Fig. 2 of Bacon et al. 2015).

Having produced fake source datasets by using rescaled real LAEs from the MUSE HDF-S dataset, we can now perform the recovery experiment. To reduce the computational cost in this experiment, we trim the fake-source inserted cubes in wavelength range to ±30Å around each insertion wavelength. The full recovery experiment is thus performed on 20×10×5×24 = 24000

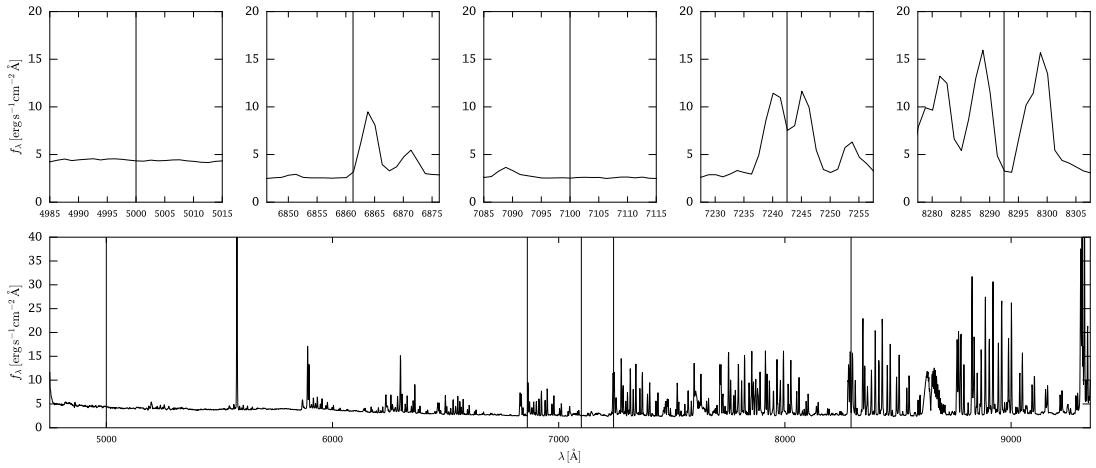

Figure 6.2: Wavelength locations where the flux-rescaled MUSE HDF-S Lyα emitters are inserted. The bottom panel shows the background noise over the whole spectral range, vertical lines indicate the positions of the insertion wavelengths. The top panels are zoomed in versions around the regions of interest.

datacubes of dimensions $\sim 300 \times 300 \times 50$ (neglecting empty edges due to the rotation of the MUSE-Wide pointings). Each of these cubes is processed with `LSDCat` (Chapter 4) using the same optimal parameters that have been used to generate the catalogue of LAEs in the 24 MUSE-Wide fields (Chapter 5, Sect. 5.3.1.3). For each recovery experiment we then count the number of recovered sources $N_{\mathrm{det.}}$ above the detection threshold $\mathrm{S/N_{det.}} = 8$ that was used in the creation of the MUSE-Wide LAE source catalogue.

Exemplarily, we show the outcome of the recovery experiment for the MUSE-Wide pointing 01 datacube in Fig. 6.3. The results in for the other datacubes are similar: We find that the completeness curves for all emitters have a very steep cut-off at line fluxes of $10^{-16} \ldots 10^{-17}$ erg s^{-1}cm^{-2}. The exact turnover point on a given curve appears to be a complicated function of a source's surface-brightness profile and its spectral profile. However, we observe that for a given source all curves are self-similar and the shift depends only on the wavelength (Fig. 6.2). Since our 10 artificially added LAEs are expected to be a subset of the overall high-z LAE population, we expect the overall LAE selection function at a specific wavelength to be the average recovery fraction over all sources $\langle N_{\mathrm{det.}}/N_{\mathrm{tot}} \rangle$ at this wavelength. In Fig. 6.4 we show these averaged recovery fractions for three different+ datacubes .

Up to this point we are equipped with LAE selection functions for the MUSE-Wide LAEs only at 5 different wavelengths within the MUSE wavelength range. However, we notice in Fig. 6.5 that the curves at the different wavelengths are self-similar and that their order in flux is always the same. This result indicates that there is a universally shaped selection function whose shift with respect to the flux axis is determined by a wavelength dependent quantity. Indeed, we find that the shift of the 50% completeness point ($f_C(F_{50}) = 0.5$) of above curves shows a nearly constant $F_{50}/\tilde{\sigma}_{\mathrm{emp.}}$ ratio for all curves, with $\tilde{\sigma}_{\mathrm{emp}}$ being the empirically determined background noise (Chapter 5, Sect. 5.3.1.1) convolved with a 250 km s^{-1} wide (full width at half maximum) Gaussian that is used in the MUSE-Wide emission line detection (Sects. 5.3.1.3 and 5.3.1.4). The ratio $F_{50}/\tilde{\sigma}_{\mathrm{emp.}}(\lambda)$ is between 400 and 460 for the different datacubes; the exact value depends on the average datacube background noise and is a function of the observing conditions. Using this scaling we can compute $f_{C,i}(F_{\mathrm{Ly}\alpha}, \lambda)$ for each of the 24 MUSE-Wide pointings: We create

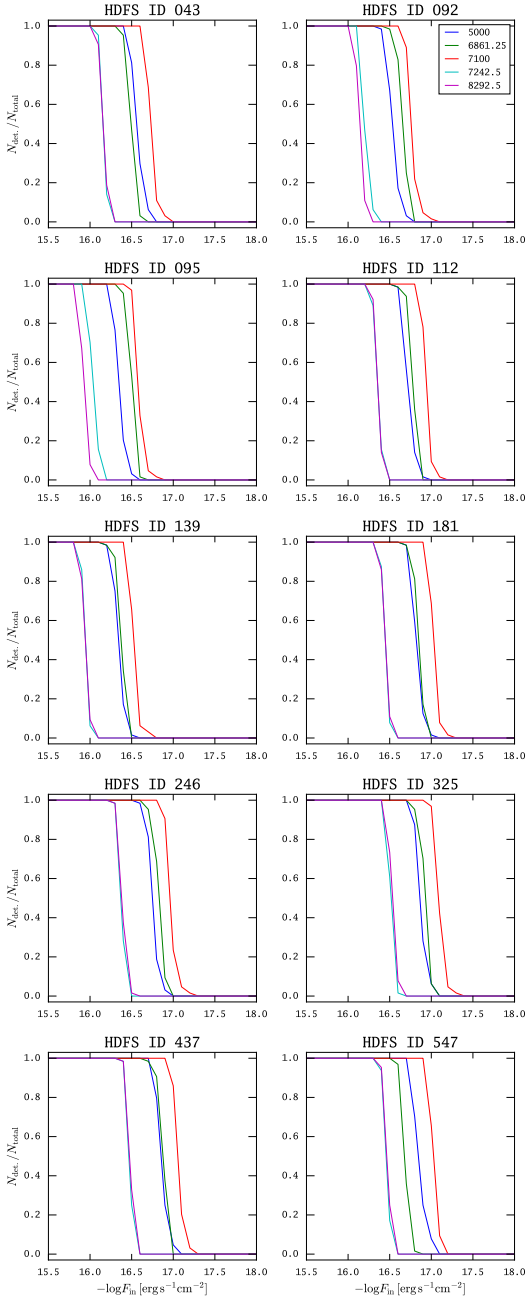

Figure 6.3: Outcome of the source recovery experiment with 10 MUSE HDF-S LAEs artificially inserted into MUSE-Wide datacube 01. Each panel displays the recovery fraction $N_{\rm det.}/N_{\rm total}$ for a particular MUSE HDF-S LAE of as a function of its scaled flux at 5 different wavelengths (5000Å: blue, 6861.25Å: green, 7100Å: red: 7242.5Å, magenta: 8292.5Å). $N_{total} = 64$ is the number of inserted sources at a given flux level and $N_{\rm det.}(F_{{\rm Ly}\alpha})$ is the number of recovered sources with same detection procedure used to construct the original catalogue.

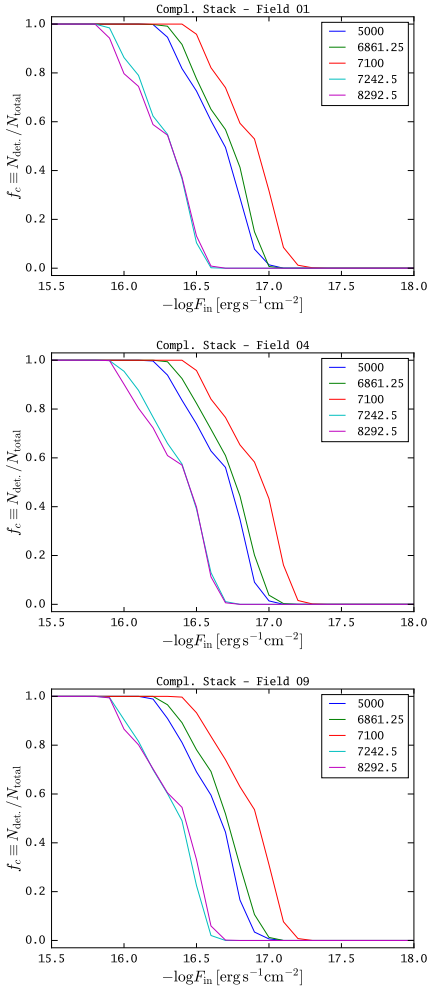

Figure 6.4: Stack over the recovery fractions $N_{\rm det.}/N_{\rm total}$ of the 10 different MUSE HDF-S LAEs used in the source recovery experiment. These curves represent the selection function at 5 different wavelengths in a MUSE-Wide datacube. Exemplarily, we show only the results for the MUSE-Wide datacubes 01, 04, and 09. The curves are similar for all other fields.

a master $f(F)$-curve from shifting the 5 stacked curves on top of each other by requiring them to have the same $f_C(F'_{50}) = 0.5$ value. For each wavelength bin we then shift this $f(F)$-master curve according to the $F_{50}/\tilde{\sigma}_{\rm emp.}(\lambda)$-proportionality to obtain $f_{C,i}(F_{{\rm Ly}\alpha}, \lambda)$. Since the area of each pointing is the same and we account for double detections in the overlapping regions by only keeping one source in the final catalogue (Sect. 5.3.2), the final selection function for the MUSE-Wide LAE catalogue is the average of all 24 selection functions (Avni & Bahcall 1980).

In Fig. 6.5 we show the resulting selection function $f(F_{{\rm Ly}\alpha}, \lambda)$. In this figure we also plot all the $F_{{\rm Ly}\alpha,i}, \lambda_i$ values of the LAEs in our sample with their 1σ error-bars on the flux measurement (Chapter 4, Sect. 4.2.3; Chapter 5, Sect. 5.3.1.5). Although $\sim 10\%$ of the LAEs are in regions where $f_C < 0.1$, none is within its error-bars in regions where the completeness is completely zero. In Fig. 6.6 we show this completeness function in redshift–luminosity space including the $L_{{\rm Ly}\alpha,i}, z_i$ values derived from our sample.

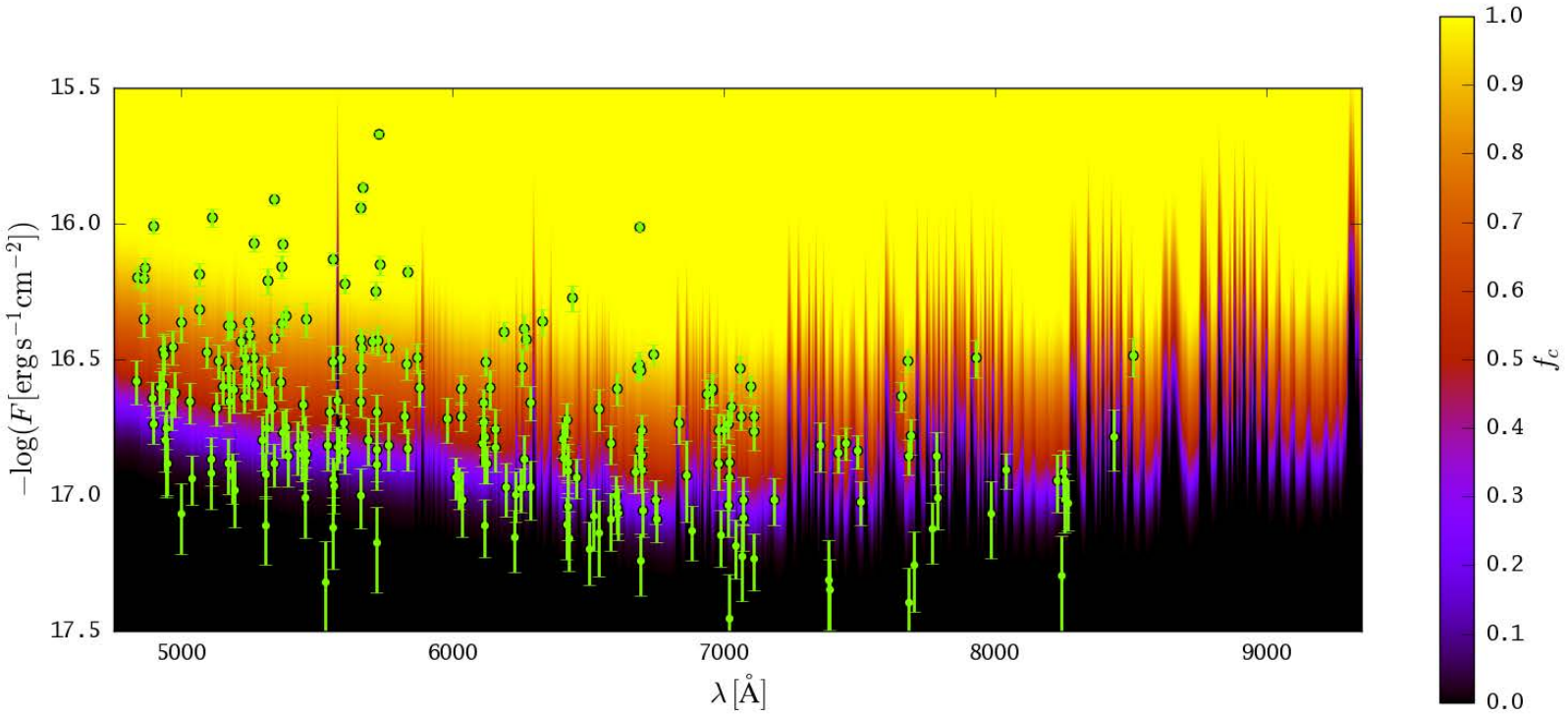

Figure 6.5: Expected completeness fraction f_C for the MUSE-Wide LAEs from Chapter 5 at a given flux as a function of wavelength from source recovery experiment with MUSE HDF-S LAEs. The value of f_C at a given flux and wavelength is equivalent to the fraction of our 22.2 arcmin^2 survey area for which our dataset reaches this flux limit for LAEs. The points mark the fluxes and 1σ errors of the detected Lyα emitters in the survey.

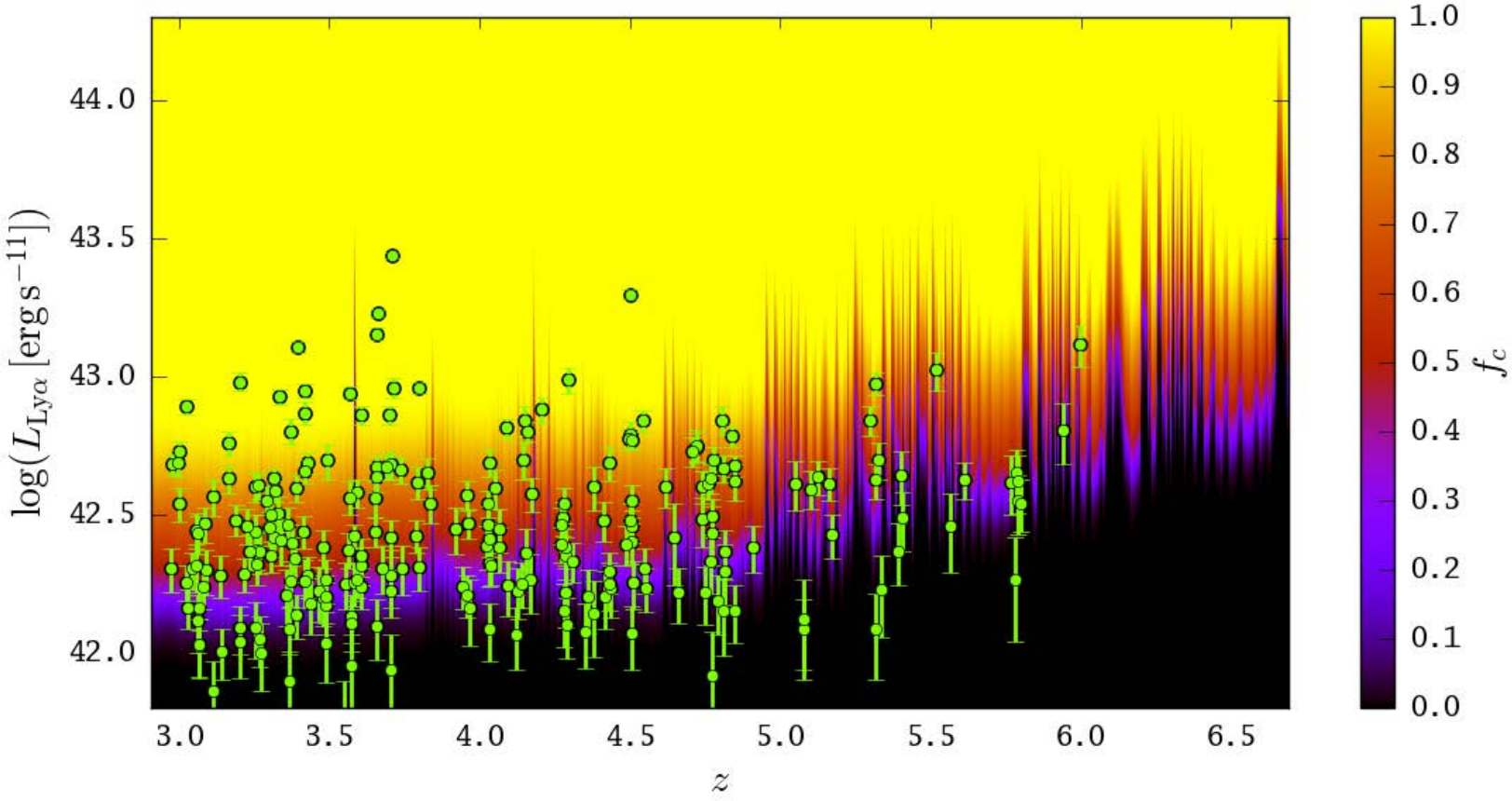

Figure 6.6: Similar to Fig. 6.5, but showing f_C for given Lyα luminosities and redshifts.

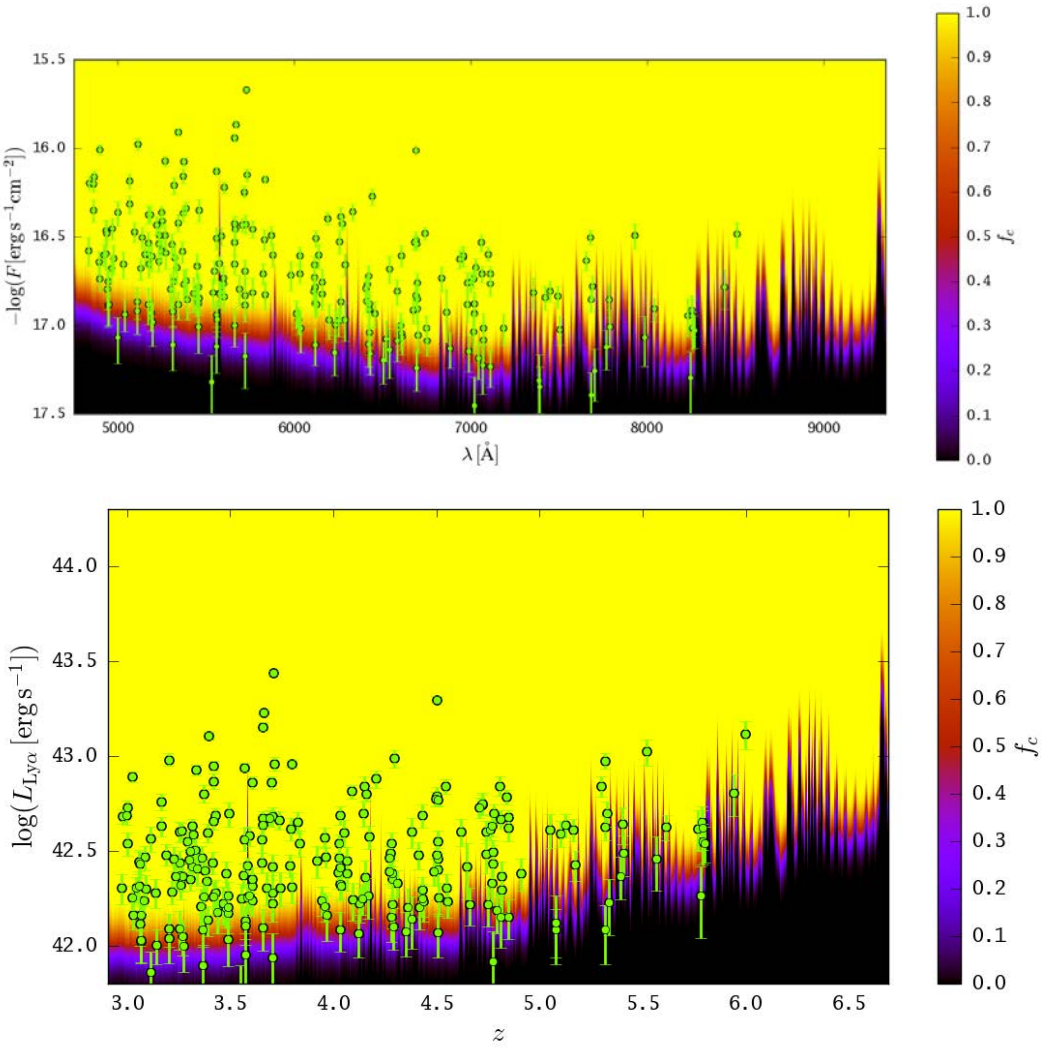

Figure 6.7: Expected completeness fraction f_C if MUSE-Wide LAEs would be perfect point sources. The *top panel* shows f_C at a given flux and wavelength , while the *bottom panel* shows it for given Lyα luminosities and redshifts.

6.3.2 Selection function from source recovery experiment with artificial point sources

We also compute a selection function for an over-simplified case where we assume that Lyα emitters are perfect point sources (modelled by a Moffat function) and that their spectral line can be regarded as a simple Gaussian of 250 km s^{-1} width. We populate the cubes with this artificial source in the same manner as outlined in the previous section. The full width at half maximum of the Moffat function is set according to PSF determination outlined in Sect. 5.3.1.3 and fixing $\beta \equiv 3$ (cf. Eq. 4.11). Then the recovery fraction is determined in complete analogy to the previous section, with the only difference that no stack over different sources needs to be constructed. The resulting selection function for a point-like line emitter is shown in Fig. 6.7.

The selection function resulting from this exercise can be seen as a limiting depth of our survey, since it resembles closely the template of the matched filter used in the emission line

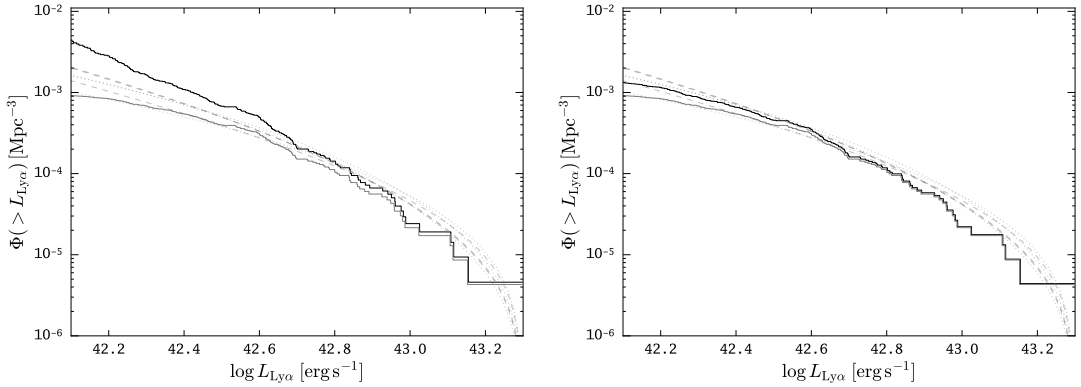

Figure 6.8: Cumulative Lyα luminosity distributions $\Phi(> L_{\mathrm{Ly}\alpha})$ of the MUSE-Wide LAE sample. The black line *left panel* shows $\Phi(> L_{\mathrm{Ly}\alpha})$ estimated using the realistic selection function from our source recovery experiment with flux-rescaled MUSE HDF-S LAEs (Sect. 6.3.1). The black line in the *right panel* shows $\Phi(> L_{\mathrm{Ly}\alpha})$ estimated using the simplified selection function that uses perfect point-sources in the source recovery experiment (Sect. 6.3.2). The grey line in both panels is the cumulative distribution without applying the selection function. In both panels we also show $\Phi(> L_{\mathrm{Ly}\alpha})$ according to the best fit Schechter analytic parameterisation (Schechter 1976) of the LF (Eq. 6.4) as derived by Ouchi et al. (2008) in their narrow-band Lyα survey. The dashed (dotted) lines show the best fits for their samples at $z = (3.1\,, 3.7,\ 5.7)$ with fixed faint-end slope of $\alpha = 2$ ($\alpha = 1.5$).

source detection (Sect. 5.3.1.3). More importantly, however, in comparison to our realistic selection function (Fig. 6.5) it also demonstrates the loss in sensitivity in LAE surveys due to the fact that these sources are not always compact. As shown by Steidel et al. (2010), Momose et al. (2014), and Wisotzki et al. (2016) LAEs often exhibit significant faint halo components (see also Momose et al. 2016). In extreme cases these extended low surface brightness structures can contain up to 90% of the total Lyα flux (Wisotzki et al. 2016). Yet, all previous surveys have not accounted for this component in their selection function construction. For example, Ouchi et al. (2008) populate their narrow band imaging data with fake point sources, and Matthee et al. (2015) rescale fluxes of other sources in the narrow-band filter that originally did not show a narrow-band flux excess. Since these studies use `SExtractor` (Bertin & Arnouts 1996) for source detection in their imaging data with parameters optimised for the detection of compact sources. we speculate that the used selection functions in those studies are overoptimistic. This becomes especially important at the faint end of the Lyα LF, where current studies at $z \sim 6.5$ appear to be in subtle disagreement (Ouchi et al. 2010; Matthee et al. 2015).

6.4 First results on the Lyα luminosity function

We construct the Lyα LF using the popular $1/V_{max,i}$-estimator (Schmidt 1968; Felten 1976). This classical non-parametric LF estimator is commonly employed in the studies of the LAE selection function (e.g. Gronwall et al. 2007; Ouchi et al. 2008; Cassata et al. 2011; Blanc et al. 2011). With this estimator the cumulative luminosity distribution

$$\Phi(> L_{\mathrm{Ly}\alpha}) = \int_{L_{\mathrm{Ly}\alpha}}^{\infty} \phi(L)\mathrm{d}L \tag{6.2}$$

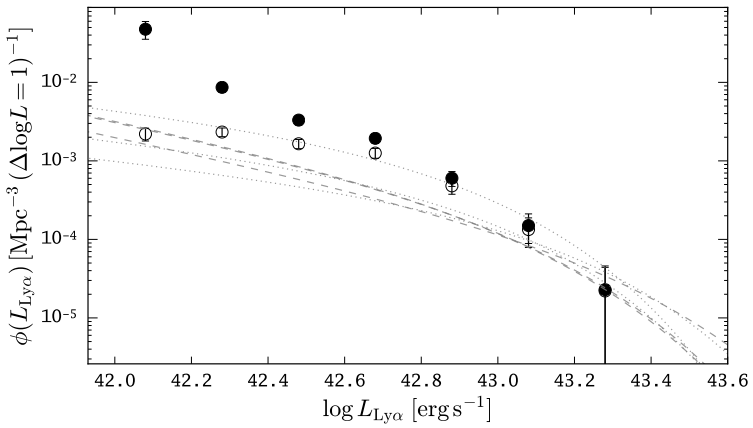

Figure 6.9: Differential LF from the $1/V_{\mathrm{max,j}}$-estimator for the MUSE-Wide LAE sample. The filled circles are completeness-corrected with the selection function from our source recovery experiment with flux-rescaled MUSE HDF-S LAEs (Sect. 6.3.1). The empty circles are completeness-corrected with the the simplified selection function that uses perfect point-sources in the source recovery experiment (Sect. 6.3.2). We also show the best fit Schechter parametrisations of the LF (Eq. 6.4) derived by Ouchi et al. (2008) in their narrow-band Lyα survey. The dashed (dotted) lines show these functions for their samples at $z = (3.1\,, 3.7,\ 5.7)$ with fixed faint-end slope of $\alpha = 2$ ($\alpha = 1.5$).

is approximated as

$$\Phi(>L_{\mathrm{Ly}\alpha}) \approx \frac{N(>L_{Ly\alpha,k})}{V} = \sum_{i>k} \frac{1}{V_{\mathrm{max,i}}}\,, \tag{6.3}$$

where the summation runs over all sources i with luminosities $L_{\mathrm{Ly}\alpha,i} > L_{\mathrm{Ly}\alpha,k}$ and $V_{\mathrm{max,i}}$ is given for each source by Eq. (6.1).

We show the so obtained cumulative luminosity distribution for the MUSE-Wide LAE sample in Fig. 6.8. In this figure we investigate the effect of our different selection functions on the recovered $\Phi(>L_{\mathrm{Ly}\alpha})$. Compared to the simplified selection function that assumes LAEs as perfect point-sources (Sect. 6.3.2), we find an increase by a factor of ~ 3 for $\Phi(>10^{42.2}\,\mathrm{erg\,s}^{-1})$ when using the realistic selection function that accounts for for the extended low-surface brightness Lyα haloes (Sect. 6.3.1). In Fig. 6.8 we also compare our results to the best-fit analytic Schechter LF parameterisations

$$\phi(L)\,\mathrm{d}L = \phi^*\left(\frac{L}{L^*}\right)^{-\alpha} \exp\left(-\frac{L}{L*}\right)\frac{\mathrm{d}L}{L^*}\,, \tag{6.4}$$

with overall normalisation ϕ^* [Mpc^{-3}], characteristic luminosity L^* [$\mathrm{erg\,s}^{-1}$], and faint-end slope α (Schechter 1976) from Ouchi et al. (2008). They derived these LFs in a narrow-band imaging survey of Ouchi et al. (2008) at three redshift slices centred at $z = (3.1\,, 3.7,\ 5.7)$. We find, that our data appears to indicate a steeper faint end slope than $\alpha > 2$. Interestingly, when we utilise the pure point-source selection function our $\Phi(L)$ distribution is in nearly perfect-agreement with the Ouchi et al. (2008) results.

We also compute an estimate of the differential LF $\phi(L)$ of our sample. Therefore we employ the non-parametric binned $1/V_{max,i}$-estimator

$$\phi(L_j)\,\mathrm{d}L \approx \frac{N(L_j - \Delta L/2 < L_j < L_j + \Delta L/2)}{V} = \sum_i \frac{1}{V_{\mathrm{max},i}}\,, \tag{6.5}$$

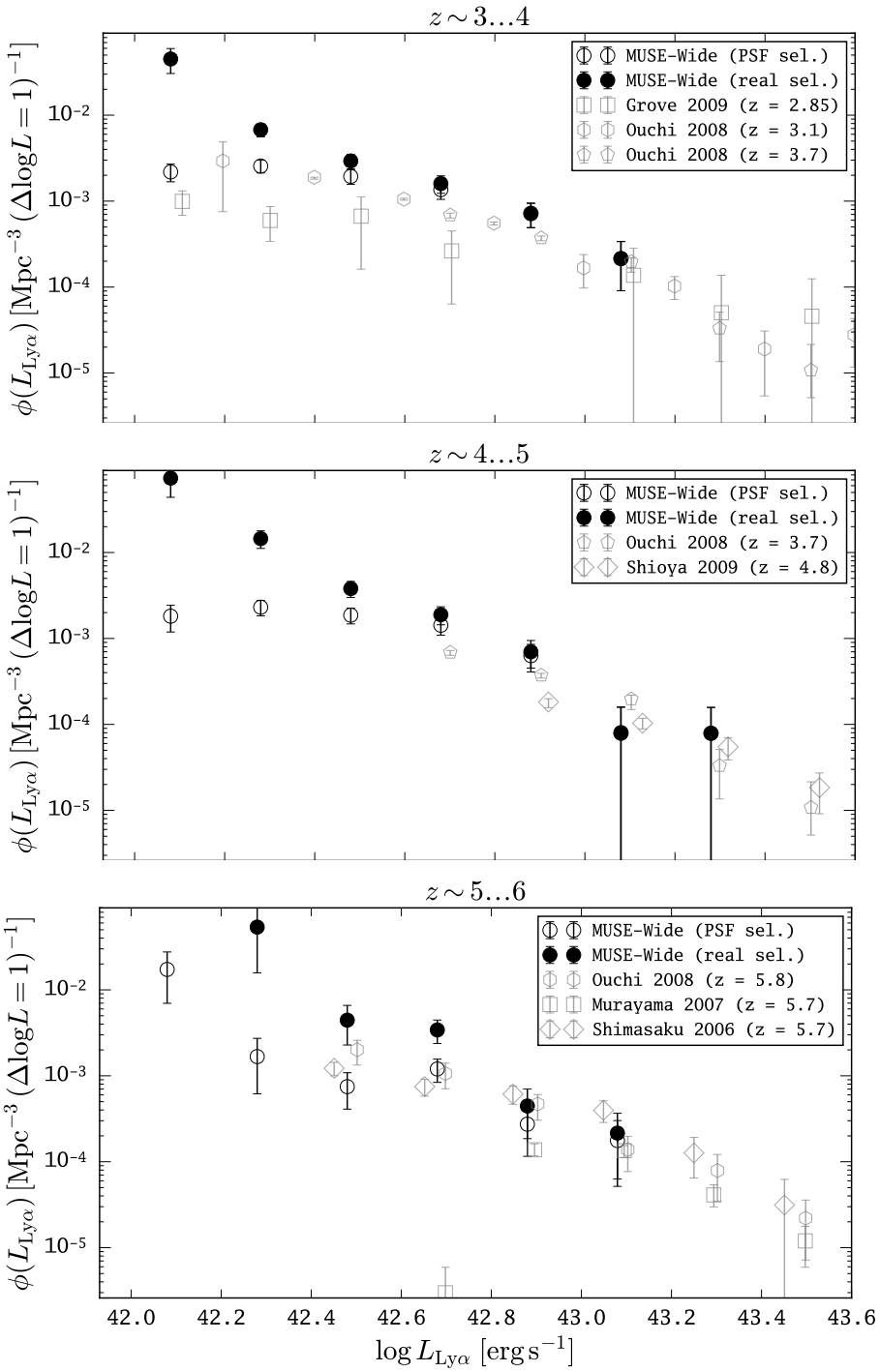

Figure 6.10: Luminosity function estimated with the non-parametric binned $1/V_{\mathrm{max},i}$ estimator for the MUSE-Wide LAE sample in three different redshift intervals (top panel: $3 \leq z < 4$, centre panel: $3 \leq z < 5$, bottom panel: $z > 5$). We contrast the differences in the LF determination between two different selection functions. Our selection functions result from source insertion and recovery experiments (Sect. 6.3). While in one recovery experiment LAEs were assumed to be perfect point sources (Sect. 6.3.2, open circles), in the other one we constructed a more realistic selection function by utilising flux-rescaled real LAEs from the MUSE HDF-S observations (Sect. 6.3.1, filled circles). In each panel we also compare to non-parametric estimates of the LAE LF at similar redshifts from the literature (see legend and text).

where the summation runs over all objects in a bin. In particular we bin logarithmically[2] in L: $\Delta \log L = 0.2$ and $\log L_j = 41.68 + j \times \Delta \log L$, $j = 1 \ldots 10$. In the following we consider only the bins $j > 3$ (i.e. $\log L_j > 42.28$) since the photometric 1σ errors on the few objects with lower luminosities are often larger than the bin-size. However, also at the considered luminosity bins photometric errors may scatter sources between different bins. For the present analysis we do not correct for this so called *Eddington* bias (Eddington 1913). Moreover, the error-bars in each bin are calculated by assuming Poisson fluctuations and homogeneity for each bin: $\sigma_{\phi,j} = (\sum_i 1/V^2_{\mathrm{max,i}})^{-1/2}$.

In Fig. 6.8 we show the so obtained estimate of the differential LF for the whole MUSE-Wide LAE sample. In analogy to the cumulative distribution we compare the result obtained with the simplified point-source selection function and the realistic LAE selection function. The difference between these two functions becomes apparent at luminosities $L_{\mathrm{Ly}\alpha} < 10^{42.7}\,\mathrm{erg\,s^{-1}}$. Again, also in this LF representation our data indicate a steeper slope at fainter luminosities. And, as already noted for the cumulative luminosity distribution, the LF of our sample is only in agreement with the LAE LF Schechter-parameterisations obtained by Ouchi et al. (2008) when we utilise the idealised selection function.

We study the redshift evolution of the differential LAE LF in Fig. 6.9. For this purpose we bin the MUSE-Wide LAEs in three different redshift intervals: $3 \leq z < 4$, $4 \leq z < 5$, and $z > 5$. In these intervals we compare with state-of-the-art luminosity functions obtained from wide-field narrow-band imaging surveys. At $3 \leq z < 4$ we compare to the results from Ouchi et al. (2008) obtained in the 1,deg^2 Subaru XDS survey at $z = 3.10 \pm 0.03$ and at $z = 3.7 \pm 0.05$ and to the results from the $z = 3.15 \pm 0.05$ VLT narrow-band imaging survey by Grove et al. (2009). At $4 \leq z < 5$ we compare again to the results from Ouchi et al. (2008) at $z = 3.7 \pm 0.05$ and to LF estimate from Shioya et al. (2009) from their $z = 4.86 \pm 0.03$ Subaru narrow-band survey in the COSMOS field. For the $z > 5$ sample we compare to the $z = 5.80 \pm 0.05$ result of Ouchi et al. (2008), and to the results at $z = 5.70 \pm 0.05$ from Shimasaku et al. (2006) in the Subaru Deep Field and from Murayama et al. (2007) in the COSMOS field.

Overall our results appear to be consistent with previous findings that there appears to be no evolution in the LAE LF at $3 \lesssim z \lesssim 6$. Moreover, MUSE-Wide – the shallowest part of the MUSE surveys – reaches at $z \sim 3 \ldots 4$ comparable depths to those narrow-band surveys. At higher redshifts MUSE-Wide probes even half a decade deeper. Notably, both the LFs estimated by Ouchi et al. (2008) and Grove et al. (2009) show a flattening towards lower luminosities, while our LF still rises. As previously seen (Fig. 6.8 and Fig. 6.10) we can reproduce this flattening when we utilise the selection function that was constructed under the premise that LAEs are perfectly point-like. However, since LAEs show extended low-surface brightness haloes that sometimes contain significant fractions of the total Lyα flux, a non-negligible amount of those faint extended LAEs is not detected. By accounting for this effect in our realistic selection function, the resulting LF must be corrected to higher number densities at the fainter luminosities.

Finally, we find that when combining our MUSE LAE LF estimate with the bright-end estimates from the wide-field narrow band surveys, that a Schechter-functional form (Eq. (6.4) does is not an optimal parametric description of the distribution. Instead, at least for the luminosity range covered so far, a simple power-law appears to be more valid. Recently Matthee et al. (2015) presented results from a shallow 4.6deg^2 wide-field narrow-band imaging campaign at $z = 6.6$. In their large volume they find two very bright, likely non-AGN, LAEs with

[2]This change to a logarithmic variable in a the LF changes the differential of the linear in L defined LF according to $\mathrm{d}L = \ln(10)\, L\, \mathrm{d}(log_{10}\, L)$.

$L_{\mathrm{Ly}\alpha} \approx 10^{44}\,\mathrm{erg\,s^{-1}}$. This translates into a volume density of $\sim 10^{-5.5}\,\mathrm{Mpc^{-3}}$ of these sources. This point would provide a natural extension of the above suggested power-law.

6.5 Conclusions and future prospects

In this final thesis chapter we provided first results on the derivation of a LAE LF from the MUSE-Wide survey. So far, the main conclusion of our project is, that extended low surface brightness emission from LAEs significantly impacts the detectability of sources near the point-source detection limit. This extended emission appears to be a generic property of high-z LAEs. However, the fraction of the total Lyα luminosity coming from this halo varies from object to object. We account for this statistically by utilising 10 real LAEs from the MUSE HDF-S observations in recovery experiment. We find that the selection function drops not as steep compared to a selection function expected for a perfect point source. Utilising such a more realistic selection function in the LF construction, leads to higher number densities of fainter LAEs. Previous studies have not taken extended Lyα emission into account when constructing the luminosity function. Intriguingly, when we employ a selection function expected for point-like emission to construct the MUSE-Wide LAE LF, we find that our results are in nearly perfect agreement with the literature. In consequence, our study indicates that the faint-end slope of the LAE LF might be significantly steeper than previously assumed.

In contrast to the projects presented previous chapters of this thesis, the derivation of the MUSE-Wide LAE LF is not finalised. We have limited ourselves to present only non-parametric LF estimators. In the LAE LF literature it is commonly found that, following construction of a binned LF (e.g. by employing the $1/V_{\mathrm{max},j}$-estimator), this estimate is χ^2-fitted with a Schechter-parameterisation (Eq. (6.4). While straight forward to implement, this approach is incorrect. It is obvious that the result of the three degenerate parameters Φ^*, L^* and α in such a fitting exercise depend strongly on the bin size. The correct approach when fitting a parametric model to observed data is to regard the observed values as a realisation of the particular model. Then one has to maximise the likelihood that this particular model reproduces the data (for a review of this approach in the context of LF derivation see e.g. Johnston 2011). Along these lines Shimasaku et al. (2006) and Ouchi et al. (2008) perform an artificial source recovery experiment in their Subaru imaging data. In their approach, they populate the image with "fake"-sources that are drawn from the Schechter-parameterisation. By repeating the experiment for a wide range of possible parameters and comparing the results with the observed datasets, they find Schechter-parameters that are most likely to reproduce the data. Of course, given the large data volume of the MUSE-Wide survey such an approach is not practical. However, given that we already have the selection function, we can perform a similar Monte Carlo experiment directly by comparing our catalogue to mock catalogues drawn from a luminosity function and observed through our selection function. For such an analysis we also aim at incorporating a model of the photometric uncertainties to control the possible *Eddington*-Bias. And of course, as our analysis has shown, the possible non-Schechter like form of the LAE LF needs to be taken into account.

MUSE-Wide is an ongoing survey. The sample used in this Chapter 5 is based on 1/4th of the planned total survey area. Increasing the sample size is not only necessary to reduce the error-bars of the existing LF. But, since extremely luminous LAEs are also very rare, a larger sample will also provide us with a better determination of the bright end. Combination with fainter luminosity samples that are collected at unprecedented depths in the MUSE-Deep project will then allow construct the LAE LF over more than six decades in Lyα luminosity from $10^{39}\,\mathrm{erg\,s^{-1}}$ to $\gtrsim 10^{45}\,\mathrm{erg\,s^{-1}}$. We emphasise that our survey of the high-z LAE population is performed in

fields with the deepest space-based imaging datasets. Thus it will provide a unique reference point for studies of galaxy formation processes in young and low mass galaxies at early cosmic epochs.

6.6 Bibliography

Avni, Y. & Bahcall, J. N. 1980, ApJ, 235, 694

Bacon, R., Brinchmann, J., Richard, J., et al. 2015, A&A, 575, A75

Bertin, E. & Arnouts, S. 1996, A&AS, 117, 393

Blanc, G. A., Adams, J. J., Gebhardt, K., et al. 2011, ApJ, 736, 31

Bouwens, R. J., Smit, R., Labbe, I., et al. 2015, ArXiv e-prints

Caruana, J., Bunker, A. J., Wilkins, S. M., et al. 2014, MNRAS, 443, 2831

Cassata, P., Le Fèvre, O., Garilli, B., et al. 2011, A&A, 525, A143

Cowie, L. L., Barger, A. J., & Hu, E. M. 2010, ApJ, 711, 928

Dunlop, J. S., McLure, R. J., Robertson, B. E., et al. 2012, MNRAS, 420, 901

Eddington, A. S. 1913, MNRAS, 73, 359

Felten, J. E. 1976, ApJ, 207, 700

Gronke, M., Dijkstra, M., Trenti, M., & Wyithe, S. 2015, MNRAS, 449, 1284

Gronwall, C., Ciardullo, R., Hickey, T., et al. 2007, ApJ, 667, 79

Grove, L. F., Fynbo, J. P. U., Ledoux, C., et al. 2009, A&A, 497, 689

Hayes, M. 2015, PASA, 32, 27

Herenz, E. C., Gruyters, P., Orlitova, I., et al. 2016, A&A, 587, A78

Hogg, D. W. 1999, ArXiv Astrophysics e-prints

Johnston, R. 2011, A&A Rev., 19, 41

Matthee, J., Sobral, D., Oteo, I., et al. 2016, MNRAS, 458, 449

Matthee, J., Sobral, D., Santos, S., et al. 2015, MNRAS, 451, 400

Moffat, A. F. J. 1969, A&A, 3, 455

Momose, R., Ouchi, M., Nakajima, K., et al. 2014, MNRAS, 442, 110

Momose, R., Ouchi, M., Nakajima, K., et al. 2016, MNRAS, 457, 2318

Murayama, T., Taniguchi, Y., Scoville, N. Z., et al. 2007, ApJS, 172, 523

Nilsson, K. K., Möller-Nilsson, O., Møller, P., Fynbo, J. P. U., & Shapley, A. E. 2009, MNRAS, 400, 232

Ota, K., Iye, M., Kashikawa, N., et al. 2008, ApJ, 677, 12

Ouchi, M., Shimasaku, K., Akiyama, M., et al. 2008, ApJS, 176, 301

Ouchi, M., Shimasaku, K., Furusawa, H., et al. 2010, ApJ, 723, 869

Press, W. H., Teukolsky, S. A., Vetterling, W. T., & Flannery, B. P. 1992, Numerical recipes in FORTRAN. The art of scientific computing

Raiter, A., Schaerer, D., & Fosbury, R. A. E. 2010, A&A, 523, A64

Schaerer, D. 2003, A&A, 397, 527

Schechter, P. 1976, Astrophys. J., 203, 297

Schmidt, M. 1968, ApJ, 151, 393

Shimasaku, K., Kashikawa, N., Doi, M., et al. 2006, PASJ, 58, 313

Shioya, Y., Taniguchi, Y., Sasaki, S. S., et al. 2009, ApJ, 696, 546

Steidel, C. C., Erb, D. K., Shapley, A. E., et al. 2010, ApJ, 717, 289

Taniguchi, Y., Shioya, Y., Ajiki, M., et al. 2003, Journal of Korean Astronomical Society, 36, 123

Tapken, C., Appenzeller, I., Gabasch, A., et al. 2006, A&A, 455, 145

van Breukelen, C., Jarvis, M. J., & Venemans, B. P. 2005, MNRAS, 359, 895

Westra, E., Jones, D. H., Lidman, C. E., et al. 2006, A&A, 455, 61

Windhorst, R. A., Cohen, S. H., Jansen, R. A., Conselice, C., & Yan, H. 2006, New A Rev., 50, 113

Wisotzki, L., Bacon, R., Blaizot, J., et al. 2016, A&A, 587, A98

Wold, I. G. B., Barger, A. J., & Cowie, L. L. 2014, ApJ, 783, 119

Appendix A

237 Lyman α emitting galaxies at $3 \lesssim z \lesssim 6$ from the MUSE-Wide survey

A.1 Catalogue

For reference we give in Table A.1 a catalogue of all 237 Lyman α emitters detected in the MUSE-Wide survey so far (Chapter 5). We list the objects with their MUSE-Wide ID, positions, redshifts, and fluxes (extracted in $3 \times R_{\mathrm{Kron}}$ radii).

Table A.1: Catalog of 237 Lyman α emitting galaxies in the MUSE-Wide region of the CDF-S

(1) MUSE-Wide ID	(2) RA [hh:mm:ss.ss]	(3) DEC [±dd:ss:mm.mm]	(4) z	(5) $F_{3R_{\rm Kron}}$ [10^{-17}cgs]	(6) $\Delta F_{3R_{\rm Kron}}$ [10^{-17}cgs]	(7) Confidence
10105016	03:32:16.56	-27:48:52.60	3.25748	2.49	0.38	2
10109024	03:32:12.66	-27:48:27.61	3.47936	2.17	0.34	1
10110025	03:32:15.76	-27:48:50.77	3.70334	1.48	0.35	2
10111026	03:32:14.70	-27:48:17.07	3.79441	3.05	0.4	2
10112027	03:32:12.96	-27:48:13.42	3.82689	3.22	0.41	2
10115031	03:32:13.57	-27:48:47.65	4.27553	1.71	0.24	3
10116032	03:32:13.04	-27:48:40.98	4.29585	5.32	0.56	3
10123043	03:32:16.24	-27:48:44.01	4.43189	2.47	0.34	3
10124044	03:32:16.16	-27:48:44.49	4.54431	3.31	0.28	3
10125045	03:32:16.45	-27:48:25.08	4.54833	0.96	0.18	2
10126046	03:32:12.23	-27:48:12.49	4.74834	0.71	0.17	2
10127047	03:32:15.29	-27:48:16.45	4.81602	0.97	0.2	2
10130050	03:32:14.75	-27:47:59.01	5.93967	1.65	0.41	1
10212085	03:32:17.95	-27:49:30.19	3.16729	6.53	0.64	3
10213086	03:32:15.95	-27:49:40.50	3.25527	4.24	0.52	3
10214087	03:32:19.20	-27:49:37.04	3.25491	2.92	0.44	1
10215088	03:32:16.57	-27:48:52.89	3.25692	2.21	0.36	2
10219097	03:32:18.39	-27:49:35.44	3.37243	6.16	0.65	3
10246172	03:32:17.08	-27:49:06.03	4.81535	0.83	0.2	2
10249176	03:32:17.87	-27:49:12.88	5.10303	1.43	0.22	2
10301001	03:32:19.19	-27:50:20.07	2.97467	2.65	0.48	2
10302002	03:32:16.13	-27:50:04.11	3.04522	2.51	0.36	2
10305045	03:32:16.88	-27:50:37.07	3.0807	2.1	0.37	3
10306046	03:32:16.62	-27:50:02.99	3.08488	3.54	0.52	3
10308055	03:32:18.22	-27:49:44.22	3.36296	2.85	0.44	2
10309056	03:32:17.93	-27:50:18.66	3.37083	1.76	0.32	2
10310057	03:32:17.01	-27:50:46.52	3.42957	1.78	0.3	2
10311058	03:32:18.41	-27:50:00.04	3.57094	1.15	0.23	2
10318081	03:32:19.14	-27:49:56.64	3.91963	1.91	0.36	3
10319082	03:32:19.18	-27:50:01.04	4.0252	1.56	0.28	3
10326097	03:32:18.77	-27:50:33.29	4.28395	1.23	0.22	2
10331105	03:32:17.02	-27:49:54.11	4.5061	1.41	0.19	3
10332106	03:32:17.31	-27:49:54.77	4.50604	1.24	0.21	3
10333107	03:32:18.32	-27:50:19.48	4.50929	0.88	0.17	2
10334108	03:32:18.37	-27:50:10.03	4.77322	0.35	0.16	1
10344120	03:32:16.66	-27:50:21.31	5.39021	0.75	0.19	1
10350126	03:32:16.57	-27:50:03.23	5.77937	0.5	0.21	2
10404029	03:32:19.37	-27:50:42.77	3.21814	2.1	0.3	3
10407038	03:32:18.84	-27:51:01.36	3.42792	4.57	0.41	3
10409041	03:32:18.68	-27:50:47.16	3.4881	1.65	0.3	2
10412048	03:32:18.24	-27:51:09.51	3.5499	0.48	0.2	2
10414050	03:32:18.85	-27:51:35.29	3.66091	13.59	0.55	3
10415052	03:32:18.28	-27:51:30.14	3.65707	3.76	0.36	3
10419059	03:32:20.84	-27:50:52.25	4.02952	1.86	0.3	2
10424069	03:32:20.26	-27:50:35.72	4.28847	0.7	0.17	1
10432086	03:32:20.59	-27:51:12.74	4.74176	1.74	0.24	2
10505027	03:32:21.59	-27:52:21.87	3.20509	10.54	0.79	3
10507031	03:32:20.34	-27:52:28.91	3.55598	1.52	0.29	2
10509034	03:32:21.36	-27:51:38.19	3.83334	2.5	0.38	2

(1)	(2)	(3)	(4)	(5)	(6)	(7)
10603018	03:32:17.95	-27:48:17.32	2.97756	6.33	0.55	3
10604019	03:32:17.08	-27:48:22.77	3.22526	3.13	0.46	3
10607033	03:32:21.07	-27:48:20.56	3.39471	12.28	0.62	3
10608034	03:32:18.64	-27:47:47.85	3.41319	2.61	0.36	2
10609035	03:32:18.89	-27:47:41.90	3.41919	1.7	0.33	2
10612043	03:32:17.29	-27:47:48.86	3.57371	1.08	0.22	2
10614046	03:32:17.22	-27:47:54.34	3.65695	11.44	0.61	3
10615047	03:32:20.67	-27:48:06.71	3.65561	1.0	0.25	3
10619055	03:32:17.53	-27:48:06.67	3.95882	2.47	0.3	3
10621059	03:32:21.13	-27:48:14.65	4.09046	4.01	0.33	3
10625070	03:32:20.22	-27:47:43.81	4.12428	1.01	0.21	2
10627072	03:32:18.82	-27:47:43.50	4.28138	1.91	0.28	3
10632083	03:32:18.13	-27:48:24.56	4.36158	0.84	0.22	2
10635088	03:32:17.16	-27:47:54.38	4.72158	2.43	0.29	2
10704077	03:32:20.19	-27:48:47.37	3.05754	3.42	0.5	2
10708086	03:32:21.93	-27:48:50.98	3.25391	1.31	0.31	3
10715098	03:32:20.15	-27:49:24.72	3.65797	3.49	0.43	3
10716099	03:32:19.63	-27:48:40.16	3.71341	7.06	0.58	3
10724120	03:32:19.52	-27:49:36.26	4.28154	0.78	0.2	2
10733150	03:32:22.47	-27:49:13.62	4.80641	2.93	0.33	2
10734151	03:32:19.43	-27:49:16.74	4.80895	1.95	0.21	3
10741159	03:32:21.12	-27:48:47.33	5.31555	3.14	0.29	3
10806104	03:32:22.90	-27:49:23.77	3.16654	4.84	0.57	2
10809107	03:32:21.93	-27:50:22.56	3.38693	2.12	0.39	2
10810108	03:32:21.86	-27:49:39.69	3.47714	1.42	0.3	2
10817130	03:32:23.00	-27:49:45.87	4.04891	2.49	0.41	2
10830156	03:32:20.04	-27:49:51.55	4.84748	1.72	0.26	2
10903027	03:32:21.38	-27:50:35.01	3.20125	1.2	0.32	2
10904028	03:32:23.85	-27:50:21.32	3.27054	2.45	0.44	2
10906034	03:32:23.58	-27:50:47.61	3.3763	2.42	0.41	2
10908036	03:32:23.77	-27:50:48.76	3.58397	1.51	0.27	1
10909037	03:32:23.18	-27:50:25.59	3.59259	3.18	0.37	3
10910038	03:32:22.71	-27:51:04.48	3.60549	1.44	0.24	2
10914056	03:32:21.98	-27:51:18.41	4.06351	1.5	0.28	3
10915057	03:32:22.60	-27:51:10.12	4.0636	1.75	0.31	3
10917059	03:32:23.99	-27:50:18.15	4.15155	4.11	0.5	3
10924083	03:32:21.52	-27:50:42.59	4.74181	1.31	0.27	2
10925084	03:32:24.70	-27:50:29.09	4.77272	1.33	0.2	3
11002003	03:32:25.14	-27:51:25.61	3.35628	1.59	0.36	2
11003005	03:32:26.74	-27:51:46.51	3.4165	6.96	0.66	2
11004006	03:32:26.07	-27:51:52.11	3.417	4.3	0.44	2
11006008	03:32:24.70	-27:51:47.65	3.70443	2.03	0.31	3
11007009	03:32:22.68	-27:51:22.11	3.70603	3.73	0.45	3
11015049	03:32:25.06	-27:52:02.09	4.14506	2.97	0.44	2
11018062	03:32:25.34	-27:51:46.27	4.64488	1.19	0.39	2
11101001	03:32:21.47	-27:47:42.28	3.09164	2.39	0.45	3
11102002	03:32:21.65	-27:48:25.24	3.48818	1.33	0.29	1
11109022	03:32:23.89	-27:48:07.76	4.2065	4.37	0.48	3
11110023	03:32:24.06	-27:47:39.86	4.28522	0.91	0.23	2
11113028	03:32:22.42	-27:47:23.80	4.37788	2.09	0.37	2
11115030	03:32:23.53	-27:48:03.84	4.48908	1.22	0.2	3
11116031	03:32:24.54	-27:47:35.59	4.50136	3.01	0.36	3
11121036	03:32:24.81	-27:47:58.81	5.99709	3.26	0.54	3

(1)	(2)	(3)	(4)	(5)	(6)	(7)
11205037	03:32:25.96	-27:49:02.47	3.05787	2.54	0.49	2
11206038	03:32:24.79	-27:48:56.93	3.33117	3.21	0.46	3
11207039	03:32:23.69	-27:48:28.93	3.46349	1.52	0.34	2
11208040	03:32:25.14	-27:48:51.97	3.49145	4.45	0.64	2
11214060	03:32:25.01	-27:49:02.16	4.28564	1.33	0.21	3
11222074	03:32:24.54	-27:49:06.94	4.77285	1.16	0.28	3
11227079	03:32:24.44	-27:48:38.70	5.12608	1.56	0.21	2
11305024	03:32:24.20	-27:49:50.61	3.26722	1.17	0.25	3
11307030	03:32:27.34	-27:49:52.37	3.65437	2.93	0.45	3
11314051	03:32:24.25	-27:49:53.47	4.15251	1.36	0.31	1
11406067	03:32:26.74	-27:50:10.12	3.43529	1.4	0.32	3
11410076	03:32:27.39	-27:50:26.70	4.03412	3.1	0.34	3
11419101	03:32:28.00	-27:50:23.17	4.72007	2.47	0.31	3
11503085	03:32:29.85	-27:51:05.80	3.70982	21.37	0.48	3
11504089	03:32:27.95	-27:51:51.44	3.0267	9.85	0.65	3
11508100	03:32:29.00	-27:51:23.14	3.11215	0.85	0.25	2
11512104	03:32:29.80	-27:51:04.40	3.31473	2.64	0.38	3
11520114	03:32:28.81	-27:51:07.05	3.58347	2.23	0.21	2
11521115	03:32:29.00	-27:51:44.07	3.59244	1.54	0.21	3
11522116	03:32:30.58	-27:51:22.82	3.60406	1.73	0.27	3
11524120	03:32:30.02	-27:51:08.11	3.69018	3.69	0.35	3
11528125	03:32:29.43	-27:51:28.16	3.7047	0.67	0.23	3
11532151	03:32:30.24	-27:51:32.37	4.03198	1.34	0.24	1
11535156	03:32:27.56	-27:50:58.69	4.12348	0.7	0.18	2
11536157	03:32:26.84	-27:51:20.71	4.31071	1.16	0.19	3
11543175	03:32:29.12	-27:51:27.04	4.77832	2.12	0.26	3
11545177	03:32:27.19	-27:51:45.81	4.84675	0.58	0.14	2
11602059	03:32:31.69	-27:50:55.97	3.06338	1.6	0.37	3
11605062	03:32:33.27	-27:51:27.50	3.11173	4.33	0.66	3
11611072	03:32:31.57	-27:51:13.79	3.27444	1.05	0.29	2
11615086	03:32:34.16	-27:51:18.00	3.48799	0.98	0.28	2
11616087	03:32:31.33	-27:51:12.90	3.60507	1.86	0.3	2
11619092	03:32:32.98	-27:50:37.10	3.70188	5.67	0.44	3
11621094	03:32:31.80	-27:51:22.71	3.70273	1.3	0.26	3
11623096	03:32:32.47	-27:51:21.36	3.94516	1.17	0.21	2
11624097	03:32:33.20	-27:51:10.24	3.96454	0.96	0.26	2
11635137	03:32:32.08	-27:51:20.38	4.77003	0.92	0.22	2
11639142	03:32:31.61	-27:50:49.33	5.32511	1.66	0.25	3
11701001	03:32:37.98	-27:50:52.67	3.02402	2.28	0.34	2
11702002	03:32:37.01	-27:50:47.76	3.02773	1.84	0.3	2
11705019	03:32:36.93	-27:51:06.21	3.36701	0.77	0.22	2
11706020	03:32:35.30	-27:50:51.08	3.57078	0.76	0.23	2
11711043	03:32:36.33	-27:50:46.25	3.9552	1.08	0.19	2
11717058	03:32:38.27	-27:50:39.43	4.43133	1.0	0.17	2
11719062	03:32:38.65	-27:50:44.36	4.79331	0.65	0.16	2
11727076	03:32:38.62	-27:50:29.79	5.31747	0.4	0.14	2
11728077	03:32:35.43	-27:50:31.01	5.40474	0.98	0.24	3
11729078	03:32:37.65	-27:50:22.46	5.52027	3.21	0.51	2
11739091	03:32:37.49	-27:50:09.89	5.76779	1.14	0.27	3
11802011	03:32:39.55	-27:50:13.25	3.13867	2.21	0.38	3
11806033	03:32:39.09	-27:50:35.32	3.65473	2.21	0.27	2
11814057	03:32:38.96	-27:50:34.58	4.09496	1.07	0.24	2
11818066	03:32:39.06	-27:50:22.87	4.41278	1.55	0.26	2

(1)	(2)	(3)	(4)	(5)	(6)	(7)
11821073	03:32:42.09	-27:49:52.99	4.41512	0.82	0.19	2
11834094	03:32:42.07	-27:50:28.07	5.29632	2.32	0.29	3
11901001	03:32:46.90	-27:50:04.50	2.99944	4.47	0.63	1
11902002	03:32:45.77	-27:49:28.53	3.0608	3.32	0.53	1
11903003	03:32:44.04	-27:50:33.68	3.30515	3.21	0.37	3
11904004	03:32:45.38	-27:50:10.45	3.31884	3.89	0.35	3
11905005	03:32:43.31	-27:49:46.83	3.33294	8.46	0.56	3
11906006	03:32:45.10	-27:50:28.00	3.39242	3.79	0.42	2
11907007	03:32:46.73	-27:50:17.10	3.39176	1.31	0.24	2
11916033	03:32:44.70	-27:50:30.81	4.033	0.78	0.18	2
11917034	03:32:43.56	-27:49:45.31	4.03858	1.31	0.21	2
11923056	03:32:44.67	-27:50:03.35	4.43612	0.87	0.18	2
11926065	03:32:44.90	-27:50:14.33	4.49961	1.48	0.21	2
11927066	03:32:45.39	-27:49:40.12	4.50419	0.57	0.15	2
11929068	03:32:43.72	-27:50:38.04	4.7573	1.75	0.21	3
11931070	03:32:43.17	-27:50:34.91	4.83644	2.53	0.22	3
11933072	03:32:45.83	-27:50:15.14	5.07705	0.45	0.13	2
11936075	03:32:45.33	-27:50:00.54	5.33352	0.55	0.18	2
11938077	03:32:43.99	-27:50:07.37	5.56662	0.85	0.27	2
11939078	03:32:42.58	-27:49:51.48	5.61373	1.24	0.19	2
11940079	03:32:46.04	-27:49:29.64	5.78712	1.22	0.25	2
12003003	03:32:50.56	-27:49:40.89	3.30388	2.29	0.29	2
12004004	03:32:47.41	-27:49:55.63	3.36632	1.2	0.23	2
12006008	03:32:50.93	-27:49:45.64	3.67807	1.61	0.32	1
12009015	03:32:48.66	-27:49:51.65	4.1586	3.75	0.3	3
12011018	03:32:48.92	-27:49:58.94	4.43252	0.9	0.18	2
12017026	03:32:50.47	-27:49:35.50	4.81227	0.6	0.19	2
12018027	03:32:48.65	-27:49:21.45	4.84882	1.96	0.17	3
12021030	03:32:47.30	-27:49:25.77	5.07608	0.49	0.19	1
12101001	03:32:51.22	-27:49:25.88	2.9978	6.32	0.7	3
12103013	03:32:52.43	-27:49:26.33	3.18818	3.37	0.44	3
12104014	03:32:51.12	-27:49:56.75	3.30316	2.9	0.41	2
12107020	03:32:50.85	-27:49:03.02	3.56177	2.02	0.31	3
12112031	03:32:50.50	-27:49:28.95	3.73933	3.5	0.4	3
12113032	03:32:51.48	-27:49:51.57	3.7408	1.54	0.31	2
12117043	03:32:50.97	-27:49:19.67	4.1712	2.2	0.31	2
12118044	03:32:51.02	-27:49:17.07	4.16939	1.08	0.26	2
12119045	03:32:53.66	-27:49:50.60	4.2713	1.38	0.2	2
12124068	03:32:50.76	-27:49:32.49	4.7704	1.83	0.22	3
12132077	03:32:50.62	-27:49:34.72	5.40286	1.4	0.31	2
12134079	03:32:52.27	-27:49:47.63	5.78934	1.14	0.27	1
12135080	03:32:51.44	-27:49:21.97	5.79078	0.96	0.23	2
12202035	03:32:28.75	-27:49:52.59	5.31902	1.4	0.21	1
12202034	03:32:28.74	-27:49:53.16	3.00275	6.92	0.55	3
12204055	03:32:30.46	-27:50:21.50	3.06515	1.3	0.32	2
12205056	03:32:33.08	-27:50:01.50	3.0648	1.77	0.3	2
12207063	03:32:33.39	-27:50:10.84	3.14273	1.16	0.24	2
12210066	03:32:30.22	-27:49:47.98	3.23756	2.51	0.36	2
12211067	03:32:31.94	-27:49:48.53	3.2914	3.68	0.43	2
12212068	03:32:32.65	-27:49:49.57	3.31417	4.34	0.37	3
12213069	03:32:31.09	-27:49:50.79	3.60612	6.02	0.48	2
12221111	03:32:33.32	-27:50:07.36	3.79896	6.67	0.34	3
12222112	03:32:32.08	-27:50:34.12	3.79857	1.5	0.26	2

(1)	(2)	(3)	(4)	(5)	(6)	(7)
12228123	03:32:32.46	-27:50:25.73	4.14251	1.06	0.2	2
12232127	03:32:31.82	-27:50:14.83	4.34987	0.63	0.17	2
12235132	03:32:32.57	-27:50:32.27	4.66123	0.74	0.17	1
12236133	03:32:32.77	-27:50:08.56	4.70682	2.36	0.29	2
12239136	03:32:31.65	-27:49:36.85	4.90871	0.96	0.19	2
12306090	03:32:33.53	-27:50:05.30	3.20188	1.36	0.27	2
12307091	03:32:34.85	-27:50:04.93	3.26495	4.23	0.43	2
12316117	03:32:36.82	-27:50:08.28	3.48971	1.43	0.29	2
12318120	03:32:34.22	-27:49:35.57	3.57051	7.41	0.4	3
12327133	03:32:34.71	-27:49:51.62	5.80174	0.94	0.2	2
12331149	03:32:34.94	-27:49:24.06	3.78873	1.96	0.26	2
12348186	03:32:34.97	-27:49:30.98	4.37893	0.73	0.22	2
12350190	03:32:36.45	-27:49:35.21	4.49551	2.93	0.25	3
12351191	03:32:33.56	-27:49:36.41	4.50745	1.74	0.23	3
12353193	03:32:35.16	-27:50:12.93	4.55389	0.82	0.15	2
12361203	03:32:35.10	-27:50:04.44	5.16289	1.46	0.2	3
12401001	03:32:40.80	-27:49:36.17	3.06788	1.31	0.31	1
12403012	03:32:39.51	-27:49:09.61	3.33652	2.56	0.49	2
12404013	03:32:39.88	-27:49:11.33	3.41916	8.39	0.51	3
12405014	03:32:36.86	-27:49:16.12	3.56996	3.11	0.44	3
12411026	03:32:40.85	-27:49:11.98	3.96061	1.96	0.24	2
12414030	03:32:40.70	-27:49:36.78	4.02789	2.2	0.25	3
12415031	03:32:37.46	-27:49:16.45	4.03176	1.64	0.23	2
12424054	03:32:37.96	-27:49:59.24	4.26939	1.61	0.25	3
12426056	03:32:38.85	-27:49:08.55	4.49957	9.73	0.37	3
12427057	03:32:41.10	-27:49:41.86	4.50369	2.89	0.21	3
12428058	03:32:39.78	-27:48:59.20	4.62066	1.84	0.29	1
12433068	03:32:39.83	-27:49:25.90	5.04732	1.53	0.31	3
12438073	03:32:39.70	-27:49:59.36	5.1724	0.95	0.17	2

A.2 Spectral Atlas

For each of the 237 LAEs we present in Fig. A.1 the observed Lyman α 1D spectral profile. The extraction of the 1D spectra is explained in Chapter 5, Sect. 5.4. The dashed line are the fits of the asymmetric Gaussian model given in Eq. (5.1). The grey line is the corresponding error to each spectral bin. In each panel the wavelength axis is in Å and the flux density axis is in 10^{-20}erg s^{-1}cm^{-2}Å^{-1}.

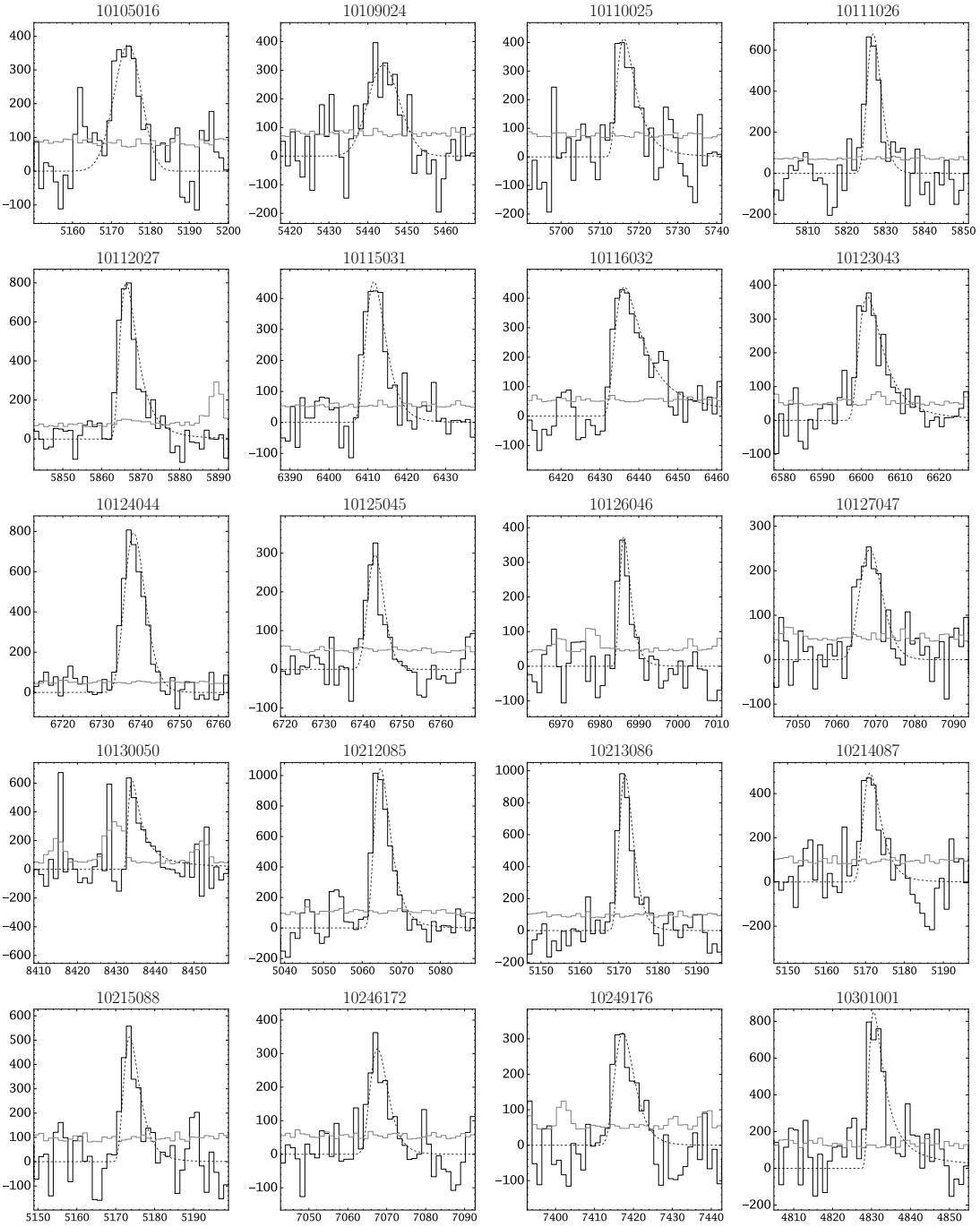

Figure A.1: Spectral Atlas of 237 Lyα 1D spectral profiles from the MUSE-Wide survey.

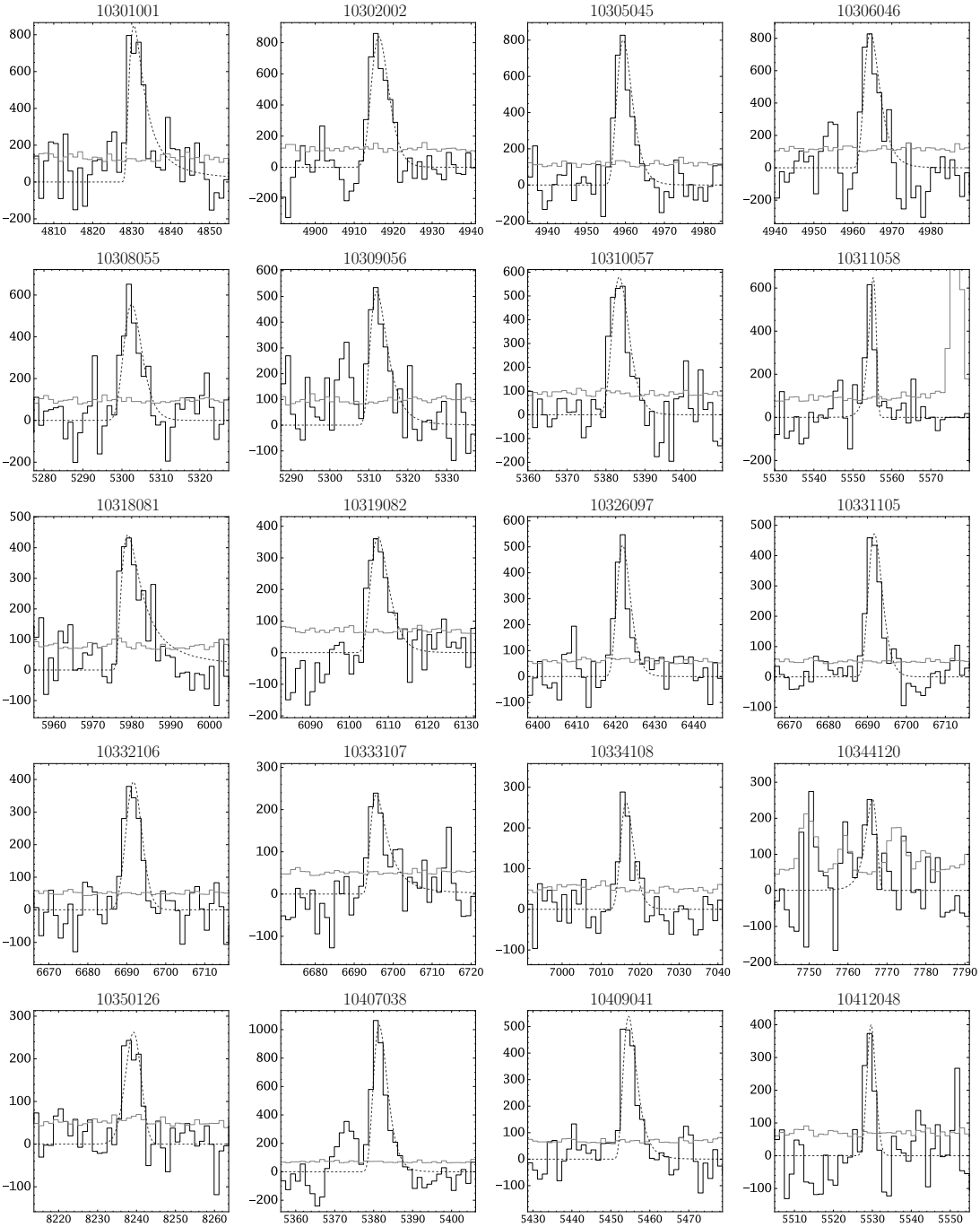

Figure A.1: Continued.

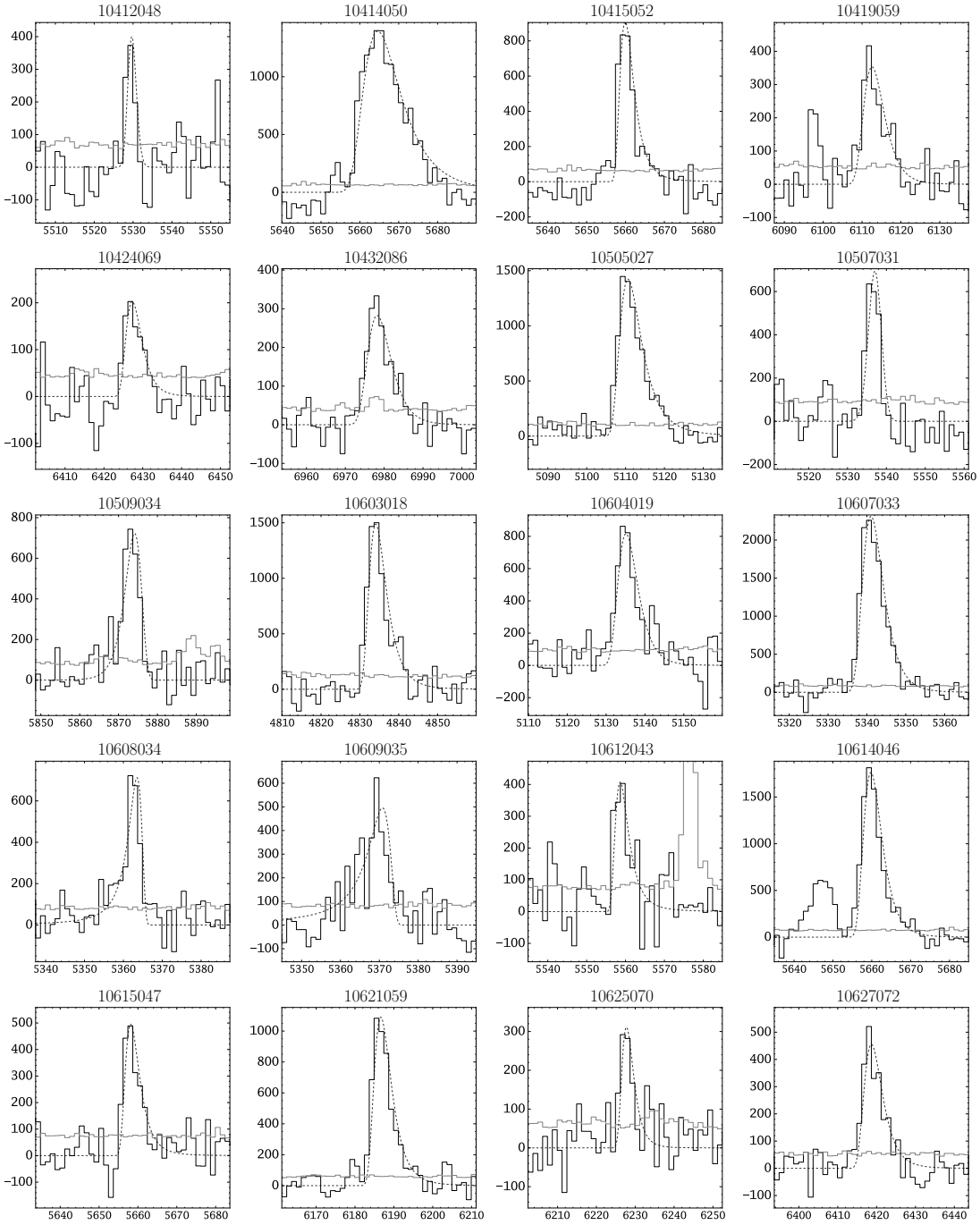

Figure A.1: Continued.

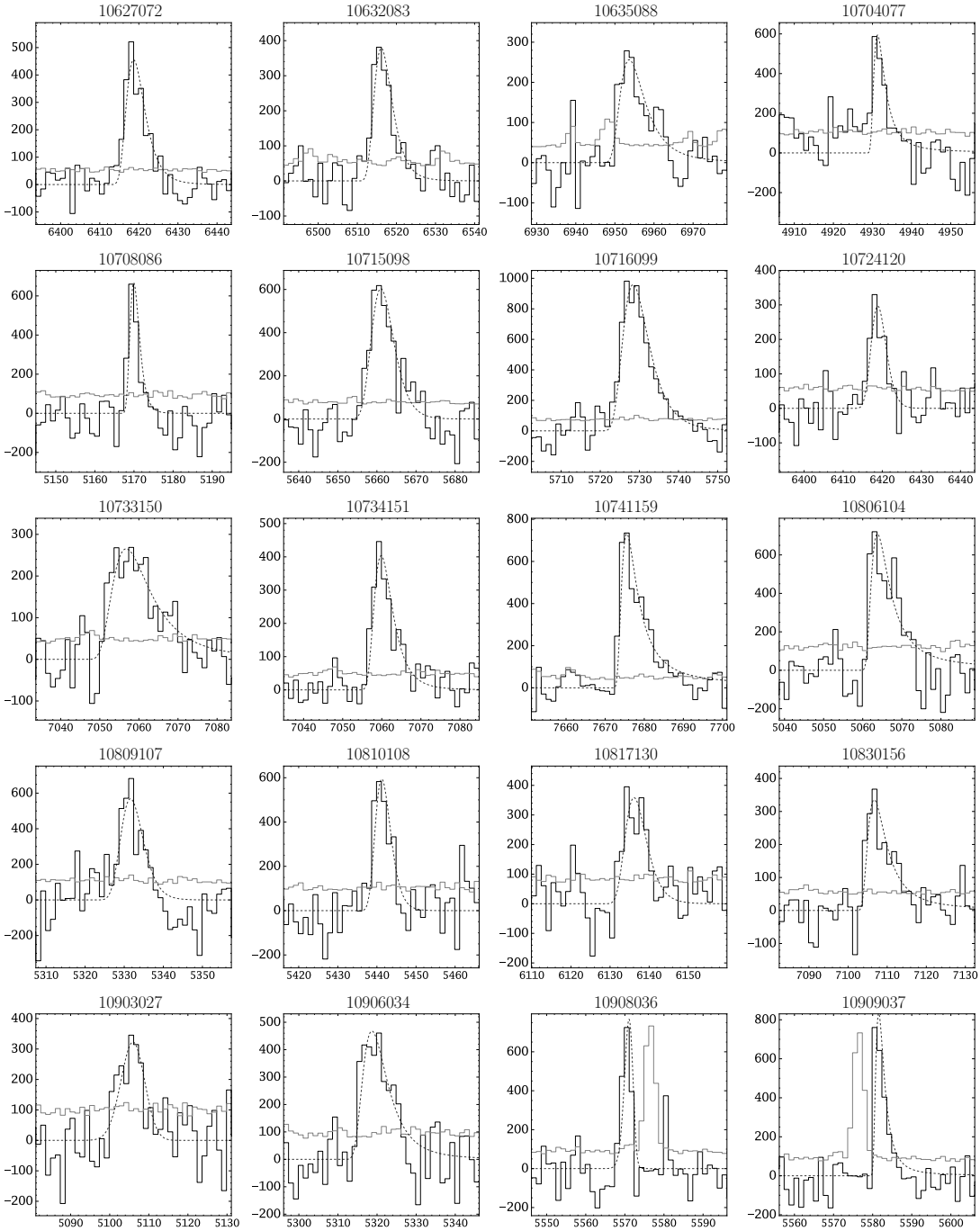

Figure A.1: Continued.

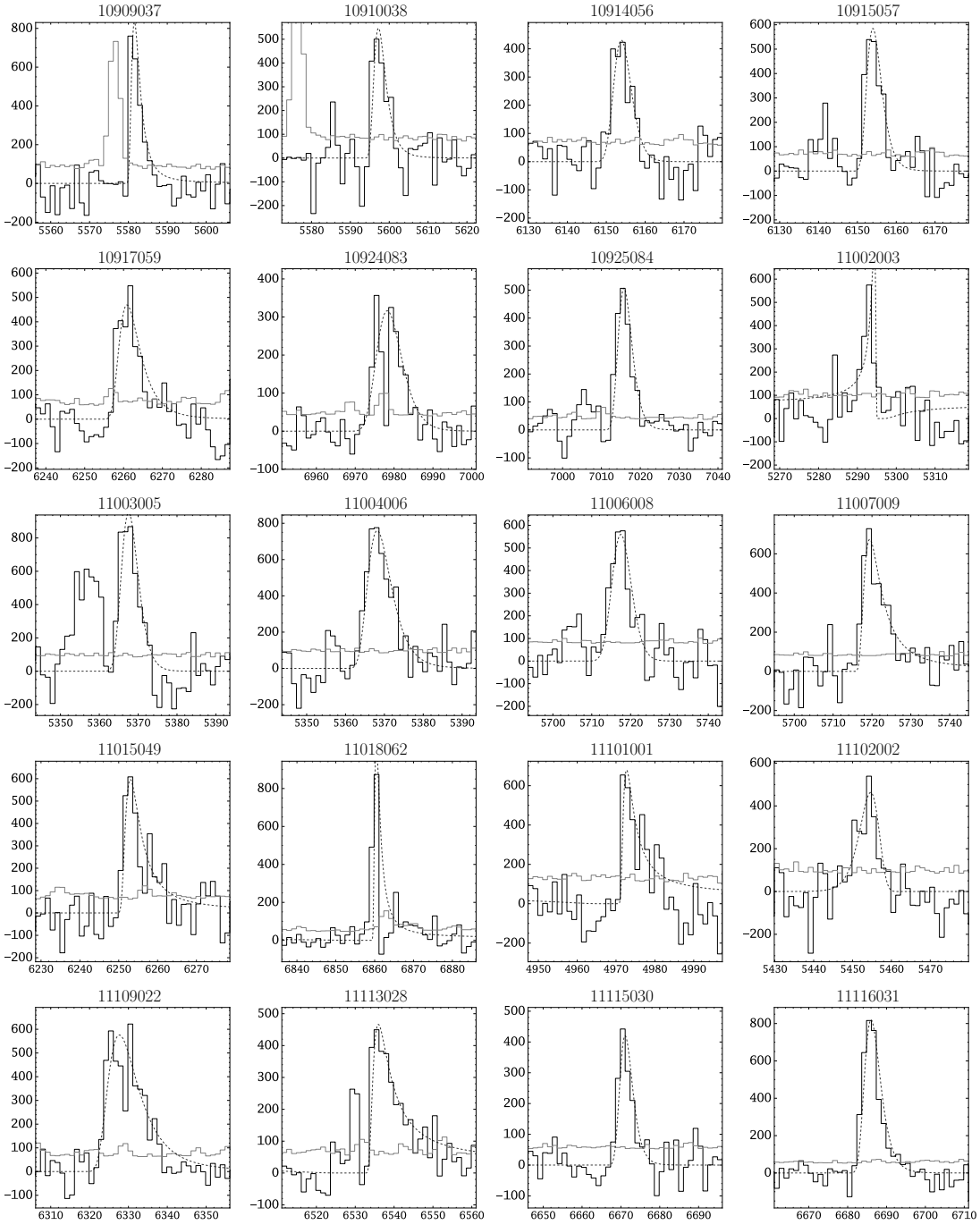

Figure A.1: Continued.

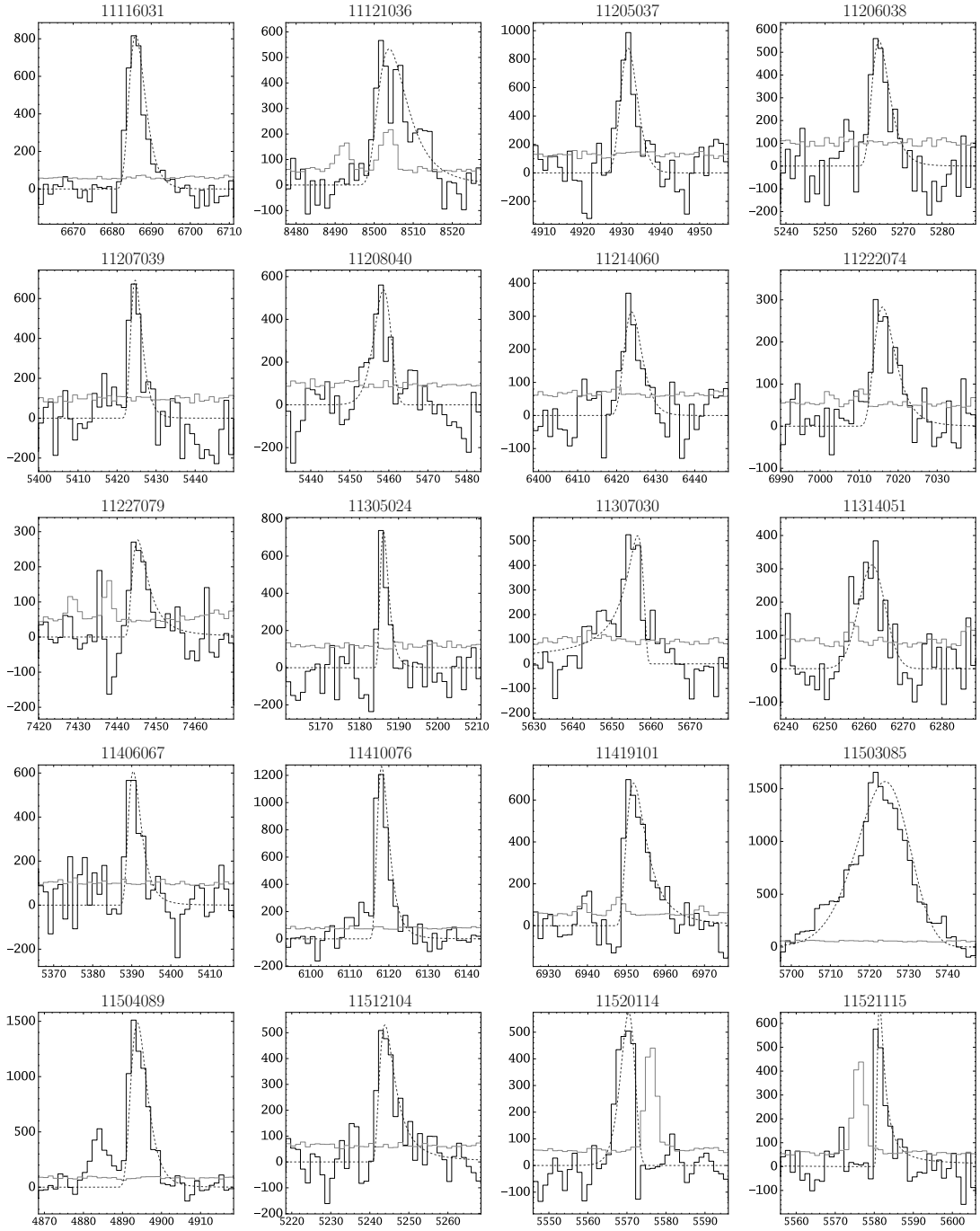

Figure A.1: Continued.

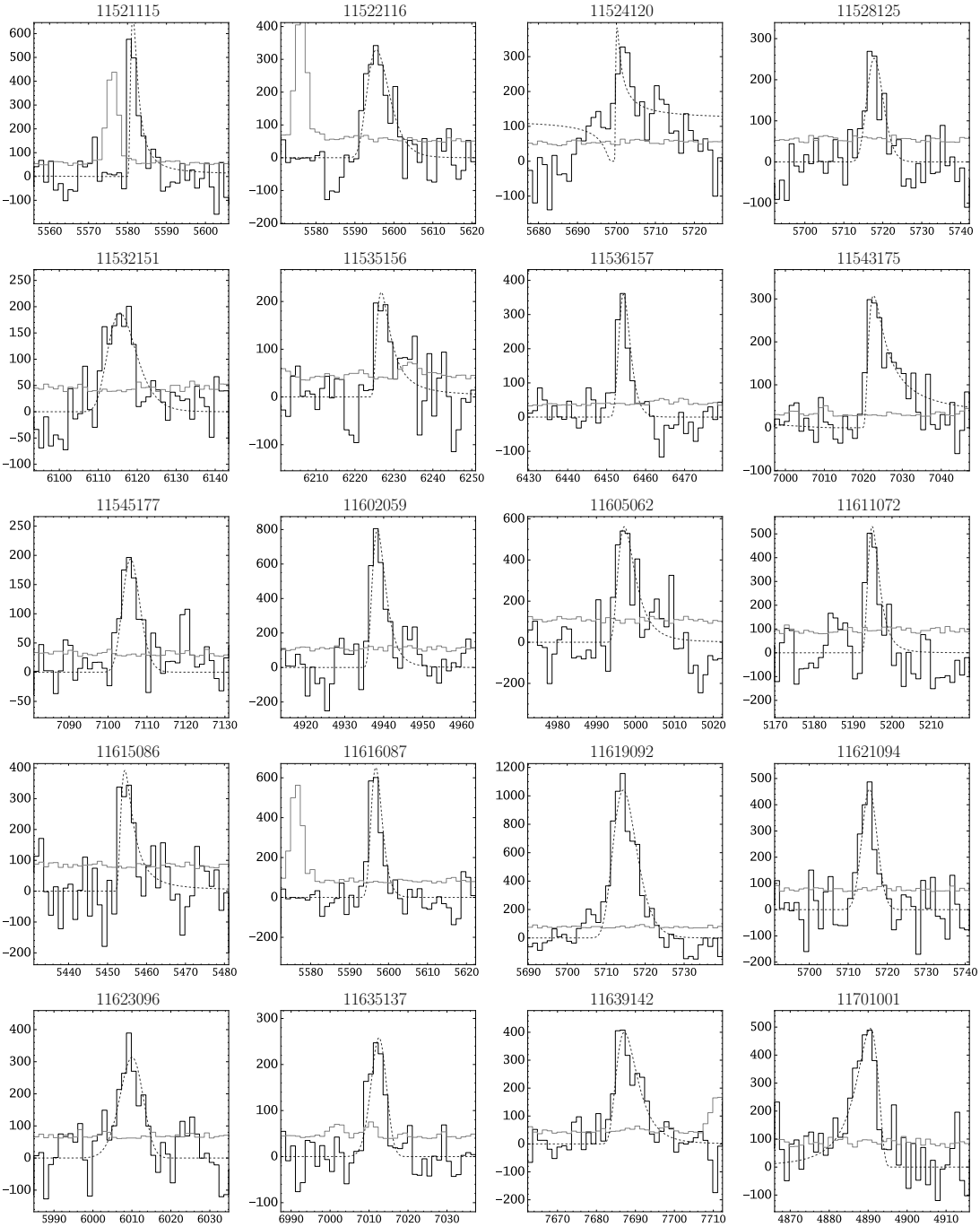

Figure A.1: Continued.

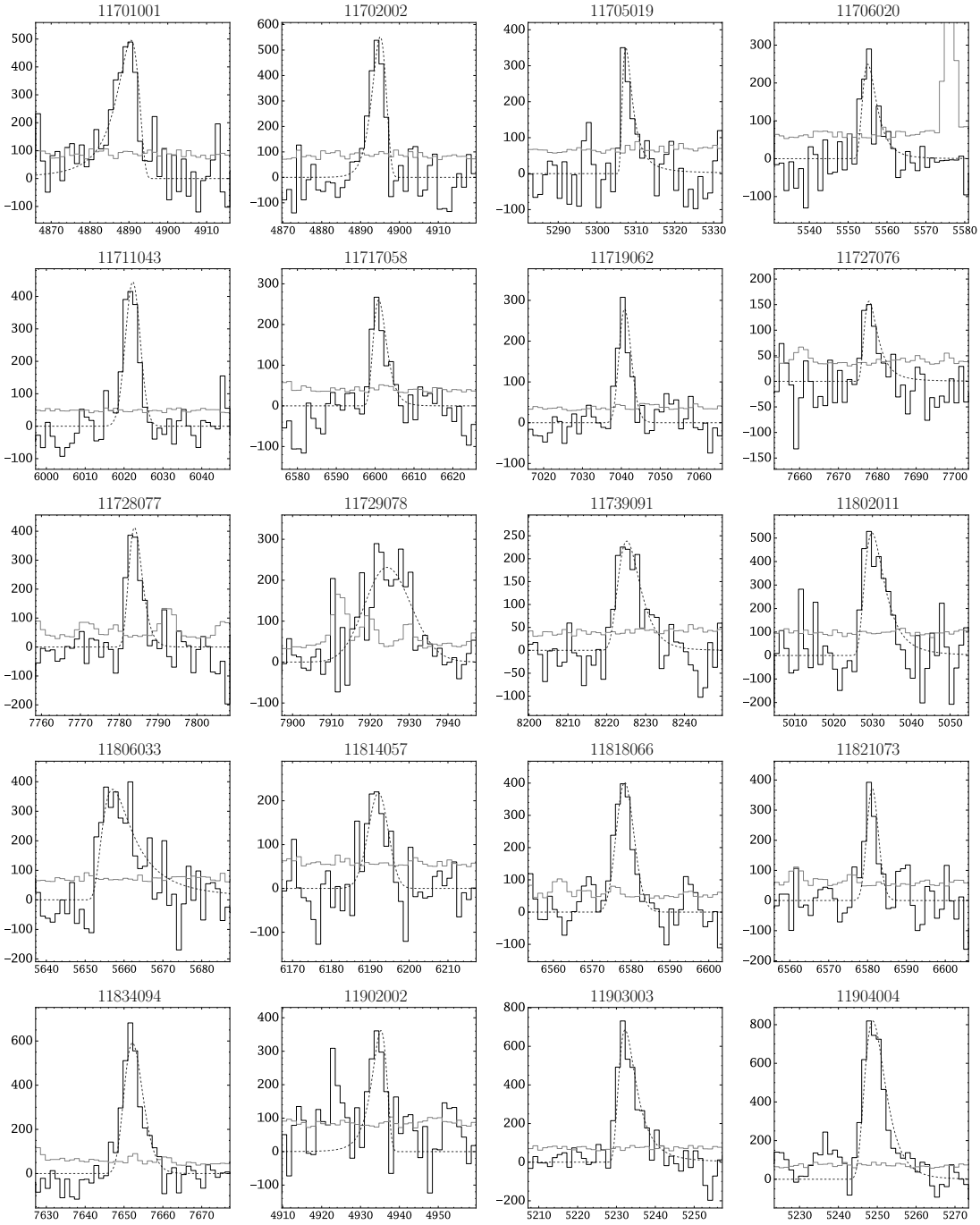

Figure A.1: Continued.

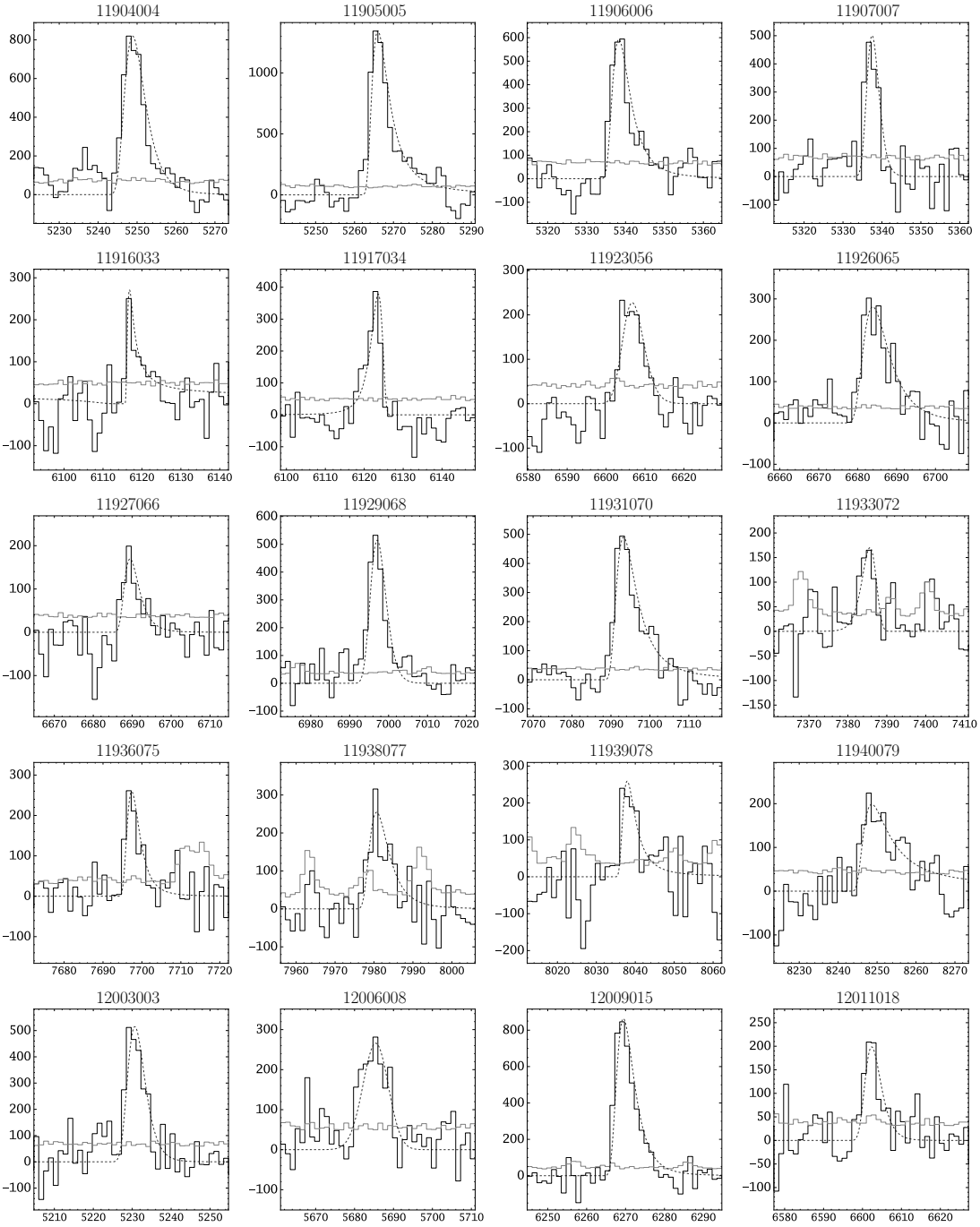

Figure A.1: Continued.

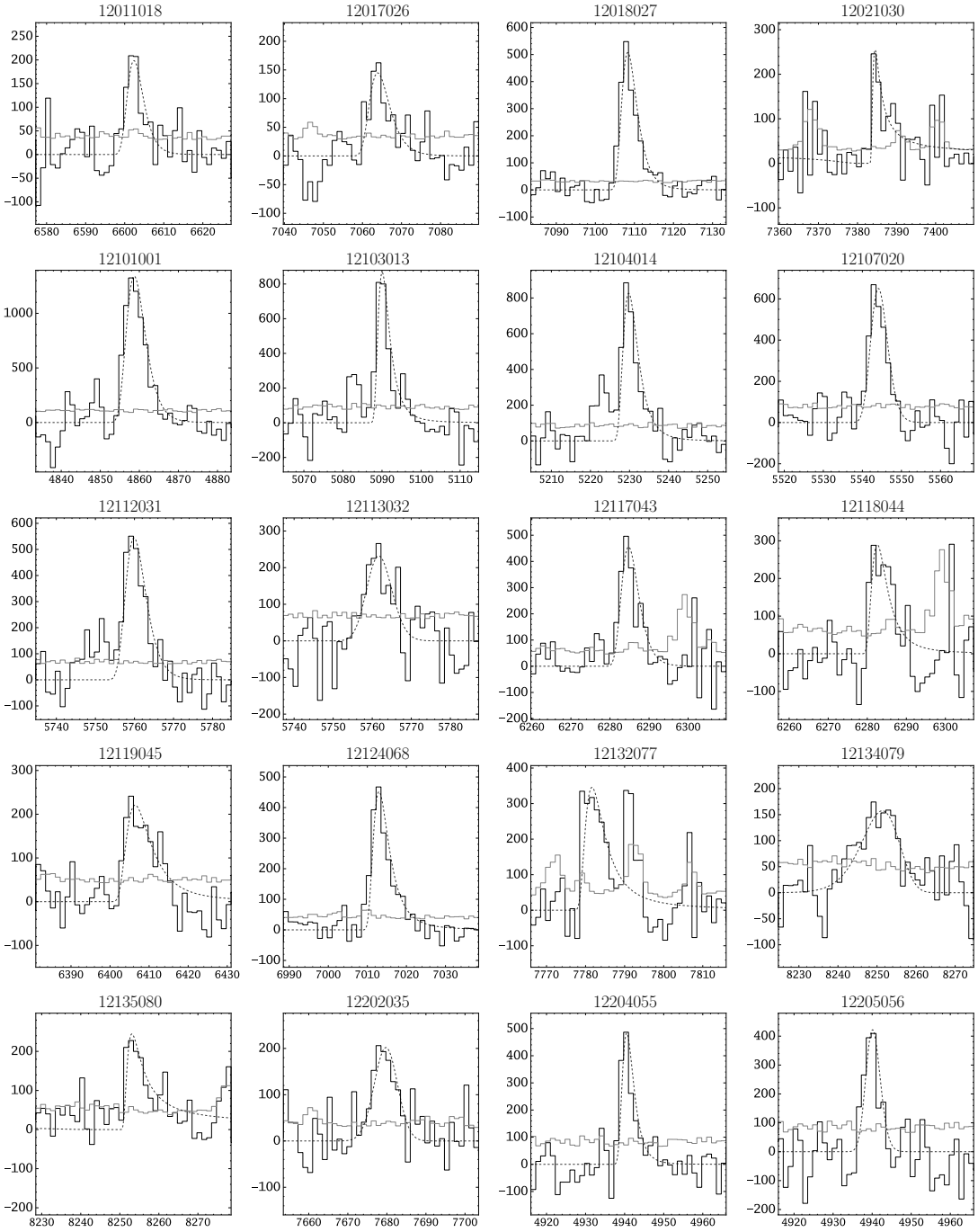

Figure A.1: Continued.

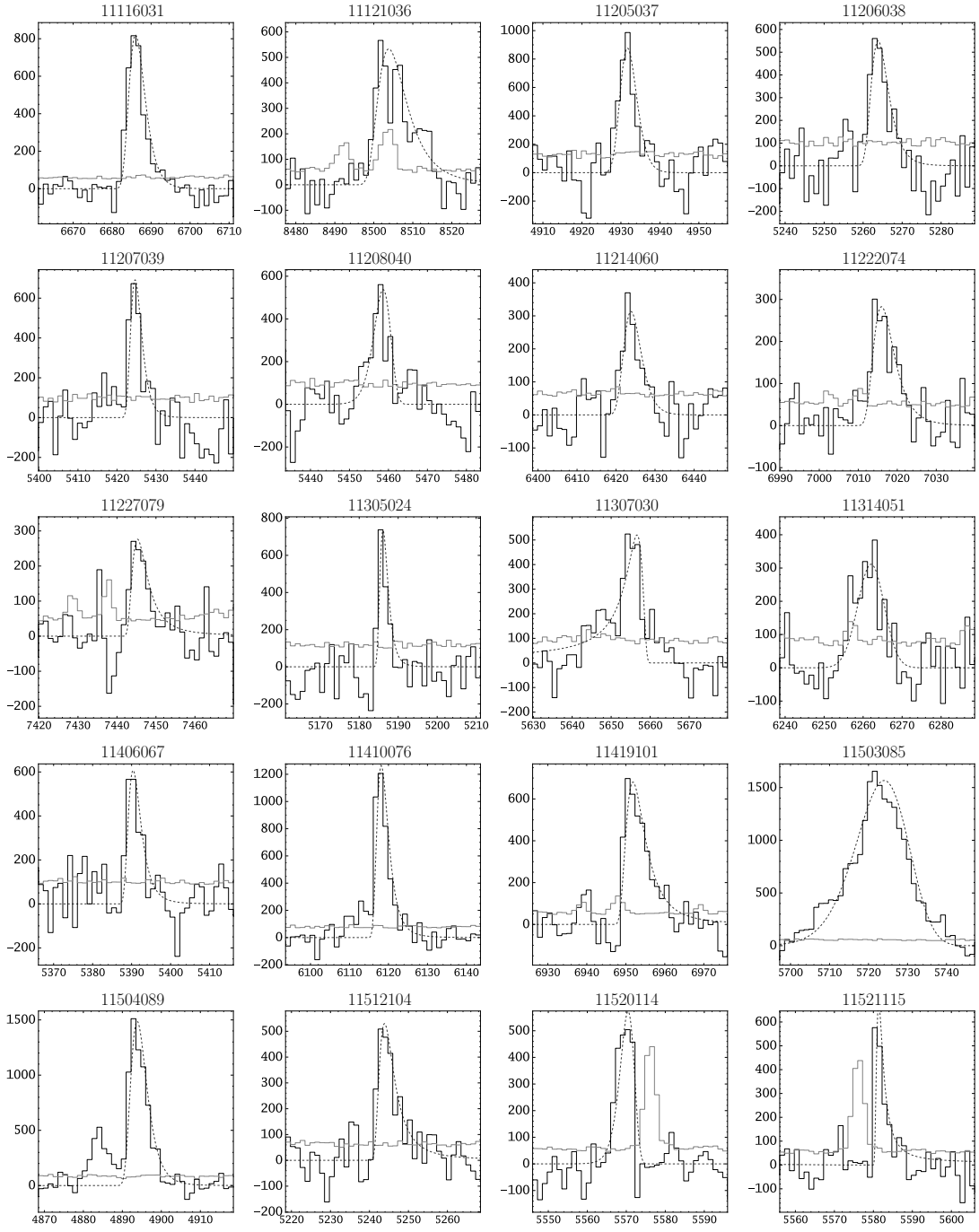

Figure A.1: Continued.

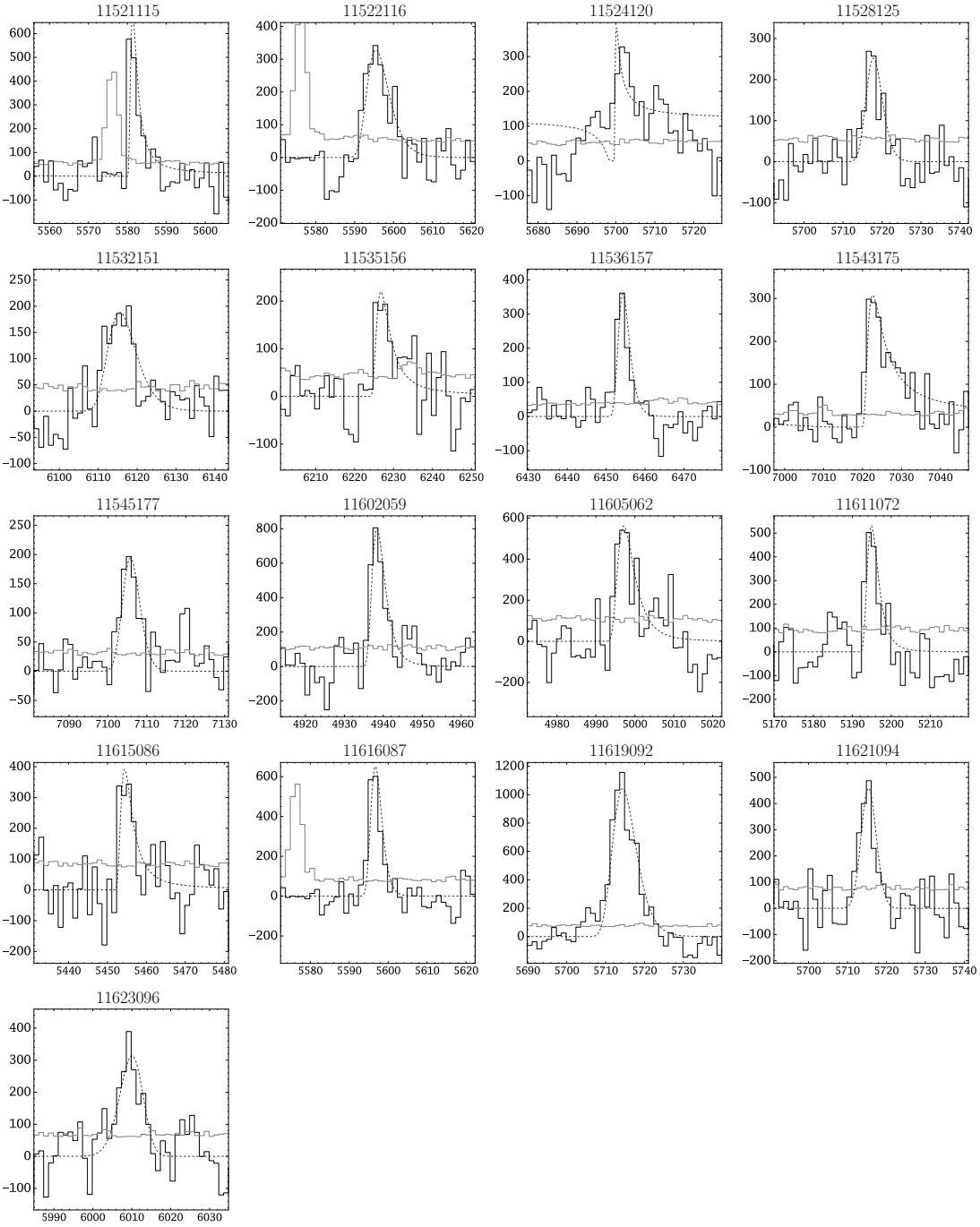

Figure A.1: Continued.

Appendix B

Publication List

The following is a list of the publications the author of this thesis. Versions of the published first author articles are presented in Chapter 2 and Chapter 3.

B.1 Lead Author

- E. C. Herenz, P. Gruyters, I. Orlitova, M. Hayes, G. Östlin, J. M. Cannon, M. Roth, et al. (2016) *The Lyman alpha reference sample. VII. Spatially resolved Hα kinematics* (2016), A&A **587**, A78
- E. C. Herenz, L. Wisotzki, M. Roth & F. Anders - *Where is the Fuzz? Undetected Lyman α Nebulae around QSOs at z∼2.3* (2015), A&A **576**, A115

B.2 Co-Author

- E. Borisova, S. Cantalupo, . . . , E.C. Herenz, . . . , (2016) *Ubiquitous giant Lyman α nebulae around the brightest quasars at z ∼ 3.5 revealed with MUSE*, ApJ submitted, `arXiV:1605.01422`
- D. Bina, R. Pello, . . . , E.C. Herenz, . . . , (2016) *MUSE observations of the lensing cluster Abell 1689*, A&A **590** A14
- L. Wisotzki, R. Bacon, J. Brinchman, J. Blaziot, E. C. Herenz, et al. (2016) *Extended Lyman alpha haloes around individual high-redshift galaxies revealed by MUSE* , A&A **587**, A98
- F. Duval, G. Östlin, M. Hayes, . . . , E.C. Herenz, . . . , (2016) *The Lyman Alpha Reference Sample. VI. Lyman alpha escape from the edge-on disk galaxy Mrk 1486*, A&A **587**, A77
- T. E. Rivera-Thorsen, M. Hayes, . . . , E.C. Herenz, . . . , (2015) *The Lyman Alpha Reference Sample. V. The Impact of Neutral ISM Kinematics and Geometry on Lyα Escape*, ApJ **805**, 14
- L. Guaita, J. Melinder, . . . , E.C. Herenz, . . . , *The Lyman α Reference Sample. IV. Morphology at low and high redshift* (2015), A&A **576**, A51
- R. Bacon, J. Brinchmann, . . . , E.C. Herenz, . . . , *The MUSE 3D view of the Hubble Deep Field South* (2015), A&A **575**, A75

- G. Östlin, M. Hayes, ..., E.C. Herenz, ...(2014), *The Lyman α Reference Sample. I. Survey Outline and First Results for Markarian 259*, ApJ **797**, 11
- S. A. Pardy, J.M. Cannon, ..., E.C. Herenz, ...(2014) - *The Lyman α Reference Sample. III. Properties of the Neutral ISM from GBT and VLA Observations*, ApJ **794**, 101
- M. Hayes, G. Östlin, ..., E.C. Herenz (2013) - *The Lyman α Reference Sample. II. Hubble Space Telescope Imaging Results, Integrated Properties, and Trends*, ApJ **782**, 6
- M. Hayes, G. Östlin, ..., E.C. Herenz, ...(2013) - *The Lyman α Reference Sample: Extended Lyman α Halos Produced at Low Dust Content*, ApJ **765**, L27

Appendix C

Danksagung

Gerüchten zufolge handelt es sich bei diesem Anhang um den Teil einer Doktorarbeit der die größte Aufmerksamkeit abbekommt. Machen wir es kurz...

Mit einem lachenden, aber auch mit einem weinendem Auge, gilt es nun Abschied zu nehmen von der schönen “Doktorandenzeit”.

Viele Personen haben einen großen Anteil daran, dass diese Arbeit überhaupt möglich wurde. Namentlich möchte ich mich bedanken bei:

- Lutz Wisotzki. Für eine sehr interesannte und lehrreiche Zeit. Und natürlich für jährlich wiederkehrenden kulinarischen Höhepunkte in Berlin-Steglitz.
- Martin Roth. Für PMAS, das Instrument welches mein Interesse an der Astrophysik geweckt hatte.
- Tanya Urrutia: Für viel Zuspruch und Diskussionen. Unvergessen unsere gemeinsame Zeit in der Lehre mit den Erstis.
- Peter Weilbacher: Für nicht endende Schokoladenreserven beim Beobachten mit MUSE.
- Jakob Walcher: Für einen ganz speziellen Anpfiff: “Du willst Doktorand sein? Du weißt ja noch nichtmal was Detektionssignifikanz bedeutet!”.
- Friedrich Anders: For Korrekktürlesen.

I also would like to thank Roland Bacon for making MUSE happen. What an awesome instrument!

Moreover, I also whish to thank my Swedish collaborators Göran Östlin and Matthew Hayes. I am looking forward working with and learning from you in the future!